LASERS AND LANDING SITES:
THE GEOMORPHOLOGY, STRATIGRAPHY, AND COMPOSITION OF MARS

A Dissertation

Presented to the Faculty of the Graduate School

of Cornell University

In Partial Fulfillment of the Requirements for the Degree of

Doctor of Philosophy

by

Ryan Anderson

January 2012

LASERS AND LANDING SITES:
THE GEOMORPHOLOGY, STRATIGRAPHY, AND COMPOSITION OF MARS

Ryan Anderson, Ph. D.

Cornell University 2012

With each new mission to Mars, the amount of available data increases dramatically. This drastic increase in data volume requires new approaches to take advantage of the available information. The goal of the work presented here is to maximize the science return from existing and future datasets.

Chapter 2 uses multiple orbital datasets to characterize Gale Crater, with a focus on the northwestern crater floor and lower mound. This work played a role in the selection of Gale Crater as the landing site for Mars Science Laboratory (MSL). It was not possible to conclusively determine the origin of the lower mound, but we interpret features on the upper mound as aeolian cross-beds.

Chapters 3 and 4 investigate methods for improving the accuracy of laser-induced breakdown spectroscopy (LIBS). In Chapter 3, the accuracy of partial least squares (PLS) and two types of neural network are compared, using several pre-processing methods including automated feature selection. We find that partial least squares without averaging typically gives the best results. Chapter 3 also investigates the influence of grain size on the accuracy of analyses, showing that >20 analysis spots may be required for heterogeneous targets. In Chapter 4, we test the hypothesis that clustering the dataset before analysis leads to improved accuracy. We observe modest improvements for five k-means clusters and with iterative application of clustering and PLS.

In Chapter 5, we use several methods to relate Mars Exploration Rover (MER) Panoramic camera multispectral observations to alpha particle X-ray spectrometer and Mössbauer spectrometer results. The correlation between the Gusev datasets is often poor although there is some improvement when only data from drilled spots is considered. The performance is better for the Meridiani data, but Meridiani PLS models are not generalizable to Gusev data. MSL ChemCam analyses and MastCam spectra may show higher correlations because the instruments have a similar information depth.

Clustering and classification methods can be used on any dataset, and as the volume of data from planetary missions continues to increase, synthesis of multiple datasets using multivariate methods such as those in this work will become increasingly important.

BIOGRAPHICAL SKETCH

Ryan Anderson was born in Detroit, MI in 1984. He was interested in science from a young age, and his parents did everything they could to encourage that interest: taking him to libraries and museums, providing model rocket kits and chemistry sets, tolerating the snakes and turtles and bugs that he caught and tried to raise, and encouraging collections of insects, shells, and rocks. In middle school Ryan discovered speculative fiction and has been fascinated by other worlds—real and imagined—ever since. In his high school astronomy class, Ryan came to the realization that it is someone's job to send missions to other planets. He thought that sounded like a pretty cool job. That same class led him to discover Carl Sagan's books, which he read over the summer of 2002 along with the Mars trilogy by Kim Stanley Robinson and the collected short stories of Arthur C. Clarke. With those influences fresh in his mind when he started as an undergraduate at the University of Michigan, it was only a matter of time before Ryan declared a double major in Physics and Astrophysics.

An initial research project doing stellar spectroscopy at the University of Michigan provided the skills and experience that led to a summer internship doing infrared astronomy at the Harvard-Smithsonian Center for Astrophysics in 2004. Ryan found himself drawn to planetary science because of its interdisciplinary nature, and he pursued this interest as a summer intern at the Lunar and Planetary Institute in 2005, where he mapped buried basins on Mars. As an undergraduate, Ryan also discovered that he enjoyed communicating science to the public, whether running the campus planetarium or building dry-ice comets with elementary school kids. He continues to seek opportunities to educate others about science whenever he can. After graduating with a B.S. from the University of Michigan in 2006, he spent a thrilling but exhausting summer in the NASA Academy at Goddard Space Flight Center, before beginning as a graduate student at Cornell University. He earned his M.S. in Astronomy from Cornell in 2009, and his Ph.D. in 2012.

This dissertation is dedicated to my parents, Theron and Kendra Anderson, who taught me to love reading and learning. All the rest follows from that.

ACKNOWLEDGMENTS

I would like to thank:

My wife Erin, for her steadfast support, for tolerating my many weeks away from home, and for reminding me that there are more important things in life than work.

Our dog Renly, because grad school stress disappears at the dog park.

Seth Humphries and Rhonda McInroy for many long hours helping me zap rocks, Trevor Graff for preparing all of the rocks and powders to zap, and Loan Le for helping me fabricate and analyze so many analog glasses, even after I spilled silica in her furnace.

Ken Edgett, for going above and beyond the call of duty in his review of my Gale Crater work, and in doing so, dramatically improving the manuscript and teaching me to be a much better geomorphologist.

Ed Cloutis for the chance to visit scenic Winnipeg and its surrounding Mars analogs, the opportunity to contribute to the LIRA project, and for funding my final semester (and countless "business meetings" at conferences). "Thank you CSA."

John Grotzinger and the Agouron Institute, Scott Rowland and the NASA Planetary Volcanology Field Workshop, and the MSL Mastcam/MARDI/MAHLI team for opportunities to

learn geology in spectacular field areas from world experts. These field experiences made me an immeasurably better geologist.

Sam Clegg and Roger Wiens for letting me use their laser, for all of their valuable time and guidance as I learned the nuances of LIBS, and for welcoming me to the ChemCam team.

Dick Morris, for serving as my *de facto* second adviser, for his valuable guidance and the use of his extensive sample library, and for giving me the chance to take a break from shuffling bits on my computer to get my hands dirty in the lab.

And finally, my adviser Jim Bell, for teaching me all of the important lessons about being a good scientist that aren't in any textbook, for letting me try a little bit of everything, and for opening so many doors and deftly guiding me through them.

This work was supported by the NASA Graduate Student Researchers Program, NASA grants and contracts from the Mars Data Analysis Program and the Mars Science Laboratory project, NASA's Johnson Space Center, and the Canadian Space Agency.

TABLE OF CONTENTS

LIST OF FIGURES

Chapter 1:

Chapter 2:

Chapter 3:

Chapter 4:

Chapter 5:

LIST OF TABLES

Chapter 2:

Chapter 3:

Chapter 4:

Chapter 5:

CHAPTER 1
EXPLORING MARS IN THE INFORMATION AGE

As the first data were downlinked from the Mariner 4 probe, it trickled down to Earth so slowly that JPL employees used colored pastels to fill in the pixels one by one, manually producing the first spacecraft image of Mars[1][2]. The Mariner 4 mission returned a total of 22 images [3], and was followed by Mariners 6 and 7, returning 26 and 33 near-encounter images, respectively[4]. A complete map of the planet's surface would have to wait for the arrival of Mariner 9 in orbit and the dissipation of a global dust storm[5]. Preliminary landing sites for the Viking landers were chosen using Earth-based radar and Mariner 9 observations [6], but images from the Viking 1 orbiter, with resolutions ranging from 100 m to 5 km per pixel, revealed that the primary landing site for Viking 1was too rugged[6], [7]. Instead, an alternate site to the northwest was selected. The lander touched down successfully, but images from the surface revealed a rocky surface which could easily have damaged an unlucky lander [8]. The initial landing site for Viking 2 was also found to be too rough in orbital images, and an alternate site in Utopia Planitia was selected. The higher northern latitude of the Viking 2 sites prevented Earth-based radar observations [6].

Modern Mars exploration no longer suffers from a lack of data. Mars Global Surveyor (MGS) orbited the planet for 7.5 Earth years and returned detailed global topography [9], color maps of the entire planet at 230 m per pixel and high-resolution images at 1.5 m per pixel [10], and thermal emission spectra and mineral maps at 3 km per pixel [11]. Following the success of MGS, the Mars Odyssey mission arrived at Mars in 2001 and has returned global daytime and nighttime

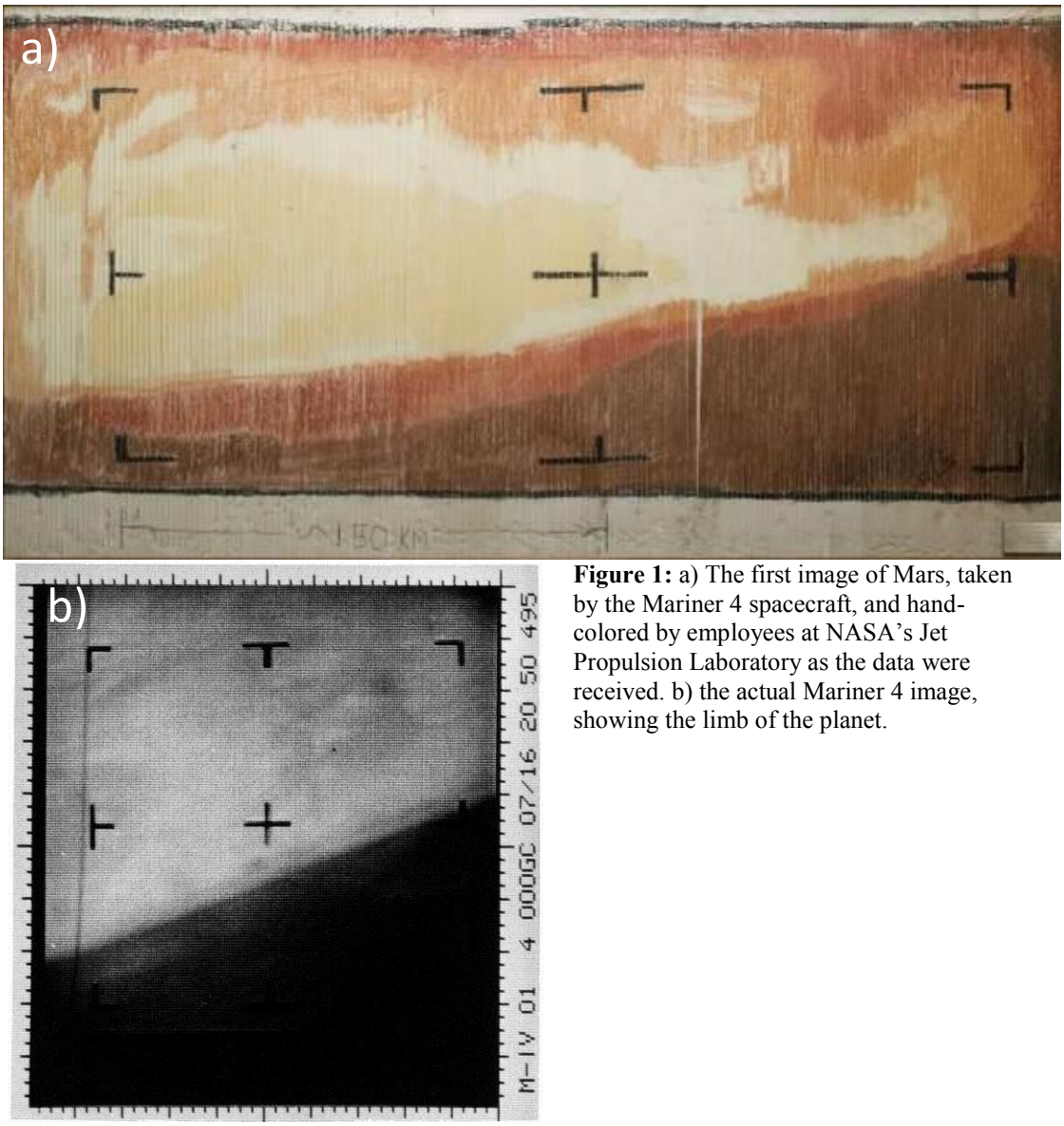

Figure 1: a) The first image of Mars, taken by the Mariner 4 spacecraft, and hand-colored by employees at NASA's Jet Propulsion Laboratory as the data were received. b) the actual Mariner 4 image, showing the limb of the planet.

thermal infrared maps at 100 m per pixel and 18 m per pixel visible images [12], along with abundance maps for K, Fe, Si, Th, U, S, H, and Cl, based on gamma-ray spectrometer data [13]. A third orbiter, Mars Express, arrived at Mars in 2003 carrying a wide range of instruments, including a visible to near-infrared (VNIR) mapping spectrometer, ground-penetrating radar, a fourier spectrometer and a UV/IR spectrometer for atmospheric studies, an energetic neutral atom analyzer, and a stereo color camera capable of collecting color stereo images at 2 m per pixel [14].

The steady stream of orbital data provided by MGS, Mars Odyssey and Mars Express became a flood with the arrival of the Mars Reconnaissance Orbiter (MRO) in 2006. MRO transmits data at ~6 Mbits per second, a significant improvement over its predecessors, and carries six science instruments. These include the High Resolution Imaging Science Experiment (HiRISE) which is capable of collecting color images at 25 cm per pixel [15]; the Compact Reconnaissance Imaging Spectrometer for Mars (CRISM), a VNIR imaging spectrometer with a spatial resolution of up to 18 m per pixel [16]; the Context Camera (CTX) which images large swathes of the surface at 6 m per pixel [17]; the Mars Color Imager (MARCI), a wide-angle camera for daily global atmosphere and dust storm monitoring[18]; SHARAD ground-penetrating radar; and the atmospheric profiler Mars Climate Sounder (MCS)[19]. MRO has now returned more data than all previous missions combined.

1. Post-Viking Landing Site Selection

The first landed mission after Viking 2 was the Mars Pathfinder mission, which relied upon Viking observations and Earth-based data, including images, radar, early topographic maps and estimates of surface physical properties (e.g. thermal inertia, roughness, albedo) to select a site. Forty potential sites were initially proposed, but the latitude (10-20° N) and elevation requirements (< 0 km elevation) of the mission narrowed this list down to 4. The landing ellipse for Mars Pathfinder was large (70 km by 200km) and a site in Ares Valles was selected because it met the engineering and safety requirements and because its position in the mouth of a large outflow channel was hoped to provide a "grab bag" of samples from diverse sources [20].

Landing site selection for the Mars Exploration Rovers (MERs) benefitted from MGS and Mars Odyssey data, permitting more a more sophisticated discussion of the scientific potential of possible sites. Out of 185 initially proposed landing sites, the Mars science community selected

25 sites on the basis of high-resolution Mars Orbital Camera (MOC) imaging and overall science potential. These were further downselected to six sites, three of which were then excluded based on engineering concerns, including horizontal wind speeds, surface slopes and rocks. The Opportunity rover landing site in Meridiani Planum was selected based on the strong thermal emission spectroscopy (TES) signature of coarse-grained hematite on the surface [21], and the Gusev Crater landing site for the Spirit rover was selected on the basis of geomorphology, indicating that the crater once was the catchment for flowing water that breached the southern rim to form Ma'adim Vallis [22]. The prediction of the physical properties of the sites such as thermal inertia, albedo, rock abundance and slopes were successful[23]. However, the geologic interpretation of the sites based on orbital data proved more difficult. The hematite detected by TES at Meridiani was interpreted upon landing to be the result of precipitation in acidic, saline groundwater [24], but the floor of Gusev Crater was found to be primarily basaltic, with no evidence for lacustrine deposits [25].

The Phoenix lander was the first mission to benefit from MRO data during the landing site selection process. Phoenix was required to land between 65° and 72° N at an elevation below -3.5 km with safe wind speeds. Within the latitude range considered, all areas satisfied the elevation and wind speed requirements, but rock abundance was a significant concern. MOC images of the preferred landing site for Phoenix suggested an acceptable rock abundance, but early HiRISE images with their higher resolution (~30 cm per pixel) revealed rock abundances exceeding the safety limit defined by the Viking 2 site. This led to the selection of an alternate landing site based on HiRISE, CRISM, CTX and THEMIS data [26]. HiRISE images also showed that much of the terrain under consideration for the Phoenix landing site exhibited pattered ground, supporting the Mars Odyssey Gamma Ray Spectrometer (CRS) results which

suggested the presence of ice or icy soil beneath a thin layer of surface soil in much of the latitude range considered [26]. This interpretation of the landing site characteristics proved to be very accurate: the first images of the landing site from the lander showed an expansive plain of patterned ground with very few large rocks, and the exhaust from the landing thrusters cleared away a thin layer of soil to reveal water ice ~5cm below the surface[27].

The landing site selection process for the Mars Science Laboratory mission has greatly benefitted from the significant volume of data from previous missions and the ability to target specific sites for detailed study with the suite of instruments on MRO. In addition, the novel MSL entry, descent and landing (EDL) system resulted in a significantly smaller landing ellipse (~20 km), allowing sites to be considered in which the primary science target was outside the landing ellipse. The selection process proceeded over 6 years and 5 landing site workshops that were open to the entire Mars science community. At the first workshop 33 potential sites were proposed, but additional data from MRO led to a total of 50 sites at the beginning of the second workshop. At the second workshop, the science potential of the sites was considered, based on the following criteria: 1) The ability to characterize the geology, 2) the likelihood of accessing a present or past habitable environment, 3) the preservation potential of the depositional setting, and 4) the ability to assess the biological potential of the deposits [28][29]. Based on these criteria and engineering considerations, the list was narrowed down to six sites shortly after the second workshop. Between the second and third landing site workshops, a call for new sites based on new MRO data went out. This call for new sites resulted in the addition of Gale crater and the replacement of the North Meridiani "ultra-safe" site with an equally safe, but scientifically more interesting South Meridiani site. Gale crater had been proposed at the first and second landing site workshops but evidence of phyllosilicate minerals was lacking.

However, after the second workshop, CRISM observations of the mound near the proposed ellipse showed evidence of both phyllosilicate and sulfate minerals [30]. The third landing site workshop resulted in a list of four "finalist" sites: Mawrth Vallis, Eberswalde Crater, Holden Crater, and Gale Crater. A second call for additional sites between the third and fourth workshops led to the proposal of seven possible sites, but after targeted MRO observations, none were deemed as attractive as the four finalists[29].

An extensive campaign of orbital observations from MRO, Mars Express, and Mars Odyssey allowed these four finalist sites to be characterized at a level of detail unprecedented in Mars exploration. All four sites were found to be extremely scientifically interesting and no clear favorite emerged at the 4th or 5th public workshops. Moreover, an extensive engineering analysis of the four sites reveals that they were essentially indistinguishable in terms of spacecraft safety. Shortly after the 5th workshop, the MSL science team ranked the four sites, listing Gale Crater and Eberswalde Crater as the top two sites, with a slight preference for Gale. Gale Crater was announced as the MSL landing site on July 22, 2011[31]. The Gale Crater landing site is discussed in detail in Chapter 2.

2. Mars Science Laboratory

The Mars Science Laboratory (MSL) mission launched on November 26, 2011 and will arrive at Mars in August 2012. MSL is intended to refine the successful "follow the water" strategy that has driven recent Mars exploration and "search for evidence of past and present habitable environments"[28]. To achieve this goal, MSL is carrying 80 kg of science instruments, and will be capable of traversing >20 km during its 1 Mars-year (~1.88 Earth year) primary mission.

Like previous missions, MSL has color cameras mounted on the mast. However, MSL's Mastcams [32] have two different focal lengths (34 mm and 100 mm).The Mastcams also use Bayer color filters to produce color images with a single exposure. In addition to the red, green, and blue Bayer filters, a filter wheel with narrow-band geological filters can be used to create multispectral observations with both the 34mm and 100 mm cameras. MSL also carries two other science cameras that make use of Bayer filters to return high-definition color images: the Mars Hand Lens Imager (MAHLI)[33] and the Mars Descent Imager (MARDI) [34]. MAHLI will serve a purpose similar to the microscopic imager on MER, providing images of targets in the rover work volume with up to 13.9 μm per pixel resolution. MAHLI is capable of focusing on targets from 20.4 mm out to infinity, so it can also be used for imaging of more distant targets, or to gain multiple perspectives of a target by moving the rover's arm rather than driving. MAHLI is also equipped with white light and UV LEDs which will enable night-time imaging and detection of fluorescent minerals[33]. MARDI is a downward-pointing camera mounted under the rover that will begin collecting 1600 x 1200 pixel frames at a rate of 4.5 frames per second as the heat shield is jettisoned during descent[34]. These images will provide high-resolution context for the landing site, and may be used to generate digital elevation models of the terrain. After collecting the descent video, MARDI may also be used during surface operations to collect images of the soil from a distance of ~70 cm and to provide visual odometry[34].

MSL will also carry several instruments for analyzing samples collected by the percussion drill on the rover's arm, which produces a powder with ~90% of particles < 150 microns [35]. The Chemistry and Mineralogy (CheMin) instrument agitates the <45 micron fraction of the powder in a resonant cell with an X-ray transparent window, and passes a Co Kα X-ray beam

through the powder to produce a diffraction pattern, allowing the identification of minerals based on their crystal structure [36]. Although the X-ray fluorescence capability on CheMin was descoped, the XRF data will still be collected and analyzed on a "best effort" basis [37]. The CheMin sample wheel holds 27 reusable sample cells and five permanent reference standards. The Sample Analysis at Mars (SAM) instrument package includes a gas chromatograph (GC) which uses six columns to separate organic compounds prior to analysis with a quadrupole mass spectrometer (QMS). The GC-QMS system has better than part per billion sensitivity for organic detection [38]. The SAM sample carousel holds 74 sample cups for powder analysis. In addition, SAM contains a tunable laser spectrometer which can detect CH_4, H_2O and CO_2 in the atmosphere and measure key isotope ratios, including $^{13}C/^{12}C$, $^{18}O/^{16}O$, and $^{17}O/^{16}O$ in CO_2, D/H in water and $^{13}C/^{12}C$ in methane. The methane detection limit is < 1ppb, and the Chemical Separation and Processing Laboratory within SAM can concentrate methane in atmospheric samples, further improving the methane detection limit [38].

The Remote Environmental Monitoring Station (REMS) on MSL is a weather monitoring package attached to the side of the rover mast, capable of measuring air and ground temperature, wind speed, humidity, and UV radiation [39]. On top of the rover body, the Radiation Assessment Detector (RAD) will assess the modern radiation environment so that future robotic and crewed missions can carry appropriate levels of shielding, and to determine any effect that radiation may have had on surface materials and potential biomarkers [40]. The Dynamic Albedo of Neutrons (DAN) instrument [41] sends pulses of neutrons into the upper ~1 meter of the martian surface and measures the amount of backscatter, allowing an estimate of the hydrogen content (a proxy for water content).

MSL also carries an alpha particle X-ray spectrometer (APXS; [42]), similar to the instruments carried on Sojourner, Spirit, and Opportunity, but with significantly (~3x) improved sensitivity and a tolerance of temperatures up to -5°C. This enables rapid (~3 hr) full chemical analyses of rocks and soils during the day on Mars [43]. APXS is restricted to measuring targets within the reach of the robotic arm, but the ChemCam instrument will provide elemental compositions for targets up to 7 meters away from the rover. ChemCam uses a technique called laser-induced breakdown spectroscopy (LIBS), which is described in the following section. ChemCam also is capable of collecting monochromatic images of its targets with a resolution of 0.1 mrad, corresponding to ~0.7 mm per pixel at a distance of 7 meters [44].

3. Laser-Induced Breakdown Spectroscopy

LIBS is an analytical technique that uses laser pulses to ablate target material and form a plasma. The spectrum of the plasma plume can then be used to determine the elemental composition of the target. The first example of using a laser plasma as the emission source for spectroscopic analysis was published in 1964, only a few years after the development of the laser [45]. This early study noted that LIBS has several advantages over spectroscopy using traditional arc or spark excitation sources, including the ability to analyze targets of any conductivity without touching them, even in inert or evacuated environments.

The ability to rapidly analyze samples from a distance with no sample preparation and the development of smaller, less expensive and more-reliable lasers make LIBS an appealing technique for space exploration [46]. Early studies of LIBS for space exploration showed that the size and brightness of the plasma plume formed is highly dependent on atmospheric pressure. At

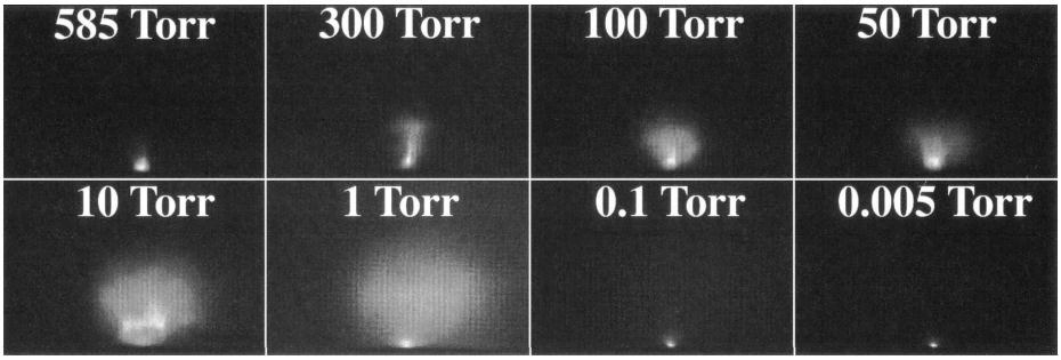

Figure 2: LIBS plasma plumes under varying atmospheric pressure. Figure 4 of Knight et al., 2000. [46]

760 Torr, the laser spark is small (2-3 mm diameter) and emission is confined to the surface of the sample, but at ~5 Torr (similar to martian atmospheric pressure) the plasma expands significantly to ~16 mm diameter and emission is greatest in the center of the plume, somewhat above the surface. At very low pressures (~0.1 torr) the plasma plume disperses rapidly and the only region with density high enough to show significant emission is at the surface of the sample. Thus, martian atmospheric pressure is near-optimal for a bright emission spectrum, with enhanced emission intensity compared to both low-pressure and high-pressure environments [46].

ChemCam will use a Nd:KGW 1067 nm laser with a spot size of 200-500 μm, pulse duration of 5 ns, and pulse energy of 14 mJ to ablate targets within 7 m of the rover [44]. This results in a power density of $\sim 9 \times 10^{13} - 1.4 \times 10^{13}$ Wcm^{-2}, well above the threshold for stoichiometric ablation (10^{9} Wcm^{-2}) [47]. ChemCam data will play an important tactical role during the mission, enabling rapid chemical analyses and identification of targets for further study by other instruments (*e.g.*, APXS, CheMin and SAM). ChemCam will provide the only chemical analyses of targets that are inaccessible to instruments on the rover's robotic arm and can detect light elements such as H, Li, Be, B, C, and N that are not detected by APXS. The

shockwave from the LIBS plasma is capable of clearing away thin layers of dust on the target, and repeated shots can penetrate thin alteration rinds and coatings [44] [48]

The strength of an element's emission lines in the LIBS plasma is influenced by "matrix effects" including self-absorption, the degree of ionization in the plasma, the degree of laser-to-sample coupling, and the abundance of other elements [49]. Initial efforts at quantitative analysis with LIBS used univariate calibration based on the area under emission lines for the element of interest (*e.g.*, [50][51]). Subsequent work has shown that multivariate techniques which make use of the information content of the entire spectrum are better at accounting for matrix effects and therefore yield more accurate results [49][52].

4. Outline of Following Chapters

Chapter 2 presents the results of a detailed characterization of Gale Crater. This study used some of the many available orbital datasets and focuses in particular on the MSL landing site and proposed traverse area. A simplified stratigraphic section of the northwestern mound is presented, along with two potential MSL traverses. The origin of the lower mound units remains ambiguous based on the data considered, but features on the upper mound interpreted as very large cross-beds suggest an aeolian origin for the upper mound. Chapter 2 was peer-reviewed and published in the online, open-access Mars journal [53].

Chapter 3 and Chapter 4 both deal with a large set of LIBS spectra of geologic materials collected with a laboratory LIBS system very similar to ChemCam. The analyses in Chapter 3 are restricted primarily to silicates with low volatile content, while Chapter 4 also includes carbonates, sulfates, and silicates with higher volatile contents.

Chapter 3 compares several multivariate analysis methods for quantitative LIBS analysis of geological materials. Partial least squares, using the full LIBS spectrum, is found to give the

most accurate predictions overall, although the use of feature selection to reduce the data volume also showed good results for many elements and merits further investigation. In addition, Chapter 3 investigates the influence of target grain size on the performance of quantitative LIBS. LIBS analyses of coarse-grained rocks often resulted in lower accuracy and precision. The average number of analysis spots required to measure the correct composition varied from ~10 on fine-grained samples to >20 for coarse-grained samples. Chapter 3 was peer-reviewed and published in Icarus [54]

Chapter 4 examines several multivariate methods of grouping LIBS spectra prior to quantitative analysis, to determine whether PLS models based on similar spectra give more accurate results than those trained on a large, diverse dataset. For the data set considered, k-means clustering with five clusters resulted in a modestly lower overall error. The iterative application of PLS and k-means clustering on the predicted values resulted in similar improvements in accuracy. The results from Chapter 4 have been submitted to Spectrochimica Acta B: Atomic Spectroscopy and are in review.

Chapter 5 applies multivariate methods to the analysis of multispectral Pancam and APXS data from the Mars Exploration rover Spirit. Soft Independent Modeling of Class Analogy (SIMCA) classification is used in an attempt to assign targets to APXS classes based on their Pancam spectra. The results were mixed, and in many cases spectra were assigned to several APXS classes. However, SIMCA shows promise as a method of more rigorously determining whether a new target represents a novel Pancam spectral class or APXS compositional class. The results described in Chapter 5 are in preparation for submission to Icarus.

Chapter 6 synthesizes the results of the previous chapters. Potential applications of the methods described in chapters 3, 4, and 5 are discussed, and areas of future work are identified.

The potential of MSL to test many of the hypotheses presented in Chapter 2, and the implications for future Mars exploration are discussed.

CHAPTER 2

GEOLOGIC MAPPING AND CHARACTERIZATION OF GALE CRATER AND IMPLICATIONS FOR ITS POTENTIAL AS A MARS SCIENCE LABORATORY LANDING SITE[1]

0. Abstract

Gale Crater is located at 5.3°S, 222.3°W (137.7°E) and has a diameter of ~155 km. It has been a target of particular interest due to the >5 km tall mound of layered material that occupies the center of the crater. Gale Crater is currently one of four finalist landing sites for the Mars Science Laboratory rover. We used visible (CTX, HiRISE, MOC), infrared (THEMIS, CRISM, OMEGA) and topographic (MOLA, HRSC, CTX) datasets and data products to conduct a study of Gale Crater, with a particular focus on the region near the proposed Mars Science Laboratory (MSL) landing site and traverse.

The rim of Gale Crater is dissected by fluvial channels, all of which flow into the crater with no obvious outlet. Sinuous ridges are common on the crater floor, including within the proposed MSL ellipse, and are interpreted to be inverted channels. Erosion-resistant polygonal ridges on the mound are common and are interpreted as fractures that have been altered or cemented by fluid. We identified key geomorphic units on the northwestern crater floor and mound, and present a simplified stratigraphy of these units, discussing their properties and potential origins. Some layers in the mound are traceable for >10 km, suggesting that a spring mound origin is unlikely. We were unable to rule out a lacustrine or aeolian origin for the lower mound using

[1] This chapter was originally published in the Mars journal: Anderson, R., Bell III, J.F.(2010), Geologic mapping and characterization of Gale Crater and implications for its potential as a Mars Science Laboratory landing site, The Mars Journal, 5, 76-128, doi:10.1555/mars.2010.0004.

presently-available data. Pyroclastic processes likely have contributed to the layers of the Gale mound, but were probably not the dominant depositional processes. The upper part of the mound exhibits a pattern that could be cross-bedding, which would suggest an aeolian dune-field origin for that unit. Aeolian transport appears to be the most plausible mechanism for removal of material from the crater without breaching the rim; however, fluvial, mass-wasting, or periglacial processes could have contributed to the breakdown of material into fine grains susceptible to aeolian transport. We have identified two potential traverses for MSL that provide access to the diverse features on the crater floor and the mound. We discuss the suitability of Gale Crater as a landing site for MSL in terms of diversity, context, habitability and biomarker preservation and conclude that Gale Crater would be a scientifically rewarding and publicly engaging landing site.

1. Introduction and Previous Work

Gale Crater is located at 5.3°S, 222.3°W (137.7°E) and has a diameter of ~155 km. It is situated in the northeastern portion of the Aeolis quadrangle on the boundary between the southern cratered highlands and the lowlands of Elysium Planitia (Figure 1), and the crater has been estimated to be Noachian in age (~3.5–3.8 Ga) [55][56] [57]. Gale has been a target of particular interest due to the mound of material that occupies the center of the crater, standing ~6 km higher than the lowest point on the floor. The age of the mound has been loosely constrained to the late Noachian/early Hesperian [30]. Gale Crater has been selected as the landing site for the MSL mission [31].

Early maps based on Viking data list a wide range of potential origins for the material in Gale Crater. Scott *et al.* [58] interpreted the material as lava flows and aeolian deposits, while others [55] suggested volcanic, aeolian or fluvial sedimentation, and Scott and Chapman [59]

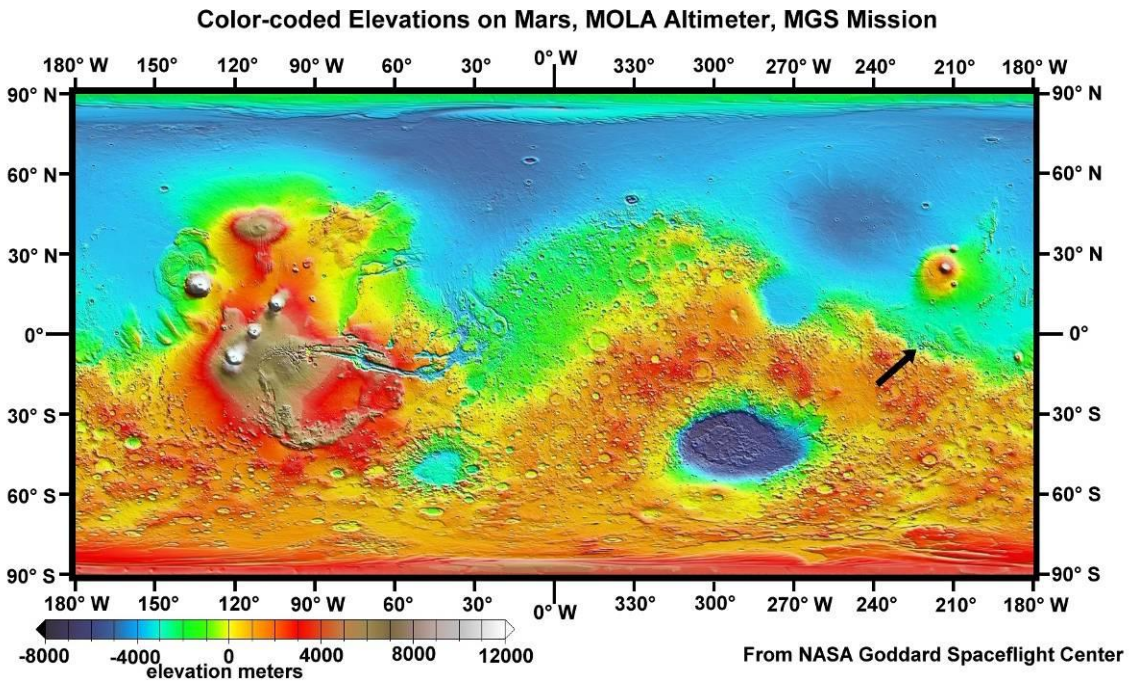

Figure 1. Global topographic map of Mars, based on MOLA data [9]. The black arrow marks the location of Gale crater.

invoked aeolian, pyroclastic, lava flow, fluvial and mass-wasted deposition. Cabrol et al. [56] used Viking images, a Viking topographic map and several early Mars Orbiter Laser Altimeter (MOLA) profiles to suggest that Gale Crater may have hosted a lake intermittently from its formation in the Noachian until the early to middle Amazonian, and to speculate that it could have provided diverse environments for martian life, ranging from warm hydrothermal waters shortly after the crater-forming impact, to cold, ice-covered water at later times.

Malin and Edgett [60]identified Gale Crater as one of a class of partially filled impact craters on Mars. They cited the fact that the peak of the Gale mound is higher in elevation than some portions of the crater rim to suggest that the entire crater was filled with layered material that was subsequently eroded. They also identified an erosional unconformity on the mound, suggesting at least two episodes of net deposition and a significant amount of erosion.

Malin and Edgett [60] also discussed a number of possible origins for the strata observed in Gale and other filled craters. Pyroclastic deposits were discussed but determined to be an unlikely source because terrestrial deposits thin very rapidly with distance from the source, and most of the layered rocks on Mars are far from potential volcanic vents. Impact ejecta was likewise ruled out because it rapidly thins with distance from the impact and therefore, to form thick deposits like the Gale Crater mound, would require "prodigious quantities" [60] of material. Aeolian deposition was considered a possible source if processes could be identified to explain the large volume of layered material and the apparent periodic nature of the layers in many deposits. Ultimately, Malin and Edgett [60] favored a lacustrine origin for the layered material, citing the thickness and rhythmic nature of many layered deposits across the planet and their affinity for closed basins such as craters.

Pelkey and Jakosky [61] conducted a study of Gale Crater using data from the Mars Global Surveyor (MGS) MOLA and the Thermal Emission Spectrometer (TES), as well as other Viking Orbiter and MGS Mars Orbiter Camera (MOC) data. They found evidence for a thermally thick dust layer on the upper mound which thins to reveal darker, higher thermal inertia material. They interpreted the northern crater floor as a dust-covered, cemented mantle, while the southern crater floor had little dust cover and variable terrain. They also found that the sand sheet in Gale Crater had a higher than expected thermal inertia and suggested some combination of coarse grain size, induration or inhomogeneities in the field of view as an explanation. They suggested that dark-toned material may be transported from the southeast into the southern portion of Gale Crater and then northward around the mound. Pelkey and Jakosky [61]concluded that interpreting the surface of Gale Crater is not straightforward, but that the surface layer varies

considerably, likely due to multiple processes, and that aeolian processes have likely been important in shaping the surface.

In a subsequent paper, Pelkey *et al.* [62] added Mars Odyssey Thermal Emission Imaging System (THEMIS) thermal inertia and visible observations to their analysis. They confirmed the observations of Pelkey and Jakosky [61] that dust cover increases with altitude on the Gale mound and that aeolian processes have played a significant role in shaping the current surface of the crater and mound. They also noted that the numerous valleys in the crater wall and mound support hypotheses for aqueous processes in Gale Crater, and that the valleys likely postdate any deep lake in the crater because they extend down to the crater floor.

Thomson *et al.* [63] interpreted ridges and fan-shaped mesas on the mound and crater rim as inverted fluvial channels and alluvial fans. They noted that there is no obvious change in slope to explain the transition from some inverted channels to fan-shaped features and suggested that this could be explained by a stream encountering a slower-moving body of water and depositing its sediment load as a fan. They also suggested that the upper mound material may be related to a widespread layered, yardang-forming unit known as the “Medusae Fossae Formation” (MFF). Recently, Zimbelman [64] has also mapped the Gale Crater mound as part of the MFF.

Rossi *et al.* [65], citing unconformities in the mound, a relatively young crater retention age, and claiming that there is "no or little evidence of fluvial activity in the immediate surroundings of the craters hosting bulges and within their rim" have hypothesized that the Gale Crater mound has a local origin as a large spring deposit.

Rogers and Bandfield [66]analyzed TES and THEMIS spectra of the dunes on the floor of Gale Crater and interpreted the results to indicate that they have a composition similar to olivine basalt, consistent with the Hamilton *et al.* [67] decorrelation stretch mosaic of Gale Crater, in

which mafic materials are displayed as magenta (Figure 2c). Analysis of OMEGA and CRISM observations confirm the presence of mafic minerals such as olivine and pyroxene in the dunes [30].

Gale Crater was proposed as a landing site for MSL at the first landing site workshop [69] [70]. The MSL landing site is located on top of a large fan-shaped feature [69] which extends to the southeast from the end of a valley at the base of the northwestern crater wall. Numerous presentations at subsequent workshops made the case for Gale Crater based on the exposure of a >5 km-thick sedimentary sequence, the numerous fluvial features on the mound and crater walls, and the detection of phyllosilicates and sulfates in the layered mound near the landing site (*e.g.*

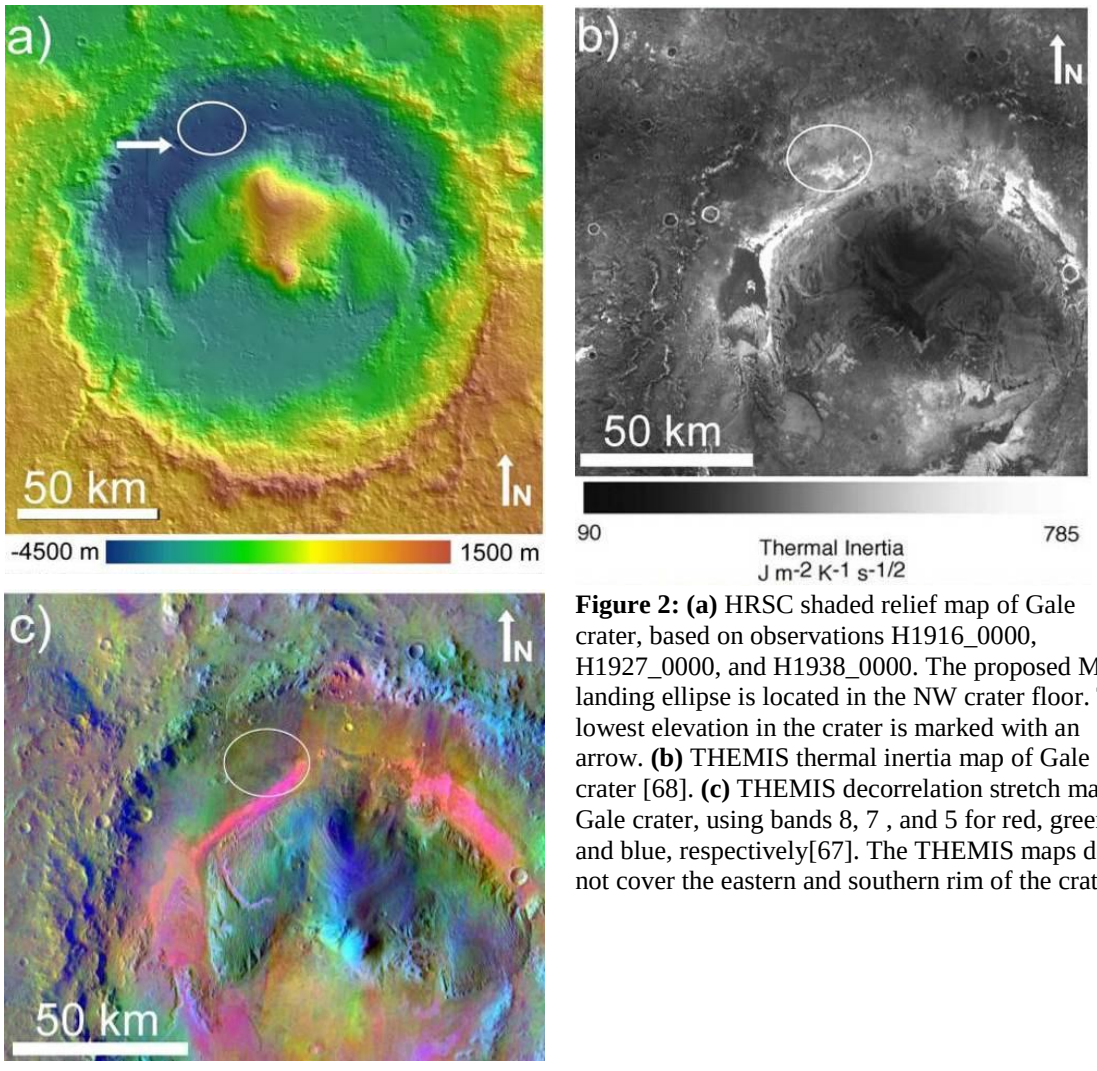

Figure 2: (a) HRSC shaded relief map of Gale crater, based on observations H1916_0000, H1927_0000, and H1938_0000. The proposed MSL landing ellipse is located in the NW crater floor. The lowest elevation in the crater is marked with an arrow. **(b)** THEMIS thermal inertia map of Gale crater [68]. **(c)** THEMIS decorrelation stretch map of Gale crater, using bands 8, 7 , and 5 for red, green and blue, respectively[67]. The THEMIS maps do not cover the eastern and southern rim of the crater.

[71][72][73]).

Prior to the detection of hydrated minerals in Gale Crater, the site was interesting primarily for its geomorphology. However, the discovery of phyllosilicates and sulfates correlated to stratigraphic units in the northwestern mound, including the specific identification of the mineral nontronite (suggesting a moderate pH and possibly reducing conditions at the time of formation), have made Gale a more appealing site in terms of potential habitability and biomarker preservation [74]. In addition, the strata of the Gale mound appear to trend from phyllosilicate-bearing lower layers to sulfate and oxide-bearing middle layers to relatively unaltered upper layers [30]. Bibring et al. [75] have proposed a global transition in climate and weathering on Mars that predicts a period of moderate pH and phyllosilicate production, followed by a period of acidic weathering with sulfate production and concluding with an era of superficial weathering to ferric oxides. It is possible that the layers of the Gale mound record this transition [30] and can be used to test this hypothesis.

Despite interest in Gale Crater as a potential landing site, the origin of the mound remains enigmatic. We have made observations from multiple datasets in an attempt to evaluate mound-origin hypotheses and to better describe the geomorphic units that a) appear to be significant in the stratigraphic sequence and b) that MSL would be likely to encounter if Gale were chosen as the landing site. As we will show, Gale Crater exposes a rich and diverse Martian history, and it is likely that a combination of depositional and erosional environments must be invoked to explain the features that are visible today.

2. Data and Methods

2.1 Visible Data

We used radiometrically calibrated data from the Mars Reconnaissance Orbiter (MRO) Context Camera (CTX) [17] to generate a 6 m/pixel mosaic of the entire crater to use as the primary base map for this study. The list of individual images in the mosaic is given in appendix Table A1. The extensive coverage and high resolution of CTX makes it ideal for mapping geomorphic units. We estimated the CTX Lambert albedo values given in the following sections by dividing calibrated radiance factor values by the cosine of the average incidence angle for the observation of interest. [76][15]

The second visible imaging dataset used for this study was ~0.27 m/pixel data from the High Resolution Imaging Science Experiment (HiRISE) instrument [15] on MRO. Because Gale Crater was selected as the MSL landing site [31], it has been targeted repeatedly by HiRISE, both in the proposed landing ellipse and in other locations on the mound and crater floor. For this study, we focused primarily on the images of the landing site and the nearby mound units where there is very good HiRISE coverage. However, we also examined HiRISE images of other portions of the mound to better understand the complete stratigraphic section. Appendix Table A2 lists the HiRISE images used in this work.

The Gale Crater mound has also been extensively imaged at ~1.5 m/pixel resolution by the MGS MOC [10]. In locations that lack HiRISE coverage, we have used MOC images to study small-scale features that are beyond the CTX resolution limit. Appendix Table A3 lists the MOC images used in the mosaic. CTX and MOC data were mosaicked using spacecraft position and pointing (SPICE) data, and using MOLA data to correct for topographic distortions. Note that in figures using high-resolution data such as HiRISE and MOC, the planetocentric latitude and longitude are provided to aid in locating the features discussed.

2.2 Infrared Data

2.2.1 Near-infrared

In addition to visible images, we used data products from the Compact Reconnaissance Imaging Spectrometer for Mars (CRISM)[16], a hyperspectral visible-near infrared imaging spectrometer on MRO. CRISM's high spatial and spectral resolution (15–19 m/pixel, 362–3920 nm at 6.55 nm/channel) allowed us to use spectral parameter maps created by [74] to correlate the geomorphology of the units at the proposed landing site with the inferred composition.

We also used data from the Observatoire pour la Mineralogie, l'Eau, les Glaces et l'Activité (OMEGA) visible-near infrared mapping spectrometer on the Mars Express orbiter [14]. OMEGA has an angular resolution of 1.2 mrad, resulting in a spatial resolution varying from ~350 m/pixel to >8 km/pixel, depending on where the spacecraft was in its elliptical orbit when the data were collected. We generated a mosaic of six OMEGA observations over Gale Crater. These observations are listed in appendix Table A4. Unfortunately, the proposed landing site and western mound had only very low (~7.2 km/pixel) resolution OMEGA coverage. We adapted the CRISM spectral parameters described by [77] to OMEGA wavelengths by using the OMEGA band closest in wavelength to the corresponding CRISM band. The adapted parameters were applied to the OMEGA mosaic to generate spectral parameter maps.

2.2.2 Thermal Infrared

We used thermal infrared data products to reveal additional details of the physical and compositional properties of the surface. In particular, we used 100 m/pix thermal inertia [68] and decorrelation stretch data products [67] derived from THEMIS measurements.

Thermal inertia is a measure of the resistance to temperature change of the upper several centimeters of the surface. It is determined by the thermal conductivity, heat capacity, and density of the material. On Mars, variations in the thermal conductivity, due primarily to

changing particle size, are considerably more significant than variations in heat capacity and material density [68]. Therefore, lower thermal inertia regions are interpreted as unconsolidated aeolian-deposited sand or dust, while higher thermal inertia regions are interpreted to have more abundant rocks or cemented materials, exposed bedrock, or some combination of those components. It should be emphasized that thermal inertia maps give information only about the upper few centimeters of Mars, and that mixing effects can be significant. For example, bedrock with small patches of fine-grained dust at scales smaller than the instrument resolution could have an intermediate observed thermal inertia that is quite different from the true thermal inertia of the rock and dust portions of the surface.

Decorrelation stretches are used to enhance variations in highly correlated data. The technique applies a principal component transformation to the data, followed by contrast-stretching and then re-projection back to the original display coordinates. In the case of images that have been assigned to a red, green and blue color space, this has the effect of exaggerating color variations without distorting the hues of the image. [78]. Decorrelation stretched images cannot be used for quantitative measurements, but they give qualitative insight into the compositional variation of the surface. The decorrelation stretch used in this work is based on THEMIS bands 8 (11.79 μm), 7 (11.04 μm), and 5 (9.35 μm), which are displayed as red, green and blue, respectively. This results in mafic materials appearing as magenta, while more felsic and sulfate-bearing materials appear yellow and dusty surfaces appear blue [67].

The THEMIS thermal inertia and decorrelation stretch maps for Gale Crater were generated by the THEMIS team, and made publicly available on the THEMIS website [12] when Gale was announced as a potential landing site for MSL.

2.3 Topography

To provide the global context for Gale crater, we used a topographic map based on Mars Orbital Laser Altimeter [79] data, shown in Figure 1.

We used three map-projected and areoid-referenced digital terrain models from the High Resolution Stereo Camera (HRSC)[14] on Mars Express (data product IDs: H1916_0000_DA4, H1927_0000_DA4, and H1938_0000_DA4) to generate a topographic map of the entire crater at 75 m/pixel (Figure 2a). This topographic data provides valuable context for the other data sets.

We augmented the regional HRSC topography with a digital elevation model of the proposed landing site, traverse path, and part of the western mound derived from CTX stereo pair images P16_007356_1749_XI_05S222W and P18_008147_1749_XN_05S222W. The procedure for generating topographic models based on CTX stereo imaging is described by Broxton and Edwards [80][81]. Briefly, the image pair is re-projected and aligned, then pre-processed to enhance edges and ensure insensitivity to biases in brightness and contrast in the stereo correlation step. For "pushbroom" cameras like CTX, the process uses a camera model to account for the changing position of the camera during image acquisition. The stereo correlation step identifies corresponding points in the pair of images, and a 3D model is created by finding the intersection between the lines of sight for each pair of corresponding pixels, thus localizing the point in three-dimensional space. A final step interpolates missing values in the elevation model.

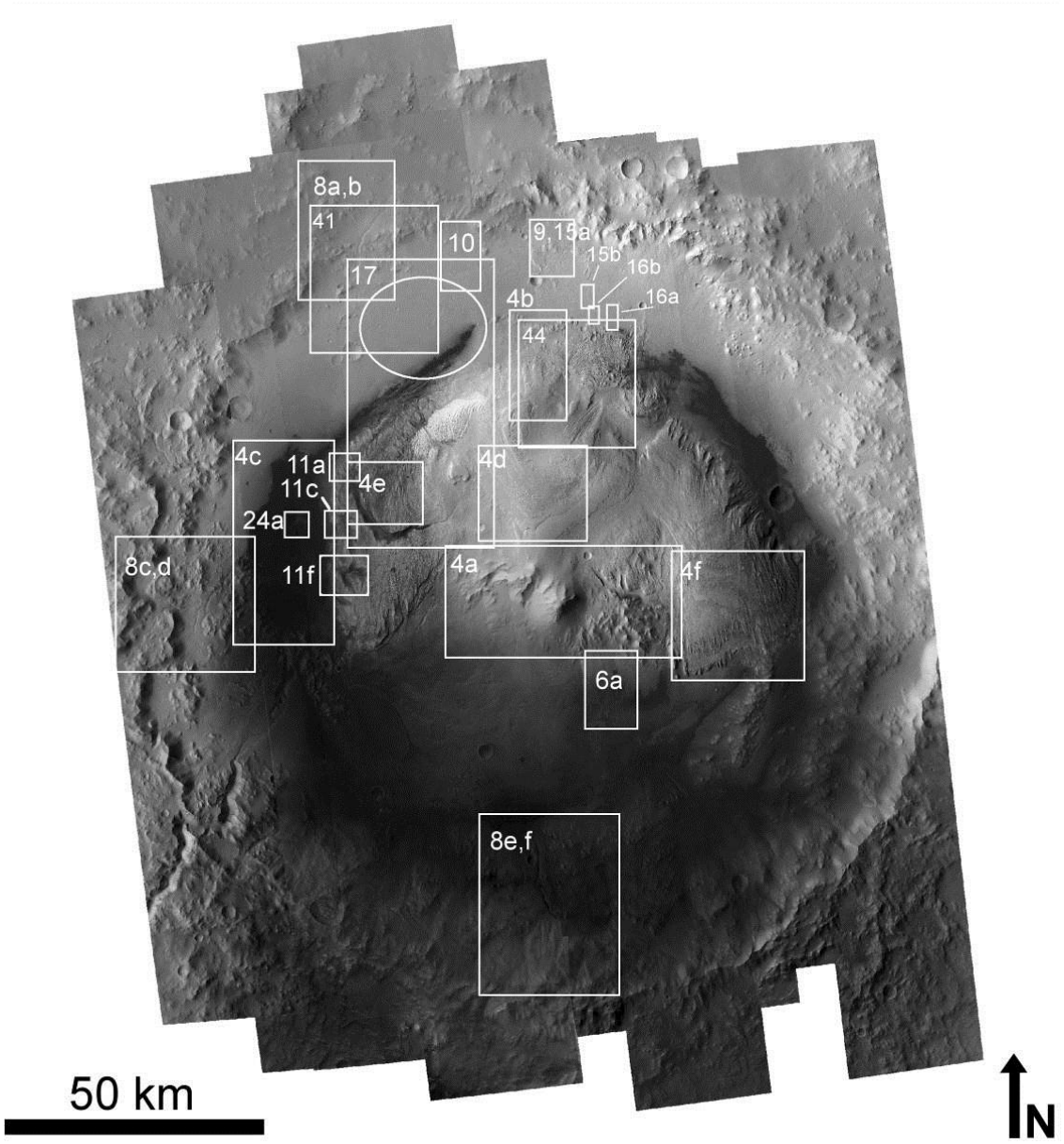

Figure 3. CTX mosaic of Gale crater. Boxes and labels indicate the locations of other Figures. The proposed MSL landing site is indicated by the white ellipse. Refer to appendix Table A1 for a list of CTX images used in the mosaic.

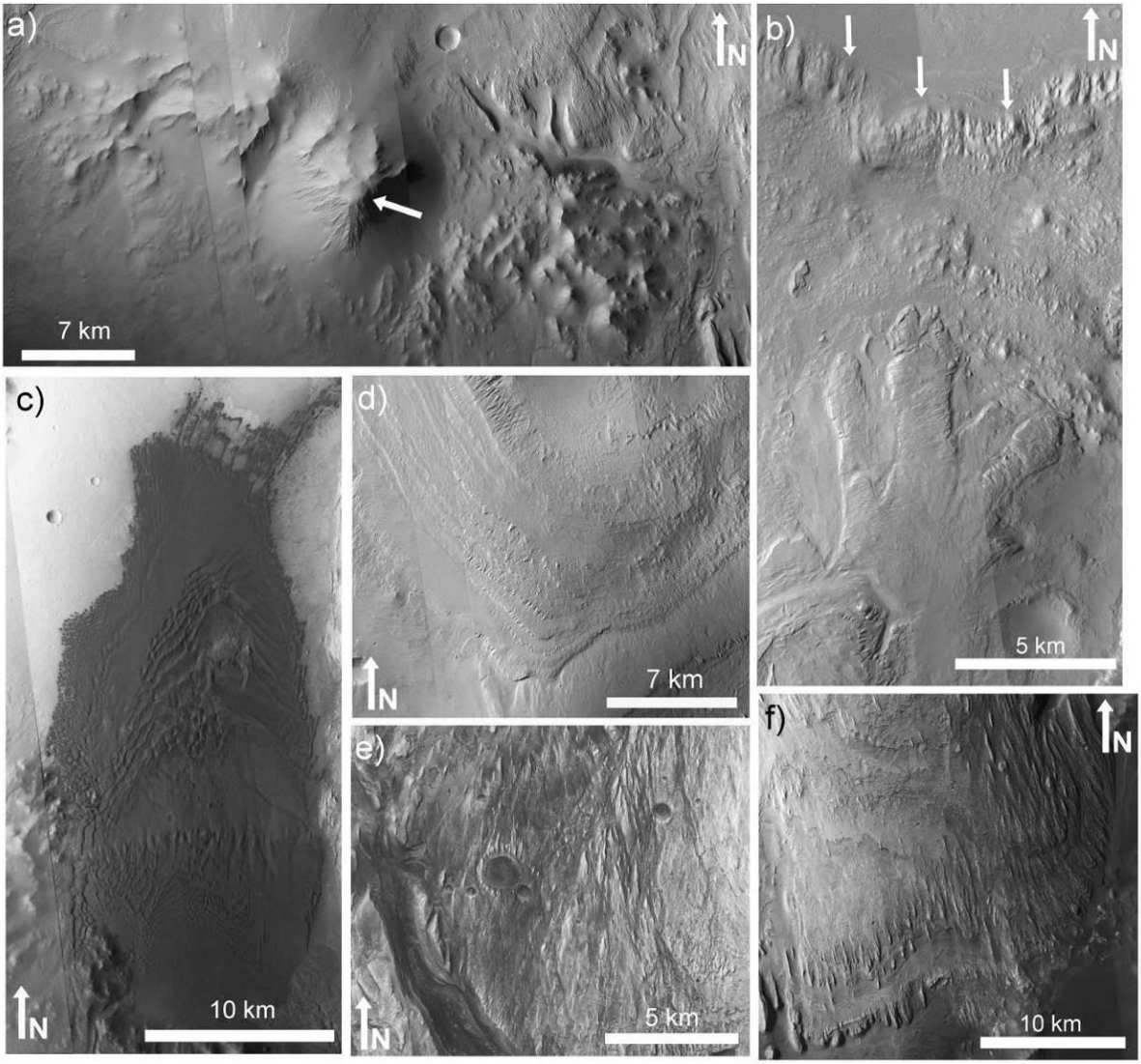

Figure 4: (a) The peak of the central mound (marked by an arrow) and its surroundings. **(b)** A row of small elongated hills (marked by arrows) outline the northern edge of the mound, and lobate features extend part of the way down to the floor. **(c)** A large sand sheet in the western crater floor. **(d)** The terraced layers of the upper mound. The western mound **(e)** and eastern mound **(f)** are layered and eroded into a yardang-like texture. Refer to Figure 3 for context. Refer to appendix Table A1 for CTX Image IDs. Illumination is from the left.

3. Gale Crater Context

3.1 Overview

Gale is a 155 km diameter crater at the boundary between the southern highlands and Elysium Planitia (Figure 1). The rim of the crater is degraded but still clearly identifiable (Figure 2), and the surrounding terrain has a knobby and mantled appearance, visible in the CTX mosaic in Figure 3. This basemap provides context for the figures discussed in this and later sections.

The large mound of layered material is shaped like a wide crescent, with the "horns" of the crescent pointing to the southwest and southeast. The peak of the mound (838 m elevation) is higher than the degraded northern rim and somewhat lower than the highest point on the southern rim (1448 m). Gale Crater is superimposed on the boundary between the southern highlands and northern lowlands, and this regional slope likely contributes to the difference in elevation between the northern and southern rim. However, the southern rim is approximately 3 to 4 km higher than the nearby floor, whereas the northern rim is ~2 km higher than the northern floor, suggesting that there is significant degradation of the northern rim and/or more material filling the northern crater floor relative to the southern portion of the crater. The lowest point in Gale Crater (-4674 m; marked with an arrow in Figure 2a) is in the northwest portion of the floor, near the location of the proposed MSL landing ellipse, which is at an elevation of approximately -4400 m.

The east and west portions of the mound have a lower elevation and are characterized by numerous yardangs (Figures 4e, 4f), thin (<20 m) layers of varying tone, and a thermal inertia varying from ~300-700 J $m^{-2}K^{-1}s^{-1/2}$. The peak of the mound and material in the 20 km to the east and west of the peak resemble the knobby terrain of the crater wall and surrounding plains (Figure 4a). The northern portion of the mound (Figure 4b) is fringed by rounded and somewhat elongated hills, and lobate features are present on the northern slopes of the mound itself.

Dark-toned aeolian material occurs on the crater floor and exhibits a variety of forms, including isolated barchan and dome dunes <100 meters in diameter, transverse ridges, and an extensive (~372 km^2) sand sheet to the west of the mound (Figure 4c). The thermal inertia of the dark dunes is ~350-400 J $m^{-2}K^{-1}s^{-1/2}$ which is consistent with loose sand-sized material [82].

The southern floor and rim have a lower albedo than the northern floor and rim and most of the mound. This corresponds to an increase in the low- and high-Ca pyroxene parameters in OMEGA maps (Figure 5). We interpret this as a region that is less mantled by ferric dust, exposing more mafic underlying material. The high-Ca pyroxene signal is highest within the crater but the low-Ca pyroxene signal extends south of the rim and correlates with the dark-toned wind streak in that area.

We used empirical equations [83] to estimate Gale Crater's pristine depth and rim height.

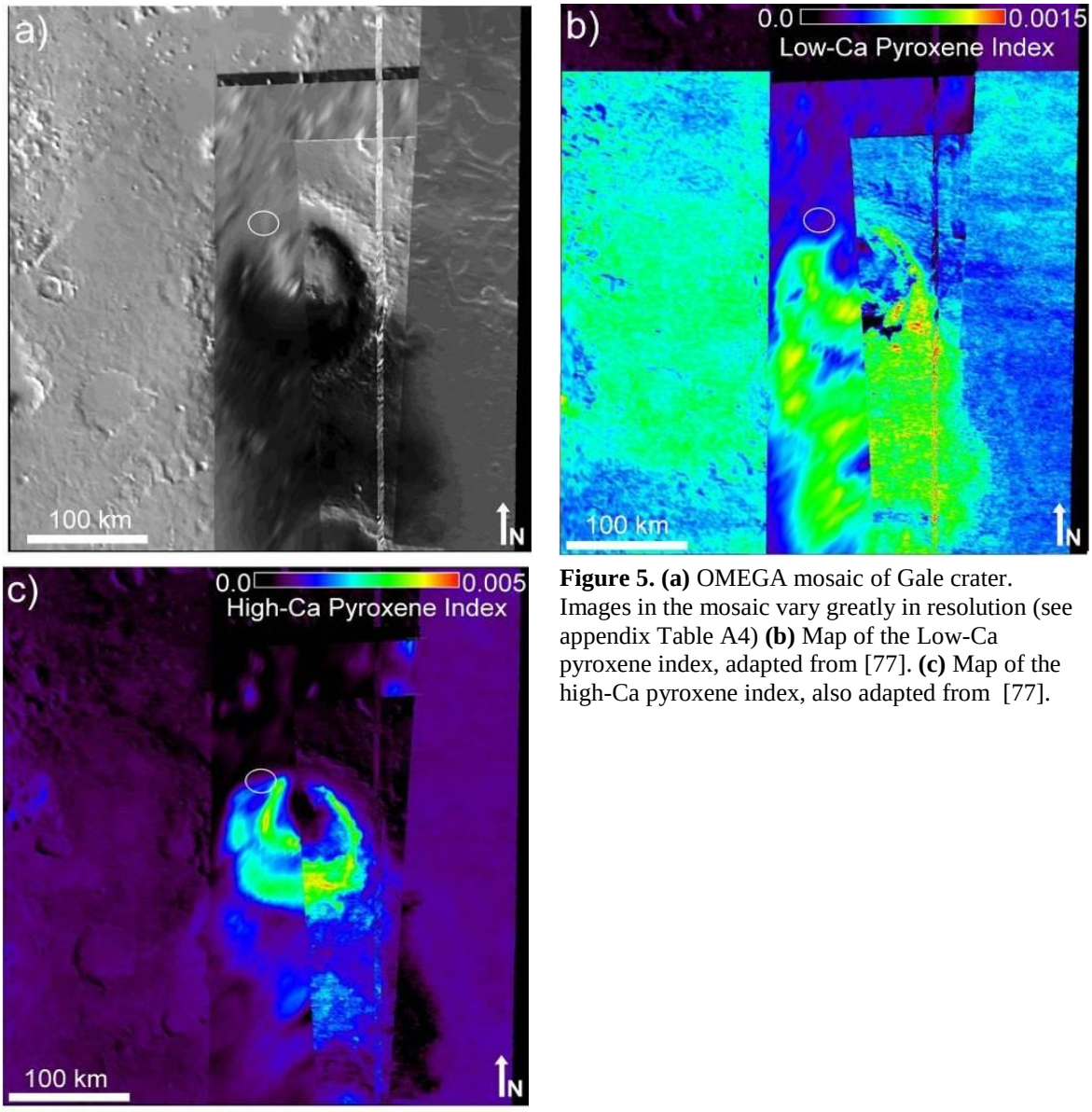

Figure 5. (a) OMEGA mosaic of Gale crater. Images in the mosaic vary greatly in resolution (see appendix Table A4) **(b)** Map of the Low-Ca pyroxene index, adapted from [77]. **(c)** Map of the high-Ca pyroxene index, also adapted from [77].

Garvin *et al.* [83] do not list a depth to diameter equation for craters larger than 100 km, so we applied their equation for complex craters ($d=0.36D^{0.49}$; 7 km < D < 100 km) to estimate a pristine depth of 4.3 km for Gale Crater (diameter D=155 km). In general, larger impact basins have a smaller depth to diameter ratio[84], so we would expect the equation for complex crater depth to provide an upper limit on the depth of the pristine Gale Crater. We used the equation for rim height of craters of diameter D >100 km ($h=0.12D^{0.35}$) to calculate an initial rim height of 0.7 km. Therefore, by adding the pristine depth and rim height, we calculate an original floor-to-rim elevation difference of approximately 5 km.

The actual maximum floor-to-rim difference for Gale is 6.1 km, implying that if the limit imposed by the equation is correct, a substantial amount of additional erosion has occurred in the northern crater, removing any crater-filling material and possibly portions of the original crater floor. We should, however, note that the 6.1 km value is the elevation difference between the highest point on the southern rim and the lowest point in the northern crater floor, so it likely is influenced by the regional slope of the dichotomy boundary. The southern part of the floor is only 3-4 km below the southern rim suggesting that parts of the crater floor have experienced partial infilling.

3.2 Survey of inferred fluvial features

Using the 6 m/pixel CTX basemap, we searched Gale Crater for valleys and sinuous ridges that may represent fluvial channels and inverted channels, respectively. Inversion of relief occurs when topographic lows, such as fluvial channels become more erosion resistant than the surrounding terrain due to processes such as filling by lava flows, cementation, and/or "armoring" by relatively coarse-grained material [85] [86]. When erosion and weathering strip away the less-resistant surrounding material, the channel remains as a raised ridge or series of

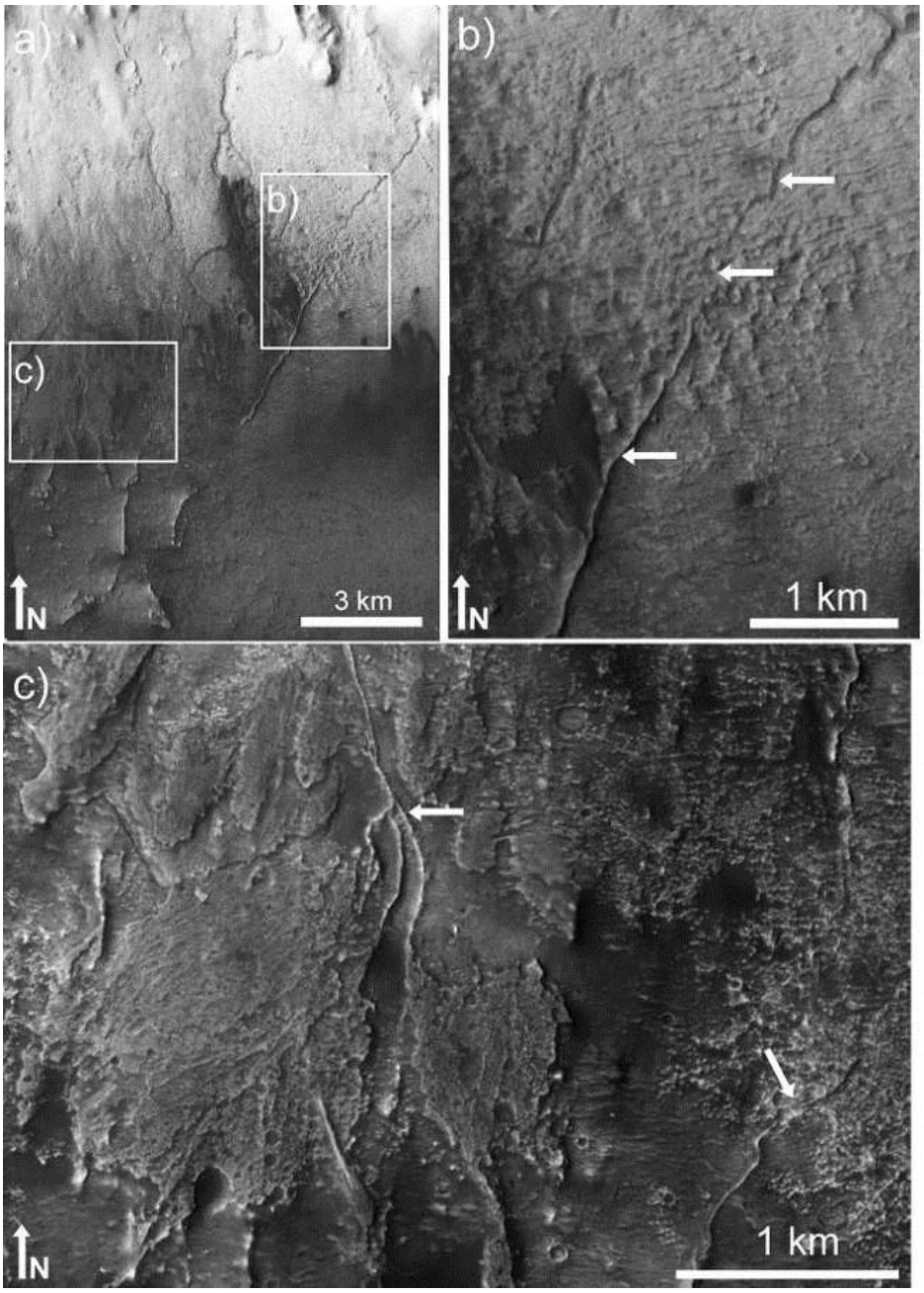

Figure 6. (a) CTX inset of the terrain to the southeast of the central mound peak. Multiple channels extend from the base of the mound onto the crater floor. White boxes indicate the insets shown in **(b)** and **(c)**. **(b)** A close-up of one channel (marked by arrows) in the pitted mound-skirting unit. Where the unit is eroded away, the channel remains in inverted relief. **(c)** This HiRISE inset shows a branching inverted channel (marked by an arrow) that feeds into a positive-relief fan-shaped feature. Another example of a channel transitioning from negative to positive relief is marked by an arrow on the right, above the scalebar. Illumination is from the left in all parts of this figure. Refer to appendix Tables A1 and A2 for CTX image IDs and HiRISE image IDs, respectively. Location: 5.653°S 138.035°E.

hills or mesas. This phenomenon is observed in arid environments on Earth such as Oman [87] and the Colorado Plateau [86], and has been suggested as the origin of the sinuous ridges that are common on Mars [88].

An alternate explanation for sinuous ridges is that they could be eskers. Eskers have been invoked to explain sinuous ridges elsewhere on Mars [89]. However, due to the lack of clear evidence for glacial activity at Gale Crater and the presence of multiple negative-relief channels which transition to sinuous ridges in more-eroded areas (Figure 6), it seems most likely that the sinuous ridges in Gale Crater are inverted channels formed by subaerial water flow. Features in Gale Crater that we interpret as fluvial in origin are shown in red (negative relief) and yellow (positive relief) in Figure 7. The crater walls are dissected by valleys, suggesting that flowing water has played a role in eroding the crater. All of the observed valleys on the crater rim appear to lead into the crater with no obvious surface outlet. Several of the valleys form third or fourth-order branching networks (Figure 8). One of these dendritic valleys in the northwestern crater rim ends at the apex of the fan-shaped feature in the proposed MSL landing site (Figures 8a & 41). Many other valleys and ridges, particularly on the northern rim, lead to fan-shaped mesas on the crater floor, as shown in Figures 9 and 10.

The largest valley (marked with an arrow in Figure 3) enters the crater through the southwestern rim and continues for ~40 km across the crater floor before disappearing beneath the western dune field. Several other canyons (also marked with arrows in Figure 3) are apparent on the western mound. The largest of these transitions headward to a shallower, narrower channel that appears to be partially exhumed from beneath the terraced layers of the upper mound. Several of the canyons on the western mound end in fan-shaped extensions of the mound

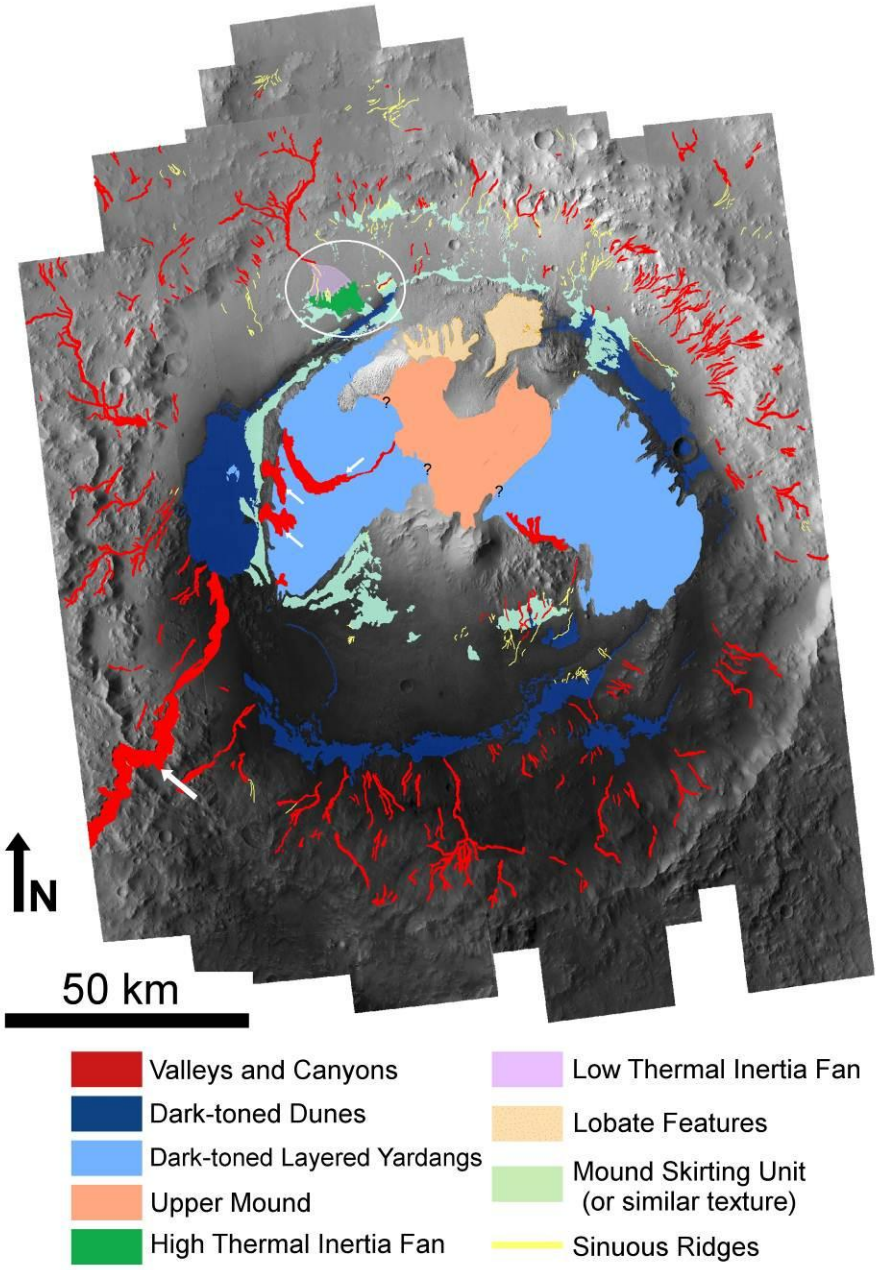

Figure 7: Unit map of Gale Crater. Refer to Figure 17 for a more detailed unit map of the proposed MSL landing site. The proposed landing site is indicated by the white ellipse. Arrows mark the large channel in the southwestern crater rim and the three large canyons on the western flank of the mound. Question marks indicate locations where aeolian material obscures the contact between the upper mound and the dark-toned layered yardangs. Uncolored areas are "undivided" or ambiguous material. Some units were mapped locally near the landing site (Figure 17) but are not shown here. Refer to appendix Table A1 for a list of CTX images used in the mosaic.

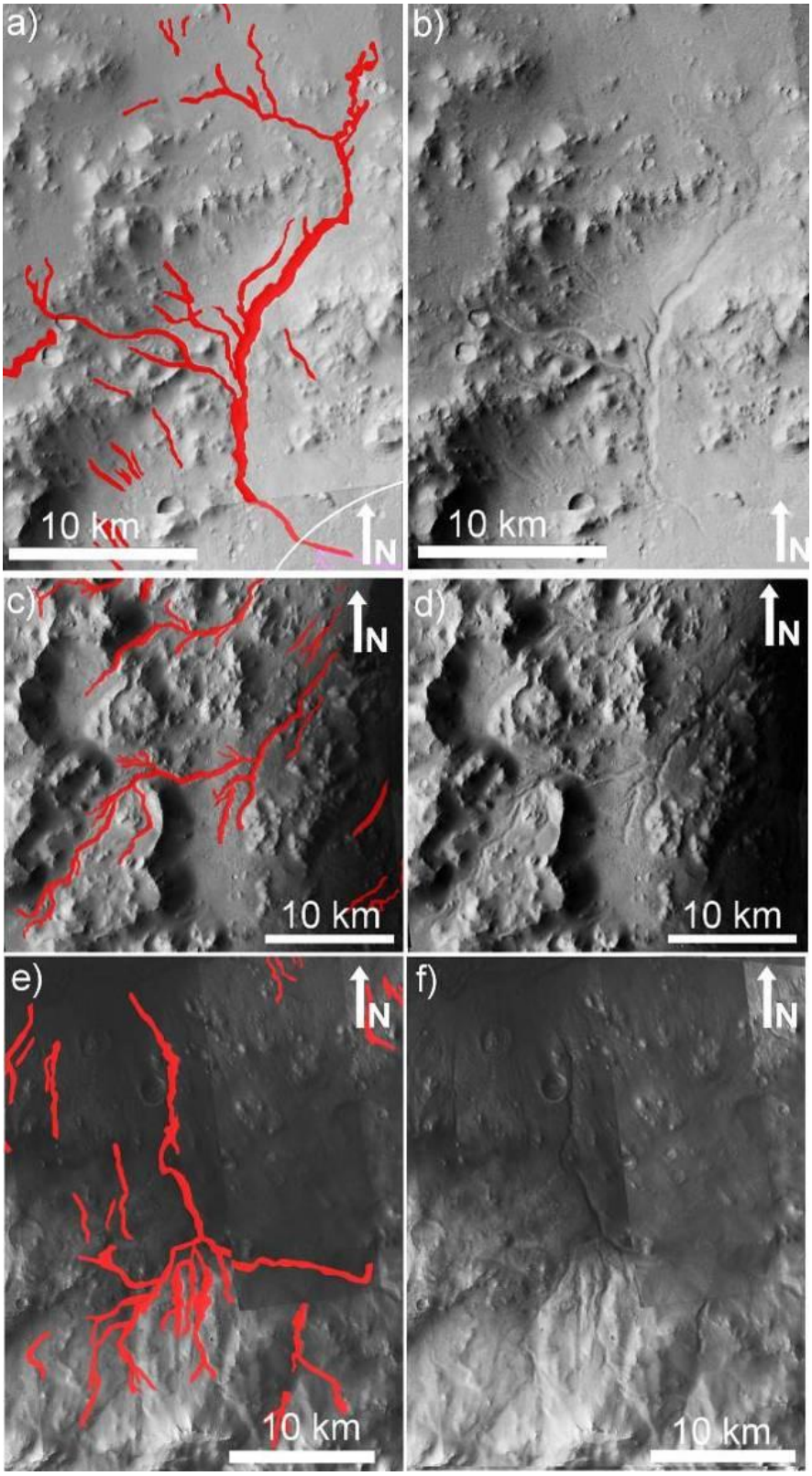

Figure 8. (a,b) The branching valley on the northern crater rim that ends in the fan-shaped feature in the proposed landing ellipse. The edge of the ellipse is visible in the lower right corner. **(c,d)** Another example of a branching valley on the western rim of Gale crater **(e,f)** A third example of a branching valley on the southern rim and floor. Refer to Figure 3 for context and appendix Table A1 for CTX image IDs. Illumination is from the left. Locations: **(a,b)** 4.237°S 137.247°E **(c,d)** 5.389°S 136.699°E **(e,f)** 6.334°S 137.782°E

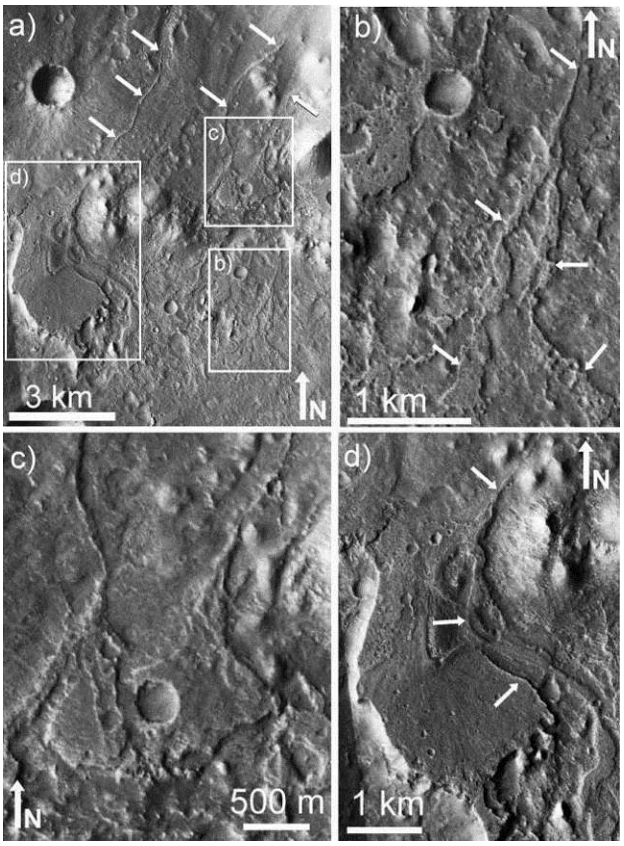

Figure 9. (a) Ridges interpreted to be inverted channels (marked by arrows) leading down from the northern rim transition to raised fan-shaped mesas. **(b)** This fan-shaped mesa maintains two distinct narrow branches. **(c)** Two inverted channels form adjacent fan-shaped mesas. **(d)** A more complex fan-shaped mesa that preserves an inverted channel along its eastern edge (marked by arrows). Refer to appendix Table A1 for CTX image IDs. Illumination is from the left. Location: 4.252°S 137.848°E.

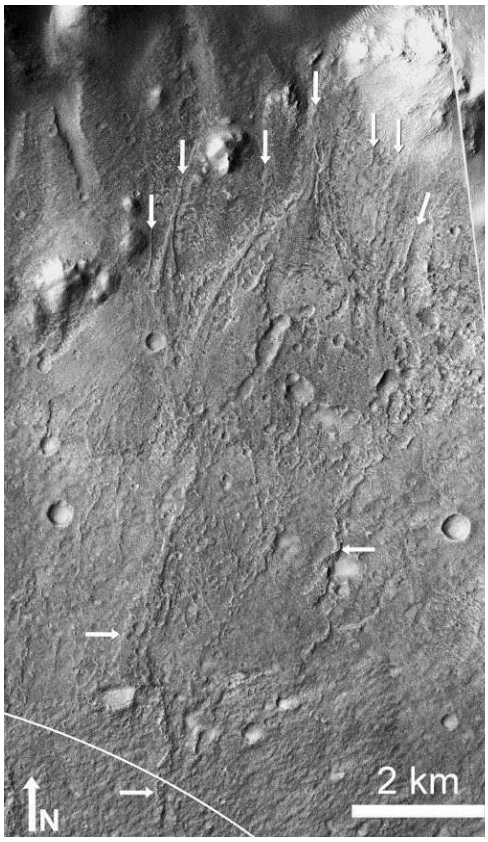

Figure 10. Ridges interpreted to be inverted channels (marked by vertical arrows) become raised fan-shaped mesas near the northern rim. Chains of mesas (marked by horizontal arrows) extend from the fan-shaped mesas across the crater floor. The northeast portion of the landing ellipse is visible in the lower left. Refer to appendix Table A1 for CTX Image IDs. Illumination is from the left. Location: 4.270°S 137.523°E

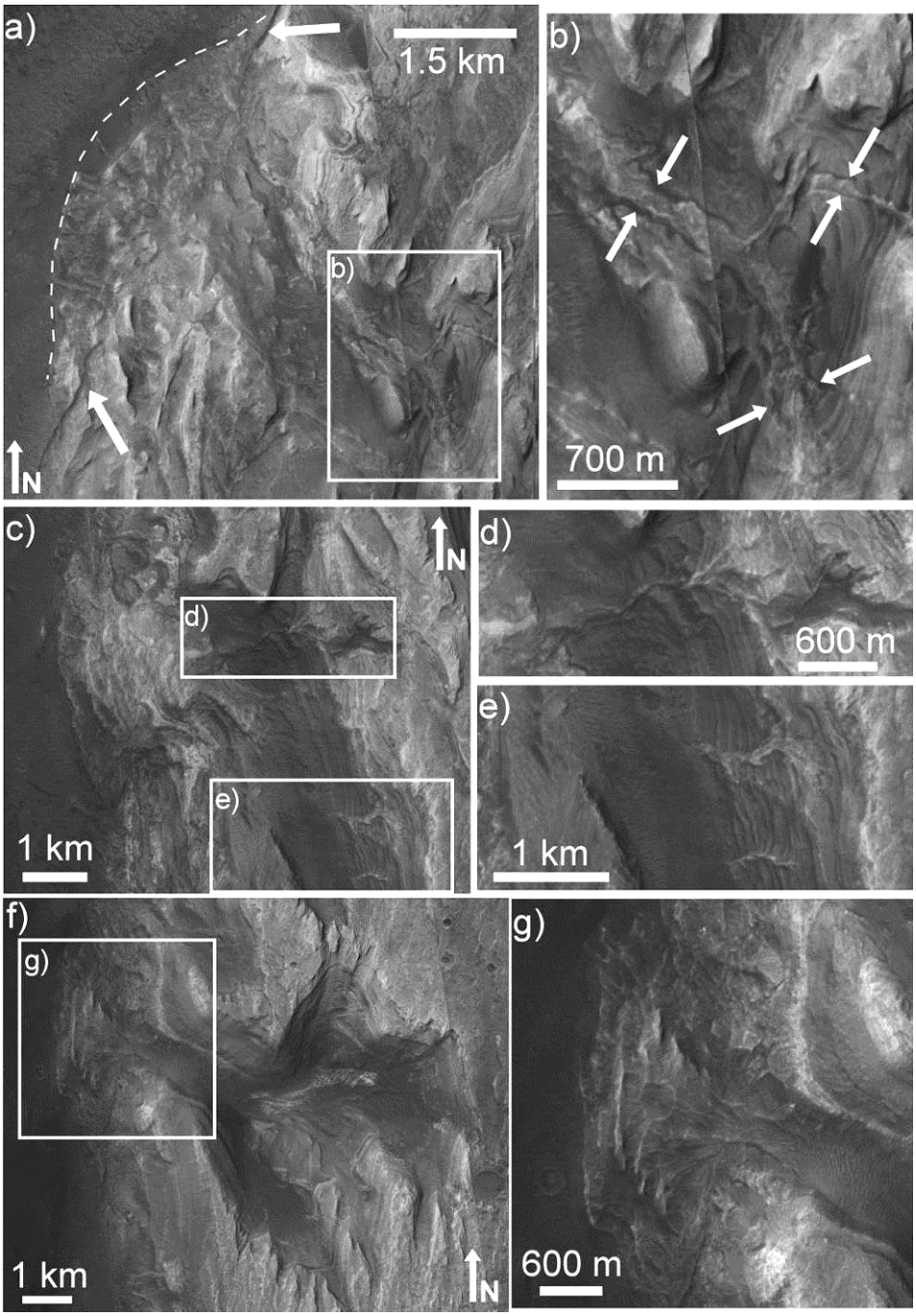

Figure 11: a) A wide fan-shaped deposit of mound material (boundary marked by the dashed line) overlaps the mound-skirting unit in this location, but is thin enough that the edge of the mound skirting unit is still apparent (marked by arrows). The material emerges from a large canyon which preserves a filled channel in its floor and walls, shown in **b)**. **c)** a second fan-shaped deposit of material overlapping the mound-skirting unit. **d)** and **e)** show the location of ridges in the wall of the canyon that leads to the fan-shaped deposit in c). **f)** a stubby branched canyon leads to a third fan-shaped deposit that overlaps the mound-skirting unit, shown in **g)**. Refer to Figure 3 for context and appendix Table A1 for CTX image IDs. Illumination is from the left. Locations: **a)** 4.951°S 137.180°E **c)** 5.126°S 137.153°E **f)** 5.277°S 137.126°E.

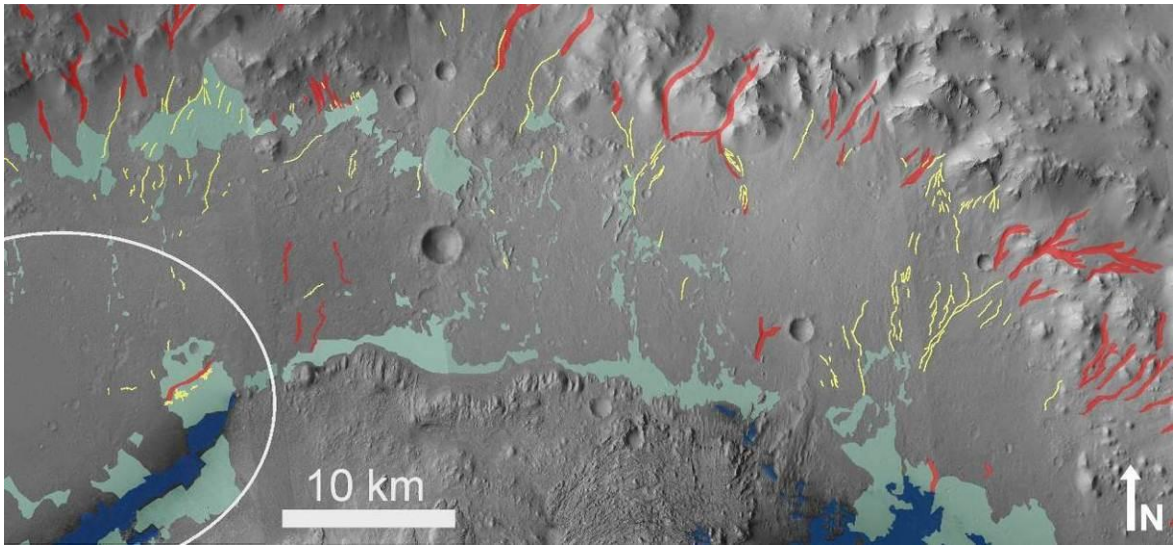

Figure 12. A closer view of the northern crater floor. Valleys interpreted as fluvial channels are marked in red and ridges interpreted as inverted channels are marked in yellow. Blue marks the location of dark-toned dunes. Light green indicates surfaces with a texture characteristic of the 'mound-skirting' unit. Note the numerous mesas of mound skirting unit and the numerous inverted channels. The landing ellipse is visible at left. Illumination is from the left. Refer to appendix Table A1 for CTX Image IDs.

that appear to overlap the underlying mound-skirting unit (Figure 11). These features are discussed in subsequent sections.

Inverted channels, typically less than 100 m in width, and in some cases >10 km long, are common on the crater floor, as shown in Figure 7 and in more detail in Figure 12. South of the mound, several channels transition to inverted channels as the unit in which they are carved becomes more extensively eroded (Figure 6). This unit is ridged and appears to be related to the mound-skirting unit discussed in a later section. The transition from negative to positive relief channels occurs at the edge of this unit, where it breaks up into a rough surface of many small outcrops (*e.g.*, Figure 6b). This boundary is not apparent in the THEMIS thermal inertia map. Several examples of sinuous ridges (sinuosity index of ~2) and finely branching ridges are exposed within the proposed landing ellipse (Figures 13 & 14). These are discussed in the sections concerning the mound-skirting and hummocky plains units.

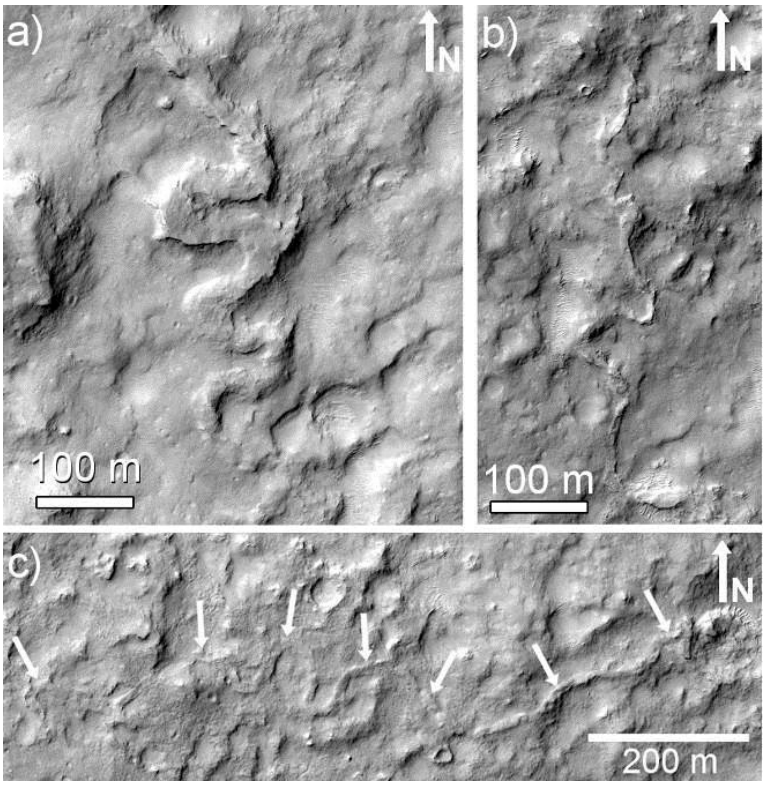

Figure 13. (a), (b) and **(c)** are three examples of sinuous ridges, interpreted to be inverted channels, in the hummocky plains unit within the landing ellipse. **(a)** has a sinuosity index of ~2, and **(b)** and **(c)** have sinuosity indices of ~1.35. All three are shown at the same scale, and are from HiRISE observation PSP_009751_1755. The inverted channels appear to have a vertical relief of several meters. Illumination is from the left. Locations: **a)** 4.404°S 137.535°E; **b)** 4.461°S 137.523°E **c)** 4.501°S 137.484°E

Also common (as shown in Figures 7 and 12) on the northern crater floor are chains of mesas that appear to be associated with the fan-shaped mesas at the base of the northern crater wall (*e.g.*, Figure 10). They have a similar surface texture (Figure 15) and in some cases the fan-shaped mesas are connected to the chains of mesas on the crater floor by channels or inverted channels. Figure 16 shows an example of the chains of mesas branching in a manner similar to fluvial channels. The chains of mesas can extend from the crater wall to the base of the mound, where they merge with the similar-textured mound-skirting unit (Figure 16).

4. Gale Crater Units

In this section, the units of the northwestern crater floor and mound are discussed in detail. Units were distinguished primarily by their geomorphologic characteristics, although thermal inertia and composition also were used in some cases. Figure 3 and Figure 7 provide context for the figures in this section. Figure 17 shows a detailed map of the landing site and northwestern

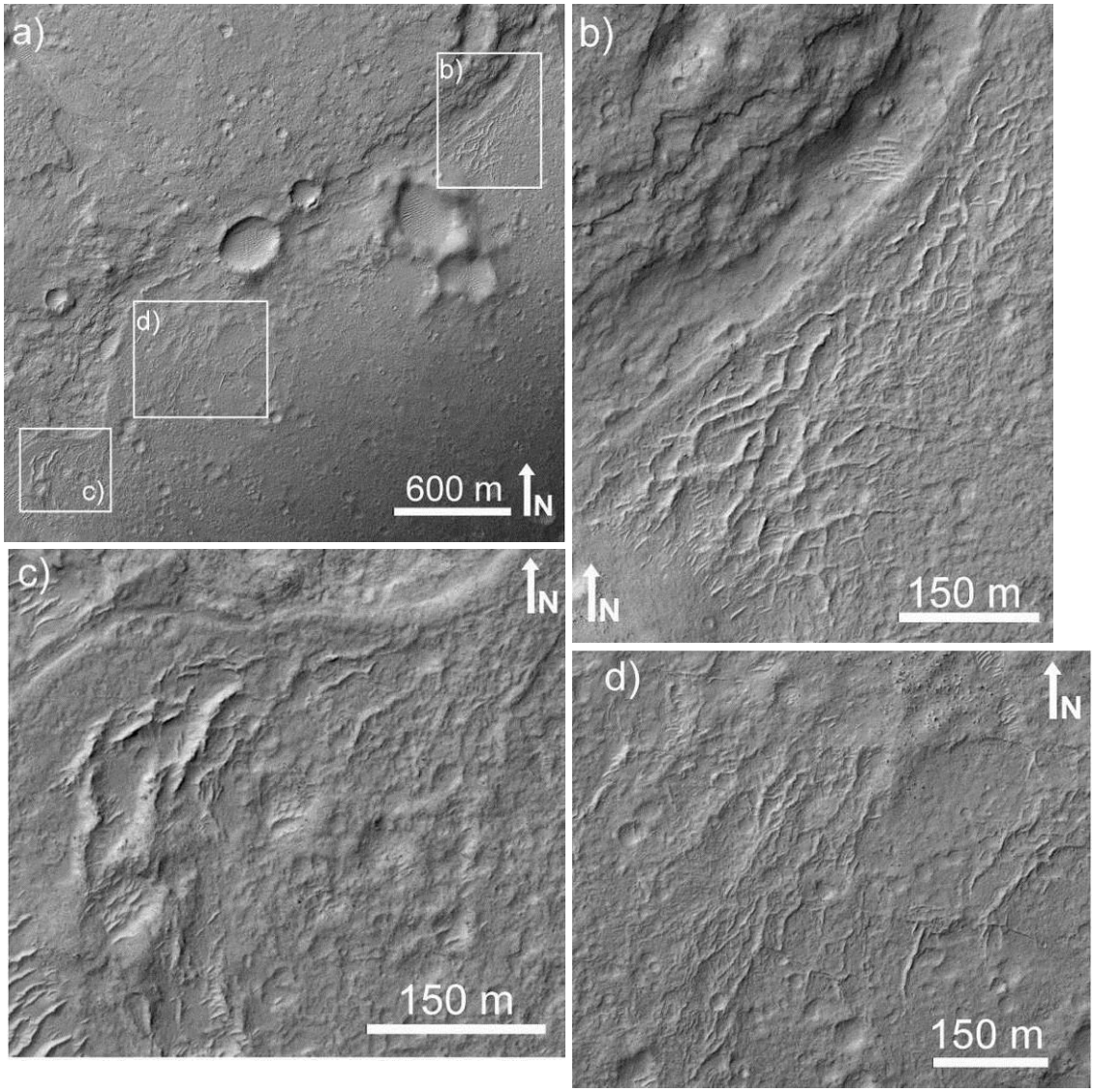

Figure 14: (a) Subframe of HiRISE observation PSP_009571_1755 showing the Gale crater floor in the eastern portion of the landing ellipse. A channel-like feature in the mound-skirting unit is flanked on its southern side by branching ridges, shown in insets **(b)**, **(c)** and **(d),** which may be inverted fluvial channels. Illumination is from the left. Location: 4.497°S 137.548°E.

mound units discussed, and Figure 7 shows units and features that were mapped over the entire crater. Regions of the maps that are not colored can be considered "undivided" material. These locations often had an ambiguous appearance, or represented terrains with less relevance to our primary focus on the proposed MSL landing ellipse and surroundings. Table 1 summarizes the unit properties. Some simplifications and uncertainties are necessarily involved in arriving at our

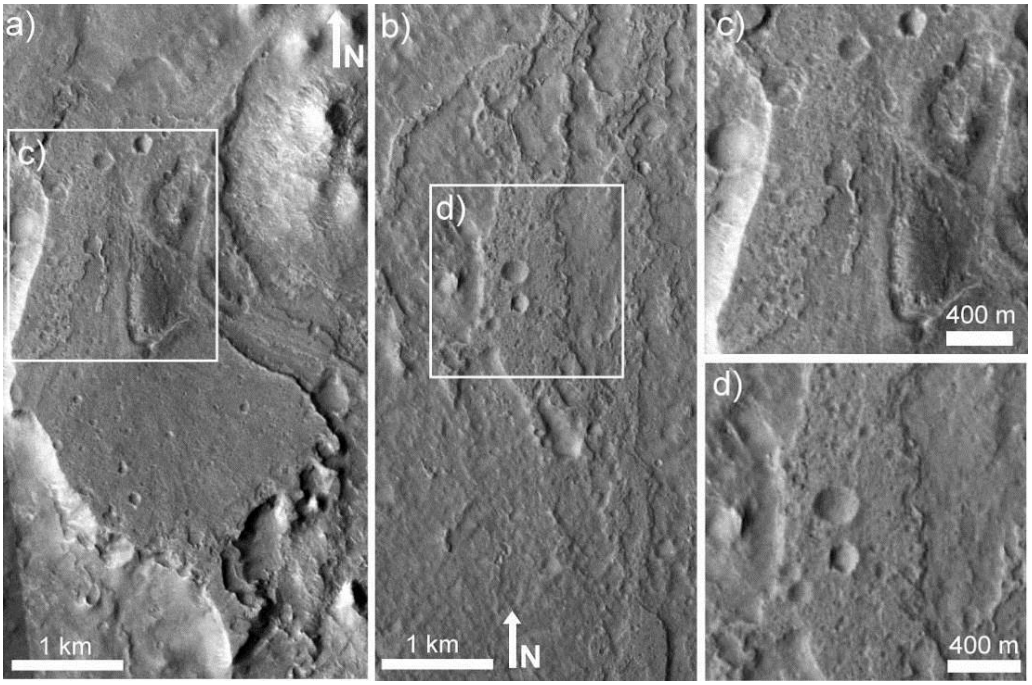

Figure 15 (a) A fan-shaped mesa (previously shown in Figure 9). **(b)** Mesas on the crater floor (see Figure 3 for context). **(c,d)** close-ups showing the texture of the mesas in **(a)** and **(b)**, respectively. Refer to appendix Table A1 for CTX image IDs. Illumination is from the left. Locations: **a)** 4.267°S 137.835°E **b)** 4.394°S 137.948°E.

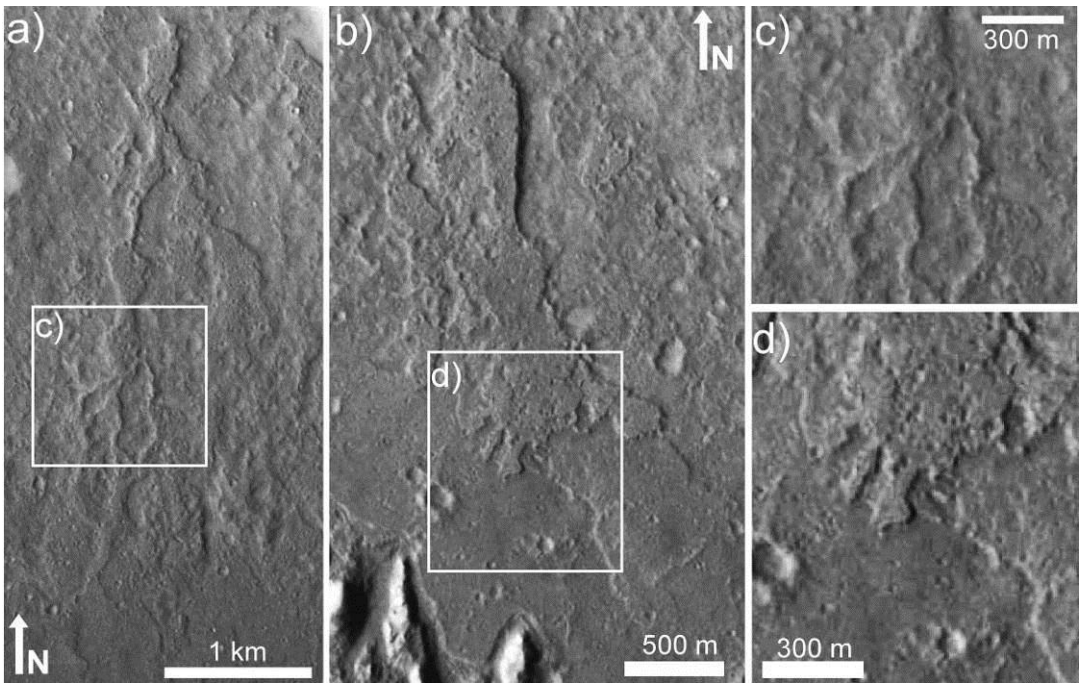

Figure 16: The mesas on the crater floor branch in a manner similar to fluvial channels, as shown in **(a)** and **(c)**. **(b)** shows a location where the mesas overlap the mound-skirting unit, which has a similar texture. Refer to Figure 3 for context. Refer to appendix Table A1 for CTX image IDs. Illumination is from the left. Locations: **a)** 4.461°S 138.032°E **b)** 4.454°S 137.967°E.

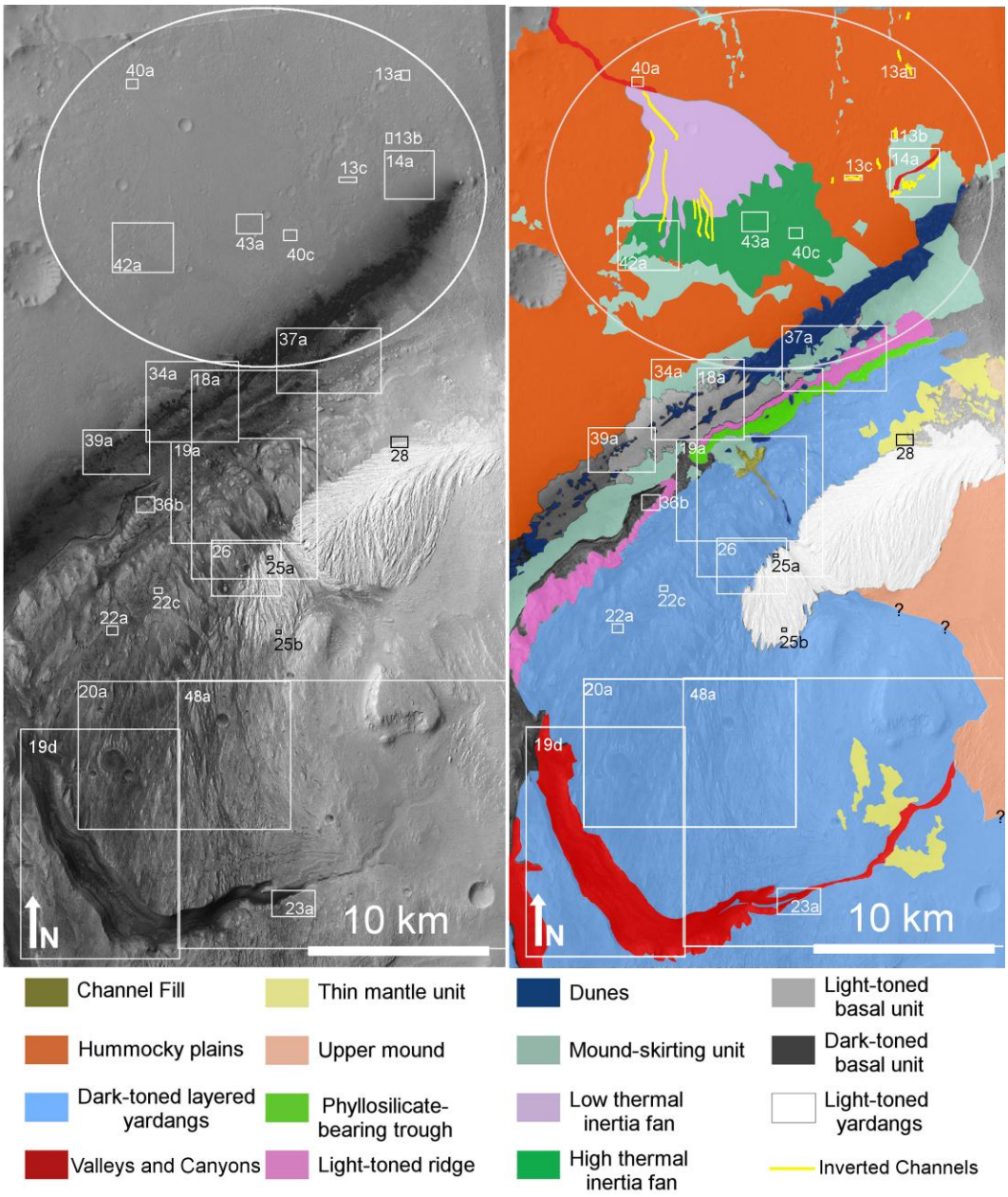

Figure 17: **a)** CTX mosaic of the proposed MSL landing site and northwestern mound in Gale Crater. Boxes show the location of other figures. **b)** A unit map of the same area shown in **a)**, with units identified in the key above. Elevation increases to the lower right in this map. Question marks indicate uncertainty in the boundary between the upper mound and the dark-toned layered yardangs due to aeolian bedforms obscuring the contact. Uncolored areas are "undivided" or ambiguous material. Refer to appendix Table A1 for CTX image IDs.

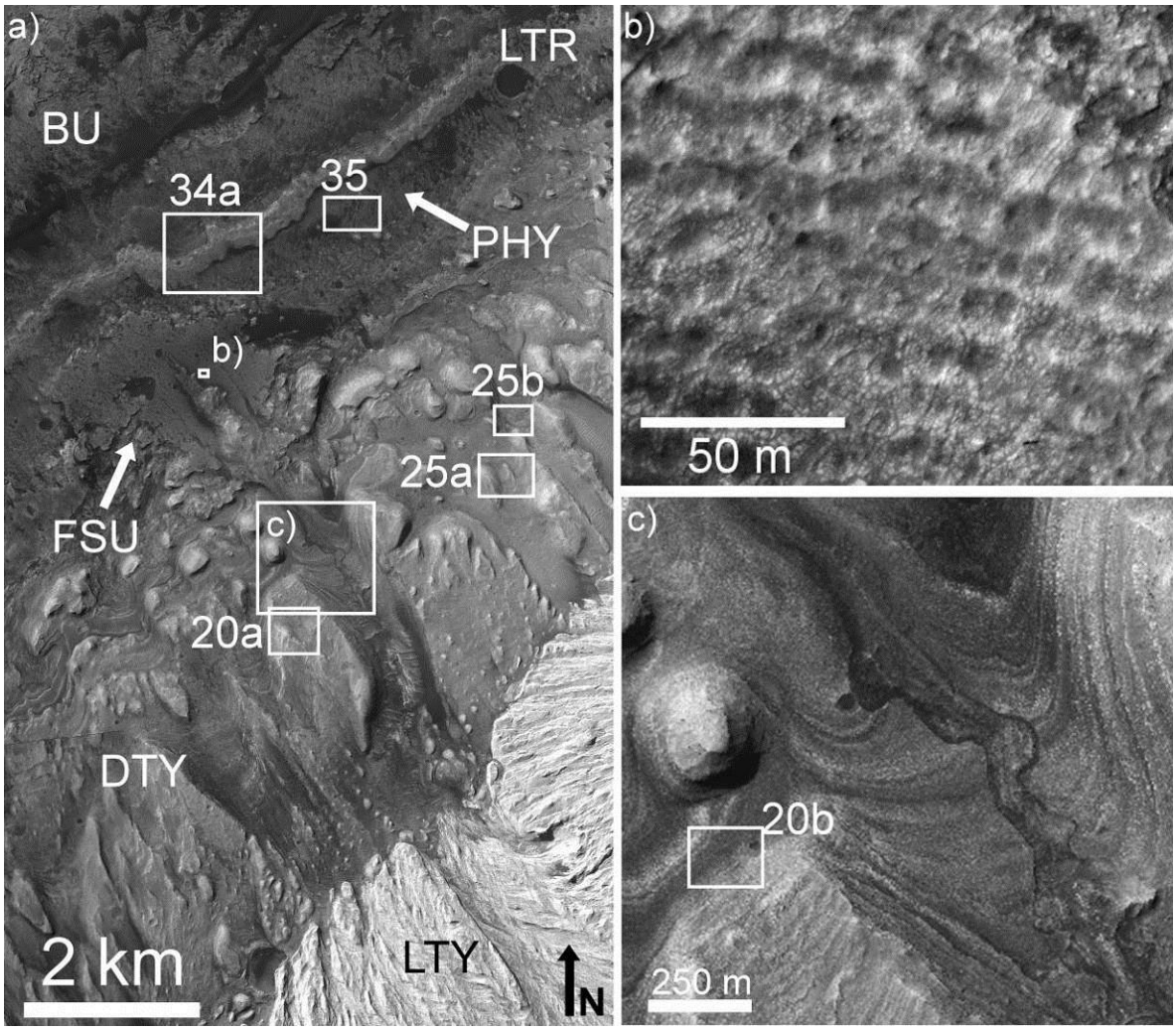

Figure 18: a) CTX and HiRISE mosaic of the area near the filled channel and outcrop of mound-skirting unit, with illumination from the left. The light-toned basal unit (BU) is in the upper left of the frame and elevation increases from -4760 to a maximum of -2800 at the lower right. The light-toned ridge (LTR), phyllosilicate-bearing trough (PHY), dark-toned layered yardang-forming material (DTY) and light-toned yardang-forming material (LTY) are all visible in this frame. **b)** A close-up of the surface of the outcrop of mound-skirting unit, showing a texture that may be due to lithified and fractured bedforms. The outcrop is associated with a filled channel, shown in **c)**, which carves the dark-toned layered yardangs. This channel was first noted by Malin and Edgett [60]. Refer to appendix Tables A1 and A2 for CTX and HiRISE image IDs. Location: 4.770°S 137.398°E.

unit map and hypothesized stratigraphy in Gale Crater. For example, in some cases units have sharp boundaries, such as the light-toned yardangs, but in other cases, the transition between units can be ambiguous, such as some contacts between the mound-skirting unit and the hummocky plains or the transition between the dark-toned layered yardangs and the upper mound.

4.1 Dark-toned layered yardang-forming unit

4.1.1 Observations

Much of the surface of the lower mound is characterized by a layered, moderate to dark-toned yardang-forming material (*e.g.* Figures 3, 7, 17). We have chosen to focus our discussion in this section on the western mound, but the eastern mound shows a similar layered and yardang-forming morphology and has therefore been mapped as dark-toned layered yardang-forming material in Figure 7. The upper extent of the dark-toned layered yardang forming material is often uncertain due to aeolian material obscuring the contact with the upper mound.

The thermal inertia of the surface of the western mound varies from approximately 300 to 700 J m-2K-1s-1/2. The dark-toned layered yardang-forming material is cut by several large canyons on the western side of the mound, as well as a small filled channel on the northwestern flank of the mound, near the proposed MSL landing site (mapped in Figure 17, shown in Figure 18c).The channel was first noted by Malin and Edgett [60] and extends from beneath aeolian bedforms at the base of the light-toned yardang-forming unit and ends in a raised ridge on top of a mesa-forming outcrop of mound-skirting unit.

At CTX and MOC scales, some portions of the dark-toned layered yardang-forming unit have clear layers of varying CTX albedo (~0.18-0.22) that are relatively easy to trace. Milliken *et al.* [30] have identified a "marker bed" (Figure 19) in the layers of the mound near the proposed MSL landing site that is also present in the stratigraphic section exposed by the large canyons in the western mound, and possibly in the layered outcrops in the southeastern mound.

Table 1. Summary of Unit Properties

Unit	Min Elevation (m)	Max Elevation (m)	CTX Albedo	Thermal Inertia ($Jm^{-2}K^{-1}s^{-1/2}$)	Morphology	Key Figures
Dark-Toned Layered Yardangs	-4460	-1800	0.18-0.22	300-700	Thin layers of varying properties forming large yardangs.	19, 20, 21 22, 23
Light-Toned Yardangs	-3390	-1674	0.26	390	Fine layering and joints, scalloped texture.	17,47,25
Thin Mantle Unit	-4070	-1140	0.20-0.23	400	Small patches that drape topography, characteristic "feathery" erosion.	21,27,28
Upper Mound	-2140	490	0.24	300	Cliff-bench layers, scalloped texture. potential cross-beds.	29, 30, 31
Mound-Skirting Unit	-4390	-2940	0.16-0.21	430-780	Pitted, mesa-forming, parallel ridges in some locations.	6, 7, 12, 15, 16, 18, 33
Light-Toned Ridge	-4320	-4170	0.19-0.21	600	Breaks into poorly defined layers downhill, ends abruptly uphill.	18, 37, 36
Phyllosilicate-Bearing Unit	-4210	-4090	0.16	550	Rippled surface but fractures and dunes on top suggest lithification.	38
Light-Toned Basal Unit	-4490	-4212	0.18-0.20	500-540	Fractured light-toned rock, possible faint layers.	34, 39
Dark-Toned Basal Unit	-4513	-4415	0.15-0.16	760	Darker-toned fractured rock.	39
Hummocky Plains	-4670	-4150	0.21	480	Hummocky, ranging from smooth to rocky.	13, 41
Low Thermal Inertia Landing Site Fan	-4500	-4190	0.21	460	Primarily smooth, possibly mantled.	40, 41, 42
High Thermal Inertia Landing Site Fan	-4520	-4440	0.21	620	Rugged fractured rock.	40, 41, 42, 43
Lobate Features	-4350	-1200	0.24	460-670	Some show erosion-resistant upper layer. Fan-shaped unit is rugged with potential pressure ridges and streamlined texture.	44, 45, 46

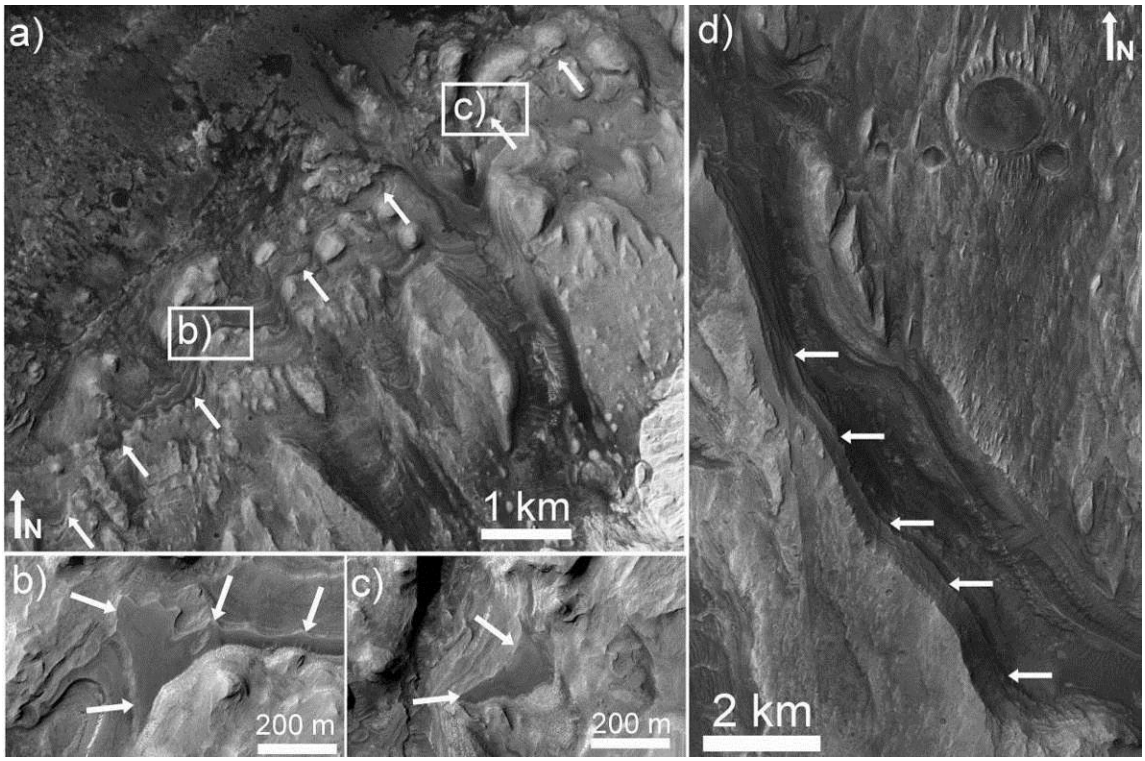

Figure 19: a) Milliken et al. [30]identified a distinctive smooth, dark-toned "marker bed" (indicated by arrows) within the dark-toned layered yardang unit that is traceable for many km. This bed is also observed in the canyon on the western mound and in the layered outcrops of the southeastern mound. The bed is erosion resistant and preserves small craters on its surface. **b)** and **c)** show two exposures of the marker bed, several km apart. **d)** The large canyon on the western mound exposes many layers that are traceable over >10 km. Refer to appendix Tables A1 and A2 for CTX and HiRISE Image IDs. Locations: **a)** 4.788°S 137.392°E **d)** 5.105°S 137.303°E.

In other locations higher on the mound the surface becomes rougher and is eroded into more densely spaced yardangs. In these locations, individual beds become difficult to trace. Figure 20 shows a typical DTY surface on the western mound. CRISM observations indicate that this dark-toned layered yardang-forming unit contains hydrated sulfate minerals, indicative of aqueous alteration [74] [30]. The beds of this portion of the mound are typically less than ~20 m thick, and have been shown to be parallel, with a dip of 2-4 degrees to the northwest [30]. The erosional expression of the layered rocks that make up the dark-toned layered yardang-forming unit varies from cliff-bench, boulder shedding layers (Figure 21a) to more-erodible layers which

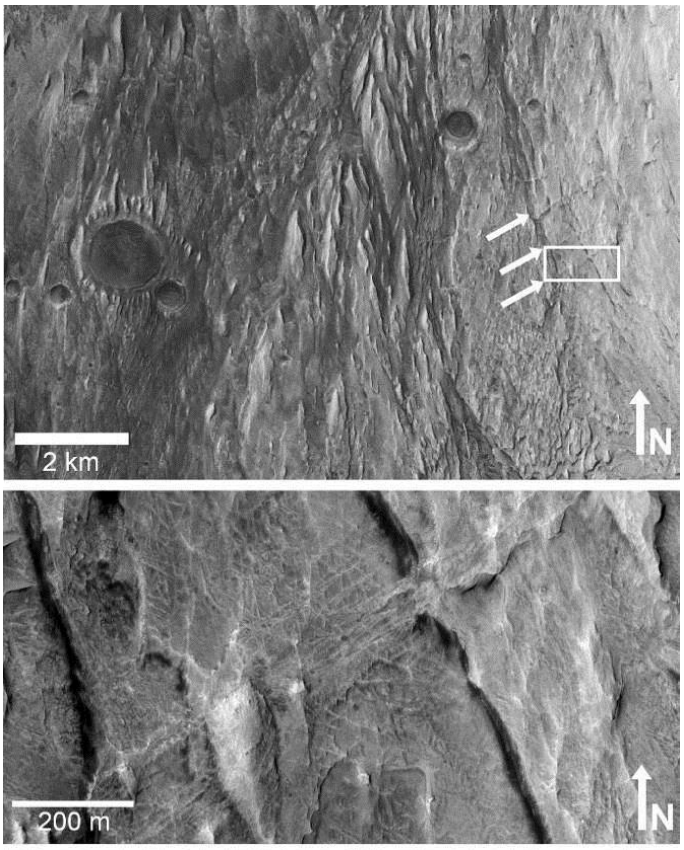

Figure 20. a) A CTX view of the dark-toned layered yardang unit. Numerous yardangs make individual layers difficult to follow. The surface shows craters many of which are eroded and may have been exhumed. On the right, several erosion-resistant fractures are marked by arrows. **b)** A HiRISE close-up of one of the large erosion-resistant fractures, revealing numerous smaller raised fractures. The larger fracture appears to be up to tens of meters high. Illumination is from the left. Refer to appendix Tables A1 and A2 for CTX and HiRISE image IDs. Location: 5.072°S 137.303°E.

form smooth slopes (generally <10°). The beds in these smooth locations appear "blurry" (Figure 21b).

The surface of the dark-toned layered yardang-forming material is often covered with polygonal ridges. (Figure 22) In some cases, a dark line marks the ridge centers (Figure 22d). The topographic lows between the ridges are darker toned than the ridges themselves. On the western mound, larger ridges and clusters of ridges cut across the yardang texture of the mound (Figure 20).

Near the head of the largest canyon on the western mound the surface of the dark-toned layered yardang-forming material is characterized by parallel east-west-oriented lineations at an interval of 30 to 50 m (Figure 23). Approximately 4.5 km to the west of the mound, in the large dark-

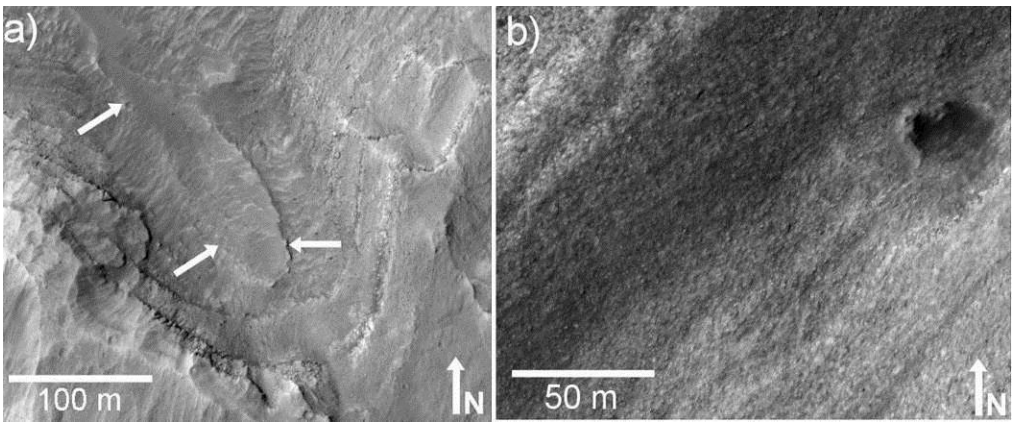

Figure 21: a) Cliff-forming, boulder-shedding layers in the dark-toned layered yardang unit. Also note the oblong patch of thin mantle unit, marked by arrows. **b)** Smooth "blurred" layers in the dark-toned layered yardang unit. In the upper right is a partially exhumed and/or heavily eroded crater. HiRISE image ID: PSP_009294_1750. Illumination is from the left. Locations: **a)** 4.796°S 137.398°E **b)** 4.787°S 137.395°E. See Figure 18 for context.

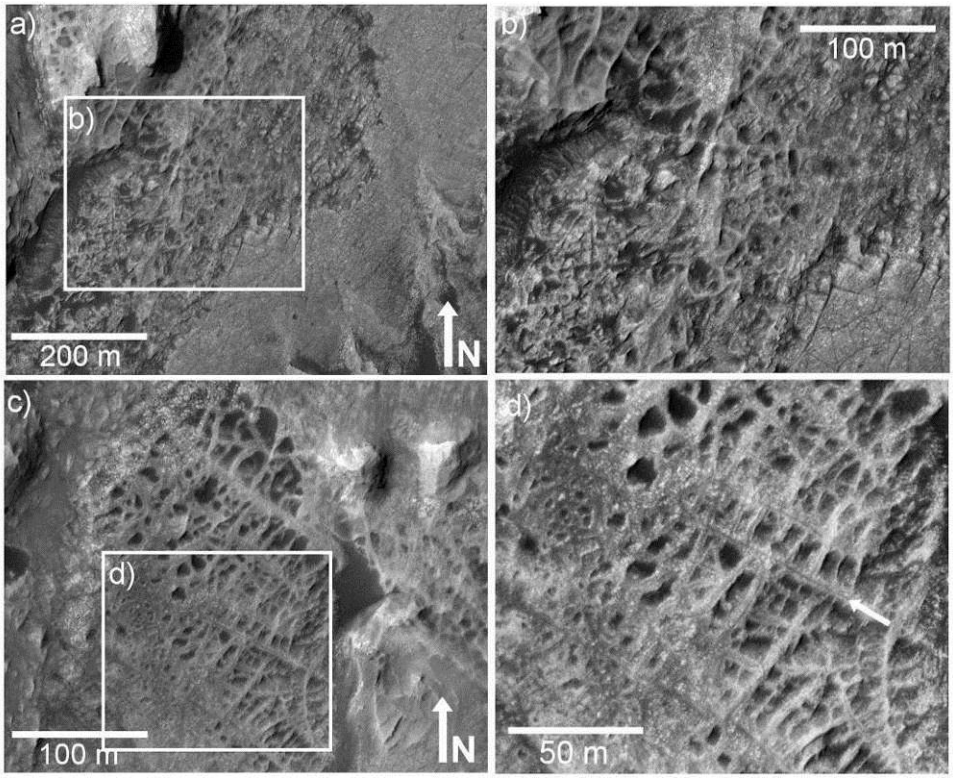

Figure 22: a) Here, a smooth but fractured surface has partially eroded away, leaving a rough surface with ridges in some places where fractures used to be, shown in a close-up in **b)**. **c)** Better-defined erosion-resistant ridges interpreted to be filled or altered fractures. **d)** is an inset of **c)**, and dark lines are visible along the center of the larger ridges (one example is marked with an arrow). HiRISE image ID: PSP_001752_1750. Illumination is from the left. Locations: **a)** 4.914°S 137.271°E **c)** 4.878°S 137.313°E.

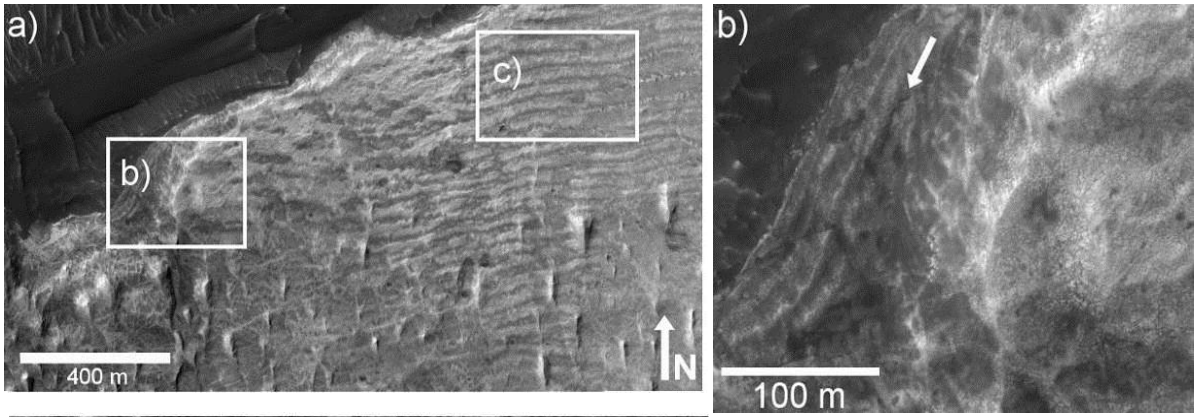

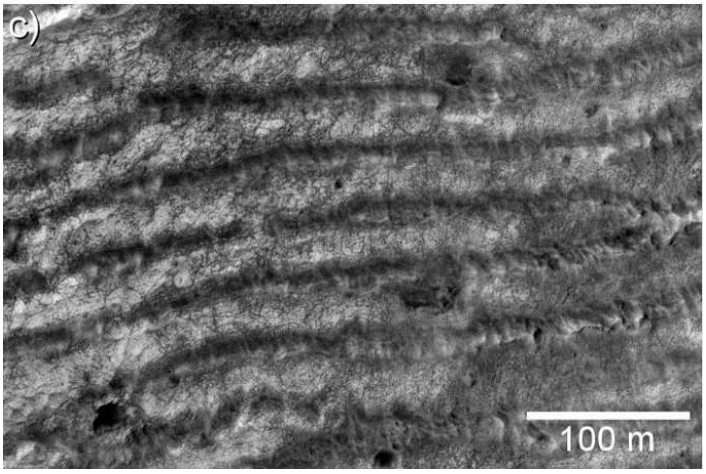

Figure 23: a) Near the end of the channel (seen at the top of this image) that forms the large canyon in the western mound, a lineated surface is being exposed beneath small yardangs. This was first noted by Edgett and Malin [90]. **b)** Close-up, showing beds in the canyon wall. If the parallel features in **a)** and **c)** were bedding planes, their orientation in plan view would correspond to the depth of erosion, following the wall of the canyon, similar to contours on a topographic map. That they do not suggests that they are not exposed bedding planes. **c)** Close-up of the corrugated surface showing that it is extensively fractured. This Figure is a subframe of HiRISE image PSP_008147_1750 with illumination from the left. Location: 5.165° S 137.430° E.

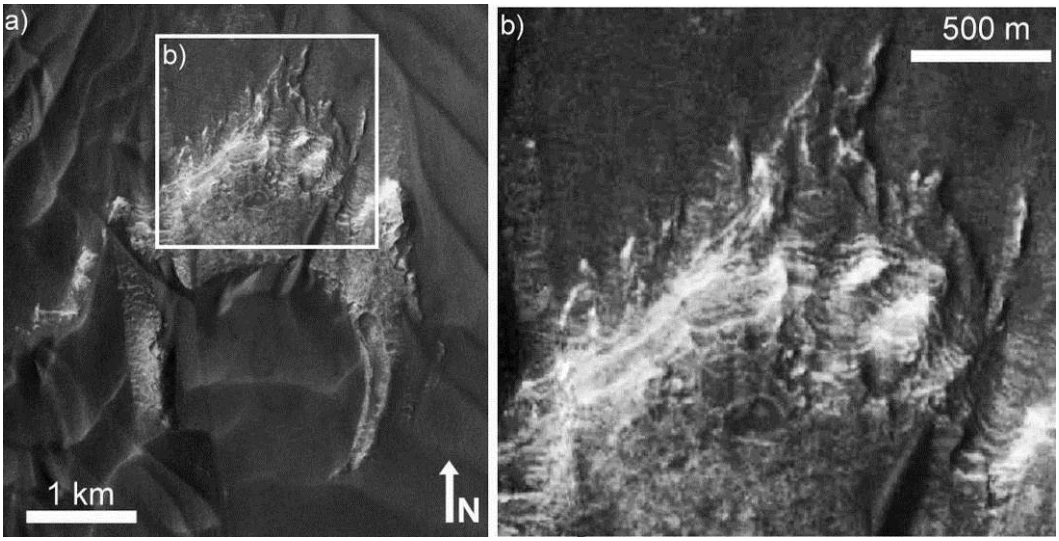

Figure 24. (a) A light-toned layered outcrop within the large dune field west of the mound supports the hypothesis that the layered mound was once much more extensive. A ~2 km crater in the outcrop is partially buried by dunes. **(b)** A close-up of the outcrop. Refer to appendix Table A1 for CTX image IDs. Illumination is from the left. Location: 5.133°S 137.213°E.

toned dune field, there is an outcrop of layered yardang-forming material that borders a circular depression. (Figure 24).

4.1.2 Interpretations

We interpret the "yardang-like" texture of the dark-toned layered yardang-forming unit to be due primarily to aeolian erosion. However, the large canyons and smaller filled channels in the dark-toned layered yardang-forming material provide evidence for fluvial erosion of the unit. This provides an important temporal constraint, implying that the unit was deposited and significantly eroded at a time when fluvial processes could still occur at the surface of Mars.

We interpret the erosion-resistant polygonal ridges on the surface of the dark-toned layered yardang-forming material to be the result of differential erosion of filled or cemented fractures, similar to the much smaller-scale "boxwork" observed in some caves on Earth [91]. Thomson and Bridges [72] first suggested this explanation for the Gale Crater ridges and similar erosion-resistant ridges on Mars have previously been interpreted as evidence of alteration and fluid flow through fractured rocks [92].

The darker line observed in the center of some ridges could be the fracture itself, while the lighter-toned ridge is formed by the surrounding erosion-resistant cemented or altered rock. Alternatively, the darker central line could represent a variation in the albedo of the material filling the fracture.

It is also possible that the erosion-resistant ridges are dikes formed by the intrusion of igneous rock along fractures. However, dike swarms tend to be parallel, en echelon, or radially oriented, rather than polygonal [93]. Given the geomorphic evidence that water has played a role in Gale Crater, and the presence of hydrated sulfates in the dark-toned layered yardang-forming material, we favor an aqueous alteration interpretation.

The observed “blurring" between thin beds with similar erosional characteristics (Figure 21b) could be due to a gradual change in the depositional setting, or due to the debris from the eroding layers obscuring an otherwise sharp contact. The continuity of bedding planes such as the marker bed shown in Figure 19 over many kilometers suggests that the depositional process that formed the layers of the lower mound was widespread and uniform.

The parallel lineations near the head of the large western canyon (Figure 23) have been interpreted as lithified subaerial or subaqueous bedforms [90]. The lineations do not appear to be due to the exposure of bedding planes in cross-section. If the lineations were due to the exposure of bedding planes, their orientation in plan view would correspond to the depth of erosion into the local topography, eventually becoming parallel with the beds in the wall of the canyon, similar to contours on a topographic map.This is not observed. An alternative hypothesis is that the features observed are due to preferential erosion along parallel zones of weakness. The surface does appear to be fractured, but there are no obvious larger joints running parallel to the features.

We interpret the outcrop of layered material to the west of the mound (Figure 24) as an outlying portion of the lower mound, possibly related to the dark-toned layered yardang-forming material. The outcrop appears to be an eroded pedestal crater with a morphology similar to those observed in the MFF [94]. The presence of this outcrop supports the hypothesis that the layered mound material was once more extensive and may have filled the crater.

4.2 Light-toned yardang-forming material

4.2.1 Observations

The light-toned yardang-forming material is a distinctive, high CTX albedo (~0.26), uncratered feature on the northwest flank of the Gale Crater mound (Figure 17). The surface of

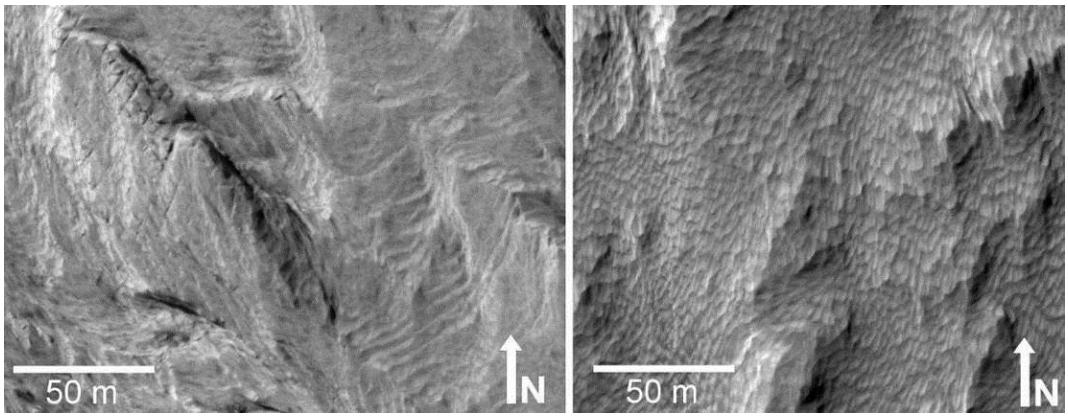

Figure 25: a) The light toned yardang unit shows very fine layering (bottom right) and numerous parallel joints in the rock (upper left). **b)** Much of the surface of the light toned yardang unit is covered with shallow hollows. Refer to appendix Table A2 for HiRISE image IDs. Locations: a) 4.854°S 137.414°E b) 4.916°S 137.419° E.

the light-toned yardang material has a low-to-moderate thermal inertia (~390 J m-2K-1s-1/2) and does not appear to be covered by the dust that mantles the upper mound unit and portions of other nearby units. In CTX and MOC images, the fine details of the surface texture are not visible, and the material appears to be a massive light-toned deposit, with a surface that has been eroded into yardangs. HiRISE images reveal that this material is actually very finely layered (Figure 25a), and in places parallel joints and boulders are visible. None of the joints in the light-toned yardangs show the erosional resistance observed in the lower mound.

Much of the surface of the light-toned yardang-forming material is covered with a texture of smooth, contiguous, shallow depressions (Figure 25b). Similar textures on Tharsis Montes and at White Rock in Pollack Crater have been referred to as "scalloped" [95]) and we adopt that term here. This texture occurs both on flat surfaces and slopes and high points within the light-toned yardang-forming unit. Boulders are not common on the light-toned yardang-forming unit and are typically found near outcrops with joints.

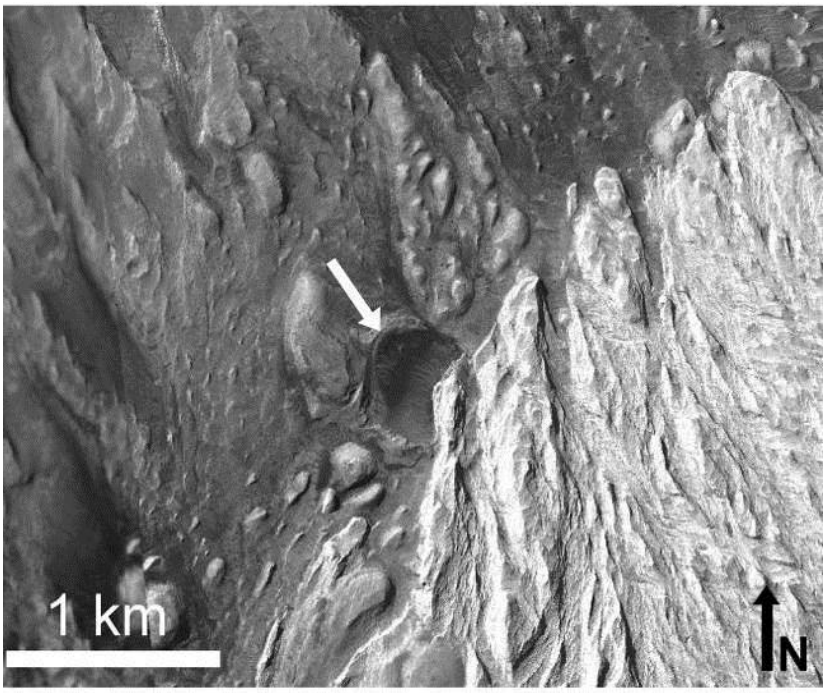

Figure 26: A crater in the dark-toned layered yardang unit is partially buried beneath the light-toned yardang unit marking an erosional unconformity previously identified by Malin and Edgett [60]. Refer to appendix Table A1 for CTX Image IDs. Illumination is from the left. Location: 4.860°S 137.420°E.

This unit has previously been noted [60] to lie unconformably on the darker-toned layered yardang surface, most clearly demonstrated by a crater that is partially exhumed from beneath the light-toned yardang-forming unit (Figure 26). In addition, the filled channel in the dark-toned layered yardang surface (Figure 18) may emerge from beneath the light toned yardangs [60].

Thomson and Bridges [72] used MOLA tracks to fit a plane to the contact between the light-toned yardang unit and the underlying mound. They found that the best-fit plane is non-horizontal. We used a CTX stereo DEM to conduct the same exercise and found that the best fit plane has a slope of roughly 12°, similar to the slope of the mound. We calculated an approximate maximum thickness of the deposit by assuming that the best fit plane represents the surface of the underlying mound. The greatest vertical distance between that plane and the surface of the light-toned yardang unit gives a maximum thickness of ~200 m.

4.2.2 Interpretations

The scalloped texture of the light-toned yardang-forming material suggests that it is soft enough for aeolian erosion to scour shallow pits into the surface. However, the presence of joints and boulders in the material indicates that it is rigid enough to fracture and for fragments to retain their shape. The presence of joints also suggests that the material is old enough to have been subjected to stresses that would cause widespread fracturing, but the observed unconformity (Figure 26) shows that the light-toned yardangs are young enough that the underlying dark-toned layered yardangs had time to erode and accumulate craters before the lighter unit was deposited.

The lack of craters on the surface of the light-toned yardang-forming material itself suggests that it is either quite young, eroding rapidly, or both. The lack of dust on the surface of the light-toned yardang-forming material may also be evidence of ongoing erosion.

Although the scalloped texture sometimes appears similar to fields of small aeolian bedforms, the presence of the texture on slopes and high points is more consistent with it being the erosional expression of the rock. Bridges *et al.* [95]have suggested that a similar texture may be due to the formation of bedforms by saltating dust aggregates and the erosion of a uniquely martian "duststone".

The light-toned layered yardang-forming material shows some similarities to "White Rock" in Pollack crater (-8S, 335W). White Rock is a ~12 km by ~15 km outcrop of relatively light-toned yardang-forming material first observed in Mariner 9 images [96] and has been studied extensively (*e.g.* [97] and references therein). White Rock exhibits a texture similar to the "scalloped" texture discussed above (Figure 25), but does not appear to have the fine-scale layering, parallel jointing, and occasional boulder-shedding outcrops observed on the light-toned layered yardang unit, suggesting that the light-toned yardang-forming material is stronger. This

is consistent with thermal inertia measurements: White Rock has a TES-derived thermal inertia of 232 +/-14 J $m^{-2}K^{-1}$ $s^{-1/2}$ [97] which is somewhat lower than the estimated THEMIS thermal inertia for the light-toned yardang unit (~390 J $m^{-2}K^{-1}s^{-1/2}$). We calculate an average CTX albedo of ~0.20 for White Rock and an average albedo for the light-toned yardang unit of ~0.26. Although the two units differ somewhat in detail, the similarities in morphology between White Rock and the light-toned yardang unit may indicate a similar origin.

4.3 Thin mesa-forming material

4.3.1 Observations

In some locations on the mound, the underlying terrain is obscured by a thin unit that occurs primarily in isolated patches or mesas (Figure 27). This thin mesa-forming material appears to conform to pre-existing topography and occurs on both the dark-toned layered yardang-forming

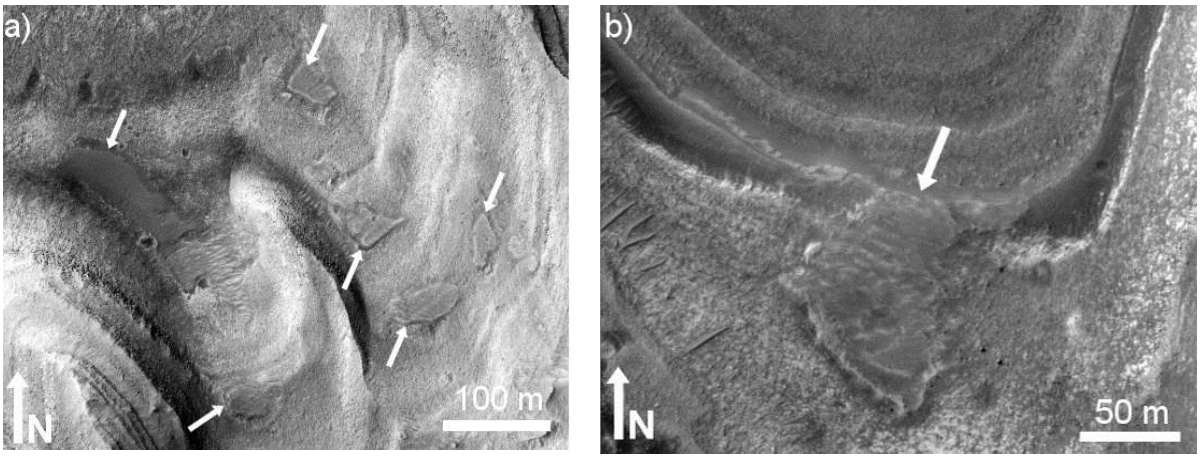

Figure 27: a) Patches of the thin mantle unit (marked by arrows) on the smooth slope of the dark-toned layered yardang unit. b) A patch of thin mantle unit obscures a layer in the dark-toned layered yardang unit. Both a) and b) are subframes of HiRISE observation PSP_009149_1750 with illumination from the left. Refer to figure 18 for context. Locations: **a)** 4.767°S 137.436°E **b)** 4.755°S 137.441°E.

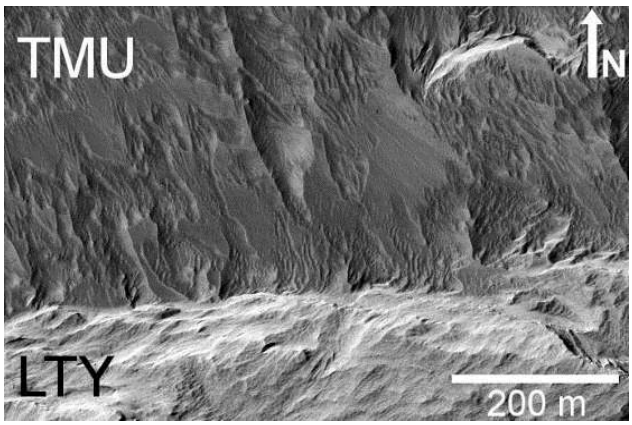

Figure 28: The thin mantle unit (TMU) has a characteristic "feathery" erosional expression, seen in the upper portion of this image. It is not clear whether the thin mantle unit is emerging from beneath or simply abuts the light-toned yardangs (LTY) in this location. This is a subframe of HiRISE observation PSP_009861_1755. Illumination is from the left. Location: 4.744°S 137.529°E.

material of the lower mound and the upper mound unit. The thin mesa-forming material shows no obvious layering in full-resolution HiRISE images.

North of the light-toned yardang-forming material, the thin mesa-forming material is more extensive and obscures the layered nature of the mound. The thin mesas are partially overlain by aeolian deposits of the same tone, giving the surface a distinctive "feathery" appearance (Figure 28).

4.3.2 Interpretations

We interpret the patches of thin mesa-forming material on the mound as outcrops of a formerly more extensive unit. The material appears to lie unconformably on top of the dark-toned layered yardang-forming material and the upper mound unit. The fact that it conforms to the underlying topography leads us to speculate that it originated as an airfall deposit. Lithified aeolian materials such as pyroclastic or impact-generated dust and ash are both possible origins for the material in the thin mesa-forming deposit. The lack of layering within the thin mesa-forming material implies that it either represents a single discrete event, or is very finely layered below the limit of available imaging resolution.

4.4 Upper mound

4.4.1 Observations

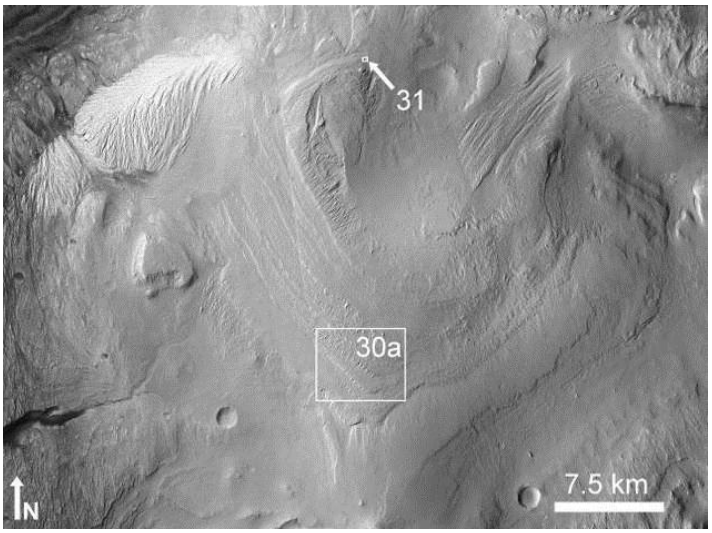

Figure 29: An overview of the layered upper mound unit. The boxes show the locations of Figures 30 and 31. Refer to appendix Table A1 for CTX image IDs. Illumination is from the left.

The upper Gale mound is characterized by large, terraced packages of finely bedded layers. The edges of the packages are highly eroded (Figure 29, 30), and the upper mound generally has a uniform, relatively high CTX albedo (~0.24) and a surface with a very low thermal inertia (~300 J m-2K-1s-1/2). Aeolian ripple-like bedforms with a similar albedo to the upper mound material are common, and often obscure the contact between the upper mound and the underlying units. No obviously fluvial features have been identified in HiRISE images of the upper mound unit.

Much of the upper mound has a similar "scalloped" texture to that seen on the light-toned yardangs. The texture does not appear to be controlled by topography: it occurs on smooth areas as well as rugged slopes, whereas bedforms tend to collect in depressions. Figure 31 shows an example of bedforms in a depression on the upper mound and the scalloped texture on nearby rugged terrain.

The bench portion of some of the large packages of upper mound layers exhibits a pattern of light and dark lines (Figure 30). In some locations the lines appear in concentric rings or as a

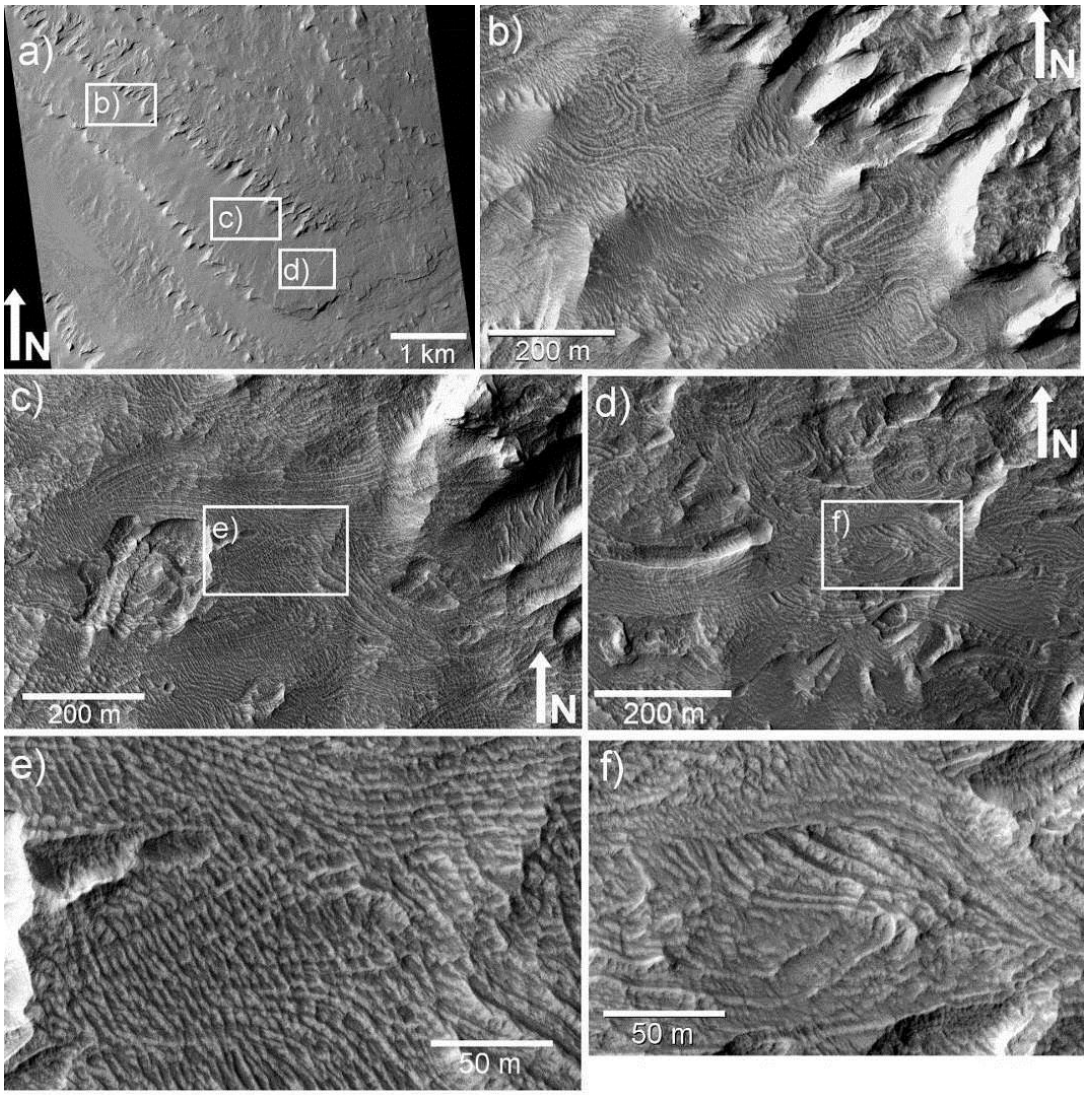

Figure 30: a) A view of the large, cliff-bench packages of layers of the upper mound (see figure 29 for context). The cliffs have been eroded by the wind into yardangs. The white rectangles indicate the locations of **b)**,**c)** and **d)**. **b)** The surface texture of the "bench" portion of the upper mound. Here it forms concentric rings, separated by bands that "pinch" together. **c)** Another location on the bench of an upper mound layer, exhibiting bands that appear to "zig-zag", as shown in **e)**. **d)** A third location, with curved groups of bands that truncate each other, similar to aeolian crossbeds. **f)** is a close-up of the potential crossbeds in **d)**. All frames in this figure are from HiRISE image PSP_001620_1750. Illumination is from the left. Locations: **b)** 5.063°S 137.726°E **c,e)** 5.087°S 137.753°E **d,f)** 5.098°S 137.767°E

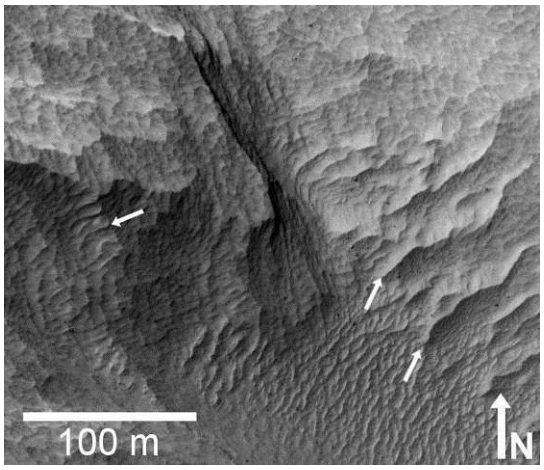

Figure 31: The upper mound unit has a "scalloped" texture similar to that observed on the light-toned yardang unit (Figure 25). The texture does not appear to be controlled by topography and occurs even on rugged slopes (for example, the location marked by the leftmost arrow), as shown in the left portion of this image. On the right, aeolian bedforms (marked by arrows) are collected in a depression. This image is a subframe of HiRISE observation PSP_009927_1750. Location: 4.732°S 137.756°E.

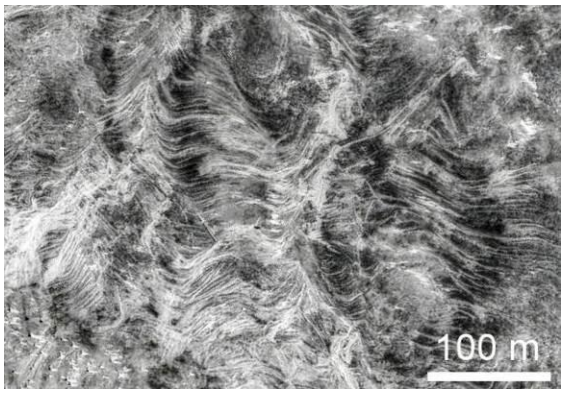

Figure 32: A contrast-enhanced example of crossbeds and sinuous patterns exposed in a playa at White Sands National Monument (32.818°N 253.679°E). The dry upper portion of the dunes has been removed by wind, revealing a horizontal cross-section through the lower moisture-immobilized portion of the dunes. The exposed beds are similar in appearance to the patterns shown in Figure 30. Image credit: USFWS/DigitalGlobe/Google.

sinuous pattern but in other locations, the lines in the pattern truncate others or form sharp angles. The surface of the bench where this occurs appears to be quite planar.

4.4.2 Interpretations

The albedo and thermal inertia of the upper mound surface have been interpreted as indicating the presence of a dust mantle (*e.g.*, [62]). Pelkey et al. [62] suggest that this dust mantle is due to control of local winds by the topography of the mound, but they acknowledge that detailed mesoscale modeling of wind patterns in Gale Crater is required to evaluate this hypothesis.

The scalloped texture on the upper mound, like that observed on the light-toned yardang-forming material, is similar in appearance to aeolian bedforms, but its presence on rugged slopes and outcrops implies that the texture may be due to the erosional characteristics of the upper

mound material. We interpret the jagged edges of the large packages of layers in the upper mound as the result of aeolian erosion into yardang-like outcrops.

The pattern on the surface of the upper mound benches initially appears to be due to finely layered rock eroding to different depths, revealing contours by exposing the edges of layers of varying tone. However, the truncating sets of lineations and sinuous nature of many of the lines is more similar to large-scale (hundreds of meters) aeolian cross-beds than to patterns produced by the erosion of parallel layers. In addition, the generally planar nature of the surface is inconsistent with the varying depths of erosion necessary to explain the pattern if it were due to the exposure of parallel layers.

Although crossbeds are more familiar on cliff faces, they can be expressed on any plane through a cross-bedded rock, and can form very complex patterns depending on the geometry of the exposure and the original bedforms [98]. Figure 32 shows an example of a horizontal cross-section of large dunes preserved in a playa at White Sands National Monument. The exposed cross-beds and sinuous beds are smaller than those observed in the upper Gale mound, but are similar in appearance. The similarity between the observed pattern in the upper Gale Crater mound and the cross-beds exposed at White Sands leads us to speculate that the upper mound unit may have been formed by the lithification of a large aeolian dune field.

An alternative to the cross-bedding hypothesis is the deformation and erosion of previously parallel layers. This combination of processes could generate complex patterns in the upper mound material, but it would have to have deformed the small-scale beds while leaving the larger beds that form the cliff-bench layers of the upper mound intact and parallel. We therefore favor the aeolian cross-bed hypothesis.

Despite the similar "scalloped" texture, the upper mound unit appears to be distinct from the light-toned yardang-forming material. The upper mound has more prominent layering, and although the upper mound unit does form yardang-like outcrops at the edges of the largest layers, the large-scale texture formed by the yardangs is distinct from that observed on the light-toned yardang unit.

4.5 Mound-skirting unit

4.5.1 Observations

The mound-skirting unit is an erosion-resistant, mesa-forming material characterized by a texture that is generally smooth over hundreds of meters, but which at smaller scales is marked by numerous small (~10-60 m) pits and/or parallel ridges (Figure 33). The ridges are several meters high and occur at regular intervals of 30-50 m. Figure 7 shows a map of the occurrence of the mound-skirting unit and other units with a similar pitted or ridged texture. As with all unit maps, this grouping is a simplification: in some cases two distinct units with this texture overlap with a sharp boundary.

The mound-skirting unit generally has high thermal inertia (~720-780 J m-2K-1s-1/2). However, in some locations along the base of the northern mound and on the mesas on the crater floor and near the northern rim, the thermal inertia is lower (~450 J m-2K-1s-1/2) despite the unit having a similar erosional expression.

The mound-skirting unit is present on the crater floor and extends up onto the lower slopes of the mound in some locations. It typically truncates in a scarp, dropping down to the lowest units of the mound (Figure 34). On the northern crater floor (Figure 12) the groups of mesas that extend from the crater wall down to the base of the mound have a texture similar to the mound-skirting unit, as do the raised fan-shaped mesas at the base of the northern wall (Figure 15).

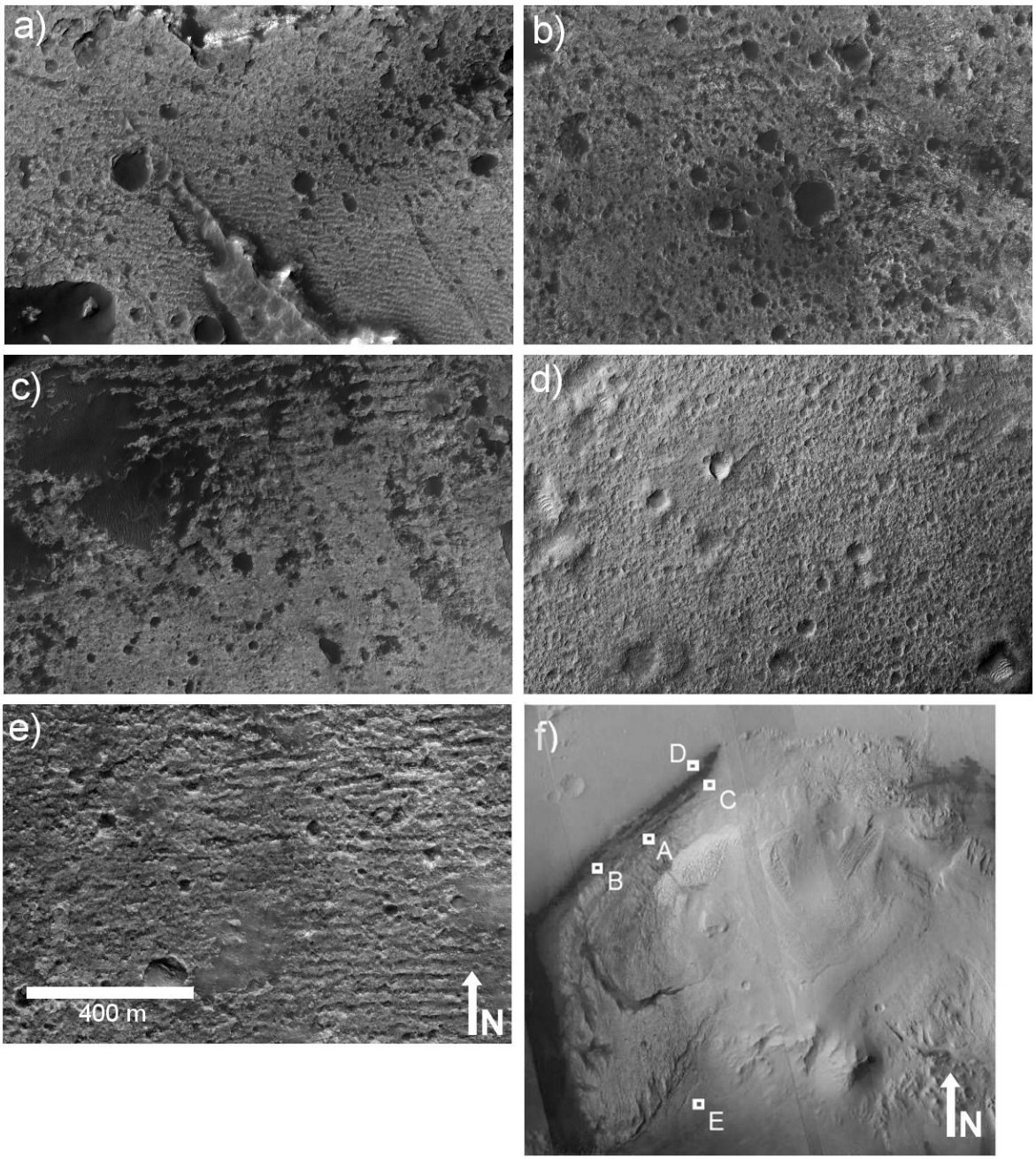

Figure 33: HiRISE images of the mound-skirting unit, all shown at the same scale, with illumination from the left. **a)** The fan-shaped outcrop of mound-skirting unit (see text for discussion). **b)** Several kilometers southwest of **a). c)** A similar texture to the northeast of **a)** transitions into a "washboard" texture of long parallel ridges. **d)** The same pitted texture appears farther out on the crater floor. It is less obvious because these pits are not filled with dark material. **e)** The "washboard" and pitted texture also appears to the south of the mound. **f)** A CTX mosaic showing the locations of **a)-e).** Refer to appendix Table A1 for CTX image IDs and appendix Table A2 for HiRISE image IDs. Locations: **a)** 4.749°S 137.381°E **b)** 4.794°S 137.266°E **c)** 4.617°S 137.510°E **d)** 4.580°S 137.490°E **e)** 5.490°S 137.497°E

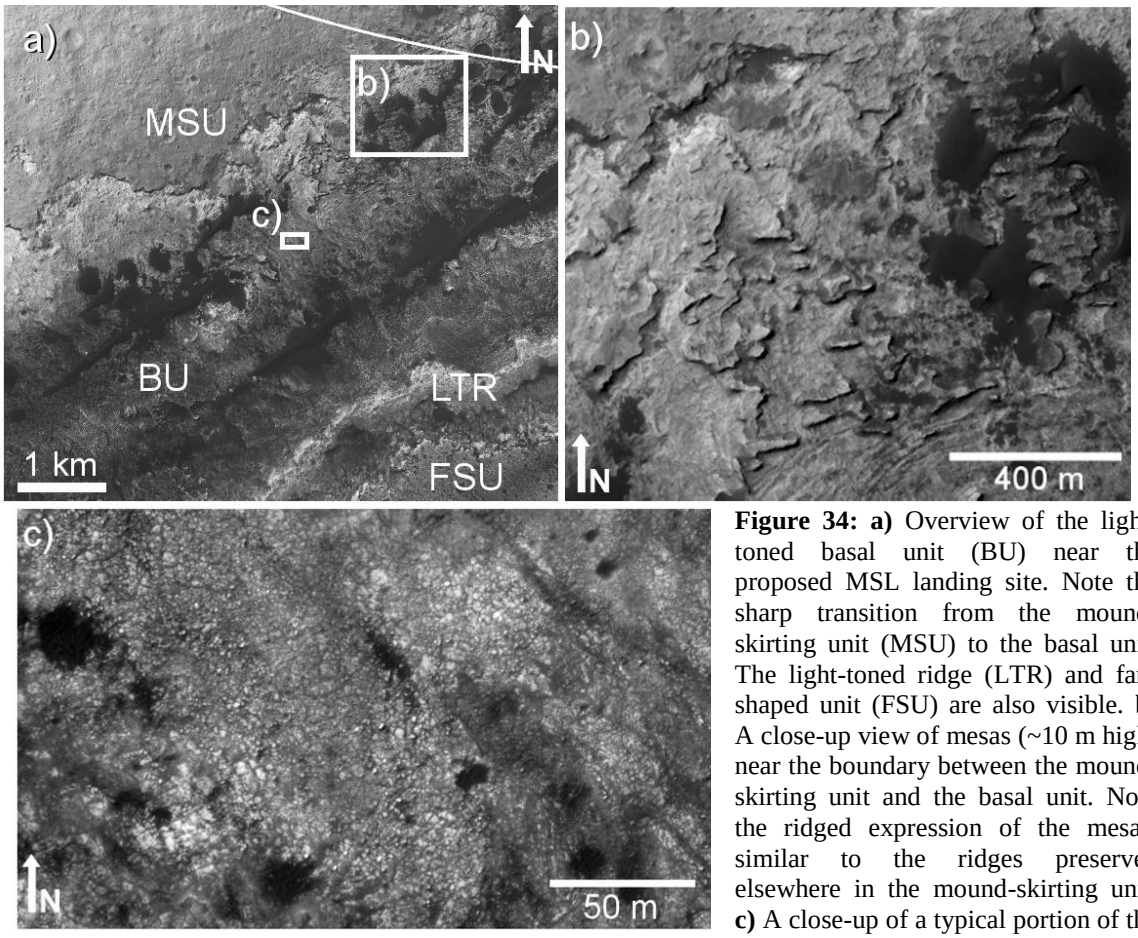

Figure 34: a) Overview of the light-toned basal unit (BU) near the proposed MSL landing site. Note the sharp transition from the mound-skirting unit (MSU) to the basal unit. The light-toned ridge (LTR) and fan-shaped unit (FSU) are also visible. **b)** A close-up view of mesas (~10 m high) near the boundary between the mound-skirting unit and the basal unit. Note the ridged expression of the mesas, similar to the ridges preserved elsewhere in the mound-skirting unit. **c)** A close-up of a typical portion of the basal unit. HiRISE Image ID: PSP_009650_1755. Illumination is from the left. Location: 4.703°S 137.345°E.

South of the mound, channels in the mound skirting unit transition into sinuous ridges at the unit's edge (Figure 6), and within the landing ellipse, a finely branching network of ridges occurs in the mound-skirting unit (Figure 14).

In several locations (Figure 11) material from the northwestern mound appears to extend out onto the top of the mound-skirting unit. These are also locations of canyons in the mound, several of which have channel- or fracture-like features in their floors or walls, cutting across the bedding of the mound.

The filled channel on the northwest flank of the mound (Figure 18) ends in a distinctive 3.5 km2 outcrop of material with a pitted texture very similar to the mound-skirting unit. Figure 18b shows a close-up view of the surface of the outcrop, which exhibits a reticulate pattern.

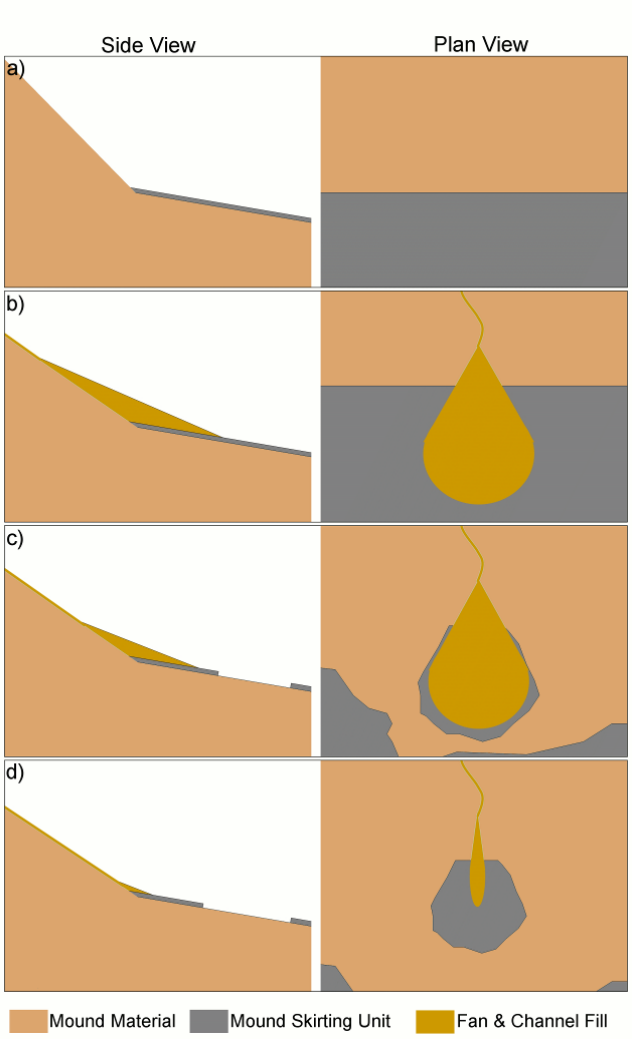

Figure 35: A cartoon showing our hypothesis for the origin of the fan-shaped unit discussed in Section 5.7. The left column shows a cross-sectional view and the right column shows a plan view. **a)** The mound-skirting unit extends part of the way up the layered mound material. **b)** The mound is eroded and a channel transports debris down slope and deposits it as a fan on top of the mound-skirting unit, similar to the fans observed elsewhere (Figure 11). **c)** Erosion causes the fan to shrink and the boundary of the mound-skirting unit to recede. **d)** Continued erosion removes most of the fan material, exposing a patch of the mound-skirting unit that has been protected by the fan.

Milliken *et al.* [73] have also noted the similarity in texture and spectral signature between this outcrop and the mound-skirting unit (Figure 33).

4.5.2 Interpretations

The characteristic texture of pits or ridges in an otherwise smooth surface may be due to a resistant layer developing defects which are then exploited by erosion. Erosion-resistant units tend to preserve impact craters [99], which may explain the numerous pits in the mound-skirting unit surface. The typically high thermal inertia suggests a coherent material, consistent with the mound-skirting unit's apparent erosion resistance. The parallel ridges that occur in the mound-

skirting unit (Figure 30) may be eroded lithified bedforms, or preferential erosion along parallel joints.

The presence in some locations of multiple overlapping units with the mound-skirting unit texture (Figure 16) suggests that in some cases multiple layers with the necessary erosional characteristics are present.

The transition between channel and sinuous ridge that occurs at the edge of the mound-skirting unit south of the mound leaves little uncertainty that the sinuous ridges are inverted channels (Figure 6). We likewise interpret the finely branching ridges (Figure 14) in the landing site as inverted channel deposits.

Alternatively, it is also possible that the finely-branching raised features are erosion-resistant fractures, similar to those observed on the dark-toned layered yardang-forming unit. However, the features branch and anastomose in a manner that is more consistent with fluvial channels than with fractures.

Another possibility is that the finely-branching features are lithified aeolian bedforms, and there do appear to be small modern bedforms between some of the features. However, the features themselves appear to follow the curvature of the southern edge of a channel-like feature in the mound-skirting unit and lack the periodicity common to aeolian bedforms. In addition, thin sinuous ridges occur that are isolated from the other ridges in the network, which would be unusual for aeolian bedforms.

The fan-shaped nature of the deposits at the base of the western mound (Figure 11) which overlap the mound-skirting unit, and their correlation with large canyons, suggests that they are debris from erosion of the mound. This provides a constraint on the time of

deposition for the mound skirting unit, suggesting that the mound was still eroding after the mound-skirting unit was emplaced. The non-bedded features in the walls of the canyons may be filled channels or fractures associated with the erosion of the mound and the formation of the canyons and fans of debris.

Due to its association with the filled channel, Thomson *et al.* [63] have suggested that the outcrop of material shown in Figure 18a is a depositional fan. However, this does not explain the similarity between this outcrop and the rest of the mound-skirting unit.

We suggest that the fan-shaped outcrop that is visible today is a portion of the more-extensive mound-skirting unit, and that the outcrop was buried by fan-shaped debris deposits similar to those shown in Figure 11. The debris may have protected the underlying mound-

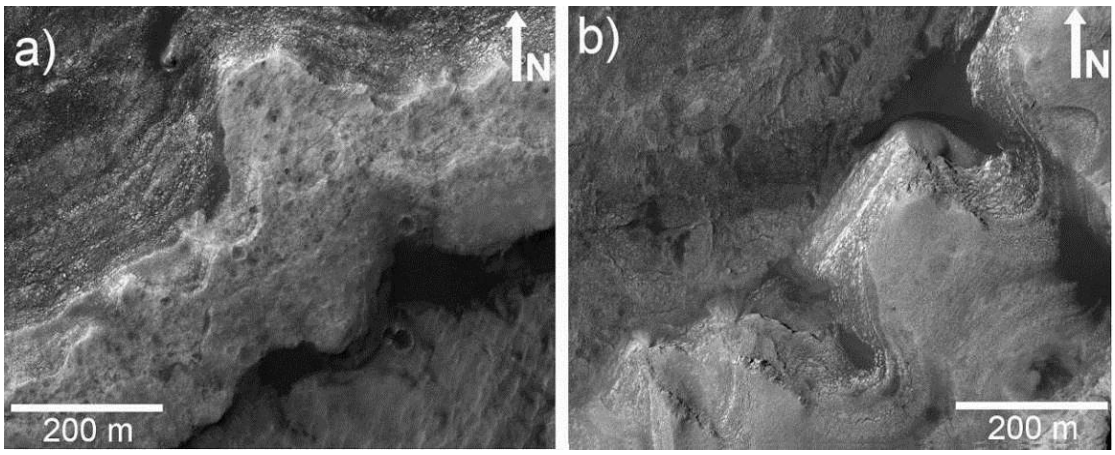

Figure 36: a) HiRISE close-up of the light-toned ridge unit. On the northwest side the ridge forms a rapidly shallowing slope comprised of fractured light-toned layers and their erosional debris. On the southeast side the ridge ends abruptly with a drop of 5 to 10 meters down to the phyllosilicate-bearing unit, detected by Milliken *et al.* (2009). **b)** Light toned layers to the southwest of **a)** exposed in a gap between the mound-skirting unit and the wall. It is possible that these are a continuation of the same material that forms the light-toned ridge. Refer to appendix Table A2 for HiRISE image IDs. Illumination is from the left. Locations: **a)** 4.722°S 137.383°E **b)** 4.799°S 137.301°E.

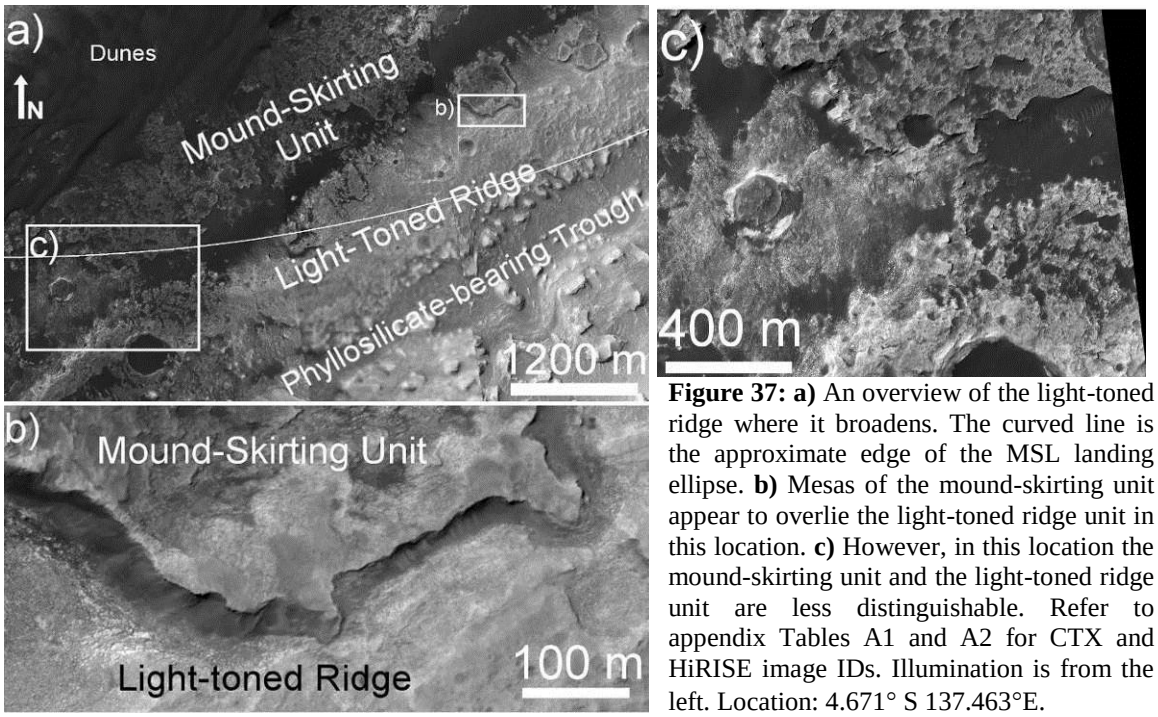

Figure 37: a) An overview of the light-toned ridge where it broadens. The curved line is the approximate edge of the MSL landing ellipse. **b)** Mesas of the mound-skirting unit appear to overlie the light-toned ridge unit in this location. **c)** However, in this location the mound-skirting unit and the light-toned ridge unit are less distinguishable. Refer to appendix Tables A1 and A2 for CTX and HiRISE image IDs. Illumination is from the left. Location: 4.671° S 137.463°E.

skirting unit surface from erosion but now has mostly eroded away, leaving a fan-shaped "footprint" on the preserved surface. A cartoon of this scenario is shown in Figure 35. This scenario reconciles the similarity of the outcrop to the rest of the mound-skirting unit with its location at the end of the filled channel. The reticulate pattern on the surface of this outcrop may be the result of lithified aeolian bedforms.

4.5 Light-toned ridge

4.6.1 Observations

The light-toned ridge is a prominent feature of the lower mound near the proposed MSL landing site (Figures 17, 18). The feature has a CTX albedo of ~0.19 with some locations as high as 0.21, and stands out against the surrounding low-albedo (~0.16) units. The surface of the unit has a relatively high thermal inertia (~600 J m-2K-1s-1/2). Close inspection with the CTX DEM and HiRISE images reveals that this light-toned unit is a ridge, not simply the edge of a layer.

On its northwest side, the ridge breaks down into a >10° slope of layered, fractured light-toned rock (Figure 36) that shallows and merges with the light-toned basal unit, which is discussed in a later section. On the southeast side, the light-toned ridge ends abruptly with a short (<10 m) drop down to a trough between the ridge and the mound.

Following the light-toned ridge from its narrowest portion to the northeast, it becomes less well defined and spreads out into a broader band of light-toned layers (Figure 37a). Where it begins to spread, the ridge has a similar texture to adjacent exposures of the mound-skirting unit (Figure 37c). However, farther to the northeast, mesas of the mound-skirting unit appear to overlie the light-toned layers of the broadened ridge (Figure 37b).

To the southwest of the fan-shaped outcrop of mound-skirting unit there is a gap between the edge of the mound-skirting unit and the layers of the mound. In this location, the lowest mound layers are light-toned, fractured material similar in morphology to the northwest side of the light-toned ridge (Figure 36b). The rock on the southeast side of the trough, across from the light-toned ridge is similarly light-toned and fractured.

4.6.2 Interpretations

The light-toned ridge appears to be part of a more extensive layer in the lower mound. We interpret the fractured light-toned outcrops on the southeast side of the trough and the light-toned outcrops to the southwest (Figure 36) as expressions of the same layer as the light-toned ridge. There is no obvious explanation for why the light-toned material eroded to form a ridge while other outcrops of the material are simply exposed as layers in the mound. We interpret the light-toned ridge as stratigraphically lower than the mound skirting unit. Near the mesas of mound-skirting unit (Figure 37b) the ridge appears to be more extensively eroded than it is in the location where it appears similar in appearance to the mound-skirting unit (Figure 37c).

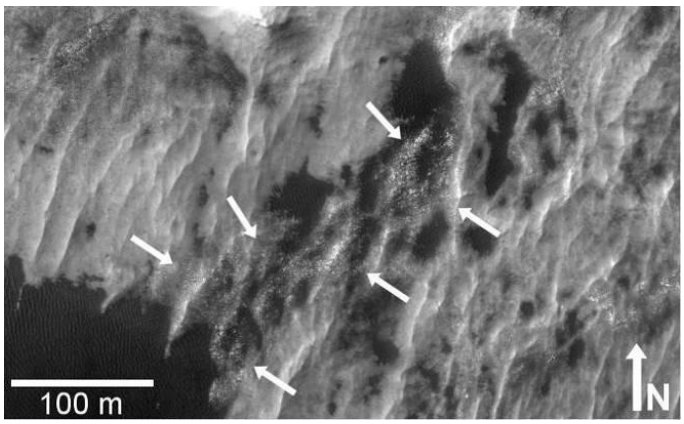

Figure 38: A typical portion of the phyllosilicate-bearing trough surface. The undulating ridges are similar to aeolian bedforms but in some locations, such as the area marked by arrows, they appear to be fractured. In addition, the dark material interacts with the ridges as if they are a hard surface, forming discrete small dunes. The phyllosilicate-bearing unit may be a soft rock that erodes to form this bedform-like morphology, or it may be lithified aeolian material. This figure is a subframe of HiRISE observation PSP_009294_1750. Illumination is from the left. Location: 4.716°S 137.411°E.

4.7 Phyllosilicate-bearing Trough

4.7.1 Observations

The phyllosilicate-bearing trough (mapped in Figure 17) is a depression that parallels the south-east side of the light-toned ridge, and shows a clear nontronite signature in CRISM observations [30]. The same phyllosilicate signature is not clearly visible on the opposite (northwest) side of the light-toned ridge, but a thin bed with a similar signature has been detected in the large canyon in the western mound [30].

The trough has a slightly lower thermal inertia (~550-590 J m-2K-1s-1/2) than the light-toned ridge. The surface of the material in the trough is characterized by undulating ridges (Figure 38). In some cases, the ridges share the light-toned, fractured texture typical of nearby bedrock, and dark material on the surface of the trough floor forms small aeolian bedforms with sharp boundaries.

4.7.2 Interpretations

The surface of the phyllosilicate-bearing trough is suggestive of aeolian bedforms (Figure 38) but we infer it to be a hard surface based on the sharp boundaries of the small dunes of dark-toned aeolian material that occur in parts of the trough floor. It is possible that the phyllosilicate-bearing unit is composed of lithified aeolian bedforms but it may also be a soft sedimentary rock

that erodes in an undulating pattern. Either possibility could be consistent with the observed moderately high thermal inertia.

The lack of a matching phyllosilicate signature on the northwest side of the light-toned ridge suggests that the phyllosilicates are present only in a thin layer which is not visible on the northwest side of the ridge due to the limited resolution of CRISM. If the observed phyllosilicates do represent the exposed surface of a very thin bedding plane, dip measurements [30] indicate that it would emerge near the base of the ridge on the northwest side.

Alternatively, the phyllosilicate-bearing material may be altered material confined to the trough. However, the presence of a thin bed with a similar phyllosilicate signature in the walls of the large western canyon [30] leads us to favor the "thin bed" hypothesis.

4.8 Light-toned basal unit

The light-toned basal unit is distinguished from the crater floor units by a sharp drop of ~10 m (Figure 34a). The light-toned basal unit has a CTX albedo of up to 0.20, and is primarily composed of fractured rock that in some locations has a subtle texture suggestive of layering (Figure 39b). It has a moderate thermal inertia ranging from roughly 500-540 J m-2K-1s-1/2. Mesas of mound-skirting unit are common on top of the light-toned basal unit (Figure 34b), and much of the basal unit is covered by dark-toned mafic dunes. The light-toned basal unit slopes upward in a series of poorly-defined fractured, light-toned layers to form the northwestern side of the light-toned ridge unit (Figure 36a).

4.9 Dark-toned basal unit

The dark-toned basal unit (Figure 39) has a higher thermal inertia (~780 J m-2K-1s-1/2) than the light-toned basal unit. It has an albedo of 0.15-0.16 and occurs to the southwest of the

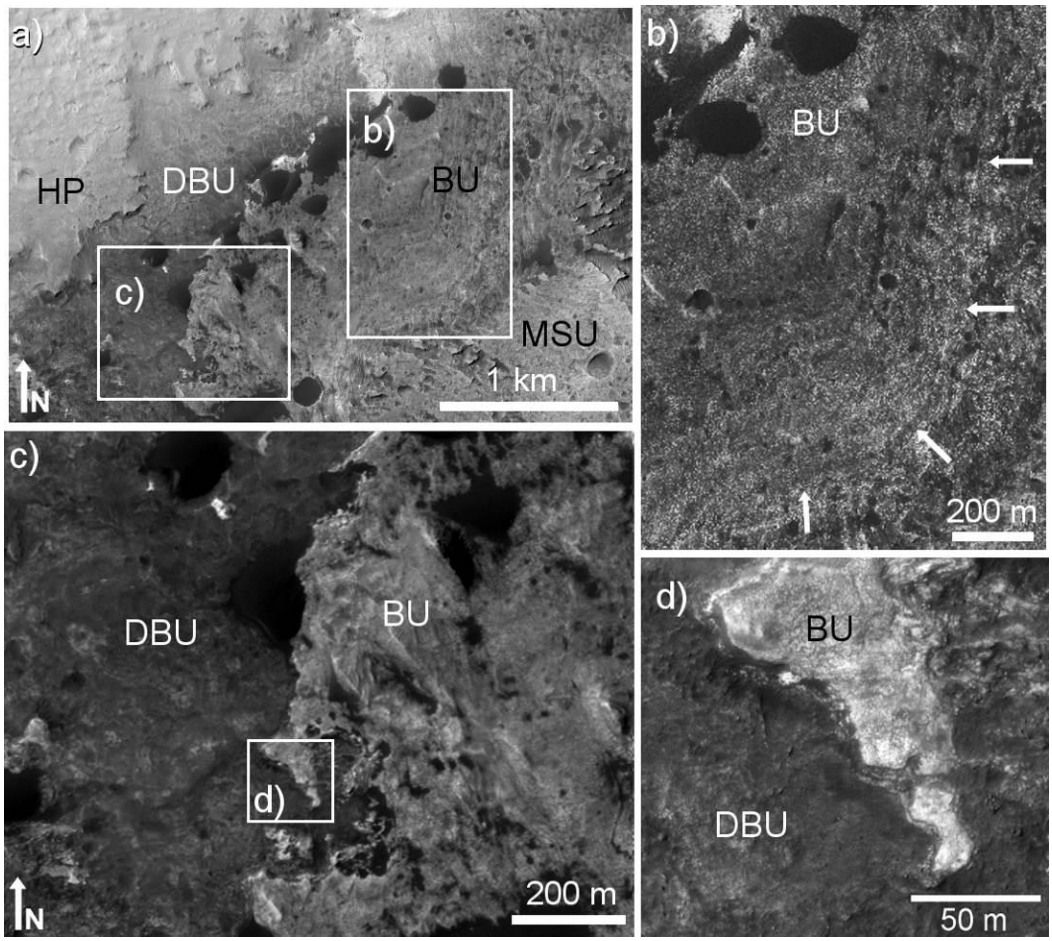

Figure 39: a) The dark-toned basal unit (DBU) is to the southwest of the light-toned basal unit (BU). Also visible is the mound-skirting unit (MSU) and the hummocky plains unit (HP). Very dark patches are small barchan dunes. **b)** The light-toned basal unit in this location exhibits a fabric that may be faint evidence of layering. The potential layers run perpendicular to the arrows. **c)** A closer view of the sharp transition between the light-toned and dark-toned basal units. d) A very close view of the transition. The light-toned basal unit appears to superpose the dark basal unit. HiRISE Image ID: PSP_001488_1750. Illumination is from the left. Location: 4.750°S 137.270°E.

landing ellipse and the light-toned basal unit. The transition between the light and dark-toned basal units (Figure 40) is sharp and the dark-toned basal unit appears to be topographically lower than the light-toned basal unit. This suggests that it is either stratigraphically lower or that the dark-toned unit is younger and fills a depression that had been eroded into the light-toned basal unit.

4.10 Hummocky plains unit

4.10.1 Observations

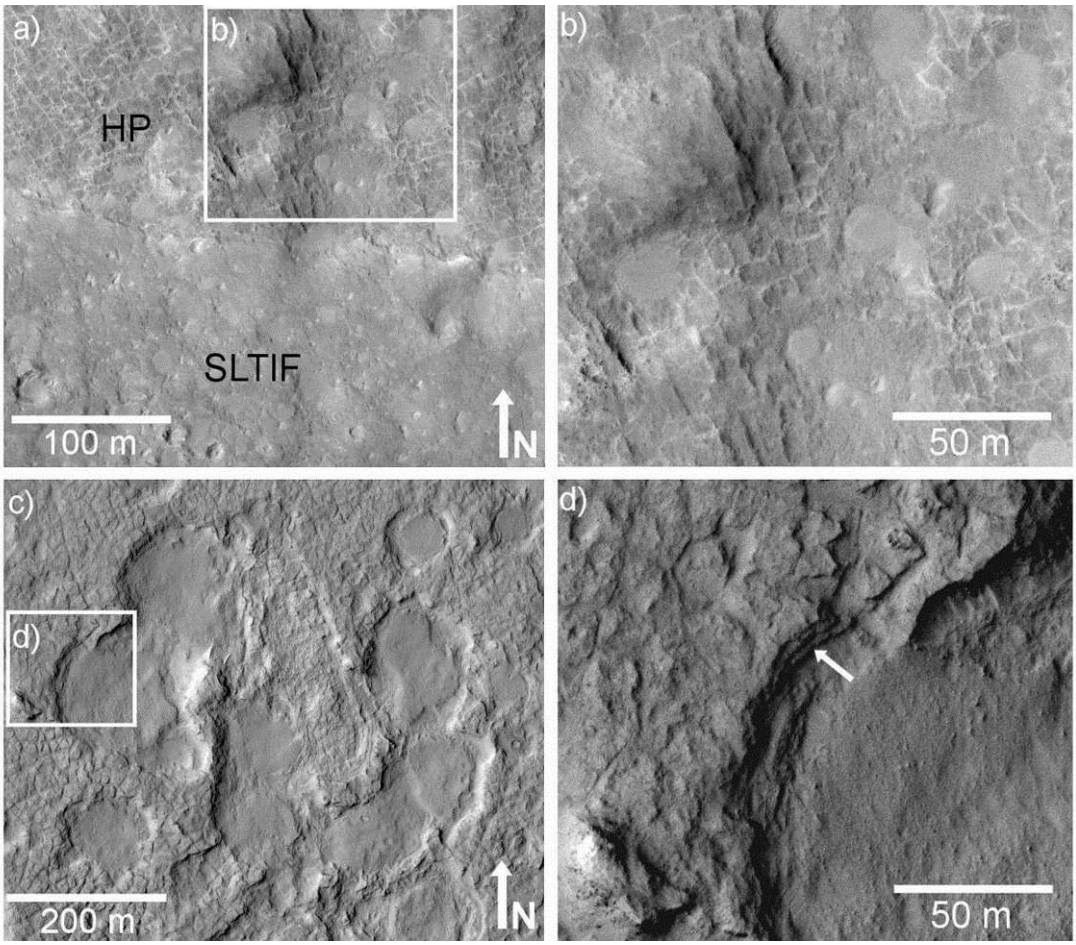

Figure 40: a) The northern boundary of the fan-shaped unit in the landing ellipse. The bottom half of this inset shows the "smooth low thermal inertia fan" (SLTIF) unit surface. This transitions sharply to hummocky plains (HP) showing light-toned polygonal features interpreted as fractures. **b)** A closer view of the hummocky plains unit, showing light-toned fractures similar to the erosion-resistant ridges on the mound. **c)** The distal end of the fan-shaped unit in the ellipse has a higher thermal inertia, consistent with its fractured, rocky appearance in this HiRISE image. Note the filled craters, some of which show layering in their walls, as indicated by the arrow in **d)**. **a)** and **b)** are subframes of HiRISE image PSP_009716_1755. **c)** and **d)** are subframes of HiRISE image PSP_010573_1755. Illumination is from the left. Location: **a)** 4.417°S 137.296°E **c)** 4.535°S 137.438°E

Much of the crater floor near the proposed landing site is a hummocky terrain of smoothly-varying thermal inertia (~480 J m-2K-1s-1/2). It has a uniform CTX albedo (~0.21) similar to other units in the northern crater floor. In locations in which the surface has a lower thermal inertia, this unit has a subdued appearance (Figure 13). In locations with higher thermal inertia, the unit appears more rugged and in some cases is marked by light-toned polygons (Figure 40).

Sinuous ridges are visible in several locations on the hummocky plains unit (Figure 13). They occur on a very shallow (~1°) slope and have a vertical relief of several meters.

4.10.2 Interpretations

The variable thermal inertia of the hummocky plains unit is likely due to varying degrees of mantling with unconsolidated material. The polygonal markings in high thermal inertia locations may be fractures, similar to the erosion-resistant fractures observed on the dark-toned layered yardang-forming unit, although less pronounced.

We interpret the sinuous ridges on the hummocky plains as inverted channels. Their sinuous nature and low slope are consistent with formation by slow-flowing water. These inverted channels also imply that the crater floor was once buried and has been eroded by at least their current height, but they do not constrain the maximum burial depth.

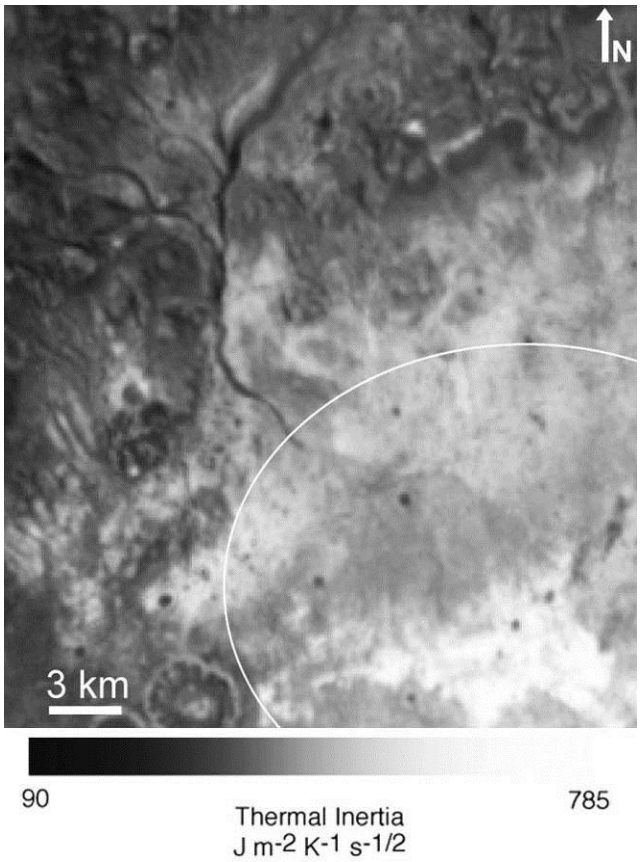

Figure 41: THEMIS thermal inertia map [68] of the fan-shaped feature in the proposed MSL landing site. The branching valley that ends at the apex of the fan-shaped feature has a very low thermal inertia. The fan-shaped feature itself is divided into a proximal low thermal inertia portion and a distal high thermal inertia portion.

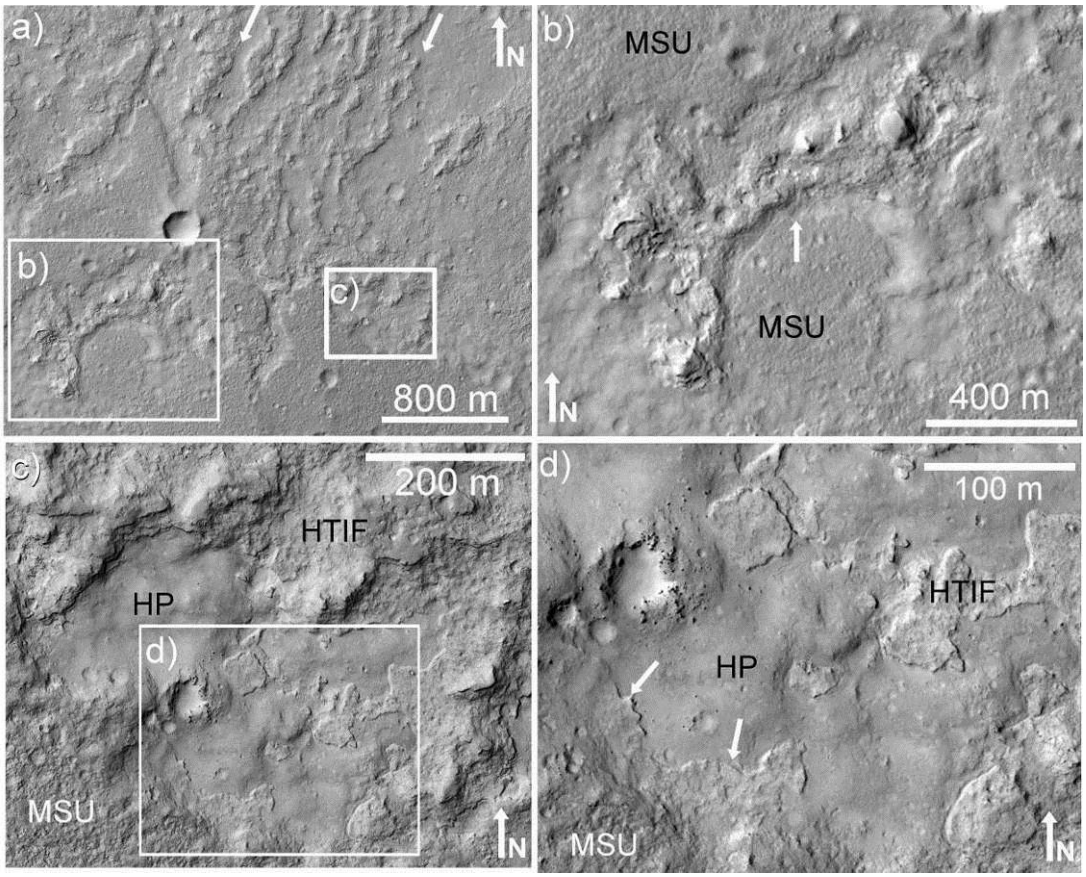

Figure 42: a) The western end of the landing site fan is characterized by numerous ridges of material roughly aligned with the direction of flow (indicated by arrows) on the fan. The mound-skirting unit (MSU) appears to embay outcrops of high thermal inertia fan and/or ridge material as shown by the arrow in **b)**. **c)** The boundary of the high thermal inertia fan (HTIF) is sometimes quite sharp. Here it drops down to a hummocky surface similar to the hummocky plains (HP; Figure 13). **d)** Arrows mark the edge of HTIF material emerging from beneath at the base of the MSU, implying that the MSU superposes the HTIF. This Figure shows subframes of HiRISE observation PSP_009716_1755 with illumination from the left. Location: 4.566° S 137.302°E.

4.11 Northwestern fan-shaped feature

4.11.1 Observations

The proposed MSL landing site in Gale Crater is centered on a large (80.4 km2) fan-shaped feature, the apex of which coincides with the end of a dendritic valley network on the northern crater wall (Figures 8a, 41). The fan-shaped feature can be divided into two units: a smooth, lower thermal inertia (~460 J m-2K-1s-1/2) unit that extends from the apex of the fan down to about two thirds of the way to the distal margin, and a rockier, high thermal inertia (~620 J m-2K-1s-1/2) unit that forms the distal end of the feature (Figure 41). Mesas

similar to the outcrops of mound-skirting unit seen elsewhere on the crater floor partially trace the borders of the fan and occur in the middle of the smooth low thermal inertia unit, The western distal end of the fan is marked by many ridges that are roughly aligned north-to-south (Figure 42). These ridges make the boundary of the western edge of the fan difficult to define precisely.

The smooth, low thermal inertia fan unit, seen in the bottom half of Figure 40a, has a subdued, mantled texture. It has many hollows which are typically filled with a smooth light-toned material.

The high thermal inertia portions of the fan-shaped unit are layered, fractured material. Evidence of layering can be seen in the walls of craters within the unit (*e.g.*, Figure 40d). Where the fan-shaped feature transitions from low to high thermal inertia, the surface becomes rockier and less mantled. Much of the high thermal inertia unit is a distinct lower

stratigraphic layer, marked by a sharp ~10 m drop. However, in many locations the thermal inertia of the terrain increases even before the drop down to the stratigraphically lower unit. In patches of the smoother surface, particularly near the transition to higher thermal inertia, the smoother surface exhibits polygonal features similar in scale to the fractures in the high thermal inertia material (Figure 43).

4.11.2 Interpretations

We interpret the northwestern fan-shaped feature as a lithified alluvial fan, based on its shape and its position at the end of a branching valley on the northwestern crater wall. The roughly flow-aligned ridges in the western portion of the fan may be inverted channels or remnants of debris flow lobes. The pits in the smooth low thermal inertia fan unit may be impact craters, filled by dust or other unconsolidated, sediment.

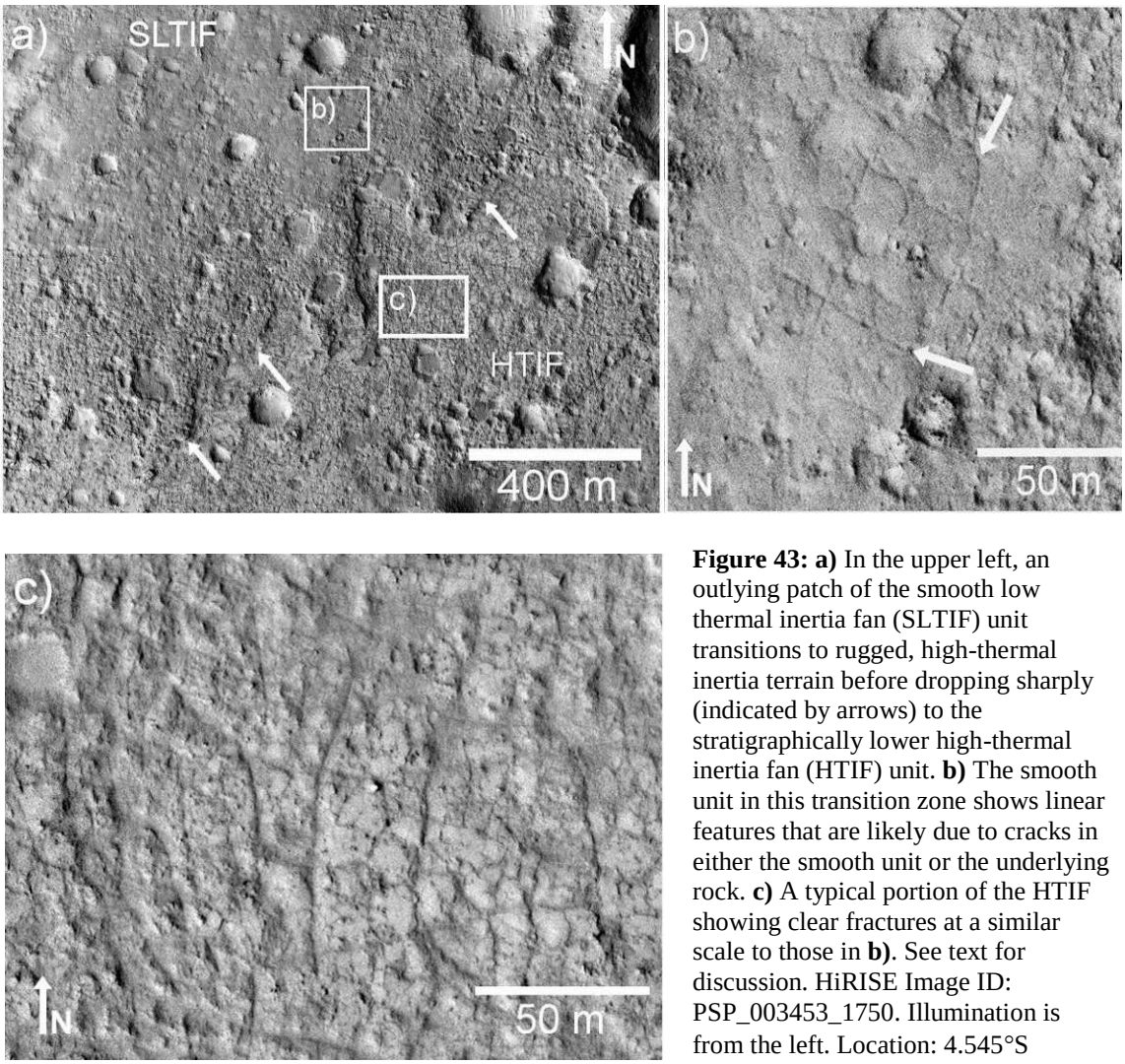

Figure 43: a) In the upper left, an outlying patch of the smooth low thermal inertia fan (SLTIF) unit transitions to rugged, high-thermal inertia terrain before dropping sharply (indicated by arrows) to the stratigraphically lower high-thermal inertia fan (HTIF) unit. **b)** The smooth unit in this transition zone shows linear features that are likely due to cracks in either the smooth unit or the underlying rock. **c)** A typical portion of the HTIF showing clear fractures at a similar scale to those in **b)**. See text for discussion. HiRISE Image ID: PSP_003453_1750. Illumination is from the left. Location: 4.545°S 137.399°E.

The polygonal features in the low thermal inertia fan suggest that it is either rigid enough to fracture, or that it is a thin (less than a few meters) unconsolidated material settling and filling cracks in the underlying high-thermal inertia material (Figure 43). Alternatively, the observed cracks could be due to volume changes in the "smooth fan" unit, such as those due to desiccation or periglacial activity. However the similarity in scale of the fractures in the smooth unit to those in the high thermal inertia fan (Figure 43) and the low thermal inertia of the smooth fan unit leads us to favor the interpretation of the low thermal inertia portion of the fan as a thin layer obscuring the high thermal inertia fan. We interpret the sharp drop that occurs near the transition

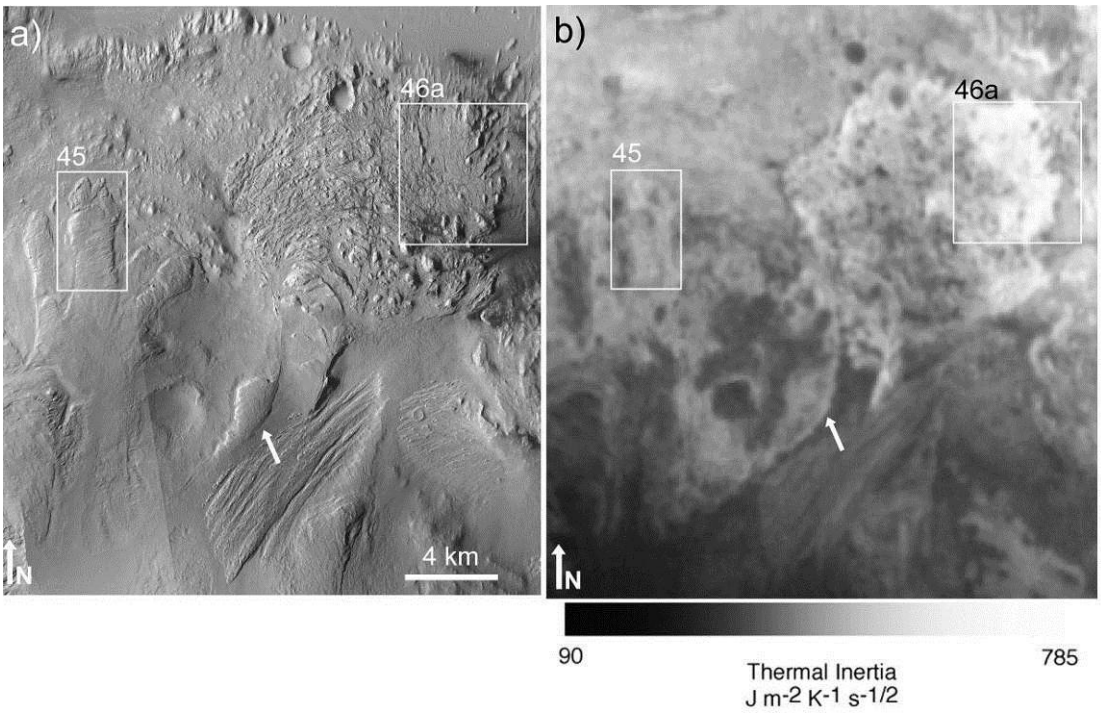

Figure 44: a) Overview of the northern flank of the Gale mound, showing the enigmatic lobate units. Illumination is from the left. Refer to appendix Table A1 for CTX Image IDs. **b)** THEMIS thermal inertia map of the same area shown in **a)** [68]. Note the high thermal inertia of the northeastern portion of the fan-shaped lobate unit. Boxes provide context for Figures 45 & 46. The arrows mark the location where the "neck" of the unit appears to truncate a mesa of mound material.

in thermal inertia as the result of scarp retreat caused by the erosion of the smooth fan and an upper layer of high thermal inertia fan, exposing another underlying high thermal inertia layer.

4.12 Lobate features

4.12.1 Observations

Several large lobate features extend down the northern flanks of the Gale Crater mound (Figure 44). Closer inspection in MOC images reveals that these features are at least coarsely layered, with a continuous sharply defined layer apparent in Figure 45. Most of the lobate features have a relatively uniform width of 1-2 km for their entire length, an approximate thickness of hundreds of meters, and have a convex surface topography with well-defined edges. The uniform-width lobes do not extend all the way down the slope of the mound. The lobate

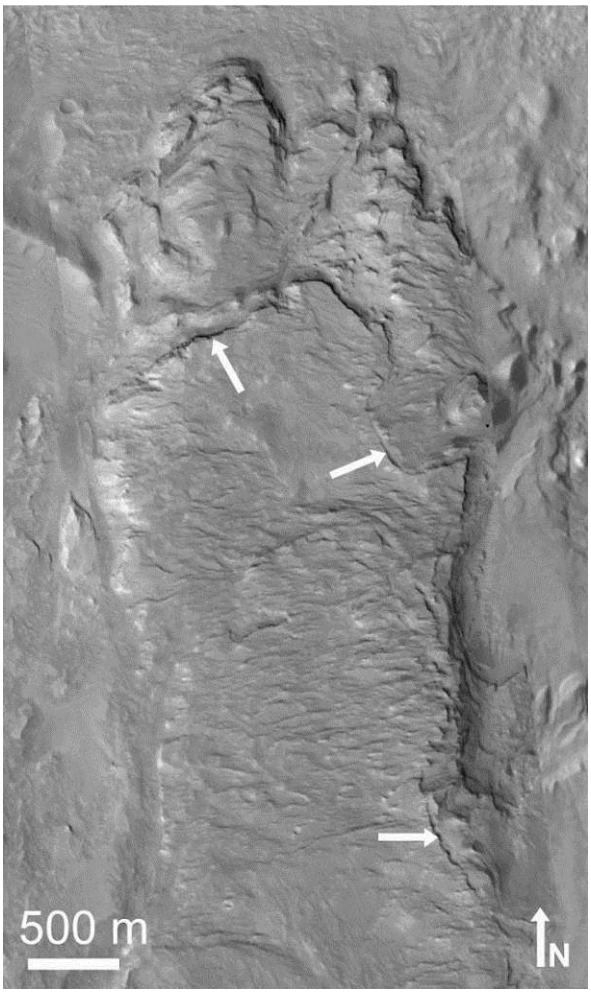

Figure 45: A closer MOC/CTX view of one of the uniform-width lobate units. Arrows mark the well-defined cliff-forming layer exposed at the edges of the unit. CTX Image ID: P01_001620_1749_XI_05S222W; MOC Image ID: M11/00989. Illumination is from the left. Location: 4.634°S 137.797°E.

features have slopes typical of the large-scale slope of the mound (~15^{o}), and a moderate thermal inertia (~460 J m^{-2}K^{-1}s$^{-1/2}$).

The HRSC elevation data do not have a high enough resolution to determine the slope at the end of the lobate deposits, but MOC and CTX images show an abrupt drop at the end of the deposits that may be as steep as the angle of repose for dry, granular material. There are not obvious boulders on the surface of the lobate features in the available MOC images.

The largest, easternmost lobate feature is fan-shaped. It begins with a narrow concave "neck" with a width of ~1.8 km, sharply defined by a narrow ridge on the western side and a large (several hundred meters) cliff on the eastern side. The "neck" extends from a large alcove in the

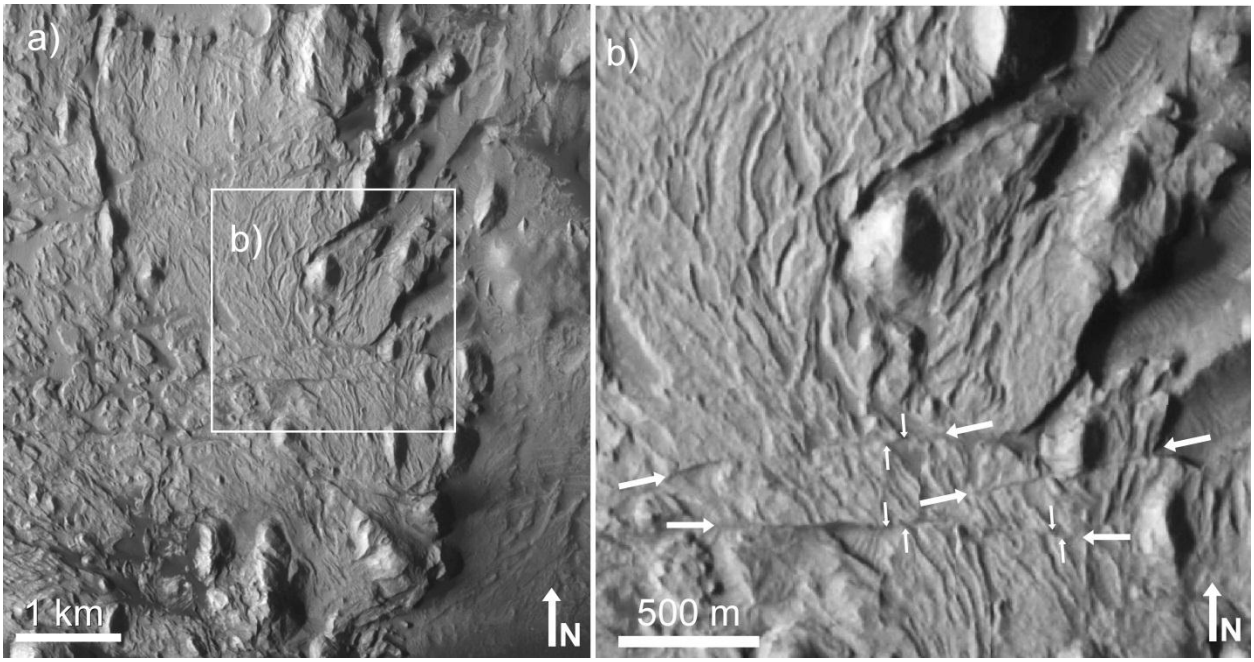

Figure 46: a) Closer view of the high thermal inertia portion of the fan-shaped lobate unit. **b)** Inset of a), showing the unusual streamlined texture of this portion of the fan-shaped lobate unit. Arrows mark the location of linear features that may be faults. Small vertical arrows mark examples of features that appear to be offset. CTX image ID: P04_002464_1746_XI_05S221W. Illumination is from the left. Location: 4.588°S 138.013°E.

mound and is partly obscured by yardang-forming material and has a low thermal inertia (~360 J $m^{-2}K^{-1}s^{-1/2}$). The "neck" appears to truncate an outcrop of material on its western side. The fan-shaped lobate feature has a break in slope from ~15o to ~5o within its narrow portion, and begins to broaden ~1.5 km downhill from that point.

The fan-shaped portion has a rugged, chaotic texture, with roughly aligned ridges and depressions. The average thermal inertia of the fan-shaped portion of the easternmost lobate feature is ~470 J $m^{-2}K^{-1}s^{-1/2}$. At the edge of the feature, the thermal inertia increases to >670 J $m^{-2}K^{-1}s^{-1/2}$ and the texture becomes dominated by streamlined mesas and troughs. Closer inspection of the high thermal inertia surface reveals several apparent faults (Figure 46).

4.12.2 Interpretations

The lobate features may be the result of large landslides or debris flows, in which case the fact that the uniform-width features do not extend all the way to the crater floor could be

attributed to limited debris supply. It is also possible that the features terminate at the former base of the slope, but the crater floor has been significantly eroded since their formation.

The erosion-resistant layer visible on the uniform-width lobate features (Figure 45) could be explained by multiple, superimposed flow events, but the vertical thickness of the lobes would make it unlikely for individual flows to follow the same path repeatedly. Alternatively, the landslide or debris flow deposits could form only the upper erosion-resistant layer, and the thickness of the lobes could be due to that layer preventing erosion of the underlying material. The erosion-resistance may be due to post-landslide cementation, possibly associated with burial if the landslide occurred prior to a period of net deposition in Gale Crater.

The apparent truncation of material by the neck of the fan-shaped lobate feature suggests that the process that deposited the feature was erosive, or that the truncated material was deposited against an obstacle that has since eroded away. The presence of yardang-forming material overlapping the neck of the fan-shaped lobate feature implies that the feature was once buried and has been exhumed.

The lobate features also are similar in morphology to terrestrial rock glaciers, although the evidence for burial beneath yardang-forming material implies that if the lobate features were glacial in origin, any ice would likely be gone. Figure 2 in [100] shows an illustration of rock glacier morphology. Rock glaciers are characterized by their "tongue-like" or lobate appearance, may have ridges and furrows on their surface, and terminate with a steep front at the angle of repose [100]. The uniform-width lobate features are most similar to the "tongue-shaped" rock glacier in the figure, although they do not originate in any obvious cirque.

The fan-shaped lobate feature does originate in an alcove on the mound, and most resembles the "piedmont or spatulate" rock glacier morphology in Figure 2 in [100]. The texture within the fan-shaped feature is similar to pressure ridges, and is consistent with a viscous, glacier-like flow.

The lobate features appear to lack the boulders that would be expected if they were rock glaciers, though this may be due to the limited resolution of MOC and CTX. The lobate features could also be mantled with younger material that obscures the individual boulders. Another weakness in the rock-glacier hypothesis is the apparent erosion-resistant layer in the uniform-width lobate features. If these deposits were rock glaciers, and therefore composed of boulders, it would be difficult to form the sharp cliff observed.

If the lobate fan-shaped feature has a glacial or periglacial origin, the streamlined texture of the fan-shaped lobate feature may be related to melting of interstitial ice. Flow of meltwater from the deposit could have carved the observed streamlined features. Alternatively, if the fan-shaped feature was deposited during or prior to a period of fluvial activity at Gale Crater, the observed texture could be due to erosion during that period. The texture of the lobate fan-shaped feature could also be related to compositional banding, which is seen in many flow features, including subaerial avalanches and debris flows, submarine debris flows, and glaciers (*e.g.*,[101] and references therein). Compositional banding can be due to the initial stratigraphy of the source material or sorting during the slide event[101]. Although most subaerial debris flows and avalanches have simpler banding than the streamlined texture observed, pre-existing topography can induce more complex flow banding [102] [101].

The faults observed in the streamline-textured surface are difficult to explain as part of the same mechanism that generated the texture. It is likely that they formed after the texture was

emplaced, perhaps due to stresses exerted by burial of the lobate feature by the deposition of subsequent mound material.

The lobate features are also morphologically consistent with volcanic lava or pyroclastic flows. However, there are no vents, cones, calderas, or other unambiguous evidence that the Gale Crater mound is a volcano [30]. Therefore we do not favor a volcanic explanation for the lobate features.

There are three publicly released SHARAD radar profiles through the Gale Crater mound, one of which comes close to the lobate features. A full interpretation of the SHARAD data products, including a comparison with simulated off-nadir surface reflection ("clutter") [103] is beyond the scope of this paper. However, the available data products do not appear to show unambiguous evidence for sub-surface reflectors.

As mentioned above, the lobate features appear to have been buried, so it is unlikely that they would retain the banding due to ice-rich and ice-poor layers observed in radar profiles of terrestrial rock glaciers [104]. The evidence for burial also makes it unlikely that they are composed primarily of ice like the lobate debris aprons observed elsewhere on Mars [105].

Although both the landslide and rock glacier hypotheses have weaknesses, we interpret the lobate features to be related to a flow of some sort. HiRISE coverage of these features would be beneficial, and could test the compositional banding hypothesis by looking for a variation in texture and clast size in the streamline-textured feature.

5. Inferred stratigraphy of the Gale Crater mound and proposed MSL landing site

Based on the observations and interpretations described above, we have inferred the basic inter-unit relationships and stratigraphy of the Gale Crater landing site and the nearby mound, illustrated in the idealized cross-section in Figure 47.

The stratigraphically lowest mound units appear to be the basal units, although it is unclear whether the topographically lower dark-toned basal unit is a lower stratigraphic layer or has simply filled a depression in the light-toned basal unit. The thickness of the basal units is unknown. On the crater floor, a sharp cliff ~10 m high (Figure 39) marks the transition up from the basal units to the hummocky plains unit and the mound-skirting unit (Figure 34). The hummocky plains unit is an ancient eroded unit that varies from a mantled surface to bare, fractured rock. The high thermal inertia distal end of the fan-shaped deposit in the landing site overlies the hummocky plains and appears to be relatively thin (Figure 42). Above the high thermal inertia fan-shaped unit is the smoother, low thermal inertia surface of the fan. This thin, smooth upper layer, along with the upper layer of the high thermal inertia fan, appear to be eroding back to expose the surface of the high thermal inertia fan unit (Figure 43). Some outcrops of high thermal inertia fan material appear to be embayed by mound-skirting material (Figure 42), suggesting that although they are topographically higher than the mound skirting surface, they are part of the older fan units.

Mesas with a texture similar to the mound-skirting unit extend from the crater wall to the base of the mound (Figures 10, 12, 15, 16), overlying the fan and crater floor units. These mesas merge with the mound-skirting unit in some places, while in other places they form sharp boundaries despite a similar texture (Figure 16). In some cases the stratigraphic relationship between the mound-skirting unit and the hummocky plains unit is ambiguous, but generally the mound-skirting unit appears to overlie the hummocky plains.

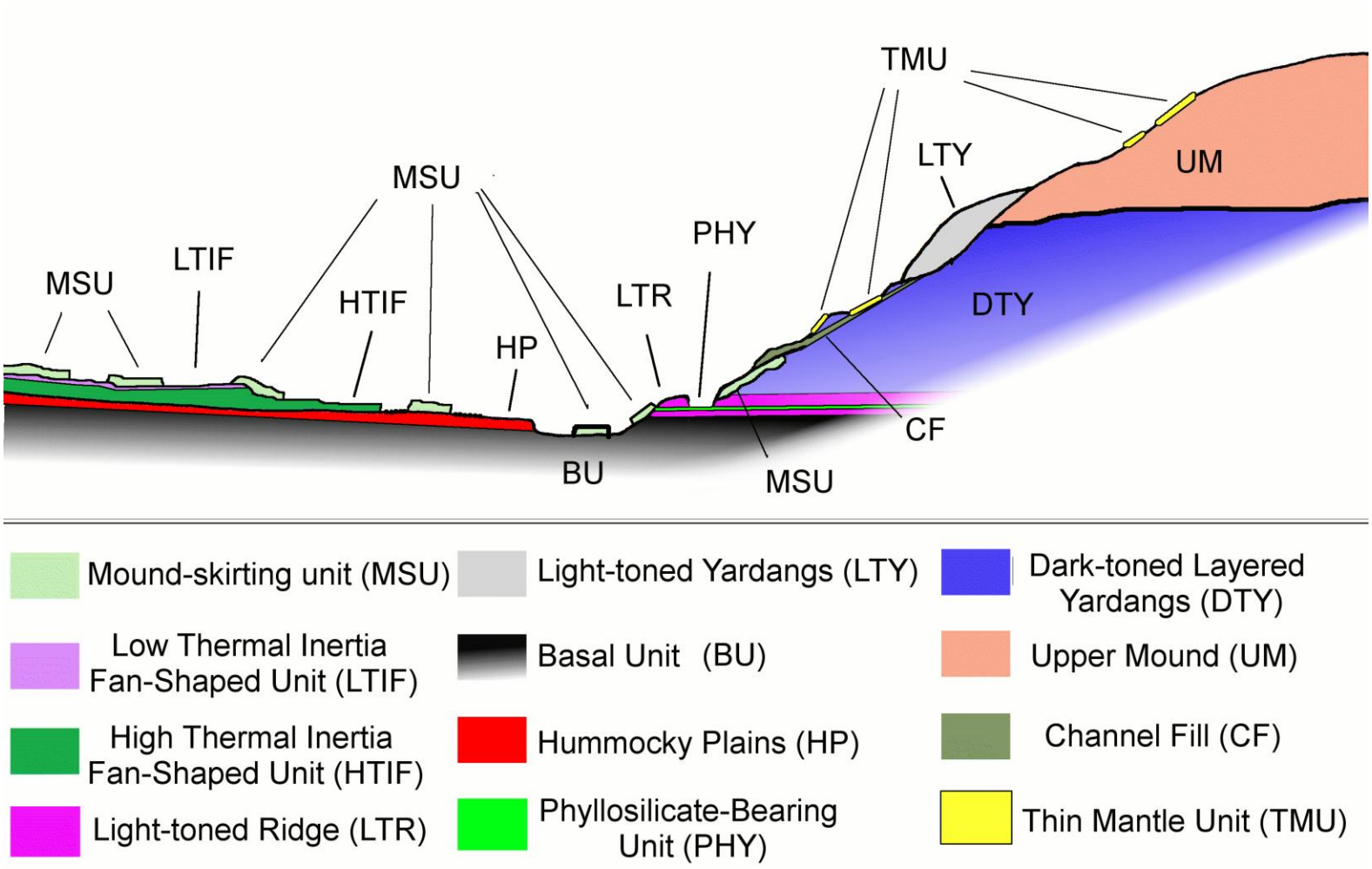

Figure 47: A cartoon of the inferred stratigraphy of the proposed Gale crater landing site and traverse region. This cartoon is not to scale, and is significantly simplified, but it does show the primary units discussed in the previous sections.

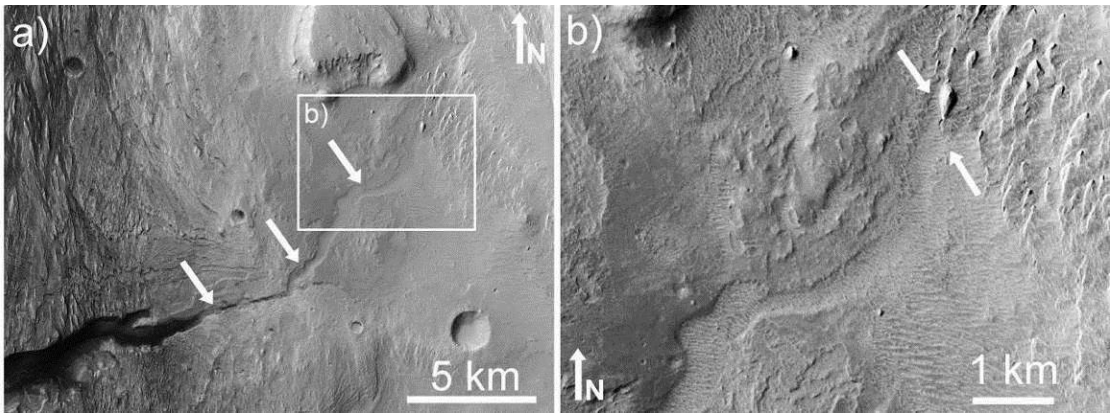

Figure 48: a) The largest canyon in the western mound becomes a shallower channel (marked by arrows) before disappearing beneath the layers of the upper mound, as shown in **b)**. An outcrop of upper mound material lies in the trough at the end of the channel, marking an unconformity between the surface into which the channel was carved and the overlying upper mound layers. Refer to appendix Table A1 for CTX Image IDs. Illumination is from the left.

At the foot of the mound, the basal unit merges in a series of poorly defined layers of fractured rock into the light toned ridge (Figure 36). Outcrops of the mound-skirting unit appear to overlie the lower layers of the light-toned ridge unit (Figure 37). On the southeast side, the ridge ends abruptly and drops down to a trough exposing a phyllosilicate-bearing surface which we interpret as the upper surface of a thin clay-bearing bedding plane. The dip of the bed and its thinness [30] could explain why it is not seen on the northwest side of the light-toned ridge.

Above the phyllosilicate-bearing trough, the first mound layers appear to be similar to those that make up the light-toned ridge, based on their tone and fractured texture. The mound slopes up at an angle of ~12o onto the sulfate-bearing dark-toned layered yardang unit. The fan-shaped patch of the mound-skirting unit is stratigraphically above the light-toned ridge and a portion of the dark-toned layered yardang unit, suggesting that the mound-skirting unit was deposited after these units. However, the fan appears to emerge from beneath a ridge of channel-filling material, constraining its time of deposition to before the channel in the dark-toned layered yardang unit was fully eroded and filled. Likewise, fan-shaped deposits of material emerging from canyons in

the dark-toned layered yardang unit on the western mound extend onto the mound-skirting unit (Figure 11).

The layers of the upper mound unit were deposited unconformably on top of the dark-toned layered yardang-forming unit after it had been eroded, as indicated by the truncation of the large valley on the western mound by the upper mound layers (Figure 48). This unconformity represents an unknown amount of time, but could indicate that the upper mound unit is significantly younger than the lower mound and possibly Amazonian in age [30].

In addition, the possibility that the upper mound material may be a lithified dune field is significant because a dune field would not be expected to form on top of a pre-existing mound. We therefore speculate that the early mound was buried after the initial erosion of the dark-toned layered yardang-forming material, allowing a dune field to form, become lithified, and erode back to the current mound.

The light-toned yardang unit also lies unconformably on top of the dark-toned layered yardangs, as indicated by a partially exhumed crater (Figure 26) [60]. The mound surface immediately above the light-toned yardang-forming material is mostly obscured by aeolian bedforms but the light-toned yardang-forming material appears to be unconformable with and younger than the upper mound unit as well. The 12° tilt of the best-fit plane to the boundary of the light-toned yardang unit is similar to the average slope of the mound. This suggests that the light toned yardangs were deposited, presumably as part of a more extensive unit, after the rest of the mound, including the upper mound unit, had already been eroded to nearly its present state.

Patches of the thin mantle unit occur on the dark-toned layered yardang unit (Figure 27) and the upper mound layers, but not on the light-toned yardangs. In some locations (Figure 28) on the boundary of the light yardangs, it is unclear whether the thin mantle unit abuts the light yardang

unit, or whether it emerges from beneath it. In other locations, the light-toned yardang unit is in direct contact with the surface of the dark layered yardang unit (Figure 26). This suggests that the thin mantle unit was already eroded away when the light-toned yardangs were deposited. Alternatively, the thin mantle unit may postdate the light-toned yardangs, but has been completely eroded off the soft light-toned yardang surface. The more erosion-resistant surface of the dark layered yardang unit might not undermine the thin mantle as rapidly, allowing it to persist.

6. Candidate rover traverses

In selecting a traverse for MSL at the Gale Crater landing site, an important consideration is what route to take to the layered, hydrated-mineral-bearing mound, the primary target of a mission to Gale. The dark-toned dunes at the base of the mound might form a barrier to MSL, preventing a direct path to the mound from the center of the landing site. However, there are two locations near the landing ellipse that would allow MSL to access the mound without having to traverse the dunes, and we discuss a possible traverse for each of these (Figure 49, Table 2). We have chosen to end both traverses when they reach the light-toned yardang unit. If the rover reached that unit, it could continue climbing up similar slopes to the upper mound, or return to study other locations on the lower mound. We have also assumed that the rover would land precisely in the center of the ellipse. If MSL lands a significant distance from the center of the landing ellipse, that could factor heavily into which traverse it would follow to reach the mound.

Table 2. Summary of Two Potential Traverses

Traverse 1 = 29.4 km			Traverse 2 = 22.5 km		
Stop	Description	Rationale	Stop	Description	Rationale
1A	Transition between low- and high- thermal inertia fan-shaped unit	Search for conclusive evidence that this unit was an alluvial fan. Determine environmental conditions for deposition.	2A	Transition between low- and high- thermal inertia fan-shaped unit	Search for conclusive evidence that this unit was an alluvial fan. Determine environmental conditions for deposition.
1B	Edge of high-thermal inertia fan-shaped unit.	Investigate the transition to the hummocky plains and mound-skirting units. Determine nature of these units (composition, depositional setting, etc.).	2B	Edge of high-thermal inertia fan-shaped unit. Near inverted channels.	Investigate the transition to the hummocky plains and mound-skirting units. Determine nature of these units. *Optional: Traverse east to inverted channels. Search for biomarkers, evidence for duration of fluvial activity, etc.*
1C	Boundary between mound-skiting unit and basal unit. Near dark dunes.	Test lithified bedform and parallel joint hypotheses for mesas and ridges in skirting unit. Test mound origin hypotheses on basal unit (first mound unit encountered).	2C	Passage through sand dunes on mound-skirting unit.	Study dark dunes and mound skirting unit. Test lithified bedform and parallel joint hypotheses for the origin of ridges in the skirting unit.
1D	Phyllosilicate-bearing unit near fan-shaped unit.	Determine depositional setting for phyllosilicate-bearing and neighboring units. Begin assembling mound stratigraphy. Search for biomarkers in phyllosilicates.	2D	Edge of skirting unit, transition to basal unit.	Test mound-origin hypotheses on basal unit (first mound unit encountered).
1E	Channel fill atop fan-shaped unit.	Test hypothesis that fan-shaped unit is part of the mound-skirting unit. Analyze channel fill material and search for biomarkers.	2E	Mesas of mound-skirting unit on basal and light-toned ridge units	Test hypothesis that the light-toned ridge unit underlies the mesas in this location. Test origin of light-toned ridge.
1F	Fine layers and channel fill.	Continue to study mound stratigraphy. Test mound origin hypotheses. Search for biomarkers in sulfates.	2F	Phyllosilicate-bearing trough.	Determine depositional setting for phyllosilicates. Search for biomarkers in phyllosilicates. Begin to construct mound stratigraphy.
1G	Erosion-resistant ridges.	Test hypothesis that ridges are cemented fractures. Determine nature of putative cementing material and search for biomarkers.	2G	Dark-toned layered yardangs, partially mantled.	Continue to construct mound stratigraphy. Test mound origin hypotheses. Search for biomarkers in sulfates.
1H	Light-toned yardangs	Investigate contact between light-toned yardang unit and dark-toned layered yardangs. Determine nature of light-toned yardangs.	2H	Light-toned yardangs.	Investigate contact between light-toned yardang unit and dark-toned layered yardangs. Determine nature of light-toned yardangs.

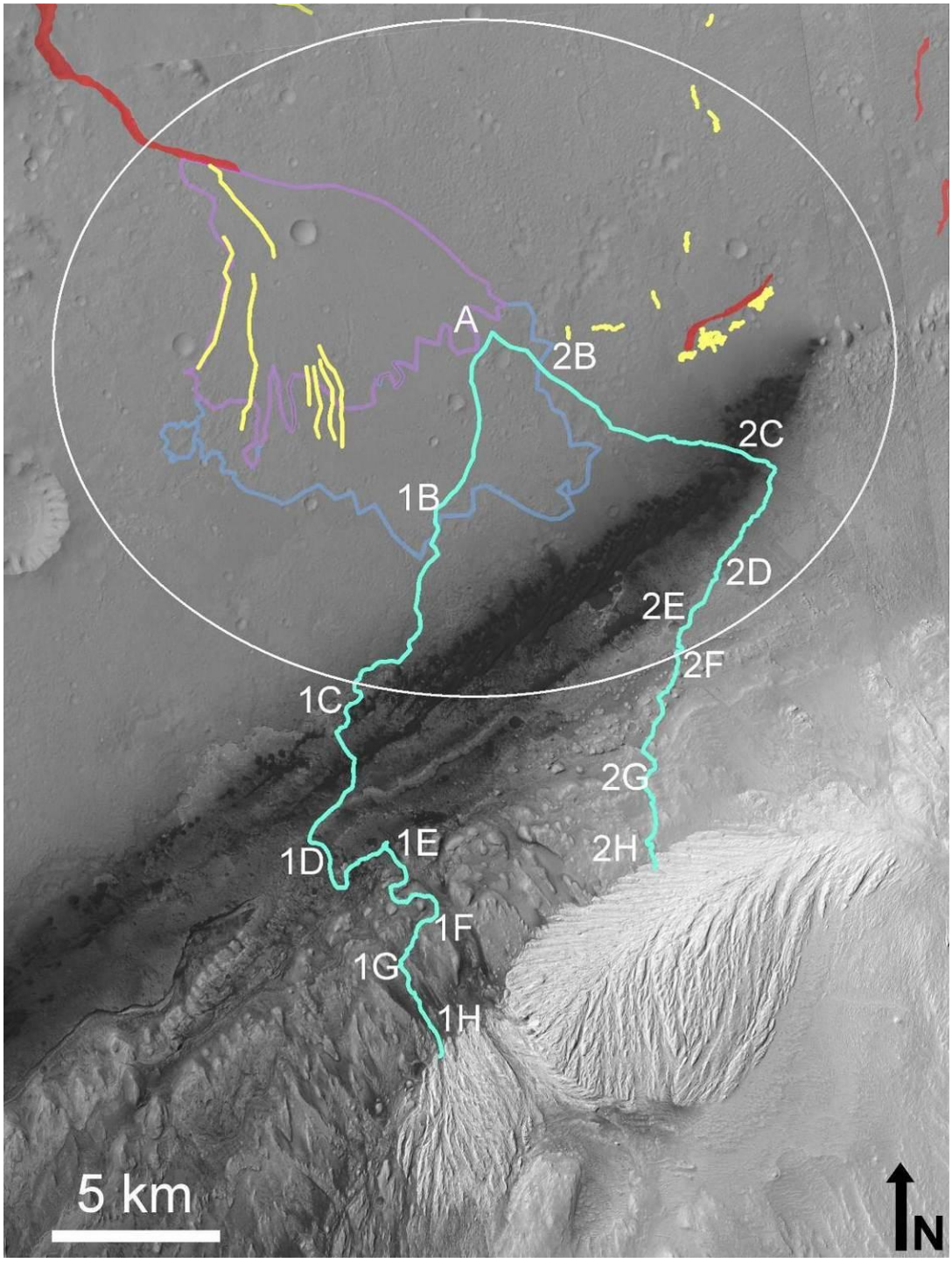

Figure 49: Two proposed MSL traverses, starting at the center of the landing ellipse and proceeding toward the two breaks in the line of dunes that provide access to the mound. See text for discussion. Refer to appendix Table A1 for CTX image IDs. Illumination is from the left.

The first possible traverse is similar to traverses previously proposed [71]. It would cover 29.4 km and begin (nominally) in the center of the landing ellipse on the fan-shaped unit and would bear toward the south-southwest. The initial portion of the traverse would allow investigation of the transition between the low- and high-thermal inertia portions of the fan-shaped deposit in the ellipse and the stratigraphy of the layers exposed in those units (Figure 49: A). The rover would then cross over onto patches of the mound-skirting unit and the hummocky plains unit (Figure 49: 1B). Continuing to the southwest, the rover would leave the ellipse and reach the sharp transition between the mound-skirting unit and the basal unit near the location of numerous ridge-like mesas of the mound-skirting unit (Figure 34; Figure 49: 1C). MSL could test the hypothesis that these ridges are due to lithified bedforms or parallel joints by studying the texture, bedding, and composition of the rocks in these outcrops. The traverse would also pass near outliers of the dune field and MSL could observe the sand to determine its composition, physical properties, and activity, similar to the observations of the much smaller El Dorado ripple field by the Mars Exploration Rover *Spirit* [106].

From this point, the rover would head south, across the surface of the basal unit and begin climbing the poorly defined layers leading up to the light-toned ridge unit. MSL would traverse through a gap between the southwest end of the light-toned ridge and the mound-skirting unit, and cross into the phyllosilicate-bearing trough (Figure 49: 1D). Here the rover would be able to determine the precise mineralogy of the phyllosilicate unit, its phyllosilicate content, its depositional setting and weathering history, and its organic content.

After a full study of the phyllosilicate-bearing trough material, MSL could study the base of the fan-shaped outcrop, and then climb up its side to study the surface and determine whether it is indeed an outcrop of the mound-skirting unit. The rover would also analyze the ridge of

channel-fill material on the fan (Figure 49: 1E). This material might provide a sample from much higher on the mound, and therefore could be valuable in understanding units that the rover might never reach.

From the filled channel and outcrop, MSL would continue to climb, analyzing the layers of the mound as it drove (Figure 49: 1F). At this point our proposed traverse differs slightly from previous traverses. The rover would turn to the southwest, away from the filled channel and climb up a set of layers of varying albedo to reach an expression of erosion-resistant ridges (Figure 49: 1G). Here the rover could determine whether the ridges are indeed fractures made erosion-resistant by alteration or cementation, or whether they are due to igneous intrusion or other processes. Finally, the rover would turn to the southeast and continue to climb the mound, following the trough between two large yardangs and eventually reaching the light-toned yardang unit near the location (Figure 49: 1C) of the partially exhumed crater shown in Figure 26.

Traverse 2 would cover 22.5 km and would begin by driving away from the center of the ellipse toward the southeast. In this direction, MSL would soon leave the fan-shaped unit and would cross onto the hummocky plains and mound-skirting units (Figure 49: 2B). It would then reach a more rugged, ridged portion of the mound-skirting unit and could continue toward the southeast while studying the unit and determining the origin of the ridges. There is a gap in the dune field on the ridged, mound-skirting unit (Figure 49: 2C), and MSL would drive through this gap and then turn toward the southwest.

After crossing ~3.3 km of ridged, mound-skirting unit, MSL would arrive at the basal unit (Figure 49: 2D). Continuing to the southwest, the rover could investigate one of the mesas of mound-skirting unit where it contacts the broadened light-toned ridge (Figure 49: 2E), and then

could proceed up the ridge itself. MSL would then descend onto the phyllosilicate-bearing trough and conduct a thorough analysis (Figure 49: 2F). Continuing to the southwest, the traverse leads up onto the layers of the dark-toned layered yardang unit. In this area of the mound (Figure 49: 2G), the thin mantle unit obscures many of the layers, but the numerous yardangs expose numerous outcrops for MSL to access so that it likely could still construct a stratigraphic column of the mound. The rover would work its way up the mound, eventually reaching the light-toned yardang unit (Figure 49: 2H).

The initial leg of Traverse 2 comes close to some of the well-preserved inverted channel features in the ellipse (Figures 13, 14). Optionally, MSL could begin by traveling directly east, and studying one or several of these features before turning south to climb the layered mound. The proximity to these features is the primary advantage to Traverse 2. Disadvantages include the long traverse over the ridged mound-skirting unit and the mantled nature of the mound near the gap in the dunes. Traverse 2 is 22.5 km long and MSL would climb 1021 m during the traverse, crossing maximum slopes of about 10 degrees. In comparison, Traverse 1 is 29.4 km long and would climb 1155 m, crossing maximum slopes of about 15 degrees. The advantages of Traverse 1 are that it would climb a well-exposed, unmantled portion of the mound, and that therefore the stratigraphy and composition of the mound at that location have been well-studied (Figure 47; [30] [74] [107]).

7. Discussion and conclusions

7.1 Mound material origin hypotheses

There are several hypotheses for the origin of the layered material of the Gale Crater mound. The spring mound hypothesis advanced by [65] predicts rapid spatial facies variations in the mound's strata, evidence for draping or progradation, and structural control of deposition. The

mound in Gale Crater does not show evidence of structural control or draping/progradation of the beds. The presence of uniform-thickness stratigraphic layers in the Gale Crater mound that are traceable for many kilometers (Figure 19) is inconsistent with the predicted rapid facies changes in a spring mound. [65] also claimed that craters with bulges lack evidence for a significant drainage basin associated with the crater. We have shown (Figure 7) that the rim of Gale Crater preserves numerous channels, inverted channels and fans that indicate that the crater was a drainage basin. Although the Gale crater mound does satisfy some of the other criteria listed by [65] for spring mounds (*e.g.* sedimentary appearance, mound-like morphology, compositional variations correlated with stratigraphic variations) these criteria are not unique to spring mounds.

Many authors have suggested or discussed an aeolian origin for the material of the Gale mound [51][54][55][60][63]. We observe textures on the upper mound unit that could be large-scale (hundreds of meters) crossbeds (Figure 30), similar to bedforms observed at White Sands National Monument on Earth (Figure 32). We interpret the observed textures as evidence that the upper mound has an aeolian origin. On Earth, crossbeds are often significantly smaller than those observed on the upper mound, so that the lack of crossbeds in HiRISE observations of the lower mound does not exclude an aeolian origin for these units. Although no crossbeds are observed in the lower mound units, the ridged morphology of portions of the mound-skirting unit and the dark-toned layered yardang unit may represent lithified aeolian bedforms.

A volcanic origin for the mound material has also been suggested [51][54][55]. Lava flows produce strong, cliff-forming, boulder-shedding layers, but these properties do not uniquely identify a layer as a lava flow. Beds with this property are present in the Gale Crater mound (*e.g.*, Figure 21). The nearest obvious volcanic edifice to Gale Crater is Elysium Mons, ~1800 km north of Gale. Cratering counts of Elysium Planitia lavas have been used to infer a young age

(<100 million years) [108] which would be incompatible with the likely Noachian/Early Hesperian age of the Gale Crater mound. We also find it unlikely that flows from an Elysium eruption could travel 1800 km south to Gale Crater. The presence of layers within the mound that do not form steep, boulder-shedding cliffs also implies that much of the mound is not composed of lava flows.

Pyroclastic deposits represent an alternative volcanic origin for the Gale Crater mound [51][55][60] [63]. Hynek *et al.* [109] have suggested that much of the light-toned layered material on Mars, including the MFF, is due to explosive volcanism, and Zimbelman *et al.*[60] have mapped the Gale Crater mound as an outlying portion of the MFF. The yardang-forming morphology of the mound and the similarities between the pedestal crater outcrop west of the mound and those in the MFF, described by Kerber and Head [90], suggest that the mound materials erode in a manner similar to the MFF. However, Malin and Edgett [60] rule out a pyroclastic origin for much of the layered rock on Mars due to the rapid thinning of pyroclastic deposits with distance from the source and the lack of sources near observed layered sedimentary rock exposures. Wilson and Head [110] have used models to show that explosive volcanism can produce "thick widespread deposits of ash and lapilli" on Mars and that small pyroclasts (~50 microns) can be transported ~10,000 km in the martian atmosphere. Wilson and Head [110] also predict that fine-grained pyroclasts would "scavenge" water from eruption plumes and would therefore form fine-grained deposits containing ice and/or hydrated minerals and low-temperature alteration products. In a more recent paper, Wilson and Head [111] calculate that on Mars a 1000 km3 eruption would form ~1 m thick pyroclastic deposits at a distance of ~1000 km from the source. Multiple extremely large and/or nearby eruptions would therefore be required to create the Gale mound entirely from pyroclastic deposits. Due to the ~1800 km distance to the

nearest obvious large volcano, it seems unlikely that pyroclastic deposits make up the bulk of the mound, though they are very likely to be present as thin beds.

Finally, Gale Crater has been suggested as the site of a former crater lake, and the mound has been suggested to comprise lacustrine or fluvial deposits [51] [56] [55] [60]. Lacustrine deposits are characterized by laterally continuous, finely-layered and highly variable bedding, confined to a closed basin [60][112]. The layers of the Gale Crater mound fit this description. The presence of hydrated minerals on the Gale Crater mound [30][70] could indicate diagenesis of sedimentary material in an aqueous setting. However, it is not diagnostic of a lacustrine setting because the aqueous minerals could also have formed elsewhere and been deposited in the crater. Thus, a lacustrine origin for the sedimentary rocks of Gale Crater cannot be ruled out based on our observations.

It would be naïve to suggest that a single process could adequately describe the entire stratigraphic column at Gale Crater. It is much more likely that the layers of the Gale Crater mound derive from a variety of sources and processes, preserving information about changing environments throughout the history of Mars.

MSL would be able to address the multiple remaining mound origin hypotheses, providing information that is unavailable from orbit. The detailed structure of the sedimentary rocks could be assessed by the cameras on the rover, revealing fine-scale layering, cross-bedding, and grain sizes. This information could immediately reveal the nature of the rocks of the Gale mound. More detailed study of the elemental, mineralogical and chemical composition would provide clues to the alteration history of Gale Crater, further constraining the depositional and post-depositional environments. The physical properties of the rocks and soils at the landing site

could also be studied, as has been done with the Mars Exploration Rovers [113], based on the interaction between the rover and its surroundings (*e.g.* tracks, trenching, drilling).

7.2 Discussion of sediment transport

The height of the mound in Gale Crater, the laterally extensive nature of the exposed beds (Figure 19, [30]), outcrops of layered material on the crater floor (Figure 24), and inverted channels (*e.g.* Figure 13) all suggest that the Gale Crater mound material once filled the crater and has been significantly eroded. Furthermore, the canyons and channels carved into the surface of the mound suggest that the mound material had already been deposited and substantially eroded at a time when liquid water still flowed on the surface of Mars.

Malin and Edgett [60] have argued that the burial and excavation of craters is common on Mars, citing other examples of large, partially exhumed craters. In the case of Gale Crater, the presence of apparent erosional unconformities in the mound suggests multiple episodes of erosion and deposition.

The excavation of Gale and other large craters requires the transport of tremendous quantities of material. As discussed by[60], the transport pathways for this material are not fully known, but the lack of craters on many exposures of layered rock suggests some degree of ongoing erosion.

Valleys interpreted as fluvial channels are common on the crater walls. However, there do not appear to be any surface channels that lead out of the crater, therefore fluvial transport mechanisms are possible sources for the crater-filling material, but cannot directly explain the extensive exhumation. Likewise, mass wasting could partially explain the degradation of the crater rim and mound, but would result in debris collecting on the floor of the crater. Fluvial

erosion and mass wasting could, however, have broken down crater-filling material until it was small enough for aeolian erosion and transport to occur.

Indeed, the only sediment transport process that appears plausible to explain the exhumation of Gale Crater is aeolian transport. This is consistent with numerous yardangs present on the mound, and ongoing or relatively recent aeolian erosion could explain the lack of numerous impact craters. To remove material from the crater entirely without breaching the crater rim, the material must be carried out of the crater in suspension. This implies that the material filling Gale and other similarly filled and exhumed craters either a) initially erodes into particles small enough to be carried out of the crater in suspension, or b) that particles generated by erosion continue to break down until they are small enough to be carried away in suspension. The latter possibility is consistent with the elevated saltation velocities of sand grains on Mars (*e.g.*,[114][115]) and the "Kamikaze" sand grain effect proposed by Sagan *et al.* [114]. In addition, other erosional processes such as fluvial erosion, could contribute to the breakdown of larger particles until they are susceptible to aeolian suspension.

7.3 Implications for MSL landing site selection

The selection of a landing site for MSL is driven by four primary criteria: diversity, context, habitability, and preservation potential [27]. As shown above, Gale Crater presents a location in which the rover could land and explore numerous distinct units distinguishable by their geomorphology, visible and infrared spectral characteristics, and thermal properties. The MSL payload could test hypotheses about each of the units discussed, as well as hypotheses regarding the relationship between units. The variety of units and the layering within the mound units suggests changing conditions at the time of deposition. This is shown most clearly by the

detection of phyllosilicates and hydrated sulfates that correlate with the phyllosilicate-bearing trough and dark-toned layered yardang units, respectively.

Malin and Edgett [60] have argued that the sedimentary rocks at Gale Crater can be placed into a global context, based on similarities between sedimentary deposits across the planet. Gale Crater is one of many large craters on Mars that shows evidence of filling and exhumation, and therefore discoveries made by MSL at Gale Crater could be extrapolated to global processes. In particular, determining the nature of the layered deposits and numerous units at Gale would allow inferences to be made for deposits elsewhere on Mars with similar properties.

If lacustrine deposits were confirmed, then sedimentary outcrops in craters of similar age could likewise be due to aqueous deposition. If a crater as deep as Gale Crater were shown to have never hosted a lake, this would have significant implications for the understanding of early Mars. If the Gale Crater layered rocks are primarily aeolian or volcaniclastic, that would confirm that those processes have been very important in shaping the martian surface. In addition, the presence of both sulfates and phyllosilicates exposed in the stratigraphic section at Gale Crater could provide insight into a key transition in the global weathering environment on Mars. [30]

The MSL mission is focused on determining the habitability of Mars, and therefore the potential for preservation of chemical and geologic evidence for past habitability is paramount in the selection of a landing site. Habitability as currently understood (through terrestrial analogy) requires water, an energy source, and carbon [27]. Numerous fluvial channels and inverted channels provide the best evidence for aqueous activity at Gale. Some (but perhaps not all) fan-shaped units may also be associated with fluvial activity, as in the case of the large fan-shaped feature in the landing ellipse that begins at the end of a branching channel. The presence of hydrated minerals on the mound, and particularly the detection of nontronite, which forms at a

moderate pH, suggests a potentially habitable environment in which water was present [70]. Furthermore, if the layers of the mound are lacustrine in origin, they could represent the preserved remains of a once-habitable environment. Alternate origins (*e.g.*, aeolian, lava flow, pyroclastic) are less favorable for habitability, but the erosion-resistant ridges on the mound may indicate alteration and/or cementation of mound materials by water (Figure 22; [72]), and therefore could be evidence of a habitable post-depositional environment.

Preservation of biological material in rocks depends on the deposition and subsequent history of those rocks. Based on studies of biomarker preservation on Earth, organic material is most likely to be concentrated in sediments deposited in aqueous environments and would likely be preserved in association with high surface-area minerals such as phyllosilicates [116][117][118][119]. Evaporites and silica deposits are also favorable for biomarker preservation and microfossil formation because organics can be entombed as minerals precipitate out of solution [118][120] [121]. The inverted channels on the crater floor preserve geomorphic evidence of liquid water, but may only be favorable for preservation in cases where the features suggest a low-energy depositional environment. If the layers of the Gale Crater mound are lacustrine sediments, then they would be favorable for preservation of organic biomarkers. An intermittent lake setting would also be favorable due to the formation of evaporite minerals, which can trap organic material due to rapid crystallization. An aeolian or volcanic origin for the layers would be less favorable, although post-depositional alteration could provide evidence of later habitability. The erosion-resistant ridges on the mound may represent a habitable environment, with preservation potential depending on the chemistry of the rocks and the fluid involved. Organic material can be preserved in contact with chemically reducing fluid, but if the rocks are composed of oxidized material or have oxidizing fluid flowing through them, then

organics are unlikely to be preserved [122]. Post-depositional contact with water can also contribute to biomarker degradation by facilitating aqueous chemical reactions, participating in hydrolysis reactions, and promoting microbial activity [123].

Smectite phyllosilicates are effective at preserving organic molecules due to their low permeability after deposition, their large surface area, and their ability to bind organics between the layers of the mineral structure [119][122]. Therefore the detection of smectites at Gale [70] is significant for biomarker preservation potential. Sulfate minerals have also been shown to preserve organic molecules such as amino acids [124]. The presence of both sulfates and phyllosilicates at Gale Crater therefore provides multiple locations with biomarker preservation potential.

Gale Crater shows relatively few impact craters on its exposed surfaces, suggesting that the exposures of sedimentary material are relatively fresh. This is also a favorable characteristic for preserving evidence of habitability because exposure to radiation and oxidation can destroy biomarkers [122][124][125].

7.4 Conclusions

We used a variety of visible (CTX, HiRISE, MOC), infrared (THEMIS, CRISM, OMEGA) and topographic (MOLA, HRSC, CTX) datasets to conduct a study of Gale Crater, with a particular focus on the region surrounding the proposed MSL landing site. We found evidence of aqueous activity, including numerous fluvial channels and inverted fluvial channels, fan-shaped deposits, erosion-resistant fractures, and hydrated minerals. We have described the major geomorphic units in the proposed MSL landing site and on the western and northern mound and crater floor, and constructed a simplified stratigraphic section of the mound along the nominal MSL traverse (Figure 47). The high-elevation upper mound exhibits apparent large-scale cross-

beds (Figure 30), suggesting an origin as aeolian dunes. At the lower elevations accessible to MSL, for example in the dark-toned layered yardang unit, the presence of layers traceable for tens of kilometers appears to preclude a spring mound origin, but an aeolian or lacustrine origin both remain as possible depositional processes. Pyroclastic materials are likely present in the mound, but probably do not represent the bulk of the material. Due to the great thickness of the stratigraphic column at Gale, it is likely that the mound formed through a combination of processes. Both aeolian and fluvial erosion appear to have played a role in exhuming the sedimentary layers of the Gale mound, but the only process that seems capable of explaining the transport of such a significant amount of material out of the crater without breaching the crater rim is aeolian suspension.

We identified two possible traverses from the center of the proposed MSL landing ellipse up onto the mound of layered sediments. The preferred traverse would access the mound in a well-exposed and therefore well-studied location. The alternate traverse comes closer to one or more of the inverted fluvial features within the ellipse before accessing the mound through a gap in the line of dunes at its base. It would climb a portion of the mound that is partially obscured by the thin mantle unit, but layered outcrops would still provide access to the stratigraphy.

Gale Crater's geomorphic diversity, thick stratigraphic sequence, similarity to other filled craters on Mars, and morphological and spectral evidence for an aqueous history make it a highly desirable landing site for MSL, and a target for substantial future orbital remote sensing studies.

Acknowledgements

We are indebted to our colleagues on the MSL Mastcam, MAHLI, and MARDI science team for stimulating discussions and insights about Gale Crater as a possible MSL landing site. We are

also grateful to our many science and operations colleagues on the Mars Global Surveyor, Mars Odyssey, Mars Express, and Mars Reconnaissance Orbiter teams who have made remote sensing observations of Gale Crater rapidly available to the broader community as part of the MSL landing site selection process. We thank Larry Edwards for creating and providing the CTX DEM. We thank Ken Herkenhoff, Aileen Yingst and Ralph Milliken for useful comments on early drafts of this paper. We also thank Ken Edgett, Nathan Bridges and an anonymous reviewer for detailed reviews and helpful comments on the manuscript. This work was supported by NASA grants and contracts from the Mars Data Analysis Program and the Mars Science Laboratory Project.

Appendix

Table A1: List of CTX images of Gale crater

Image ID	Figures 3 & 7	Figure 4	Figure 6	Figure 8	Figure 9	Figure 10	Figure 11	Figure 12	Figure 15	Figure 16	Figure 17	Figure 18	Figure 19	Figure 20	Figure 24	Figure 26	Figure 29	Figure 33	Figure 37	Figure 44	Figure 45	Figure 46	Figure 48	Figure 49
P01_001356_1747_XN_05S221W	X	X						X																
P01_001422_1747_XN_05S222W	X			X																				
P01_001488_1751_XI_04S222W	X																							
P01_001554_1745_XI_05S221W	X	X						X										X						
P01_001620_1749_XI_05S222W	X	X	X		X	X		X			X						X	X		X	X			X
P02_001752_1753_XI_04S222W	X																							
P03_002253_1746_XN_05S221W	X	X																						
P04_002464_1746_XI_05S221W	X	X	X		X			X	X	X							X	X		X		X		
P04_002530_1745_XI_05S223W	X	X		X																				
P04_002675_1746_XI_05S222W	X																							
P06_003453_1752_XI_04S222W	X																							
P13_005998_1746_XI_05S222W	X			X																				
P13_006143_1745_XN_05S223W	X	X		X											X			X						
P14_006644_1747_XI_05S222W	X	X		X		X	X	X			X						X	X					X	X
P15_006855_1746_XN_05S222W	X	X		X			X	X			X		X		X			X						X
P16_007356_1749_XI_05S222W	X	X		X		X	X	X			X	X	X	X		X	X	X	X				X	X

Table A2: List of HiRISE images of Gale Crater

Image ID	Figure 6	Figure 13	Figure 14	Figure 18	Figure 19	Figure 20	Figure 21	Figure 22	Figure 23	Figure 25	Figure 27	Figure 28	Figure 30	Figure 31	Figure 33	Figure 34	Figure 36	Figure 37	Figure 38	Figure 39	Figure 40	Figure 42	Figure 43
PSP_001488_1750				X											X		X			X			
PSP_001620_1750													X										
PSP_001752_1750								X															
PSP_002099_1720																							
PSP_003453_1750																	X	X					X
PSP_005998_1745															X								
PSP_006288_1740	X																						
PSP_007356_1750						X																	
PSP_008147_1750									X														
PSP_009149_1750				X							X												
PSP_009294_1750					X		X			X					X				X				
PSP_009571_1755		X	X															X					
PSP_009650_1755																X							
PSP_009716_1755					X																X	X	
PSP_009861_1755												X			X			X					
PSP_009927_1750														X									
PSP_010573_1755																					X		

Table A3: List of MOC images of Gale crater

Product ID			
E01-00067	E14-02234	M11-00989	R16-00139
E01-00538	E16-01112	M12-00231	R16-02163
E01-01026	E16-01641	M12-02852	R18-00974
E02-00942	E18-01261	M14-01617	R19-01648
E02-01579	E20-00143	R01-00210	R20-00784
E02-02493	E20-01495	R01-00595	S05-00434
E03-01733	E21-00160	R01-00946	S06-00098
E03-01915	E21-00428	R01-01335	S06-02328
E04-01829	E21-00521	R02-00546	S09-00404
E04-02461	E21-00833	R02-00913	S11-00421
E05-00772	E22-00419	R09-02667	S11-02858
E05-02541	E23-01009	R09-03892	S12-01881
E06-00143	M02-01391	R10-04983	S12-02067
E09-01039	M03-01521	R11-04327	S13-00501
E10-00863	M03-06805	R12-00567	S14-00576
E10-02079	M07-01419	R12-00762	S16-00680
E11-01254	M08-01028	R12-01498	S17-00627
E11-02505	M08-02542	R13-00776	S19-00656
E12-01615	M09-01696	R14-01644	S20-00585
E13-01884	M10-01253	R15-00805	S22-00845

Table A4: OMEGA data cubes used in Gale Crater mosaic

Product ID	Spacecraft-to-surface distance (km)	Resolution (km/pixel)
ORB0436_2	1149.6	1.4
ORB0436_3	1778.1	2.1
ORB0469_3	1833.4	2.2
ORB1002_6	292.0	0.4
ORB1339_1	1090.0	1.3
ORB1577_3	5971.5	7.2

CHAPTER 3

THE INFLUENCE OF MULTIVARIATE ANALYSIS METHODS AND TARGET GRAIN SIZE ON THE ACCURACY OF REMOTE QUANTITATIVE CHEMICAL ANALYSIS OF ROCKS USING LASER INDUCED BREAKDOWN SPECTROSCOPY[2]

0. Abstract

Laser-induced breakdown spectroscopy (LIBS) was used to quantitatively analyze 195 rock slab samples with known bulk chemical compositions, 90 pressed-powder samples derived from a subset of those rocks, and 31 pressed-powder geostandards under conditions that simulate the ChemCam instrument on the Mars Science Laboratory Rover (MSL), Curiosity. The low-volatile (<2 wt. %) silicate samples (90 rock slabs, corresponding powders, and 22 geostandards) were split into training, validation, and test sets. The LIBS spectra and chemical compositions of the training set were used with three multivariate methods to predict the chemical compositions of the test set. The methods were partial least squares (PLS), multilayer perceptron artificial neural networks (MLP ANNs) and cascade correlation (CC) ANNs. Both the full LIBS spectrum and the intensity at five pre-selected spectral channels per major element (feature selection) were used as input data for the multivariate calculations. The training spectra were supplied to the algorithms without averaging (*i.e.* five spectra per target) and with averaging (*i.e.* all spectra from the same target averaged and treated as one spectrum). In most cases neural networks did not perform better than PLS for our samples. PLS2 without spectral averaging outperformed all other procedures on the basis of lowest quadrature root mean squared error (RMSE) for both the

[2] This chapter was originally published in the journal Icarus: R. Anderson, R. Morris, S. Clegg, J.F. Bell III, R.C. Wiens, S.D. Humphries, et al., The influence of multivariate analysis methods and target grain size on the accuracy of remote quantitative chemical analysis of rocks using laser induced breakdown spectroscopy, Icarus. 215 (2011) 608-627.

full test set and the igneous rocks test set. The RMSE for PLS2 using the igneous rock slab test set is: 3.07 wt. % SiO_2, 0.87 wt. % TiO_2, 2.36 wt. % Al_2O_3, 2.20 wt. % Fe_2O_3, 0.08 wt. % MnO, 1.74 wt. % MgO, 1.14 wt. % CaO, 0.85 wt. % Na_2O, 0.81 wt. % K_2O. PLS1 with feature selection and averaging had a higher quadrature RMSE than PLS2, but merits further investigation as a method of reducing data volume and computation time and potentially improving prediction accuracy, particularly for samples that differ significantly from the training set. Precision and accuracy were influenced by the ratio of laser beam diameter (~490 μm) to grain size, with coarse-grained rocks often resulting in lower accuracy and precision than analyses of fine-grained rocks and powders. The number of analysis spots that were normally required to produce a chemical analysis within one standard deviation of the true bulk composition ranged from ~10 for fine-grained rocks to >20 for some coarse-grained rocks.

1. Introduction

To demonstrate the capabilities of LIBS as a quantitative tool for planetary missions and to assess which multivariate technique is best suited for quantitative analysis of realistic samples, we have analyzed LIBS spectra from a suite of 195 rock slab samples, 90 pressed-powder samples derived from a subset of the rocks, and 31 pressed powder geostandards. To visualize the full data set and distinguish sample types based on their spectra we used principal components analysis (PCA), which has been shown to be an effective with LIBS data (*e.g.*[49] [126]). For quantitative analyses, we restricted the data set to silicate samples with low loss on ignition (<2 wt. %), giving a set of 90 geologic slab samples and 22 geostandards. Previous experiments using ANN for LIBS calibration (*e.g.*, [127], [128]) relied on the multilayer perceptron (MLP) ANN architecture, with the structure of the network determined by trial and error. We instead implemented a genetic algorithm to optimize the network. In addition to MLP

ANNs, we also investigated cascade correlation (CC) ANNs, which determine their own topology during training. We also compared several data pre-processing techniques, including feature selection using a genetic algorithm to select five spectral channels per element to use for multivariate analysis as opposed to the full LIBS spectrum, and averaging all spectra for samples of identical composition in the training set so that each unique training composition is represented by a single spectrum.

2. Samples

The 31 powder geostandards [129] were obtained from a commercial source and include andesites, basalts, dolomites, gypsum and olivine. The suite of 195 rock slab samples was obtained from the Mars analog sample collection at NASA's Johnson Space Center. For the 90 low-volatile silicate samples, powders were prepared by crushing in an alumina shatterbox until all the powder passed through an 80 mesh stainless-steel sieve. Grinding was stopped at this particle size to avoid significant contamination of the sample with Al_2O_3 from the shatterbox. The major element chemistry of the rock slab samples was determined from representative powders by X-ray fluorescence (XRF) using a $Li_2B_4O_7$-sample flux-fusion-glass procedure and a Philips 2404 XRF spectrometer configured with a 4kW Rh X-ray tube [130]. Loss of weight on ignition (LOI) was determined by heating to 900°C in air for >1 hour, and the amount of Fe^{2+} was measured on unheated samples using a modified Reichen and Fahey [131] procedure. Because the major element analyses were done on the residue of LOI heating, total Fe is reported as Fe_2O_3T.

The geostandard and rock slab chemical compositions are shown on an igneous total alkali *vs.* silica (TAS) classification plot (Figure 1). Many of the rock samples and several of the

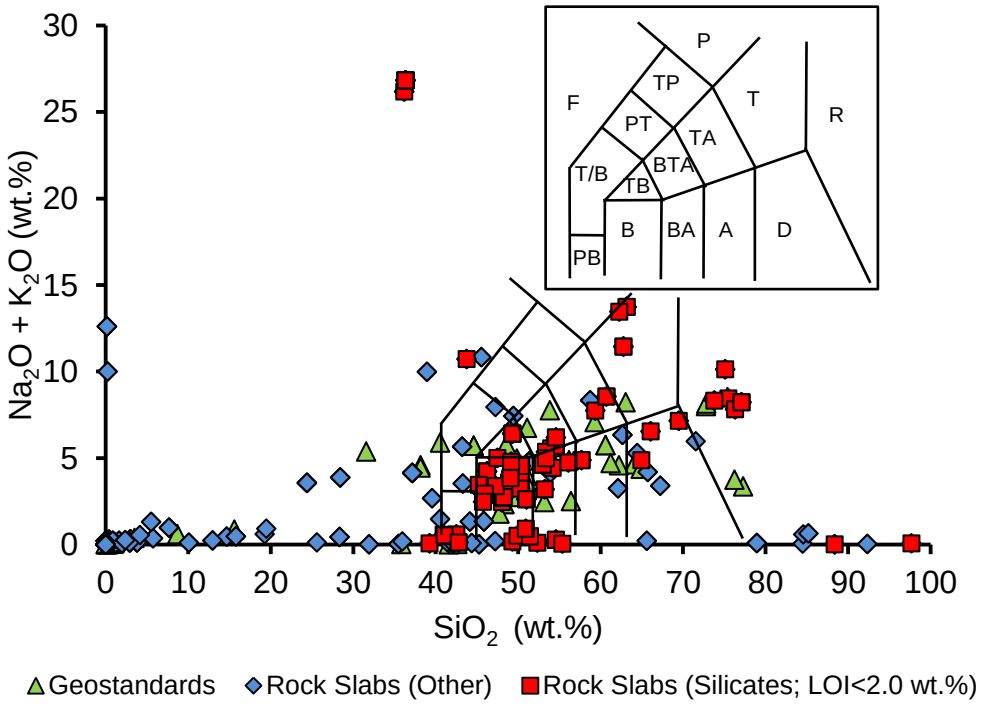

Figure 1: Total alkali *vs.* silica (TAS) classification plot showing the range of compositions of the rock slab samples and the pressed-powder geostandards. Inset indicates the igneous rock types for each portion of the TAS diagram. F: Foidite; PB; Picrobasalt; T/B: Tephrite/Basanite; B: Basalt; TB: Trachybasalt; PT: Phonotephrite; BTA: Basaltic Trachyandesite; TA: Trachyandesite; P: Phonolite; TP: Tephriphonolite; BA: Basaltic Andesite; T: Trachyte/Trachydacite; A: Andesite; D: Dacite; R: Rhyolite. Many samples are not igneous silicate rocks and therefore plot outside the classification range.

geostandards are not igneous rocks, and therefore plot well outside the typical range of the TAS plot.

The rock slabs were also used for calibration of the flight MastCam instrument [32] on MSL, and many are common to those being analyzed (in different physical forms) by test bed versions of the MSL CheMin [37] and Sample Analysis at Mars (SAM; [38]) instruments. Subsets of the JSC collection were also used in connection with flight instrument validation on other robotic missions to Mars (*e.g.*, [16], [132])

3. LIBS Experimental Methods

All LIBS spectra used in this study were collected at Los Alamos National Laboratory with a laboratory analog of the MSL ChemCam instrument, similar to that described by [49], [52], [126], and [133]. The laboratory set-up uses a Nd:YAG laser operating at 1064 nm, pulsed at 10 Hz with a pulse energy of 17 mJ/pulse. Targets were placed in a vacuum chamber back-filled with ~7 Torr CO_2 at a stand-off distance of 7 m. To partially offset effects of sample heterogeneity, LIBS spectra were acquired for at least 5 spots on each rock slab and geostandard target.

Plasma emission was collected with a telescope and directed via an optical fiber through a demultiplexer to three Ocean Optics HR2000 spectrometers covering the UV (225.00-325.97 nm), VIS (381.86-471.03 nm) and VNIR (494.93-927.06 nm) wavelength regions. The full-width at half maximum intensity resolutions for the UV, VIS, and VNIR spectrometers are 0.1, 0.09, and 0.42 nm, respectively. Each spectrometer has 2048 spectral channels, yielding a full spectrum of 6144 channels. ChemCam has a similar wavelength range (240-850 nm), number of channels (6144) and spectral resolution. Our spectra were subsequently reduced to 6117 channels because 27 detector channels gave spurious values and were excluded from the analysis.

The LIBS plasma brightness from the rock slabs varied significantly depending on composition. Figure 2 shows the average relative LIBS signal intensity for the full set of rock slabs. Slabs containing significant amounts of Fe (*e.g.* sulfides, Fe oxides, and siderite) coupled best with the laser beam, while samples containing little Fe and higher amounts of Al (*e.g.* Al_2O_3, bytownite, and alunite) or Si (*e.g.* flint, chalcedony, opal) tended to couple poorly. Prior to statistical analyses, we followed the procedure used in previous LIBS studies (e.g. [49], [52], [126], [133]) and normalized the spectra so that the sum of the signal across all observed wavelengths was equal to one. This reduces the effect of shot-to-shot variations and differences

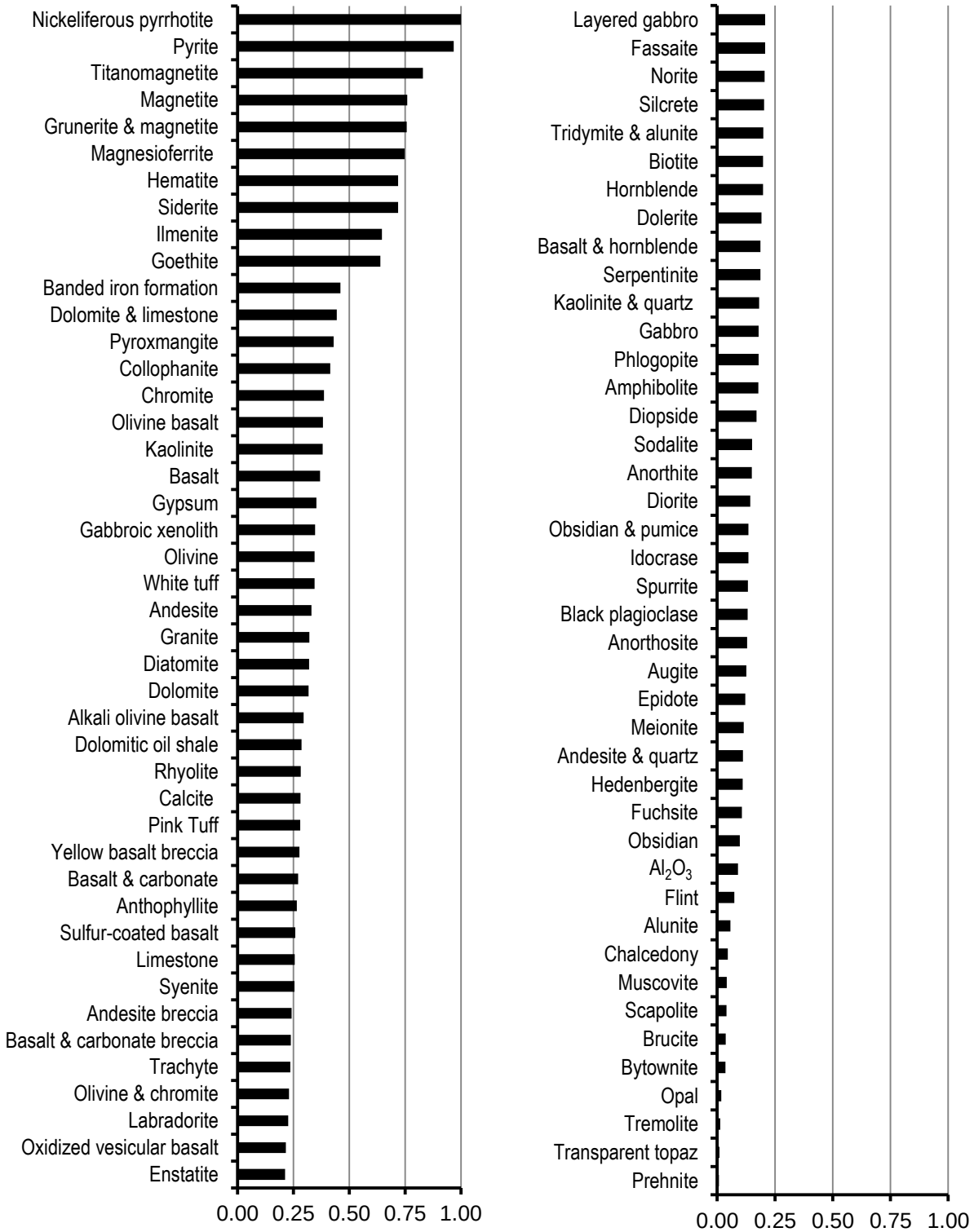

Figure 2: Relative average signal strength for the sample types in our full data set. Iron-rich samples generally had the brightest plasmas and high signal strengths, igneous rocks had intermediate signal strengths, and aluminum- and silica-rich, iron-poor samples had low signal strengths.

in laser-to-sample coupling. We briefly investigated the accuracy of LIBS predictions without normalization and found them to be comparable or worse than the predictions with normalization, but a more rigorous study of the effect of normalizing the LIBS spectra should be conducted. We did not apply any continuum removal to our data prior to analysis. [52] have investigated continuum removal with LIBS data and found that the resulting predictions were equivalent to or less accurate than predictions using the spectra without continuum removal.

4. Principal Components Analysis

PCA is a commonly-used method for reducing the dimensionality of a dataset by expressing it as the combination of a small number of linearly independent variables or "principal components" (*e.g.* [134]). PCA of LIBS spectra does not directly provide chemical compositions but does subdivide the samples according to their dominant spectral components (*e.g.* [49], [126], [133]). Thus, an unknown geologic target can be constrained to one or more compositional class (*e.g.*, basalt, sulfate, carbonate, etc.) by a PCA calculation including spectra from a large number of targets with known compositions.

The spectral variability of the LIBS data for the complete set of samples (195 rock slabs and 31 geostandards) is shown in Figure 3, as a scatter plot of the first and second principal components. Silicate rocks samples are plotted in Figure 3a and silicate minerals and ilmenite are plotted in Figure 3b, and other non-silicates are plotted in Fig 3c. Figure 3d, Figure 3e and Figure 3f are the same as Figure 3a, 3b and 3c respectively, but the PCA model was run with sodalite and the synthetic Al_2O_3 samples excluded. Overlapping to distinct clusters correspond to groups of samples that have similar spectra. For example, the rock-forming minerals olivine, pyroxene, and plagioclase cluster in different locations, and these locations are distinct from the clusters formed

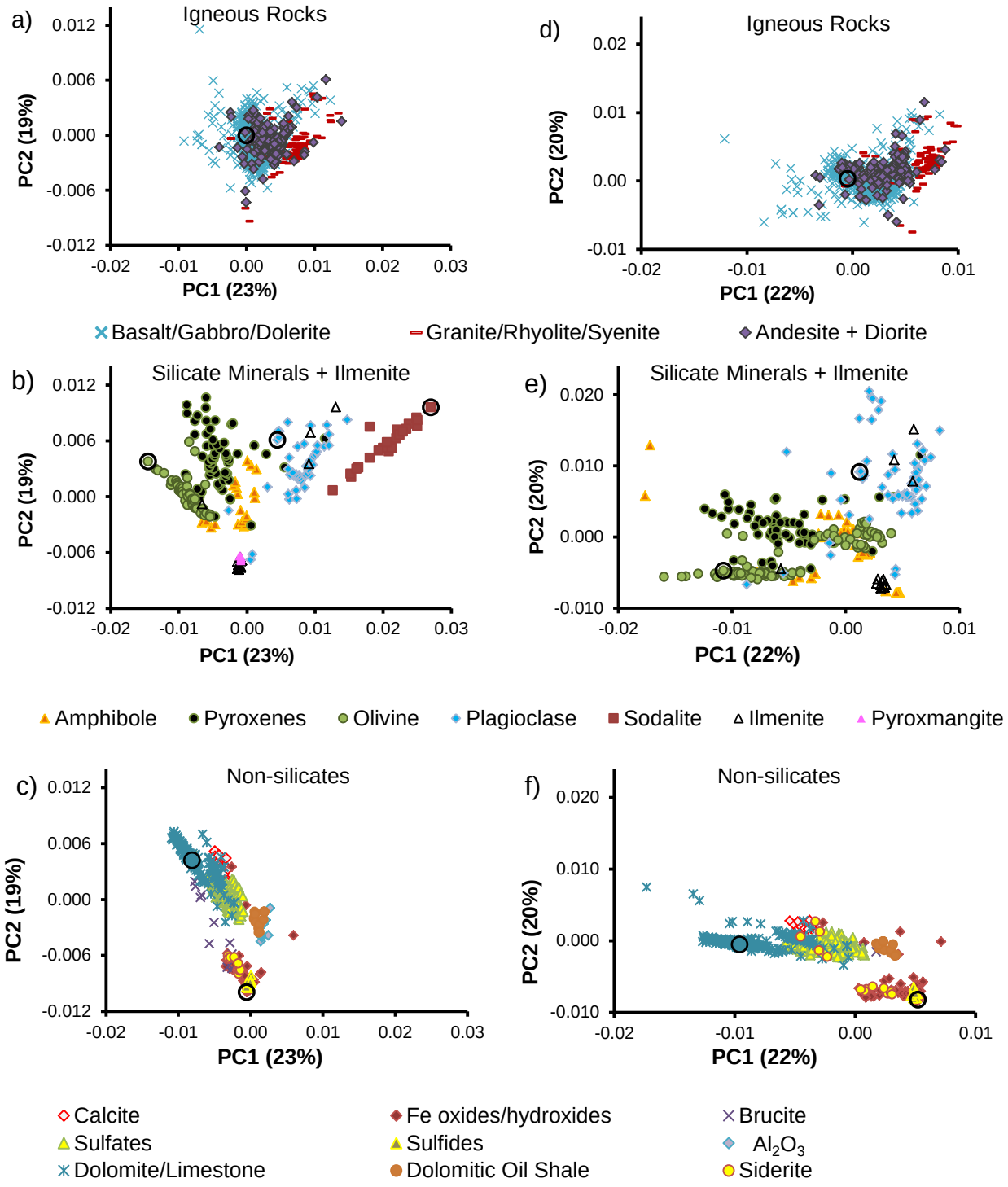

Figure 3: Scatter plots of the first two principal components of the LIBS dataset. The percentage of total variance in the dataset explained by each component is indicated. Points have been color-coded according to the known sample type, and similar samples tend to cluster together. (a,d) Silicate rock samples. (b,e) Silicate minerals and ilmenite. Some of the samples classified as olivine contained calcium as well, causing them to form a separate cluster closer to pyroxenes in (e). (c,f) Non-silicates. For plots (d), (e) and (f) sodalite, pyroxmangite and synthetic Al_2O_3 were excluded from the PCA model. Refer to Figure 4 for the spectral loadings for PC1 and PC2 in (a), (b) and (c). The circles in the scatterplot correspond to the spectra shown in Figure 5.

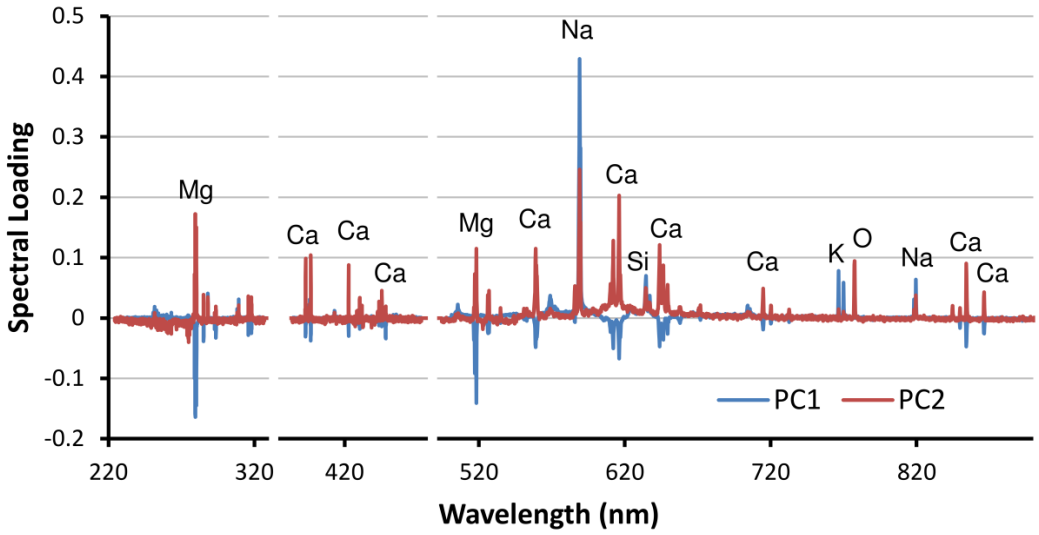

Figure 4: Spectral loadings for the first two principal components shown in Figure 3a, 3b and 3c. The sharp positive and negative peaks correspond to elemental emission lines.

by igneous rocks that are combinations of these minerals. Similarly, the carbonates cluster according to the major cation.

The spectral loadings for the first two principal components in Figure 3a and 3b are shown in Figure 4, and they can be used to interpret the location of points on the scatter plots. If a sample has emission lines which correspond to positive spectral loadings, it will have a positive value on the PCA scatterplot. Likewise, negative loadings result in negative values on the scatter plot. For example, sodalite plots in the upper-right quadrant because both PC1 and PC2 have a strong positive loading corresponding to the 589 nm Na emission line. Likewise, olivine and most of the carbonates plot in the upper left because of a negative correlation with Ca and Mg lines in PC1 and a positive correlation in PC2. The igneous silicate rocks show significant overlap on the plot, but as they range from mafic to felsic they tend to become more positive in PC1, because of a positive correlation with potassium emission lines. With sodalite excluded, the first principal

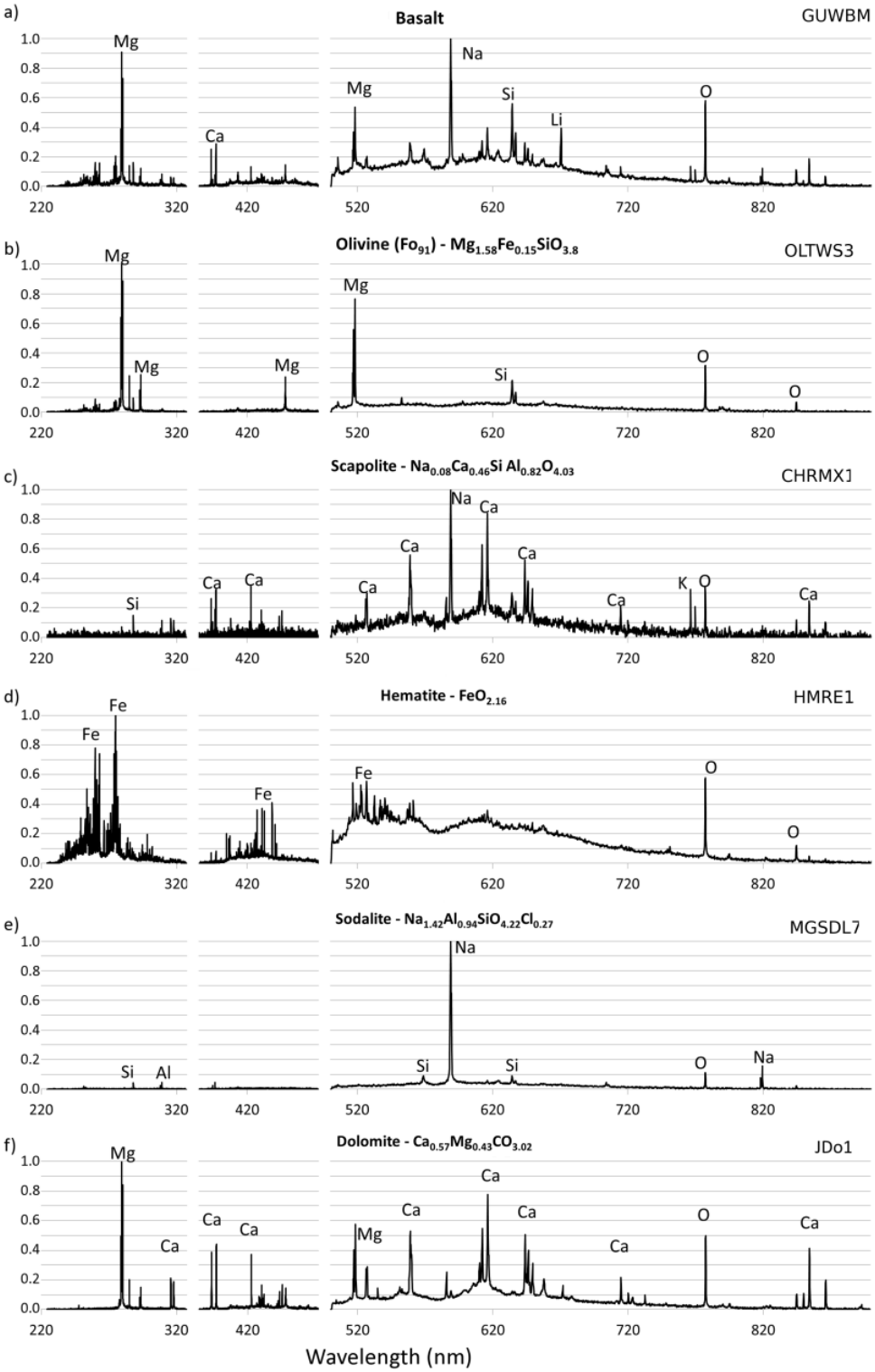

Figure 5: Six example LIBS spectra. The points corresponding to each spectrum on the PCA scatter plot are marked in Figure 3. Strong emission lines have been labeled. The spectra have been normalized so that the total integrated signal is equal to 1 and then scaled to the strongest emission line in the spectrum. Gaps in spectral coverage between the three detectors have been removed. The equations represent the atomic fraction of the major elements in each mineral, normalized to Si for silicates, Fe for hematite, and C for dolomite.

component in Figs. 3c and 3d corresponds to magnesium content. Figure 5 shows six example LIBS spectra from clusters in Figure 3, with strong emission lines labeled. The points corresponding to each spectrum are marked in Figure 3.

5. Multivariate Analysis

5.1 Sample Considerations

The compositions of the JSC analog samples and geostandards, originally expressed as oxide weight percent, were converted to atomic fraction for quantitative analysis, because the intensity of LIBS emission lines depends upon atomic fraction in the LIBS plasma rather than oxide weight percent in the solid sample [49]. The model predictions were converted back to equivalent oxide weight percent by assigning an appropriate amount of oxygen to each element, calculating the mole fraction of each oxide, and normalizing so that the sum of the oxide fractions totaled to 100%. For the purposes of this conversion, Fe was assigned to Fe_2O_3 and the samples were assumed to have no P_2O_5, H_2O, SO_3, or CO_2. It is important to note that the conversion from oxide wt. % to atomic fraction for a given element incorporates the uncertainty in the determination of all of the major element oxides. When converting back from atomic fraction to oxide wt. %, errors in the LIBS prediction of one element can affect the normalized abundance of all elements. Additionally, the total of the major element oxides is forced to equal 100% which is not necessarily the case for samples with significant volatiles or unusual compositions. Tucker et al. [52] showed that calculations performed using oxide weight percent resulted in more accurate predictions than those using atomic fraction.

To compare the quantitative multivariate analysis methods, we focused on low-volatile (LOI < 2 wt. %) silicate samples and excluded several samples with unusual compositions (*e.g.* pyroxmangite) or poor laser-sample coupling. This reduced the sample set to

Table 1: List of the sample types, number of analyses, number of unique compositions, sample names and geostandards in the training, validation and test sets.

Type	# of Analyses	Unique Compositions	Samples	Geostandards
			Training Set	
Andesite	11	4	TMGNV5	AGV2, GBW07110, MO12
Anorthosite	4	2	MCCSG1, TECNY1	
Basalt	62	9	CA9LJ1, HWMK124, HWMK104, HWMU574-170	BCR2, BHVO2, GBW07105, GUWBM, JB2
Dolerite	3	1	PSNJ1	
Flint	1	1	DCENG1	
Gabbro	6	2	WI0ML1, MU80-41	
Granite	3	2	LANTX1	GBW07103
Norite	5	1	MCCSG20, MCCSG21	
Obsidian	2	2	CA9OB1, CA9OB2	
Olivine	8	4	OLJC1, OLTWS3	DH4909, DH4911
Labradorite	1	1	NANLB1	
Augite	3	2	HARAG1, BRLKCD1	
Diopside	4	1	DIHUQ1	
Fassaite	1	1	HLNMT1	
Rhyolite	2	2	CA9KRY1, BICCA1	
Sodalite	1	1	MGSDL1	
Syenite	2	1	SYMPCA5	
Vesuvianite	1	1	CQRSCA1	
Total	*120*	*38*		
			Validation Set	
Anorthosite	1	1	WD228	
Andesite	4	1		JA2
Basalt	7	3	CP-5, HWHL100	688
Fassaite	1	1	HLNMT1	
Rhyolite	4	2	BICCA2, BICCA5	GBW07113
Sodalite	4	1	MGSDL7	
Syenite	1	1	SYMPCA1	
Diorite	1	1	BSTQBC1	
Total	*23*	*11*		
			Test Set	
Anthophyllite	1	1	WRCA1	
Andesite	9	4	CA9LVNP1	GBW07104, JA1
Andesite + Quartz	1	1	SQWCMT1	
Anorthite	1	1	GSVCA1	
Banded Iron Formation	2	2	WI0BIF1, WI0BIF3	
Basalt	18	11	CP-5, CA9WRN1, WIME101, CHFCO1, KICCA1, CA9VA1	JB-1b, JB3, MO13, MO14
Diorite	1	1	LDNVA5	
Gabbro	3	3	MU80-37B, MASEX1, MU80-03A	
Phlogopite	1	1	SYONT1	
Olivine	2	1		DH4912
Other Plagioclase	1	1	PLAGWM1	
Bytownite	2	2	CBBYT1, CBBYT5	
Enstatite	1	1	BAMNOR1	
Rhyolite	2	1		JR1
Silcrete	1	1	GR820	
Trachyte	2	1	HWHL101	
Total	*48*	*33*		

Table 2:
Range and distribution of compositions in the training set with and without spectral averaging.

	Minimum	1st Quartile	Median	3rd Quartile	Maximum	(Max-Min)/Median
			Training Set			
SiO_2	35.85	49.51	49.51	53.20	97.71	1.25
TiO_2	0.00	0.57	1.14	1.14	3.20	2.81
Al_2O_3	0.35	13.50	16.25	16.25	30.66	1.87
Fe_2O_3	0.07	6.54	9.68	10.37	17.46	1.80
MnO	0.00	0.10	0.14	0.16	0.28	2.03
MgO	0.02	3.59	7.47	7.47	56.14	7.51
CaO	0.14	6.47	6.47	9.80	37.22	5.73
Na_2O	0.02	2.63	4.19	4.65	25.96	6.19
K_2O	0.00	0.20	0.20	1.12	12.05	60.27
			Training Set with Spectral Averaging			
SiO_2	35.85	48.93	50.96	54.58	97.71	1.21
TiO_2	0.00	0.25	0.57	1.14	3.20	5.60
Al_2O_3	0.35	11.85	13.83	16.83	30.66	2.19
Fe_2O_3	0.07	2.97	6.54	10.79	17.46	2.66
MnO	0.00	0.08	0.12	0.19	0.28	2.41
MgO	0.02	1.84	4.34	7.43	56.14	12.93
CaO	0.14	3.78	9.40	10.70	37.22	3.94
Na_2O	0.02	1.68	3.13	4.28	25.96	8.30
K_2O	0.00	0.14	0.45	1.82	12.05	26.56

90 rock slabs, their powders, and 22 geostandards. The rock slab samples have a much broader range of chemical compositions than the pressed powder geostandards. Therefore, we sorted the combined rock and geostandard samples by their XRF-derived SiO_2 concentration and alternately assigned samples to training and test sets for multivariate analysis. When the same sample was analyzed multiple times or when multiple rock slabs were cut from the same parent rock, all spectra corresponding to a given composition were assigned to either the training or test set to avoid testing the predictive ability of the models on "known" samples. A subset of samples was removed from the test set and used as an independent validation set to determine stopping criteria for neural network training and to determine which wavelengths to select during feature selection. Table 1 lists the rock and mineral types, the number of unique compositions and the

total number of analyses for each composition. Table 2 summarizes the range and distribution of compositions in the training set.

5.2 Quantifying and Comparing Results

A common metric used to evaluate the predictive capability of multivariate methods is the root mean squared error (RMSE), which is defined as:

$$RMSE = \sqrt{\frac{\sum_{i=0}^{n}(y_i - \hat{y}_i)^2}{n}}, \quad (1)$$

where y_i and $\hat{y}_i$ $(i = 1,2, \ldots, n)$ are the actual and predicted compositions (in wt. %) and *n* is the total number of samples. All reported RMSE values in this study are in wt. % oxide.

It is important when comparing methods to determine whether the variations in RMSE values across the models are meaningful. To do this, we used the Student's *t* test to determine whether the null hypothesis, that the results of two models are statistically indistinguishable, is true. We first calculated an estimate of the uncertainty in the RMSE for each model. Because RMSE is functionally equivalent to the equation for standard deviation [135](Eq. 10), with the known composition y_i substituting for the mean, we calculate the variance of the RMSE (s^2_{RMSE}) according to the equation for the variance of the standard deviation [136], where Γ is the Gamma function.

$$s^2_{RMSE} = \left(\frac{RMSE^2}{n}\right)\left[n - 1 - \frac{2\Gamma^2\left(\frac{n}{2}\right)}{\Gamma^2\left(\frac{n-1}{2}\right)}\right] \quad (2)$$

We then calculate the Student's *t* value for the two methods being compared using their RMSE and s^2_{RMSE} [135] (Eq. 22)

$$t = \frac{RMSE_A - RMSE_B}{\sqrt{s^2_{RMSE_A} + s^2_{RMSE_B}}}. \quad (3)$$

The associated degrees of freedom (f) for the Student's *t* distribution are given by [135](Eq. 23):

$$f = \frac{\left(s^2_{RMSE_A} + s^2_{RMSE_B}\right)^2}{\frac{s^4_{RMSE_A}}{n_A - 1} + \frac{s^4_{RMSE_B}}{n_B - 1}}. \quad (4)$$

Finally, the *t* values and degrees of freedom can be used to calculate the two-tailed Student's *t* distribution probability (p). This value is interpreted as the likelihood that the null hypothesis is satisfied: a low value means that the differences between the results of two methods are statistically significant. For example, if the *p*-value for the comparison between the results of two models is less than 5% then we can say with better than 95% confidence that the differences between the methods are statistically significant. In the following discussion, the 95% confidence level is used to define a "significant" difference between models.

5.3 Feature selection

We used a genetic algorithm (GA) to test the effect of feature selection on the performance of the multivariate algorithms. Feature selection is a pre-processing step in which portions of the LIBS spectrum containing the most information on chemical composition are identified and used instead of the full spectrum, thereby simplifying multivariate models, reducing computation time, and potentially improving the predictive ability of the model [137].

Genetic algorithms are commonly used to perform feature selection on spectroscopic data prior to PLS or other multivariate analyses (*e.g.* [138–140]). GAs are search algorithms based on the process of natural selection and are efficient at solving problems with many possible solutions [141]. For a given optimization problem, a set of possible solutions are generated and tested. A fraction of the population with the lowest error is propagated to the next generation while solutions that perform poorly are removed. To repopulate the set of solutions, the most-fit

candidates are allowed to reproduce, resulting in offspring that combine the properties of the parent solutions. Often, random mutations are introduced to allow the algorithm to avoid local minima by maintaining a diverse population of possible solutions.

We used the genetic algorithm within the open-source multivariate analysis program PYCHEM [142]) to conduct feature selection. The algorithm was run 1000 times per major element, each time using a population of 100 sets of 5 spectral channels. The number of features was limited to 5 channels so that only the channels most relevant to the element of interest would be chosen. The fitness of each set of 5 channels in the population was tested by training a PLS1 model for the element of interest using only the intensity of the spectrum at those channels as input. The models with the lowest mean-squared error for the validation set in each generation were used to populate the subsequent generation. The GA was initialized with randomly selected channels, so each initialization of the algorithm tested the performance of 500 out of the 6117 channels in the spectrum. By running the algorithm 1000 times, we ensured that on average, each channel was chosen in one of the initial populations more than 80 times. Each run of the GA terminated when the 5 channels chosen as the best solution did not change after five generations.

For each element, the algorithm yields the frequency with which each of the spectral channels were chosen in the final model. Figure 6 shows a plot of selection frequency *vs.* wavelength for calcium. The most frequently selected channels correspond to Ca lines, but the channels for the brightest Ca lines were not always the most frequently selected. This indicates that the brightest lines are not optimal for PLS regression, likely due to self-absorption and other matrix effects. Using an automated feature selection method has the advantage that it makes no assumptions about which channels are likely to be optimal, and therefore avoids bias toward the

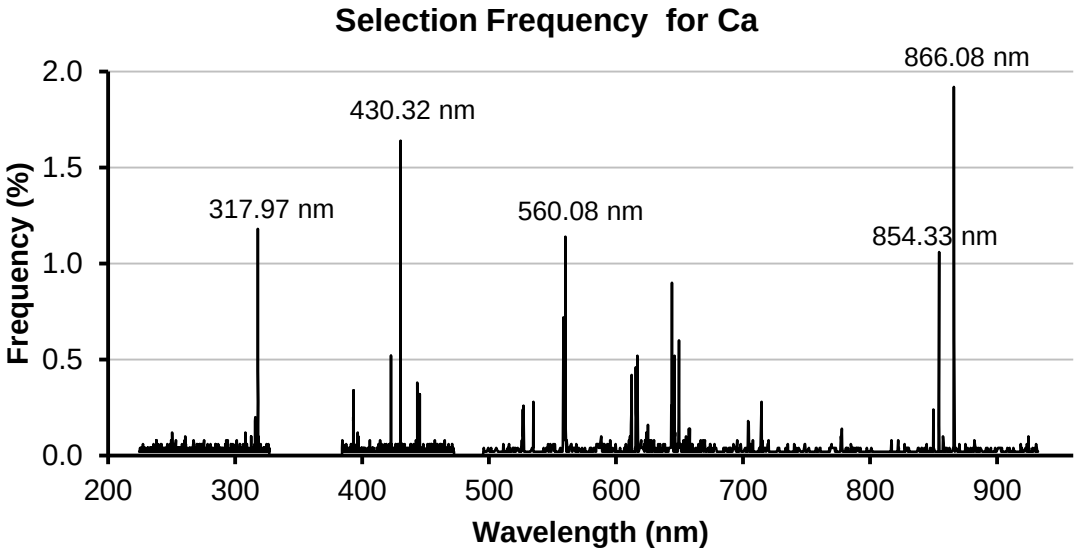

Figure 6: A plot of the frequency with which each channel in the LIBS spectrum was chosen by the 1000 runs of the genetic algorithm as part of the best PLS1 model for predicting Ca. The plotted values sum to 100%. Although this is not a spectrum, the wavelengths of the most commonly chosen channels correspond to calcium emission lines (Table 3).

brightest lines. The intensities at the 5 most-frequently chosen channels for each element were used to train our models.

Because the selected channels are element-specific, we predicted each element separately when feature selection was used. For most elements the algorithm appears to have identified at least one channel at a wavelength corresponding to an emission line for that element, and in some cases the majority of the channels selected correspond to strong emission lines (Table 3). The wavelengths associated with the emission lines listed in Table 3 are based on emission wavelengths in vacuum in the NIST atomic spectral database (http://physics.nist.gov/asd). The LIBS wavelengths assigned to the spectral channels in this study are based on the factory calibration of the three spectrometers. We did not perform an independent wavelength calibration because the wavelengths assigned to the spectrometer channels have no effect on the performance of the multivariate methods that we used. Relying on the factory calibration does however result in slight uncertainty in the identification of spectral lines corresponding to the

genetic algorithm-selected channels, particularly in regions of the spectrum with abundant emission lines.

For some elements the selected channels did not correspond to the element of interest, but instead corresponded to emission lines from a geochemically-related element. For our samples, Si is the clearest example of this effect: the five most-frequently selected channels for Si correspond to K emission lines. The selection of K emission lines for Si results from the natural correlation between these two elements in igneous rocks; granitic rocks are high in both Si and K relative to basalts. The element Ti shows a similar effect, with the majority of the selected channels corresponding to bright Fe lines rather than Ti emission lines because of the natural association of Ti and Fe in minerals like ilmenite and titanomagnetite.

5.4 Multivariate Method Descriptions

In this section we describe and compare the results of three multivariate methods (PLS, MLP ANN and CC ANN) using both the full LIBS spectrum (*i.e.* all 6117 channels) and the 5 channels per major element that were identified by feature selection as input data. The spectra for the training set were configured in two ways. One way uses all available training set standards, including multiple spectra of the same target. The other way reduces the number of training spectra to one spectrum per composition by averaging the spectra for multiple measurements of the same target. For example, the basalt geostandard GUWBM was included in every set of LIBS measurements, resulting in significantly more spectra of GUWBM than any of the other members of the full training set. The permutations of multivariate methods and pre-processing steps yields 12 sets of results that can be compared for their respective predictive capability.

Table 3:
Five wavelengths (in nm) corresponding to channels most frequently selected by the genetic algorithm for each major element and the associated elemental emission lines.

Element	Selected	Inferred	Selected	Inferred	Selected	Inferred	Selected	Inferred	Selected	Inferred
Si	766.54	K (766.7)	766.75	K (766.7)	769.70	K (770.11)	769.91	K (770.11)	770.13	K (770.11)
Ti	256.32	Fe (256.33)	259.97	Fe (260.02)	273.97	Fe (273.81)	274.93	Fe (274.77)	430.11	Ti (429.98)
Al	394.34	Al (394.4)	516.50	Mg (516.73)	516.73	Mg (516.73)	624.71	Al (624.34)	818.49	Na (818.48)
Fe	273.97	Fe (273.81)	274.27	Fe (274.32)	274.93	Fe (274.77)	275.58	Fe (275.52)	275.63	Fe (275.71)
Mn	253.86	Mn (253.87)	278.35	Fe (278.36)	393.32	Mn (393.26)	396.76	Fe (396.76)	396.81	Fe (396.85)
Mg	447.94	Fe (447.93)	516.73	Mg (516.88)	516.96	Mg (516.88)	517.42	Mg (517.41)	518.34	Mg (518.50)
Ca	317.97	Ca (318.025)	430.32	Ca (430.37)	560.08	Ca (560.0)	854.33	Ca (854.4)	866.08	Ca (866.45)
Na	568.69	Na (568.98)	591.67	Na (589.75)	818.29	Na (818.55)	818.49	Na (818.55)	819.53	Na (819.7)
K	766.12	K (766.7)	766.54	K (766.7)	766.96	K (766.7)	770.13	K (770.11)	780.00	Rb (780.24)

The next three sections describe the three multivariate analysis methods that we used. The results are discussed in Section 5.5.

5.4.1 Partial Least Squares (PLS1 and PLS2)

Partial Least Squares (PLS) is a multivariate regression algorithm that builds on the results of PCA. It is especially well suited to applications like quantitative LIBS where the goal is to predict a limited number of output values (elemental concentrations) from a very large number of input variables (intensity at multiple wavelengths) [143]. We used two forms of the PLS algorithm. When intensities at channels identified by feature selection for a specific element were used as input, we used PLS1 to predict only that element. When the entire LIBS spectrum was used as an input, we used PLS2, which is capable of predicting multiple elements at once.

To implement the PLS alforithm, we used the Unscrambler v9.8 software package (Camo, Inc.) with leave-one-out cross validation, in which each sample in the training set is successively left out and treated as an unknown while the model is trained. Although computationally expensive, PLS2 with leave-one-out cross validation produces the most robust PLS2 model and has been shown to be effective at predicting the composition of pressed powder silicate rock standards [49], [52] and carbonate mineral hand-samples [126]. PLS1 has also been shown to predict the S atomic fraction in sulfur-bearing samples with an absolute accuracy of 2.4-37.9 % when trained with an appropriate training set and with manual feature selection to limit the input spectra to channels corresponding to sulfur emission lines [133].

The Unscrambler identifies the optimum number of components to use in the final PLS model as the number which minimizes the residual validation variance. The software automatically adds a 1% penalty to the residual validation variance for each additional component used in the model to avoid overfitting the training data. Note that the 1% penalty in

residual validation variance is simply a way to force the program to choose a conservative number of components and does not result in 1% greater prediction error with each additional component used. A more thorough investigation of the accuracy of LIBS predictions using different numbers of components in the PLS models should be conducted, but is beyond the scope of this study.

5.4.2 Multilayer Perceptron Artificial Neural Network (MLP ANN)

Artificial neural networks (ANNs) are algorithms based loosely on the functioning of biological neurons. Rather than a single central processor, the network completes calculations by passing data through a large number of simple, interconnected nodes. The network stores information in the weighted connections between these artificial neurons. This architecture gives neural networks several advantages over traditional algorithms, including a tolerance for noise and the ability to model non-linear relationships. ANNs also do not make prior assumptions about the distribution of input data and can accurately generalize when presented with new data [144]. ANNs have been shown to be effective for calibration of spectral data [145] and have been used in many geologic applications similar to quantitative LIBS, such as inferring SiO_2 content or elemental composition based on infrared spectra [146]; [147]

The most commonly-used ANN is the multi-layer perceptron (MLP; [148]). MLP ANNs consist of several layers of artificial neurons whose outputs are a nonlinear function of their weighted inputs. For a neuron with *n* input signals, each with an associated weight *w*, the neuron output *y* is given by:

$$y = tanh(\sum_{i=0}^{n} w_i x_i - \mu) \quad (5)$$

In this equation, μ is a threshold or "bias" weight, and a sigmoid function such as tanh (the hyperbolic tangent) is commonly used. For LIBS spectra, the intensity at each spectral

channel is an input into a neuron of the input layer. The layers of neurons between the input layer and the output layer are referred to as "hidden" layers. MLPs with a single hidden layer are capable of modeling differentiable functions to arbitrary accuracy and are commonly used in applications of MLP ANNs to laboratory and remote sensing applications [146], [147], [149], [150]. MLPs are typically trained using the back-propagation algorithm [151]) or similar variations which iteratively update the network weights to minimize the output error for the training set.

Inakollu [152] employed MLP ANNs for quantitative LIBS calibration, and found that they result in a lower average relative percent error than traditional calibration methods based on the area of relevant emission lines. Sirven et al. [127] conducted a study of multivariate analysis techniques for LIBS, comparing traditional calibration curves, PLS, and MLP to predict the concentration of chromium in two doped soil samples. They found that MLP ANN predictions had a lower average relative percent error than PLS on samples for which there were significant non-linearities because of self-absorption.

Ferreira et al. [153] used a MLP ANN to predict Cu abundances in pressed powders derived from 59 Brazilian soils, using manual feature selection. Motto-Ros et al. [128] investigated the performance of MLP ANNs on LIBS spectra of four natural rock samples: two impact glasses, a sandstone, and a volcanic glass. They applied manual feature selection, choosing one spectral channel per element of interest, and they found that the MLP ANN was able to predict the concentrations of Fe_{total}, MgO, SiO_2, MnO, Al_2O_3, CaO, and Ti_2O_3 with RMSEs ranging from 0.03 wt. % for MnO to 3.3 wt. % for SiO_2.

A common difficulty when working with MLPs is choosing the optimum number of neurons in the hidden layer. In a fully-connected MLP (*i.e.*, each neuron is connected to every

neuron from the previous layer), each additional hidden node significantly increases the number of weights computed during training, making larger networks slower to train. In addition, a network with too many nodes will require more training data to achieve good generalization, while a network with too few nodes will be unable to learn the training set satisfactorily [154].

Previous work with ANNs for LIBS has relied on a trial-and-error approach to select the number of hidden nodes in the MLP [127]. We followed the approach of [155] and [156] and used a GA to identify the optimum number of hidden nodes. We used the Synapse software package (Peltarion, Inc.) to conduct our MLP neural network calculations and to optimize the number of neurons in the hidden layer of each MLP ANN using the built-in genetic optimizer. The optimizer used double-point crossover [157], a mutation probability of 10%, and ran for ten generations with 200 candidate models per generation.

We trained the optimized network, using the validation set to ensure that the network was not overtrained. If there was a minimum in the error for the validation set, the training was stopped manually at that point. Commonly, both the training and validation error decreased rapidly and then stopped improving, in which case training stopped when the network showed no improvement after more than ~100 epochs of training.

5.4.3 Cascade Correlation Artificial Neural Network (CC ANN)

As an alternative to MLP ANN, we tested the performance of the cascade-correlation (CC) ANN algorithm [158]. The CC ANN algorithm begins with the simplest possible network, consisting of only an input and an output layer. The network is trained until additional training does not significantly reduce the error for the training set. At this point a new hidden layer consisting of a single node is added to the network and training continues. Each time the network

stagnates, all of the weights in the network are frozen, a new single-element hidden layer is added, and the training continues.

By automatically determining its own structure, the CC ANN avoids the difficulty in determining the number of hidden nodes that is faced when using MLP ANNs. In addition, by freezing the weights of the trained network prior to adding a new node, the algorithm avoids the "moving target" problem [158].

We implemented CC ANNs using FannTool, a publicly-available graphical interface for the open-source Fast Artificial Neural Network (FANN) library [159]. Instead of introducing individual hidden layer nodes, a set of candidate nodes are trained by the FannTool CC algorithm and the one with the best performance (lowest mean-squared error) is inserted into the network. We allowed the CC algorithm to run until 100 hidden nodes were introduced and then selected the network with the lowest mean squared error for the validation set. Often the selected network was very small, with 0, 1, or 2 hidden nodes.

5.5 Results from Multivariate Methods

Prior to converting the predicted atomic fractions to oxide weight percent, we calculated the average atomic fraction totaled across the nine major elements for each of the multivariate methods considered. A total that is much less than 1.0 would indicate a significant error in the prediction of one or more of the major elements. For all of the methods, the average total atomic fraction was close to 1.0, ranging from a minimum of 0.95±0.04 for CC ANN with feature selection and averaging, to a maximum of 0.97±0.06 for MLP ANN with feature selection and averaging.

The results for SiO_2 for the PLS2 method for the rock slabs are shown in Figure 7 as plots of LIBS-determined versus XRF-determined concentrations. Each data point is the average of

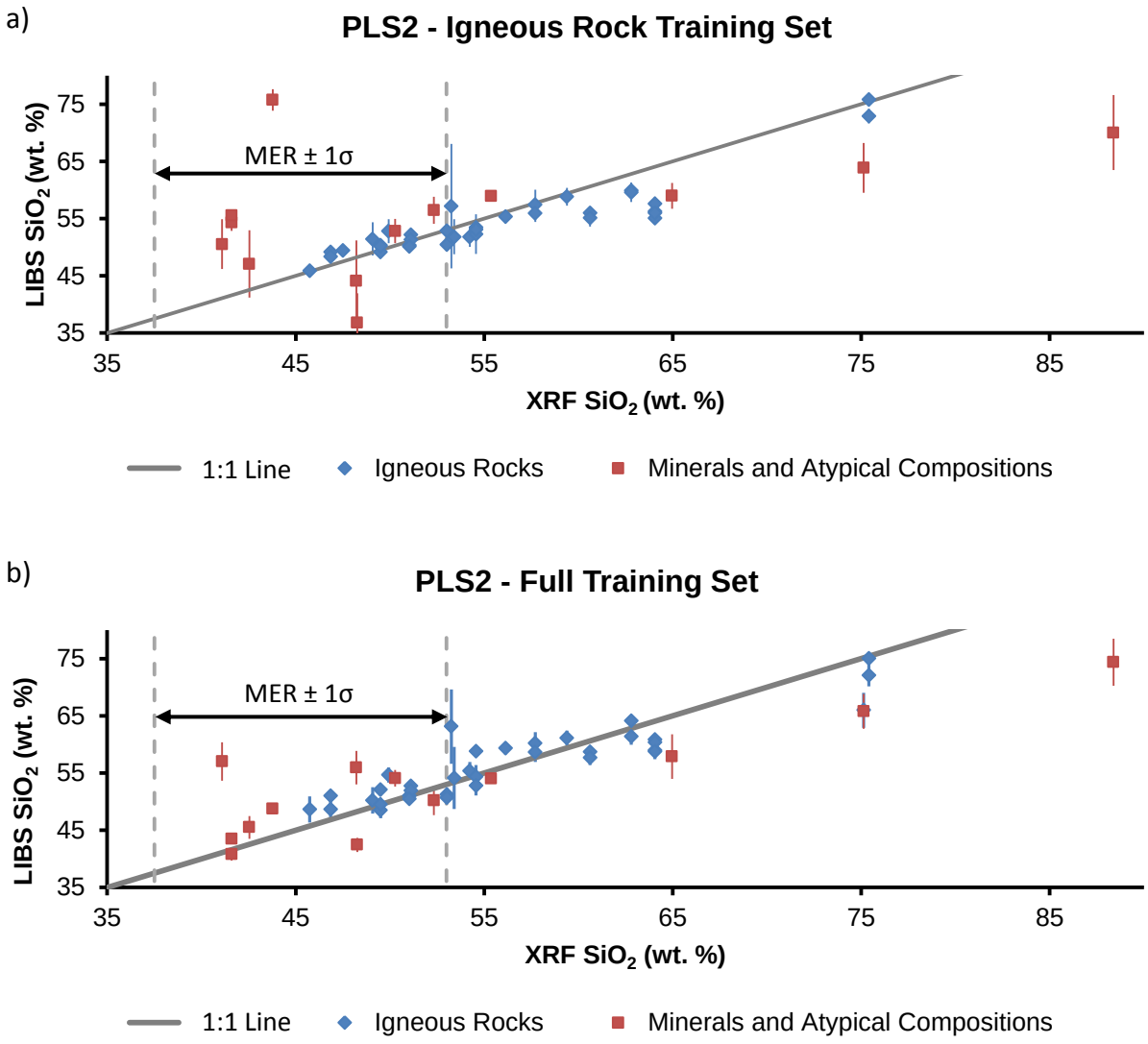

Figure 7: PLS2 results for SiO_2, trained using (a) only igneous rocks and (b) trained using the full training set. Vertical dashed lines mark the "typical" range of sample compositions observed by APXS on MER (*Gellert et al.*, 2006; *Ming et al.*, 2008; *Squyres et al.*, 2008).

five predictions, one for each of the five LIBS spots on the target. The vertical error bars are the standard deviation of the five predictions. For purposes of comparison, the XRF concentrations are taken as the actual concentrations so that a "perfect" prediction of the SiO_2 concentration from LIBS spectra and PLS2 analysis would fall along the one-to-one line. When trained on the igneous rock slab and pressed powder targets from the training set (Table 1; 44.6-51.0 SiO_2 wt.

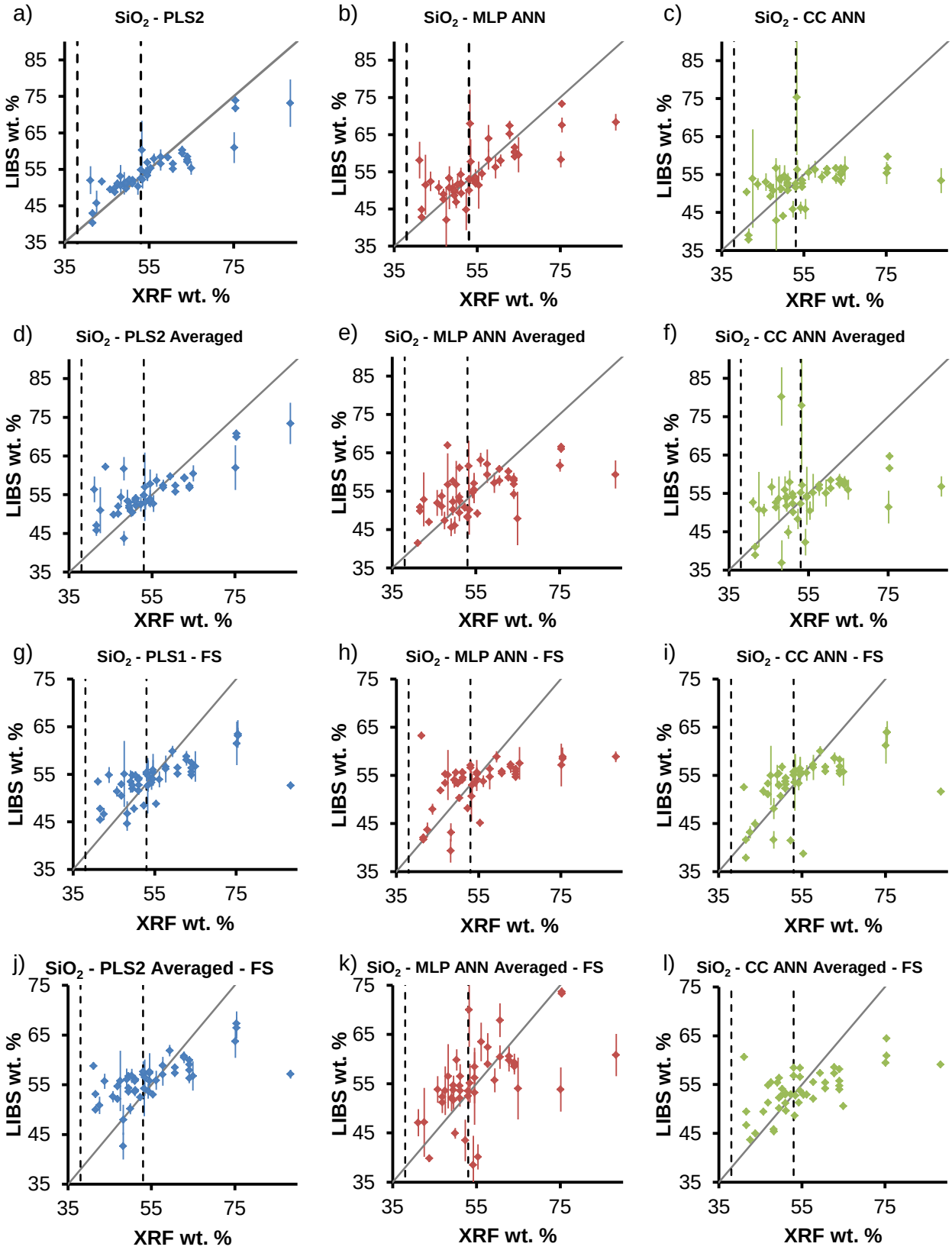
a)
SiO2 - PLS2
b)
SiO2 - MLP ANN
c)
SiO2 - CC ANN
d)
SiO2 - PLS2 Averaged
e)
SiO2 - MLP ANN Averaged
f)
SiO2 - CC ANN Averaged
g)
SiO2 - PLS1 - FS
h)
SiO2 - MLP ANN - FS
i)
SiO2 - CC ANN - FS
j)
SiO2 - PLS2 Averaged - FS
k)
SiO2 - MLP ANN Averaged - FS
l)
SiO2 - CC ANN Averaged - FS
LIBS wt. %
XRF wt. %
35
45
55
65
75
85

Figure 8 (Previous Page): Plots of the LIBS predicted SiO2 weight percent vs. the XRF SiO2 weight percent for (a) partial least squares (PLS2), (b) multilayer perceptron (MLP) artificial neural network (ANN), (c) cascade correlation (CC) ANN, (d) PLS2 with spectral averaging, (e) MLP ANN with spectral averaging, (f) CC ANN with spectral averaging, (g) PLS1 with feature selection (FS), (h) MLP ANN with FS, (i) CC ANN with FS, (j) PLS1 with FS and averaging, (k) MLP ANN with FS and averaging, (l) CC ANN with FS and averaging. Vertical dashed lines indicate the typical (median±1σ) range of compositions observed by MER APXS. A perfect prediction would fall along the solid diagonal 1:1 lines.

%), the predicted SiO_2 concentrations for igneous rocks in the test set had a RMSE of 3.3 wt. % (Figure 7a; blue data points).

The SiO_2 concentrations for pure minerals and samples with atypical composition, such as banded iron formation or silcrete, are poorly predicted by PLS2 when trained only on igneous rocks (RMSE of 12.5 wt. %). This occurs when correlations between elements in the training set are not present in the test set, or the matrix effects differ significantly. Additionally, several samples in the test set had compositions outside the range of compositions in the igneous rock training set, resulting in large errors. The RMSE is somewhat lower (8.9 wt. %) if only the samples with SiO_2 concentrations within the igneous training set range are considered. Low signal to noise can also contribute to prediction errors or to reduced precision if only some spots on a heterogeneous target coupled well. In addition, because the conversion from predicted atomic fraction to oxide weight percent involves normalizing to the total number of grams per mole of the sample, a significant error in the predicted atomic fraction for one element can cause other major elements to be poorly predicted.

Inclusion of minerals and samples with atypical compositions in the training set significantly increases the range of SiO_2 concentrations (35.9-97.7 wt. %) used to generate the PLS2 model. This reduces the SiO_2 RMSE for minerals and atypical samples in the test set from ~12.5 wt. % to 7.7 wt. % (Figure 7b). The SiO_2 RMSE for igneous rocks in the test set is essentially unchanged (from 3.3 wt. % to 2.8 wt. %; Figure 7b). For all comparisons between multivariate methods discussed below, unless specified otherwise we used the full training set,

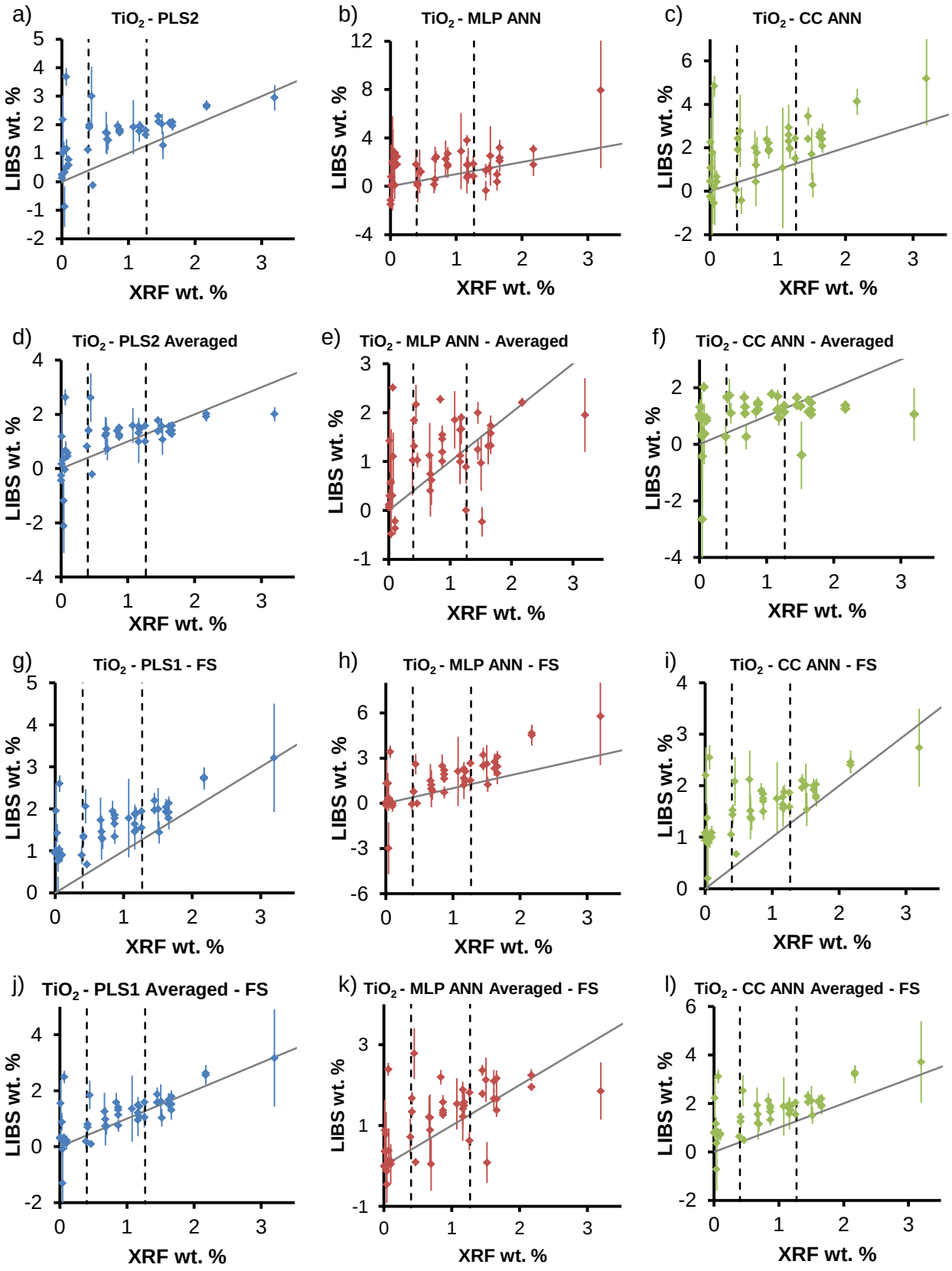
a) TiO2 - PLS2
b) TiO2 - MLP ANN
c) TiO2 - CC ANN
d) TiO2 - PLS2 Averaged
e) TiO2 - MLP ANN - Averaged
f) TiO2 - CC ANN - Averaged
g) TiO2 - PLS1 - FS
h) TiO2 - MLP ANN - FS
i) TiO2 - CC ANN - FS
j) TiO2 - PLS1 Averaged - FS
k) TiO2 - MLP ANN Averaged - FS
l) TiO2 - CC ANN Averaged - FS
LIBS wt. %
XRF wt. %

Figure 9 (Previous Page)**:** Plots of the LIBS predicted TiO_2 weight percent *vs.* the XRF TiO_2 weight percent for (a) partial least squares (PLS2), (b) multilayer perceptron (MLP) artificial neural network (ANN), (c) cascade correlation (CC) ANN, (d) PLS2 with spectral averaging, (e) MLP ANN with spectral averaging, (f) CC ANN with spectral averaging, (g) PLS1 with feature selection (FS), (h) MLP ANN with FS, (i) CC ANN with FS, (j) PLS1 with FS and averaging, (k) MLP ANN with FS and averaging, (l) CC ANN with FS and averaging. Vertical dashed lines indicate the typical (median±1σ) range of compositions observed by MER APXS. A perfect prediction would fall along the solid diagonal 1:1 lines.

including minerals and atypical compositions, to predict the concentrations of all major elements, and we calculate values of RMSE with respect to both the full test set (including igneous rocks, minerals and atypical samples) and the igneous rocks test set. Although the training set did contain pure minerals (*e.g.,* olivine, pyroxene, plagioclase, and sodalite) the majority of the training samples were igneous rocks. The full test set has higher values of RMSE compared to the igneous rock test set for all MVA analysis methods.

The results of our predictions for the SiO_2, MgO, and TiO_2 concentrations of the full test set are shown graphically in Figures 8, 9, and 10. These oxides were chosen because they represent limiting cases where the oxides are present at high (SiO_2), low (TiO_2), and variable (MgO) concentrations.

The RMSE values in Table 4 summarize the results of the 12 combinations of multivariate methods and pre-processing procedures for both the full test set and for the igneous rocks test set. "FS" indicates that feature selection was employed and "Ave" indicates that spectral averaging was applied prior to calculation. For each major element, the lowest RMSE is bolded. Methods with *p*-values indicating that they are statistically indistinguishable from the most-accurate method for a given element at the 95% confidence level are shaded. The values in the "Quadrature RMSE" column are the result of adding the RMSEs for the major element oxides in quadrature. This parameter is used to summarize the overall performance of the 12 procedures across all elements. The last two columns summarize the number of times a procedure was the most accurate and the number of times a procedure was equivalent to the most

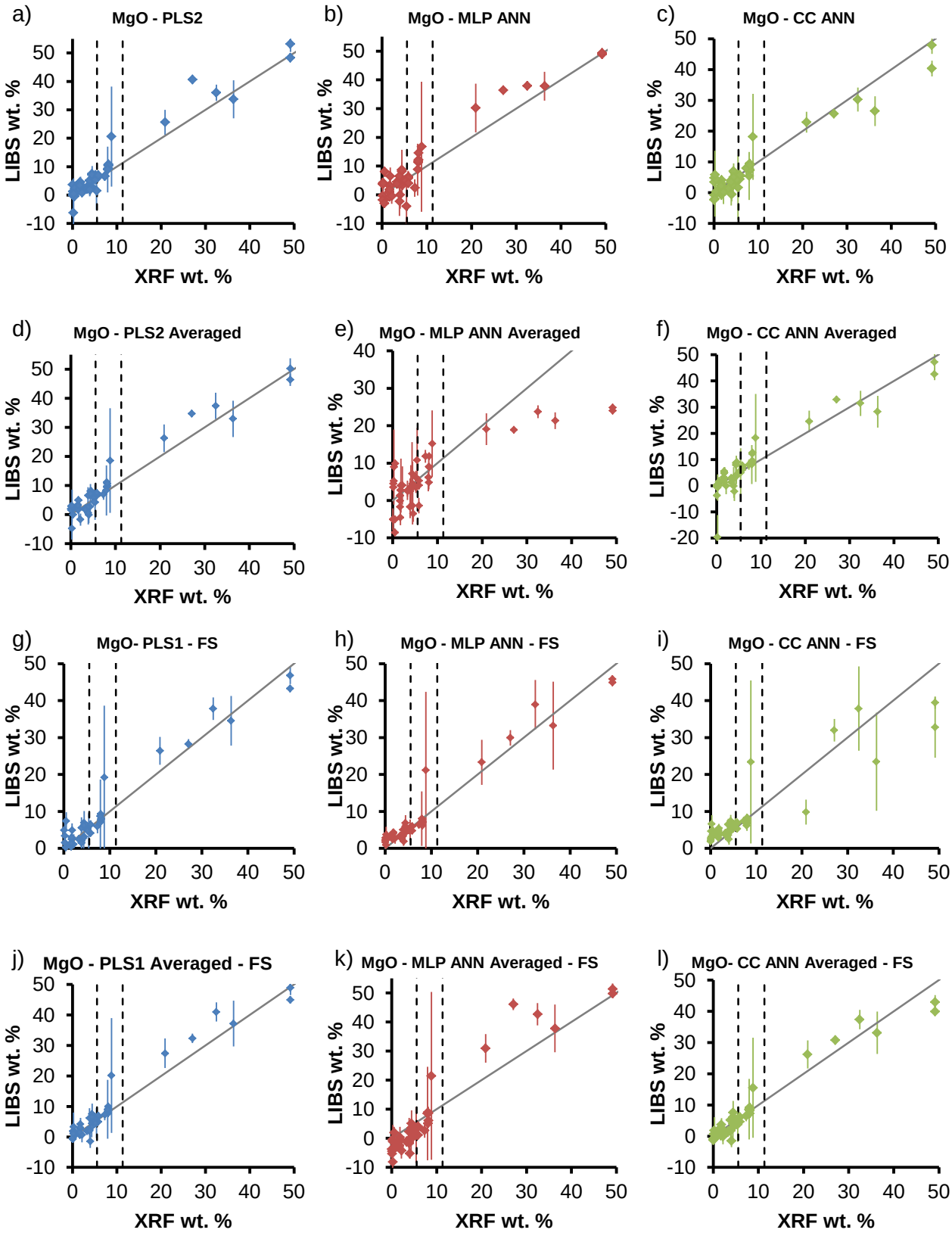
a)
MgO - PLS2
b)
MgO - MLP ANN
c)
MgO - CC ANN
d)
MgO - PLS2 Averaged
e)
MgO - MLP ANN Averaged
f)
MgO - CC ANN Averaged
g)
MgO- PLS1 - FS
h)
MgO - MLP ANN - FS
i)
MgO - CC ANN - FS
j)
MgO - PLS1 Averaged - FS
k)
MgO - MLP ANN Averaged - FS
l)
MgO- CC ANN Averaged - FS
LIBS wt. %
XRF wt. %

Figure 10 (Previous Page)**:** Plots of the LIBS predicted MgO weight percent *vs.* the XRF MgO weight percent for (a) partial least squares (PLS2), (b) multilayer perceptron (MLP) artificial neural network (ANN), (c) cascade correlation (CC) ANN, (d) PLS2 with spectral averaging, (e) MLP ANN with spectral averaging, (f) CC ANN with spectral averaging, (g) PLS1 with feature selection (FS), (h) MLP ANN with FS, (i) CC ANN with FS, (j) PLS1 with FS and averaging, (k) MLP ANN with FS and averaging, (l) CC ANN with FS and averaging. Vertical dashed lines indicate the typical (median±1σ) range of compositions observed by MER APXS. A perfect prediction would fall along the solid diagonal 1:1 lines.

accurate procedure at the 95% confidence level for any given major element. In all cases, the RMSE for each oxide and method when tested on the full test set is greater than the RMSE for the same oxide and method when testing only on igneous rocks. This result implies that the pure minerals and atypical samples in the full test set dominate the prediction errors. A graphical depiction of the RMSE values for the igneous rock samples is shown in Figure 11.

For comparison with the LIBS RMSE values, the one-sigma absolute errors for major element concentrations made by the MER Alpha Particle X-ray Spectrometer (APXS) were calculated using the square root of the sum of the squared accuracy and precision values (calculated from [160] for integration times >1 hr). The APXS makes precise measurements so the majority of the APXS total error (Table 4) results from the accuracy error. We also list the errors for the XRF method used to determine the "true" composition of our samples. The XRF precision is given by the standard deviation of the major element abundances derived for three sample/flux fusion glass disks of the geostandard powder 98-54 [163]. The accuracy is based on analyses of the two geostandards BHVO-2 and QLO-1 [129]. The XRF error values reported in Table 4 are the square root of the sum of the squared accuracy and precision values. The values of quadrature RMSE for MER APXS and laboratory XRF are factors of ~3 and ~15 lower, respectively, than the values for PLS2 for the igneous rocks test set .

In comparing the remote LIBS RMSE values to the contact APXS and laboratory XRF values it should be emphasized that the LIBS measurements in this study were made at the maximum ChemCam standoff distance of 7 m with an integration time of 5 seconds per spot and

5 spots per target. In one hour (the minimum time required to obtain an optimized MER APXS analysis) a ChemCam experiment could analyze 240 spots. Additionally, the ChemCam spectrometers have significantly higher signal to noise ratio than the spectrometers used in this study.

Based solely on quadrature RMSE, PLS2 is the preferred method for LIBS analysis of our rock slabs, for both the full test set and the igneous rocks test set (Table 4). PLS2 predicts the concentration of SiO_2 with the least error (4.88 and 3.08 wt. %, respectively). If an emphasis is not placed on minimizing the RMSE for SiO_2, PLS2 Ave, and PLS1 FS, PLS1 FS Ave, and MLP perform well. In particular, PLS1-FS-Ave has the smallest RMSE for 5 of the major elements (TiO_2, Fe_2O_3, MnO, Na_2O and K_2O). In general, the ANN-based methods (MPL ANN and CC ANN) perform comparably or slightly worse than the PLS-based methods (Table 4). Despite its poor performance for SiO_2, feature selection performed well for other elements using only 5 out of 6117 channels in the spectrum per element (0.08% of the available input data). Feature selection appears to be more effective when applied with spectral averaging than without. We speculate that this is because, with only five input variables rather than 6117, noise in those variables has a more pronounced effect on the resulting prediction. By averaging, the effects of noise are reduced while the advantages of feature selection are preserved. PLS1 with feature selection and averaging appears to be more robust for samples with compositions that differ significantly from the training set, but showed no advantage over other methods when the test set was restricted to igneous rocks.

Training with averaged spectra did not make a statistically significant difference for PLS, but the performance of MLP ANN for Al_2O_3, MgO, CaO and K_2O was significantly worse for

Table 4: Summary of RMSEs[1] for each major element for each combination of method, preprocessing and training and test sets.

Method	SiO_2	TiO_2	Al_2O_3	Fe_2O_3	MnO	MgO	CaO	Na_2O	K_2O	Quadrature RMSE	Lowest RMSE	Equiv. to Lowest Oxide RMSE
Rock Slabs: Full Training Set and Full Test Set												
PLS2	**4.88**	1.07	4.14	5.46	0.51	2.93	**1.67**	1.51	1.44	**9.4**	2	5
PLS2 Ave	6.13	0.82	4.55	5.96	0.51	2.68	2.31	1.25	1.74	10.6		8
PLS1 FS	7.79	0.88	4.49	5.25	0.50	2.44	2.19	1.33	0.93	11.1		7
PLS1 FS Ave	7.58	**0.61**	4.60	**4.82**	**0.49**	2.37	3.15	**1.06**	**0.87**	10.9	5	7
MLP ANN	6.12	1.42	**3.77**	6.05	0.51	3.83	2.92	1.31	1.05	10.8	1	6
MLP ANN Ave	7.89	0.80	6.80	5.83	0.50	7.04	6.53	1.52	2.00	15.6		3
MLP ANN FS	8.49	1.24	3.84	6.28	0.51	**2.04**	2.53	1.37	1.03	11.9	1	6
MLP ANN FS Ave	10.02	0.79	5.62	5.37	0.51	5.07	4.96	2.24	2.15	14.9		3
CC ANN	9.21	1.68	5.23	6.35	0.53	2.88	3.35	1.88	1.83	13.5		2
CC ANN Ave	10.08	0.93	6.21	5.63	0.57	4.06	3.88	3.21	2.18	14.8		2
CC ANN FS	8.14	0.93	6.52	5.33	0.52	4.44	2.12	1.35	2.90	13.1		4
CC ANN FS Ave	7.95	0.97	4.74	4.92	0.51	2.51	2.43	1.68	0.89	11.3		5
Full Training Set and Test Set Excluding Geostandards												
PLS2 (Slabs)	5.49	1.22	5.81	6.88	0.65	4.06	1.99	1.82	1.74	11.8		
PLS2 (Powders)	4.34	0.70	4.05	6.92	0.64	3.50	2.27	0.70	1.97	10.3		
Rock Slabs: Full Training Set and Igneous Rocks Test Set												
PLS2	**3.07**	0.87	2.36	2.20	0.08	1.74	**1.14**	0.85	0.81	**5.1**	2	8
PLS2 Ave	3.86	0.57	2.81	2.50	0.08	2.27	1.14	**0.66**	0.95	6.1	1	5
PLS1 FS	5.13	0.74	2.56	2.65	0.08	1.49	1.73	0.90	0.74	6.9		6
PLS1 FS Ave	4.82	**0.37**	2.81	2.26	**0.07**	1.67	1.71	0.71	0.73	6.6	2	6
MLP ANN	3.19	1.47	**2.00**	**2.15**	0.09	3.19	2.04	1.16	0.78	6.1	2	5
MLP ANN Ave	5.06	0.63	4.20	2.66	0.08	3.67	2.90	1.14	1.08	8.7		2
MLP ANN FS	6.40	1.15	2.41	3.41	0.08	**1.41**	1.82	0.81	0.72	8.1	1	5
MLP ANN FS Ave	4.92	0.67	3.77	2.84	0.09	4.00	3.77	2.18	1.35	9.1		2
CC ANN	6.38	1.23	2.79	3.42	0.10	1.75	2.62	1.47	0.91	8.6		3
CC ANN Ave	5.64	0.74	3.93	2.89	0.16	2.20	2.65	2.18	1.30	8.6		1
CC ANN FS	5.03	0.78	2.93	2.67	0.08	2.64	1.85	0.73	0.70	7.3		4
CC ANN FS Ave	5.77	0.81	3.69	2.66	0.08	1.55	1.95	0.69	**0.65**	7.9	1	5
Full Training Set and Igneous Rocks Test Set Excluding Geostandards												
PLS2 (Slabs)	2.02	0.88	2.66	2.80	0.10	1.83	1.25	0.89	0.87	5.1		
PLS2 (Powders)	3.16	0.46	2.70	2.81	0.09	2.06	1.77	0.60	0.77	5.8		
Tucker *et al.* (2010)[2]	3.13	0.57	1.85	1.73	0.03	2.13	1.41	0.77	0.62	4.9		
Other Instrumental Methods[3]												
MER APXS	1.35	0.21	0.72	1.23	0.02	1.33	0.43	0.35	0.06	2.4		
XRF	0.28	0.02	0.12	0.21	0.01	0.10	0.03	0.12	0.01	0.4		

[1]Units for oxide RMSEs are wt. %. Quadrature RMSE is the result of adding oxide RMSEs in quadrature.

[2]Data listed here are from Row 5 of Table 1 in Tucker *et al.* (2010). See text for discussion.

[3]APXS errors derived from Gellert *et al.* (2006). XRF errors based on values at http://www.fandm.edu/earth-and-environment/precision-and-accuracy.

FS: The model was generated using the intensity at 5 channels selected by genetic algorithm; Ave: Training spectra were averaged.; Shaded cells are statistically equivalent (p-value >5%) to the most accurate method for that column.

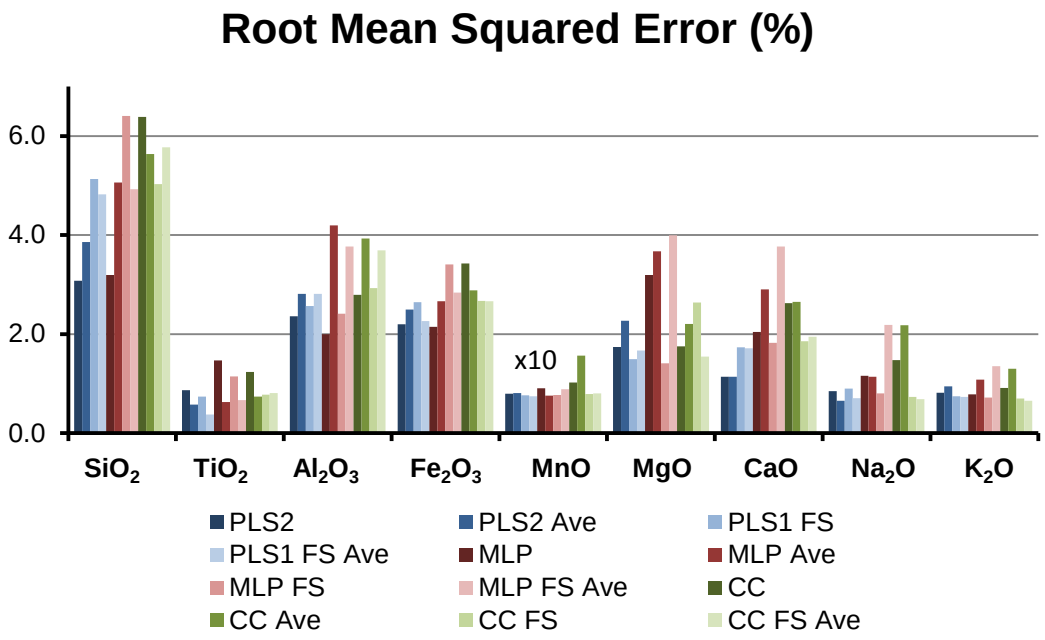

Figure 11: A graphical summary of the RMSE values for igneous rocks in the test set reported in Table 4. All oxide RMSEs are in wt. %. RMSEs for MnO are multiplied by 10.

both the full spectrum and with feature selection when spectral averaging was applied.

However, averaging appears to have been beneficial for predicting TiO_2, reducing the RMSE for PLS2 from 1.07 wt. % to 0.82 wt. % and reducing the RMSE for MLP and CC by 0.6 wt. % and 0.8 wt. % respectively (using the full test set; Table 4). This may be because the titanium lines in the individual training spectra were only slightly above the noise, so reducing the noise by averaging improved performance. For most elements (SiO_2, Al_2O_3, MgO, CaO, Na_2O, K_2O, and MnO), averaging decreased the performance of CC when the full spectrum was used, although the change in RMSE was only significant for MgO, Na_2O and TiO_2.

The vertical black lines in Figs 7, 8, 9 and 10 indicate the "typical" range of compositions observed by APXS on MER, defined as ±1 standard deviation from the median[160–162]. An important observation from these figures is that the compositional range of our samples does not strongly overlap the range for the MER samples. To optimize quantitative LIBS on Mars with

the ChemCam instrument, a Mars-like training set should be developed based on laboratory LIBS measurements of martian meteorites and synthetic Mars-like compositions.

6. Effects of Rock Grain Size and Representative Sampling for LIBS

To obtain chemical compositions that are characteristic of bulk material with LIBS, representative sampling of the target material must be done. This is particularly important for the ChemCam instrument on MSL because it will provide the only quantitative chemical composition for samples that are otherwise inaccessible or for which there is not enough time to use APXS, CheMin or SAM for a detailed analysis. For the LIBS technique, an important consideration is the diameter of the laser beam compared to the scale of target heterogeneity. For example, if the target is homogeneous on a scale small compared to the beam diameter, a representative analysis is possible even for one analysis spot. One common approach (*e.g.* [49], [52], [133]) used to obtain representative targets for laboratory LIBS analysis is to grind a representative volume of a heterogeneous material to a fine powder and make a pressed powder target from a portion of that powder.

The majority of rock slab targets in this study are heterogeneous on the scale of the laser beam diameter (~490 μm) and the heterogeneity can vary from element-to-element. For example, in a gabbro, an enstatite grain and a labradorite grain can have similar SiO_2 concentrations (59 wt. % and 56 wt. % respectively) but dissimilar MgO (~40 wt. % and ~0 wt. % respectively) and Al_2O_3 (~0 wt. % and ~30 wt. % respectively) concentrations.

The LIBS spot size is small enough to analyze individual grains in some targets. This provides more detailed information about the spatial variation in the target composition than bulk analysis methods. To obtain representative compositions using LIBS from samples that are heterogeneous on the scale of the laser beam diameter, it is necessary to collect LIBS spectra

from a sufficiently large number of analysis spots, where the required number of spots is governed by the grain size of the rock. We collected spectra from 5 spots per analysis for every rock slab target in this study, but this number may not have been sufficient to obtain representative analyses for all rocks. Below, we investigate the relationship between representative sampling with LIBS and rock grain size in three ways. We first compare values of RMSE as a function of rock grain size for our standard 5-spot analyses. Next we determine values of RMSE as a function of number of analysis spots for the same target. And finally, we compare RMSEs for the rock slabs to corresponding values for LIBS measurements made on their fine powders. For LIBS on MSL (ChemCam) it will be important to understand the relationship between representative sampling and the number of analysis spots so that appropriate trades can be made between available power, time and data volume.

6.1 RMSE and Rock Grain Size

We divided the rock slabs of basaltic to basaltic-andesitic composition (SiO_2 45-57 wt. %, K_2O+Na_2O 0-6 wt. %) into three groups on the basis of grain size. LOI was not used to restrict this sample set, but the highest volatile content for rocks within this set was still relatively low (~3 wt. %).

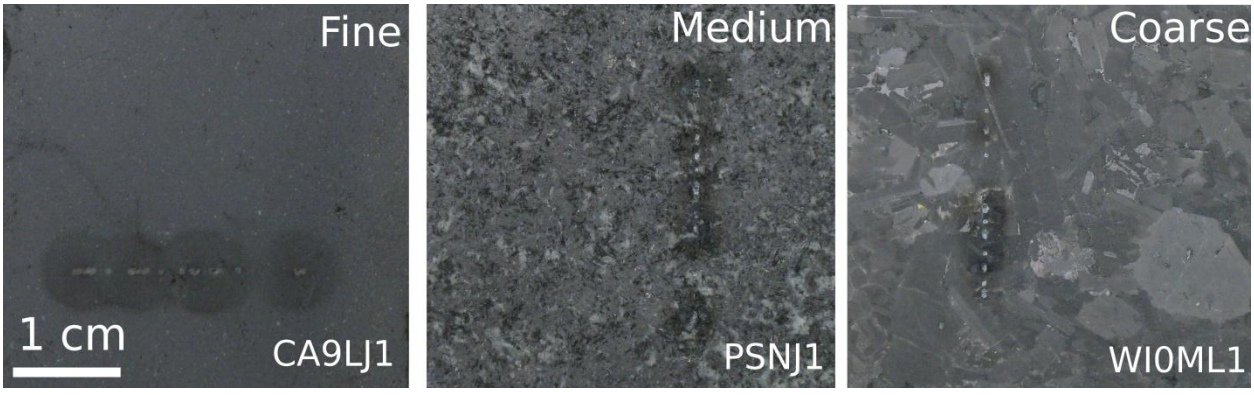

Figure 12: From left to right, examples of fine-grained, medium-grained and coarse-grained rock slab samples used in the grain size study. All three images are shown at the same scale, and the laser ablation spots are visible as small white points surrounded by a discolored halo from the LIBS plasma.

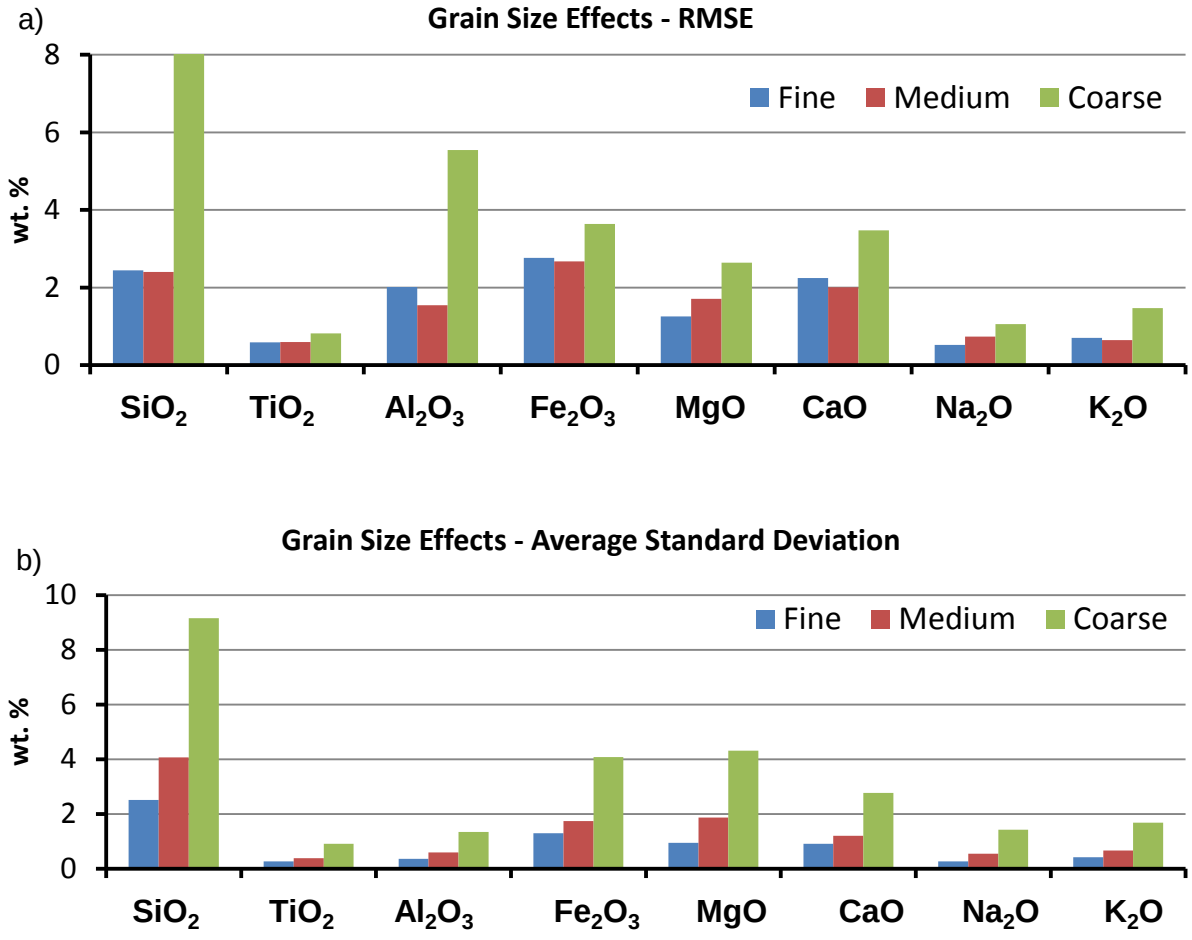

Figure 13: Charts showing (a) RMSE and (b) average standard deviation for major oxide predictions of samples with varying grain size.

Our investigation was concerned with overall trends with grain size, rather than a precise quantitative determination of the grain size. We therefore did not apply a rigorous quantitative method to determine the exact grain size statistics of each sample, and the grain sizes discussed below should be regarded as approximate. The samples were sorted qualitatively based on their apparent grain size, and then assigned to three groups. Limits on the grain sizes for each group were determined by manually measuring grains in high-resolution digital photographs of the samples. Group 1 had typical grain sizes of <1 mm, Group 2 had typical grain sizes of 1-2.5 mm, and Group 3 had typical grain sizes >2 mm. A representative member from each group is shown

in Figure 12. The diameter of the laser pit is on the order of ~490 μm, meaning that the laser beam diameter is not necessarily larger than the grain size even for some of the finest-grained rock slabs.

We trained a PLS2 model on the silicate rock pressed powder geostandards using the full spectrum without averaging and predicted the composition for groups 1, 2, and 3. The RMSE was larger for the coarsest-grained (Group 3) samples than for the finest-grained (Group 1) and intermediate-grained (Group2) samples for all major elements (Figure 13). The RMSE for Group 2 samples was lower than the RMSE for Group 1 samples in some cases but was higher in others.

In addition to the RMSE for each element, we also calculated the standard deviation of the five predictions (one per LIBS analysis spot) for each sample. The standard deviation is a better measure of representative sampling than RMSE because the former is independent of the XRF-derived composition. The average standard deviation shows a clear trend with grain size, with the average standard deviations increasing with increasing grain size (Figure 13).

6.2 RMSE and Number of Analysis Spots

Although each individual rock slab sample in our study was analyzed in 5 spots, several slabs in each grain size group were cut from the same parent rock, resulting in a larger effective number of analysis spots. This allowed us to investigate the effect of the number of spots analyzed on the accuracy of the resulting predictions. We used the same PLS2 model as in the preceding section (Section 6.2) to predict the sample composition based on the spectrum from each spot and then calculated the average prediction and the standard deviation for every unique combination of individual spots, resulting in a distribution of possible predictions for each number of spots.

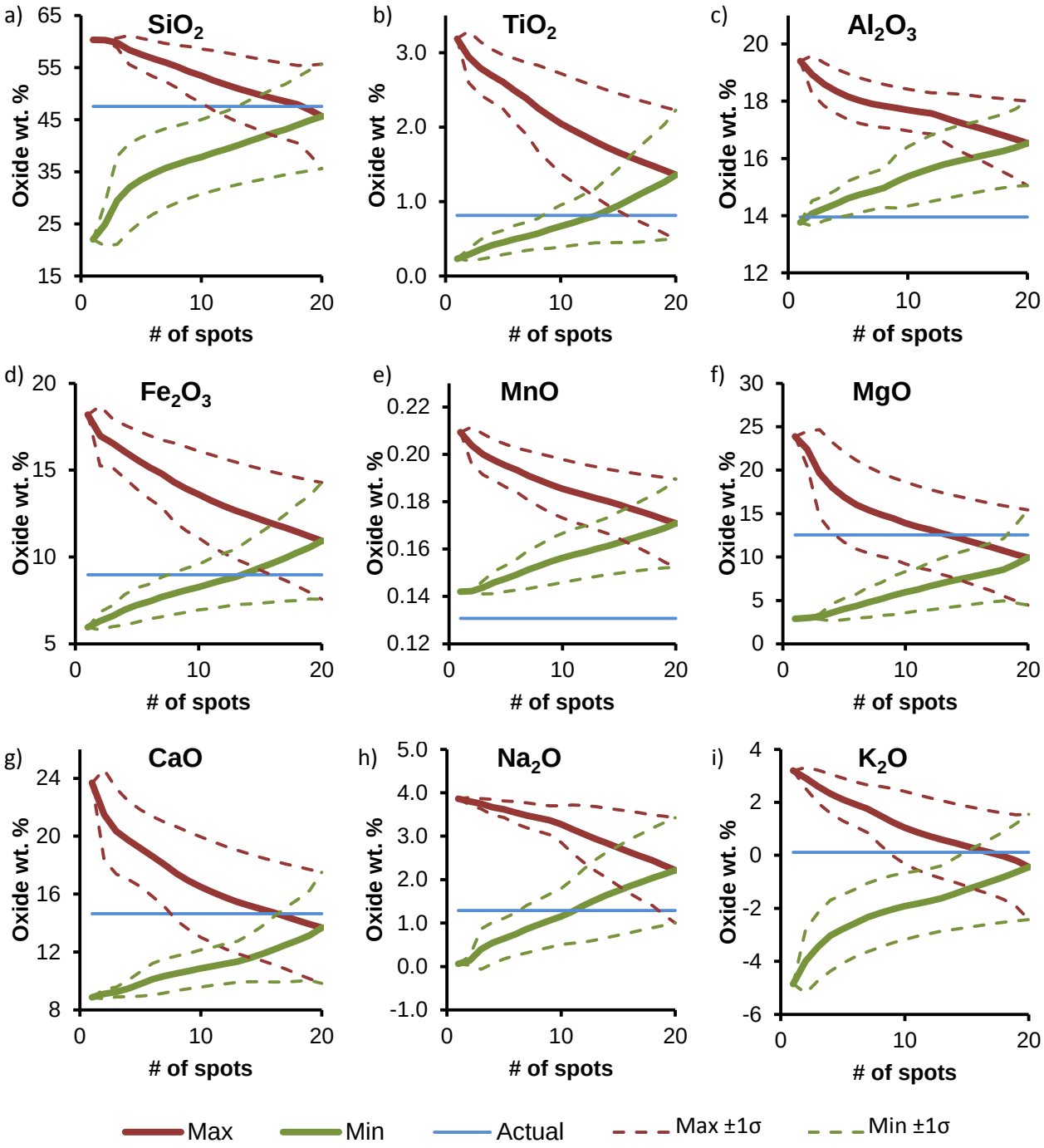

Figure 14: Plots of the maximum and minimum predictions in the distribution of possible PLS predictions for all combinations of *n* spots on a coarse-grained xenolith sample, with *n* ranging from 1 to 20. When only a small number of spots are considered, the range of possible predicted values can be quite large due to the influence of single points that differ significantly from the majority of other points. As *n* approaches 20, the maximum and minimum possible predictions converge to the average of all of the individual predictions. Dashed lines indicate the uncertainty in each prediction, and the horizontal black line marks the actual composition. When the true composition is within the error bars for both the maximum and minimum possible predictions, the analysis is considered to have converged accurately. Note that Al and Mn were poorly predicted for this sample, and did not converge on the true composition after 20 spots.

Table 5: Number of laser analysis spots required to converge on the actual composition for rocks with fine, medium and coarse grain sizes.

	Major Element (wt. %)									Number	
Parent Rock	SiO_2	TiO_2	Al_2O_3	Fe_2O_3	MnO	MgO	CaO	Na_2O	K_2O	Slabs	Spots
Fine-Grained Rocks											
AZFJS201					10	10	10	8		2	10
WIME101	4	4				4			5	1	5
HWMK124				9			8	8		2	10
HWMU574-170				5	5					1	5
CA9LJ1	3									1	5
CRBSW1	10					9			7	2	10
CRBSW1[1]	4	5	5	5		5	5	4	4	1	5
CA9VA1	5	5			4		4	5	4	1	5
KICCA1	10					15	7	13	11	3	15
Average	*6.0*	*4.7*	*5.0*	*6.3*	*6.3*	*8.6*	*6.8*	*7.6*	*6.2*	-	-
Medium-Grained Rocks											
AZSC201	9	8	6	10				8	5	2	10
HWHL100	7		7	7	9	6			10	2	10
MU80-41	8					8	9	8	10	2	10
MASEX1	4		4	4		5	3	5	5	1	5
CA9LVNP1	5	5		5		5	5		5	1	5
CA9WRN1	8			9	5		9	10	9	8	10
PSNJ1	14	14		14		13	13	15	13	3	15
CP-5		13								3	15
Average	*7.9*	*10.0*	*5.7*	*8.2*	*7.0*	*7.4*	*7.8*	*9.2*	*8.1*	-	-
Coarse-Grained Rocks											
WD123				4		5		2	5	1	5
BSTQBC1	4					5	5	4		1	5
HWMK9R-30A	13	16		16		19	17	19	15	4	20
WI0ML1		18		20		20	17			4	20
MU80-03A								4		1	5
MCCSG20	16	13		16		16	18	17	21	5	24[2]
LDNVA5	5					5	4	5	5	1	5
MU80-37B	5	4	5	5		5	5	4	3	1	5
Average	*8.6*	*12.8*	*5.0*	*12.2*		*10.7*	*11.00*	*7.9*	*9.8*	-	-

[1] This sample is repeated because two XRF analyses, yielding slightly different compositions, were conducted on this rock.
[2]One spectrum was excluded because of low signal to noise.

We then found the maximum and minimum of the distribution of possible predictions for each number of spots and their corresponding standard deviations. For small numbers of spots, some combinations result in very high or low predictions (represented by the red and green lines in Figure 14), while other combinations of spots are more representative of the bulk rock. As the number of spots averaged together increases, the maximum and minimum predictions become less extreme, until eventually the predicted value for all possible sets of spots converges on the average of the individual predictions. This is shown in Figure 14 for 20 analysis spots on 4 slabs of the same parent xenolith from grain size group 3. The prediction is considered to have converged accurately if the actual composition is within the 1σ uncertainties for both the

maximum and minimum possible predictions. Based on our samples, it appears that five to 10 spots should be used when analyzing coarse-grained samples, and that 15 or more points are desirable to ensure representative sampling. This is consistent with the findings of [51] that 10-15 spots were sufficient for estimating the bulk composition of a coarse-grained martian meteorite.

Table 5 shows the number of spots required for the predicted composition to converge to within one standard deviation of the true (XRF-derived) composition for each sample and major element. Cases where the LIBS prediction did not converge on the true composition are left blank in the table. For most elements, the average number of spots required for accurate predictions of each major element was lowest for Group 1 samples and highest for Group 3 samples. The required number of spots averaged across all major elements and rounded to the nearest whole number was six for Group 1, eight for Group 2, and 10 for Group 3. The Group 3 samples are strongly bimodal, with some samples converging relatively rapidly, and others requiring >15 spots to converge on the correct composition.

It should be noted that our results may be biased because there were more rocks in Group 3 with a large number of analysis spots. A more thorough study of the number of spots required for representative sampling of coarse-grained rock composition, using a large, uniform number of spots for all samples, is necessary. However, the number of spots required for convergence for a given sample is independent of the number of spots that are analyzed. The presence of several coarse-grained samples for which the predicted composition does not converge on the true composition until 15-20 spots are analyzed suggests that it is prudent to analyze at least 15 spots on coarse-grained targets for accurate results.

An additional limitation of our grain size study is that the heterogeneity of the grains was not considered. A coarse-grained sample with grains of uniform composition could theoretically be accurately characterized based on only one spot. Because our reference compositions were for the bulk rock, we cannot group the samples based on compositional homogeneity. However, many of the slab samples in our study appear to be compositionally heterogeneous based on visual variations in their grain properties, and given that they are primarily igneous rocks this is likely to be the case. Therefore our recommended number of analysis spots may be higher than strictly necessary for more homogeneous rocks. Additional work using samples with known degrees of heterogeneity is needed to fully investigate this issue.

6.3 Comparison of RMSE for Rock Slab and Pressed Powder Samples

To directly investigate the difference between LIBS analyses of homogeneous pressed powder samples and natural rock slab samples, we crushed ~10 g of the same parent rocks as the slabs used in our training and test sets and collected the LIBS spectra of the powders. LIBS spectra of the powdered training set samples were used to train a PLS2 model for the major elements. The model was then tested on the spectra of the powdered test set samples and the resulting predictions were compared with the results from the rock slab analysis (Table 4). Geostandards were excluded from the slab and powder test sets for this comparison so that the results were only based on predictions of the geologic samples and corresponding powders. The RMSEs for powders were lower than the full-test-set RMSEs for slabs for most of the major elements. When only igneous rocks were considered, the slab and powder results were similar. SiO_2, MgO and CaO predictions were more accurate with igneous rock slabs, but TiO_2, Na_2O, and K_2O were more accurate with igneous rock powders. Predictions of Al_2O_3, Fe_2O_3 and MnO were essentially the same for igneous rock slabs and powders.

Tucker *et al.* [52] used LIBS to analyze a suite of 100 pressed powder samples derived from the <45 μm size fraction of igneous rocks. In Table 4, we include data from Tucker *et al.* ([52]; Table 1, Row 5) for comparison with our igneous slab and powder predictions. Row 5 was chosen because it most closely corresponds to the calculation procedure we employed (PLS2 using element atomic fractions). Given that the powders used by Tucker *et al.* [52] are finer than the powders used in this study (<45 μm versus ~90 μm) and that Tucker *et al.* [52] scaled the element atomic fractions by their respective standard deviations prior running PLS2, the values of RMSE obtained for the two suites of igneous rock powders are in satisfactory agreement.

We plotted our PLS2 predictions for the pressed-powder and rock slab samples and the XRF-measured bulk compositions on TAS plots to visualize the ability of quantitative LIBS to classify samples from predictions of SiO_2, K_2O and Na_2O concentrations (Figure 15). The data plotted in the figure show that the accuracy of our LIBS analyses for the pressed-powder and rock slab samples is not always sufficient to correctly classify the samples according to the TAS scheme. This suggests that a multivariate classification method such as Soft Independent Modeling by Class Analogy (SIMCA)[49]or Independent Components Analysis (*Cousin et al.*, 2011) is preferable for LIBS rock identification. The accuracy of LIBS analyses and therefore the accuracy of classification using the TAS plot can be improved by careful selection of the training set. For example, Tucker *et al.* [52] (Table 1) were able to lower their 1σ error for SiO_2 from 2.18-3.66 wt. % (depending on method) to 1.52 wt. % by splitting the training and test sets according *a priori* knowledge of the SiO_2 abundance in the samples.

The error reported by Tucker *et al.* [52] for SiO_2 using the split training set (1.52 wt. %) is comparable to the error associated with the MER APXS instrument (1.35 wt. % Table 4). To achieve similar accuracy for unknown samples (*e.g.* targets analyzed by ChemCam on Mars)

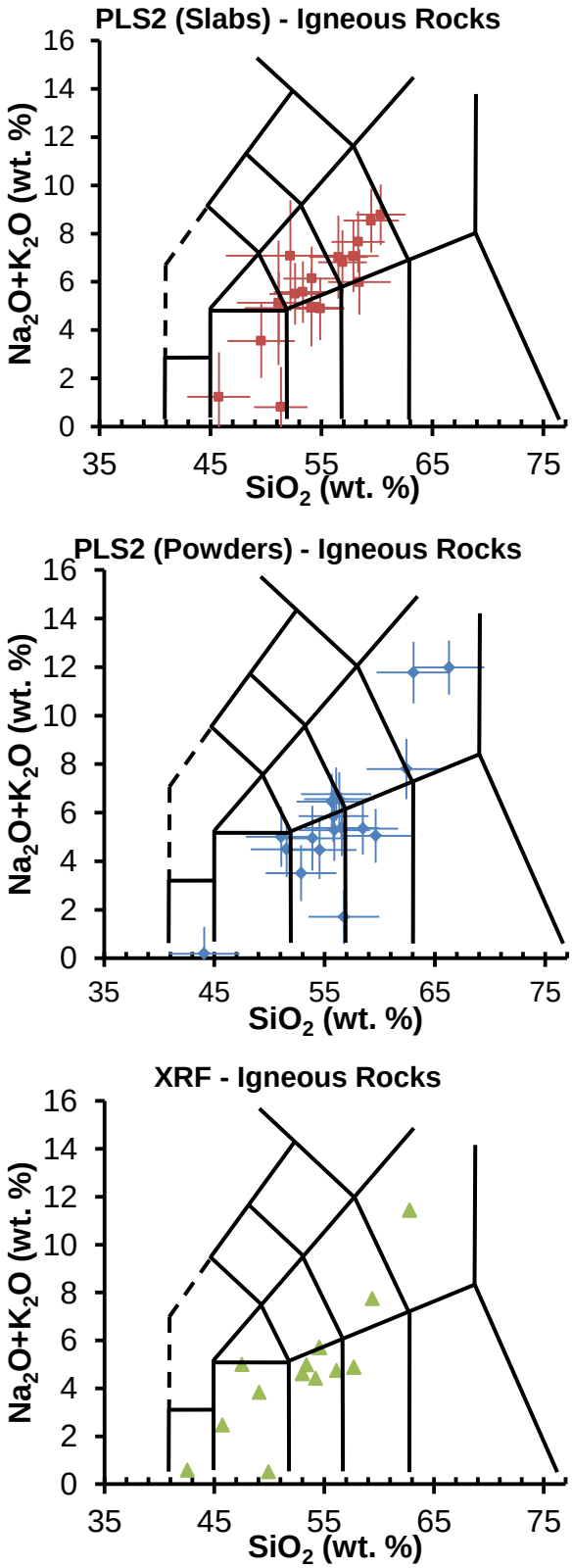

Figure 15: Total alkali (Na_2O+K_2O) *vs.* silica (SiO_2) plots for chemical data derived from (a) LIBS analysis of igneous rock slabs PLS2 analysis method, (b) LIBS analysis of pressed-powders of the same igneous rock slabs, and (c) XRF analysis of the same igneous rocks. Error bars are based on the standard deviation of predictions for each sample, added in quadrature with the RMSE from Table 4.

procedures must be developed to constrain selection of training sets without *prior* knowledge of the target composition. Qualitative methods such as PCA (Section 4) or SIMCA may serve as a first step in grouping similar training and test samples prior to quantitative analysis. Additionally, iterative use of PLS2 in which the results of an initial model are used to split the samples into smaller subsets may improve the accuracy without requiring prior knowledge of the test set.

7. Summary

We analyzed a compositionally and mineralogically diverse set of geologic rock-slab and pressed-powder samples with a stand-off LIBS system similar to the ChemCam instrument on MSL. PCA was used to visualize the spectral diversity of the dataset without calculation of chemical compositions. Three multivariate methods (PLS, MLP ANN, and CC ANN) were used to calculate chemical compositions from LIBS spectra with and without the preprocessing steps of averaging the training spectra and applying feature selection (Table 4).

PLS2 without spectral averaging had the best overall performance (*i.e.* lowest quadrature RMSE) for both the full test set and the igneous rocks test set. The error in SiO_2 concentration, which is particularly important for analysis of silicates, was lowest for PLS2 compared to all other methods (Table 4). In general, the ANN-based methods did not improve over PLS-based methods, suggesting that the LIBS spectra of our samples did not exhibit significant nonlinearities.

The average number of analysis spots on the rock slabs required for accurate predictions increased with grain size from ~6 analysis spots for finer-grained rocks to ~10 for coarser-grained rocks. Several coarser-grained rocks required 20 or more analysis spots to achieve a representative bulk chemical composition. Our comparison of predictions for finer-,

intermediate- and coarser-grained rocks showed that the precision of the predictions decreased with increasing grain size for all major elements and the accuracy for finer- and intermediate-grained samples was better than the accuracy for coarser-grained samples. The accuracy and precision of pressed powder and rock slab samples gave similar results, with improved accuracy and precision for most major elements when analyzing homogeneous powders, although in some cases the rock slab results were more accurate.

If data volume and/or computation time are factors for chemical analyses by LIBS, feature selection and/or spectral averaging can be employed, with some decrease in accuracy relative to PLS2 for some elements (Table 4). The most accurate methods involving feature selection and/or averaging are PLS2 Ave and PLS1 FS Ave, and a combination of feature selection and averaging often resulted in lower errors than either pre-processing step alone. Reduction in data volume and/or computation time will likely be important during MSL operations of the ChemCam instrument. Very small data products, comprising a pre-selected subset of the full ChemCam spectrum, can be stored, transmitted to Earth and used to estimate the composition of a target even in cases with limited downlink or onboard memory availability. Additionally, PLS or other methods require significantly less time to generate a model when feature selection is used, allowing rapid interpretation of the data, and our results indicate that PLS1 with feature selection and averaging may be more accurate at predicting the composition of samples that are very different from the training set.

When data volume is not restricted, we recommend using the full LIBS spectrum for analyses, but if available data is limited or there is reason to suspect that the target may be significantly different from the training set, feature selection should be considered. If automatic feature selection is used, the selected spectral channels should be examined to ensure that they

correspond to the element of interest. If they do not, then manual feature selection or a larger number of automatically-selected channels may give better results. We recommend further investigation of feature selection for LIBS to better understand its potential benefits and to minimize sources of error.

Our chemical analyses of terrestrial rock slabs by LIBS point to several ways to optimize quantitative LIBS on Mars with the MSL ChemCam instrument by improving the selection of training samples. Initial work on this topic by [165] suggests that a statistical method of training set selection is needed to improve LIBS analyses. Clustering, classification methods, or iterative application of PLS-based methods could be used to group spectrally similar samples in the training and test sets. If it is possible to group compositionally similar samples prior to analysis, then geochemical correlations in the training set are more likely to be applicable to the test set, resulting in more accurate predictions. This is particularly important when feature selection is used because the information available to the algorithm is reduced. Alternatively, a very diverse training set containing many different sample types may result in more accurate predictions of unknown samples because the correlations identified would be more broadly applicable to all sample types.

Another way to improve quantitative LIBS on Mars is to develop training sets that have chemical compositions appropriate for the martian surface, such as synthetic glasses with bulk chemical compositions identical to martian meteorites and martian surface materials as measured *in situ* by the Mars Pathfinder and MER APXS instruments. Future work will also expand our multivariate analyses to the full suite of rock slab samples to test the performance of quantitative LIBS on volatile-bearing and highly altered rocks, focusing particularly on rock and mineral types relevant to the MSL landing sites.

Acknowledgements

This work was supported by the NASA Graduate Student Researchers Program, by the Mars Program Office through MSL, and by the NASA Johnson Space Center. We thank Suniti Karunatillake for helpful discussions of statistical significance testing and Roger Jarvis for assistance with the PYCHEM software.

CHAPTER 4

CLUSTERING AND TRAINING SET SELECTION METHODS FOR IMPROVING THE ACCURACY OF QUANTITATIVE LASER-INDUCED BREAKDOWN SPECTROSCOPY[3]

0. Abstract

We investigated five clustering and training set selection methods to improve the accuracy of quantitative chemical analysis of geologic samples by laser induced breakdown spectroscopy (LIBS) using partial least squares (PLS) regression. The LIBS spectra were previously acquired for 195 rock slabs and 31 pressed powder geostandards under 7 Torr CO_2 at a stand-off distance of 7 m at 17 mJ per pulse to simulate the operational conditions of the ChemCam LIBS instrument on the Mars Science Laboratory Curiosity rover. The clustering and training set selection methods, which do not require prior knowledge of the chemical composition of the test-set samples, are based on grouping similar spectra and selecting appropriate training spectra for the partial least squares (PLS2) model. These methods were: (1) Hierarchical clustering of the full set of training spectra and selection of a subset for use in training; (2) *K*-means clustering of all spectra and generation of PLS2 models based on the training samples within each cluster; (3) Iterative use of PLS2 to predict sample composition and *k*-means clustering of the predicted compositions to subdivide the groups of spectra; (4) Soft independent modeling of class analogy (SIMCA) classification of spectra, and generation of PLS2 models based on the training samples within each class; (5) Use of Bayesian information criteria (BIC) to determine an optimal number of clusters and generation of PLS2 models based on the training samples within each

[3] This chapter has been submitted for publication in the journal Spectrochimica Acta Part B: Atomic Spectroscopy, and is currently in review: R.B. Anderson, J.F. Bell, R.C. Wiens, R.V. Morris, S.M. Clegg, Clustering and Training Set Selection Methods for Improving the Accuracy of Quantitative Laser Induced Breakdown Spectroscopy, Spectrochimica Acta Part B: Atomic Spectroscopy. Submitted (2011).

cluster. The iterative method and the *k*-means method using 5 clusters showed the best performance, improving the absolute quadrature root mean squared error (RMSE) by ~3 wt. %. The statistical significance of these improvements was ~85%. Our results show that although clustering methods can modestly improve results, a large and diverse training set is the most reliable way to improve the accuracy of quantitative LIBS. In particular, additional sulfate standards and specifically fabricated analog samples with Mars-like compositions may improve the accuracy of ChemCam measurements on Mars. Refinement of the iterative method, modifications of the basic *k*-means clustering algorithm, and classification based on specifically selected S, C and Si emission lines may also prove beneficial and merit further study.

1. Introduction

1.1 Laser-Induced Breakdown Spectroscopy

Laser induced breakdown spectroscopy (LIBS) is an analytical technique that uses intense laser pulses to ablate target material and form a plasma. The emission spectrum of the plasma is then collected and analyzed to classify the target material and to determine its elemental composition[166]. LIBS can be used in-situ or at stand-off distances of many meters. The ChemCam instrument on the Mars Science laboratory (MSL) rover "Curiosity" will be capable of collecting LIBS spectra up to 7 meters away from the rover [44].

The ability to conduct a chemical analysis at a distance is a significant advantage for LIBS over other methods on a planetary mission like MSL because targets of interest may not be accessible by the robotic arm. ChemCam also serves a valuable tactical role, interrogating targets from a distance prior to committing the rover to a multi-day analysis campaign using the arm-mounted instruments. The synergy of ChemCam and APXS is particularly important. Rapid ChemCam analyses can be followed up with more sensitive APXS measurements. Comparison

of the elemental chemistry results from two independent methods and the ability to detect light elements and conduct limited depth profiling with LIBS will provide a more complete understanding of the target composition.

In this study, we build on our previous work [54] and explore methods for improving the accuracy of quantitative LIBS by grouping the spectra prior to PLS analysis. For this grouping to be useful in applications with truly unknown samples, such as ChemCam operations on Mars, it must be shown to be effective without using prior knowledge of the test set sample composition. Our data set comprises LIBS spectra that were acquired with a laboratory experiment designed to simulate ChemCam for 195 rock slabs and 31 pressed powder geostandards under Mars-like atmospheric conditions [54].

1.2 Quantitative Methods

Deriving quantitative compositional information from LIBS spectra has been an important goal since the technique was first conceived. Early studies used the peak intensity or area of selected emission lines in the spectra of several samples to create a linear regression between the LIBS emission line and the abundance of the emitting element. This type of univariate calibration met with limited success [51], partly because the relationship between LIBS emission line intensity and elemental abundance is typically complicated by matrix effects such as laser-to-sample coupling efficiency, self-absorption, trace element abundances, etc. [49].

Multivariate methods that use information from the entire spectrum rather than a single emission line have been shown to yield more accurate results for major element abundances [49], [52], [54]. The most commonly used quantitative multivariate method for LIBS analysis is Partial Least Squares (PLS). Although in some cases nonlinear methods such as artificial neural networks have proven more accurate than PLS [127], PLS is generally the most accurate method

for the analysis of typical geologic materials [54]. Feature selection methods such as genetic algorithms, which reduce the number of spectral channels used in calculations, can improve the results in some cases [54], but all analyses in this paper use the full LIBS spectrum. In this work, we use the PLS2 algorithm in the Unscrambler v9.8 software package, which is capable of predicting multiple compositions at once. For all PLS2 models, we used the number of principal components recommended by the software, as described by [54] and [52].

Following the procedure in [54], we judged the performance of the PLS2 predictions by calculating the mean predicted composition for each sample based on the five individual spectra of that sample. The predictions were then compared to the known composition of the samples and the absolute root-mean-squared error (RMSE) for each major element oxide was calculated. To summarize the overall performance of each prediction, the RMSE for each of the major element oxides were added in quadrature, resulting in a single "quadrature RMSE" value for each PLS2 prediction.

1.3 Rationale for Clustering

The choice of a training set has a significant influence on the accuracy of quantitative LIBS. Our previous work showed that a PLS model trained on silicate rocks predicted the composition of pure minerals relatively poorly, but the inclusion of several pure mineral samples in the training set significantly improved the results [54]. Additionally, methods such as dividing samples into groups based on silica content have been shown to improve the accuracy of PLS predictions [52]. However, when dealing with unknown samples it is not possible to divide the training and test samples in this way, and [165] showed that even training sets deliberately chosen on the basis of expected geochemical trends do not necessarily improve performance. It has been suggested [165] that instead automated statistical methods could prove more effective

in selecting training sets that result in improved performance. We have implemented several clustering-based methods for training set selection and assessed their influence on the accuracy of LIBS predictions.

2. Sample and Data Set

The dataset analyzed here is the same as that used in [54] and consists of LIBS spectra of 31 powder geostandards [129] and 195 rock slab samples from the Mars analog sample collection at NASA's Johnson Space Center. The major element chemistry was measured independently by X-ray fluorescence (XRF) analyses [54], [130]. Table 1 summarizes the properties of the laboratory set-up, which was designed to be similar to ChemCam.

Table 1: Details of laboratory set-up

Laser	Nd:YAG
Laser wavelength	1064 nm
Pulse frequency	10 Hz
Pulse energy	17 mJ
Stand-off distance	7 m
Sample chamber pressure	7 Torr
Sample chamber atmosphere	CO_2
# of spectrometers	3
Spectrometer type	Ocean Optics HR2000
Total # of spectral channels	6144
UV spectral range	225.00-325.97 nm
VIS spectral range	381.86-471.03 nm
VNIR spectra range	494.93-927.06 nm

Our previous work with this dataset focused primarily on silicate rocks and minerals with loss on ignition (LOI) of <2 wt. %. LOI is a measure of the mass lost when the sample is heated to ~925°C, and typically includes volatiles such as water, CO_2 and SO_3. The present work does not impose any restrictions on composition or LOI of the samples considered. The LIBS plasma brightness varied significantly depending on composition [54], and for the present study we

excluded the 5% of spectra with the lowest total integrated signal, caused by poor sample-to-laser coupling. The total emission intensities for the excluded samples were <3.4 % of the

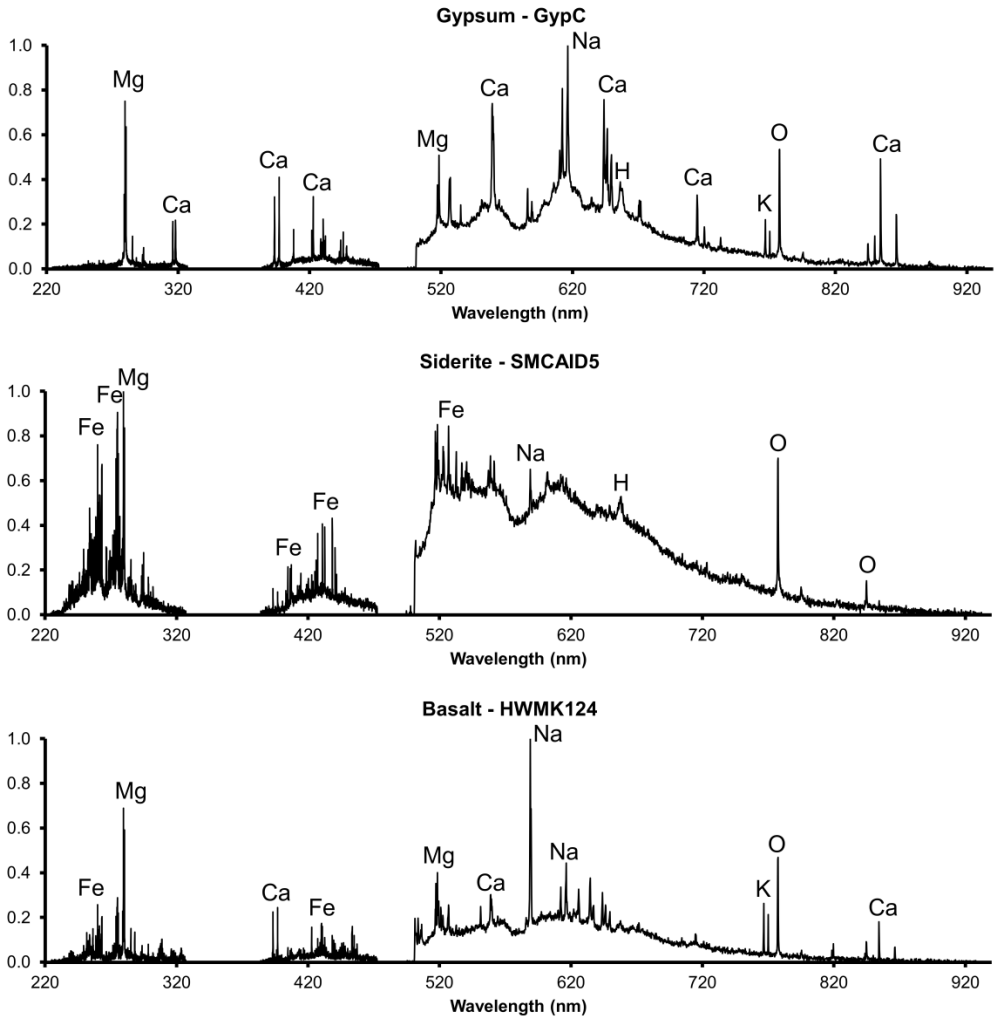

Figure 1: Example LIBS spectra of gypsum, siderite, and basalt. Each spectrum has been normalized to its highest value for ease of comparison, and strong emission lines are labeled.

brightest sample in the training and test sets. Prior to analysis, we followed the practice used in many other LIBS studies [49], [54] and normalized the LIBS spectra so that the sum of the signal across all observed wavelengths was equal to one, reducing the effect of shot-to-shot variations and differences in plasma brightness. Example spectra of basalt, gypsum, and siderite are shown in Figure 1. The spectra in Figure 1 are normalized to their highest values for ease of visual

comparison, but all calculations in this work were done on spectra normalized to the total integrated signal as described above.

Each sample in the full dataset was designated as a training sample or a test sample prior to applying any of the clustering and classification methods discussed in section 3. It has been shown that quantitative LIBS performs better when samples of the types present in the test set are also present in the training set [54]. To ensure that both the training set and test set contained diverse samples, we placed all of the samples into 12 categories based on their known type: carbonates, oxides and hydroxides, high-SiO_2 samples, amphiboles, pyroxenes, olivines, phyllosilicates, igneous silicate rocks, sulfates, sodalite, plagioclases, and "other" samples. Each category was then sorted by SiO_2 content and samples were manually assigned to the training set or the test set. In general, for categories with a large number of samples, one out of four samples was assigned to the test set, while the remaining three-fourths were assigned to the training set. In categories containing less than ten samples, the split between training and test sets was approximately even. Some samples, such as the phosphate collophanite and the synthetic pure Al_2O_3 sample were unique, and were assigned to the training set. All samples from the same source rock (and therefore having the same composition) were assigned so that they were exclusively in either the training or the test set. Table 2 summarizes the sample categories and the training set and test set assignments. Although sample type information was used for this initial division to ensure diversity in both the training set and the test set, the test set sample type information was not used in any of the methods described in section 3. The training set sample type information was only used to define the classes in soft independent modeling of class analogy (SIMCA) method described in section 3.4.

It has been shown that quantitative results can be improved by using PLS1 to predict major element oxide weight percentages rather than atomic fraction [52]. The effect of several different methods of scaling the oxide abundances were also investigated by [52] and they found that dividing the abundance of each major element by that element's standard deviation resulted in more accurate predictions.

We tested several of the scaling methods discussed in [52] by using the full set of training spectra to generate leverage cross-validated PLS2 models with the compositions scaled differently and then predicting all major elements in the full test set. These calculations were done with the sample compositions in the training and test sets expressed as atomic fraction, oxide wt. %, oxide wt. % scaled to the maximum value of each element in the training set ("max scaled"), and oxide wt. % scaled to the standard deviation of each element in the training set ("stdev scaled"). The quadrature RMSE was used to assess the overall performance of each scaling permutation. These values and the RMSE values for each individual element are listed in Table 3. Using unscaled oxides resulted in the lowest quadrature RMSE (20.70 wt. %). Scaling by the standard deviation did improve the accuracy for some elements, but it was detrimental in other cases, particularly for iron which had a RMSE of 19.13 wt. % with standard deviation scaling, but only 9.25 wt. % with unscaled oxides. These results suggested that working in oxide weight percent without scaling is appropriate for our sample set, so all subsequent calculations were done in oxide wt. %.

Table 2: Sample types and training and test set assignments

Test Set			Training Set		
Sample Type	**# of samples**	**Sample Names**	**Sample Type**	**# of samples**	**Sample Names**
			Igneous Rocks		
Andesite	3	CA9WRN1, GBW07104, MO12	Andesite	12	OYCO1, CA9LVNP1, TMGNV1, TMGNV5, CA9LVNP1, AGV2, GBW07110, JA1, JA2
Basalt	4	CHFCO1, CA9LJ1, BCR2, JB3	Basalt	29	688, 2116-81, CP-5, HWMK124, HWMK104, CA9WRN1, BPNTX1-A, HWHL100, AZFJS201, WIME101, HWMU574-170, BHVO2, GBW07105, GUWBM, JB1B, JB2, MO13, MO14
Andesite with quartz	1	SQWCMT1	Sulfur-coated basalt	1	CA9SB1
Basalt & carbonate breccia	2	BRLCOR1	Basalt with carbonate	3	CRBSW1
Diorite	2	LDNVA5, BSTQBC1	Basalt Scoria	4	CA9VA1, KICCA1
Dolerite	3	PSNJ1	Basalt Breccia	3	HWMK745R
Layered Gabbro	2	MU80-41	Layered Gabbro	2	MU80-03A, MU80-37B
Gabbro	6	WD123, MASEX1, WI0ML1	Gabbroic Xenolith	4	HWMK9R-30A
Norite	5	MCCSG20, MCCSG21	Granite	2	LANTX1, GBW07103
Rhyolite	3	CA9KRY1, GBW07113, JR1	Obsidian	2	CA9OB1, CA9OB2
			Syenite	3	SYMPCA5, SYMPCA1
			Trachyte	2	HWHL101
			Rhyolite Tuff	3	BICCA1, BICCA2, BICCA5
			Carbonates		
Siderite	1	SMCAID5	Siderite	1	SIDCL01
Dolomite & Limestone	1	GBW07108	Dolomite & Limestone	7	ILTQ1, AZGW713R, JDo1, GBW07216a, GBW07217a, ATKONT1
Basalt & carbonate breccia	2	BRLCOR1	Dolomitic Oil Shale	3	RFLCO1
			Calcite	4	TXAC1, TXGRF1
			Spurrite	1	MEXUL701
			Oxides/Hydroxides		
Banded Iron Formation	1	WI0BIF3	Banded Iron Formation	2	BIFWM2, WI0BIF1
Chromite	1	MMNMT1	Brucite	1	BRLDN1
Ferricrete	1	6SC-E2	Ferricrete	3	6SC-E2
Magnesioferrite	1	LVSW1	Goethite	2	GTBK3
Hematite	2	HMCL1, HMIR1	Hematite	4	HMRE1, HMIR3
Magnetite	1	MTMA2	Magnetite	4	MTISH1, MTMA3
			Ilmenite	3	ILMKRN5, AREF295
			Titanomagnetite	2	MTLAC1
			High SiO_2		
Silcrete	1	GR820	Flint	1	DCENG1

Banded Iron Formation	1	WI0BIF3	Tridymite & Alunite	1	MNTPNV1
Diatomite	1	LSBCA2			
Chalcedony	1	PMDCDY1			
			Amphiboles		
Hornblende	1	WD129BR	Amphibolite	1	MNMBA1
Anthophyllite	1	WRCA1	Hornblende	3	COBONT5
Grunerite	1	MMMI1			
			Pyroxenes		
Fassaite	1	HLNMT1	Diopside	4	DIHUQ1
Augite	2	HARAG1	Fassaite	1	HLNMT1
Hedenbergite	1	YRLCNV1	Enstatite	1	BAMNOR1
			Augite	1	BRLKCD1
			Olivines		
Olivine & chromite	1	OLTWS2	Olivine & chromite	2	OLTWS3
Olivine	2	DH4912, OLJC1	Olivine	2	DH4909, DH4911
			Phyllosilicates		
Kaolinite & quartz	1	MTMAZ1	Kaolinite	1	WD143
Biotite	1	BITONT1	Serpentinite	1	CA9SRP2
Muscovite	1	MUSSD1	Phlogopite	1	SYONT1
			Fuchsite	1	FUSBZ1
			Sulfates		
Gypsum	2	GypB, GypD	Gypsum	2	GypA, GypC
Alunite	1	WD151			
			Sodalite		
Sodalite	1	MGSDL1	Sodalite	4	MGSDL7
			Plagioclases		
Anorthite & Anorthosite	2	WD228, GSVCA1	Anorthosite	4	MCCSG1, TECNY1
Bytownite	1	CBBYT1	Bytownite	2	CBBYT1, CBBYT5
Labradorite	1	NANLB1			
Other Plagioclase	1	PLAGWM1			
			Other		
Al_2O_3	2	AD998A, AD998B			
Epidote	1	AZGW711R			
Vesuvianite	1	CQRSCA1			
Meionite	1	MEICD1			
Collophanite	1	IDCDA1			
Pyroxmangite	3	MNSCO1, MNSCO2			
Scapolite	1	CHRMX1			
Unknown	1	GSPAUS1			

Table 3: Comparison of RMSE values for each method of scaling composition values.

	SiO_2	TiO_2	Al_2O_3	Fe_2O_3T	MnO	MgO	CaO	Na_2O	K_2O	P_2O_5	SO_3	CO_2	H_2O	**Quadrature RMSE**
Oxides	9.41	4.65	5.57	9.25	1.49	4.21	5.95	1.85	1.01	1.56	8.27	7.37	4.09	20.70
Oxides - Max Scale	10.12	4.72	5.78	13.49	1.72	4.14	6.18	1.86	0.97	1.33	8.20	7.65	4.23	23.41
Oxides - Stdev Scale	10.36	4.47	5.30	19.13	1.20	4.01	6.40	1.80	0.94	1.90	8.17	7.53	4.23	22.77
Atomic Fraction	9.98	3.83	5.05	12.49	1.53	3.76	5.92	1.93	1.13	1.66	9.51	7.53	4.02	27.00

3. Methods Tested

3.1 Training Set Selection by Clustering

In some cases where numerous potential training spectra are available, selection of a suitable subset of these spectra can improve the accuracy of predictions while reducing the computational burden. Næs [167] and Zemroch [168] suggested a technique for selecting an optimum set of training samples from a large number of infrared spectra using hierarchical clustering. This method clusters the potential training spectra using a furthest-neighbor (complete linkage) clustering tree [169]. The user specifies a desired number of training samples, and the algorithm finds the level in the clustering tree with that number of clusters. For each cluster, the sample that is farthest from the cluster center is selected, so that as much variation as possible is encompassed by the selected samples [169]. By selecting only one sample per cluster, the problem of multiple redundant training samples is avoided while still ensuring that the selected samples span the range of variations in the training set. Isaakson and Næs [169] found that when using this algorithm with near-infrared emission spectra, a subset of 20 training spectra gave better results than using the full set of 114 available training samples.

We implemented this algorithm in the Interactive Data Language (IDL) array processing software by first applying principal components analysis (PCA) to the potential LIBS training set spectra and then using the principal components (PCs) to create a dendrogram, using euclidean distance. This differs slightly from the algorithm as implemented by [169], in which the PCs were standardized by subtracting the mean and dividing by the standard deviation. However, Isaakson and Næs [169] found that they achieved better results by restricting the clustering to the first few PCs. By skipping the standardization step, the magnitude of the PCs relative to each other is preserved, such that the PCs that explain the most variance in the data dominate the

clustering. This has a similar effect to imposing a limit to the number of PCs used, but does not prevent higher order PCs from influencing the clustering if they do represent a significant source of variance. We used the algorithm to select training sets of 50, 100, 200, 300, 400, 500, 600, 700 and 800 spectra out of the 1299 possible training spectra.

3.2 *K*-means clustering

K-means clustering is one of the most commonly used clustering algorithms. The algorithm seeks to divide a dataset into a user-defined number of clusters (*k*). It is initialized with randomly-located cluster centers and each data point is assigned to the nearest cluster center. Then the cluster centers are updated to the centroid of the points in the cluster. This process is repeated until the cluster centers no longer change with each subsequent iteration [170]. Because of the random initial conditions, the results of any given run of the algorithm are likely to converge on a local rather than global minimum. Therefore it is common to run the algorithm many times with different initial cluster centers and use the result with the minimum sum of squared distances from the cluster centroids to the samples in each cluster.

We ran *k*-means clustering on the full dataset (training and test set spectra) using between two and ten clusters. Unless otherwise specified, the clustering was done in the LIBS spectral phase space (i.e. one dimension for each of the 6117 spectral channels). For each number of clusters, the algorithm was run 100 times to ensure that the resulting clustering was robust. We used the Euclidean distance to measure the separation between points. For each resulting cluster, the training samples in that cluster were used to train a PLS2 model and predict the composition of the test samples in the same cluster. Each sample typically had multiple spectra in the test set, so the resulting predictions for each individual spectrum are averaged together to find the overall

prediction for the sample. Note that spectra from a single sample can be assigned to different clusters.

In addition to *k*-means clustering in the spectral phase space, we also conducted clustering in the phase space defined by the first 10 PCs and the first 4 PCs of the dataset to test the hypothesis that, by excluding higher-order components of the variation in the spectra, a more accurate PLS2 model could be trained. We again used the Euclidean distance measure, but increased the number of runs to 500 to take advantage of the decreased calculation time.

3.3 Iterative *k*-means and PLS2

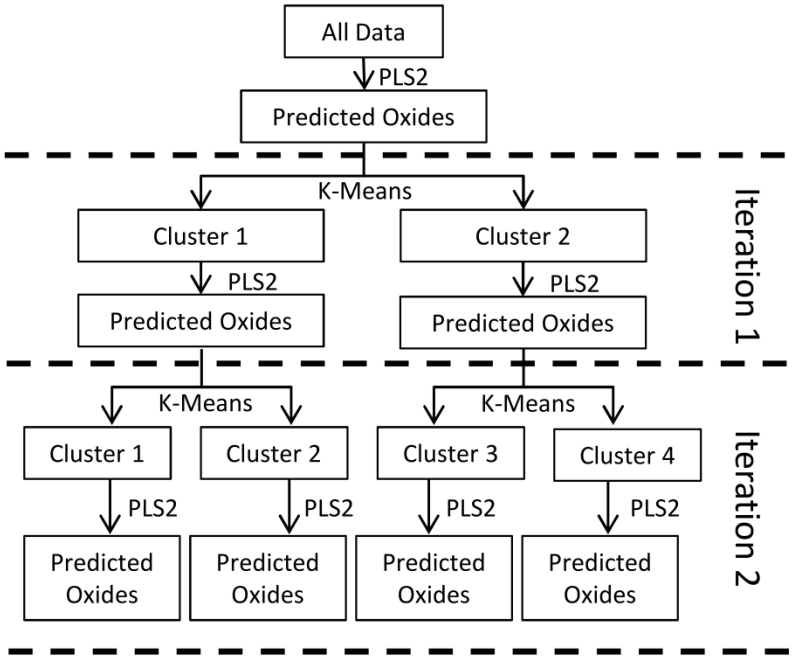

Figure 2: Schematic diagram illustrating the iterative use of *k*-means and PLS2 to group similar samples. The PLS2 predictions are always based on the full LIBS spectra and the *k*-means clustering is applied to the predicted oxide values to split the sample sets for the next iteration.

We also investigated the results of an iterative use of *k*-means clustering and PLS2 regression, illustrated in Figure 2. The intent of this algorithm was to split the training and test sets based on their composition without using prior knowledge of the composition of samples in

the test set. This technique begins by training a PLS2 model on the full set of training spectra and using it to predict the major oxide compositions of the full data set. *K*-means clustering, using Euclidean distance and 500 iterations, is then run on the oxide compositions and used to assign the spectra to two clusters. A PLS2 model is then trained using the training spectra in each cluster, and used to predict the compositions of the samples in that cluster. Each cluster is again split by applying *k*-means clustering to the predicted oxides. This process was repeated three times, until the smallest clusters had fewer than 20 samples in the training set.

3.4 SIMCA

Soft independent modeling of class analogy (SIMCA) is commonly used for classification in chemometrics [171], [172] and has recently been successfully applied to the classification of igneous rock samples based on their LIBS spectra [49]. In SIMCA, the training samples are divided according to their known classification, and a PCA model is generated based on the spectra of the samples in each class. All of the PCA models are then supplied to the SIMCA algorithm and used to classify the unknown test set samples. SIMCA is capable of assigning an unknown sample to more than one class if it is sufficiently similar to multiple classes. If the sample is significantly different from all of the possible classes, SIMCA does not classify the sample, making it a useful tool for identifying unusual samples which might be poorly predicted. The classification of a sample is dependent upon the distance from the sample to the other members of the class in the space defined by the principal components for that class. Typically, the threshold for including a sample in a class is given by a significance level. The Unscrambler software allows this level to be adjusted to 0.5%, 1%, 5%, 10%, and 25%, where the percentage represents the fraction of samples that are true members of a class which are excluded from that class. A higher percentage results in a “stricter” classification that excludes

more samples, erring on the side of false negatives. A low percentage results in most samples that are true members of a class being properly classified, but many "borderline" samples are also classified (i.e. more false positives) [173].

For SIMCA classification, we used ten of the classes described in Section 2 and in Table 2, excluding the "other samples" and "sodalite" classes because of the small number of spectra in each class. PCA was run on the training samples in each class, and the ten resulting PCA models were used to apply SIMCA classification to all of the test spectra. We tabulated the SIMCA classifications at all of the available statistical significance levels and assigned each sample spectrum to the class or classes at the strictest level where classification occurred. For example, if a sample was unclassified at the 25% level, was classified as basalt at 10% significance level, and as both basalt and amphibole at the 5% confidence level, we recorded the classification as basalt. Once the samples were classified, all of the training spectra in each class were used to train a PLS2 model, which was used to predict the compositions of the test samples in the same class. For some samples, different spectra were assigned to different classes, so the final predicted compositions from each individual spectrum were averaged together to yield one result per sample. In cases where the same spectrum was placed in multiple categories at the same level of confidence, the average of the predictions for the multiple categories was used. Figure 3 illustrates the basic process of SIMCA classification and PLS2 prediction.

In a significant number of cases, igneous rocks were classified as amphiboles and/or phyllosilicates in addition to being placed in the igneous rock class. This is likely because many phyllosilicates and amphiboles are compositionally similar to minerals found in igneous rocks. To investigate the influence of the spurious classifications, we also found the results of PLS2

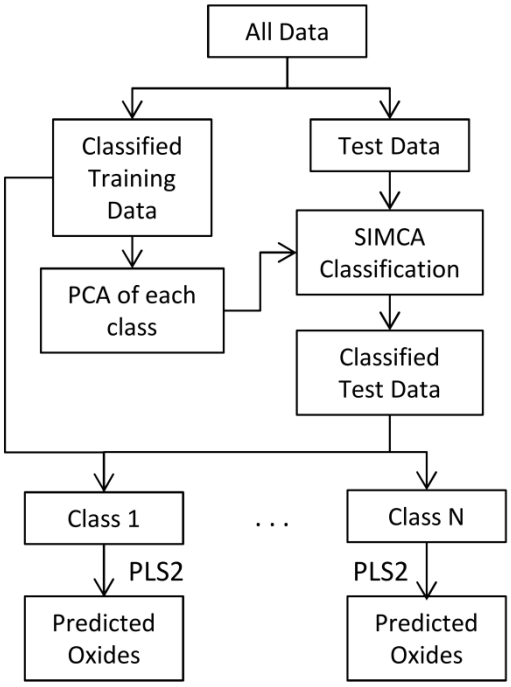

Figure 3: Schematic diagram of the SIMCA method. The final oxide values for each sample are the average of the predictions based on individual spectra, which may be in different classes. Refer to Section 3.4 for more detail and descriptions of the variations of the SIMCA method employed.

predictions using two modified cases of SIMCA classification. The first case, referred to as "SIMCA Limit", limited the effect of the spurious classifications by ignoring the amphibole and phyllosilicate classification except in cases where the sample was assigned to no other class. The second case, referred to as "SIMCA None", removed those two classes entirely.

Finally, to ensure that allowing different spectra from a single sample to be assigned to different classes did not degrade the accuracy of the resulting predictions, we applied a "voting" criterion which identified the most commonly assigned class for the spectra of a sample and assigned all spectra from that sample to that class. For example, if three spectra from a sample were classified as igneous rock and two were classified as olivine, then all five spectra were placed in the igneous rock class and PLS2 calculations were run for these modified classes. This case was referred to as "SIMCA Vote".

3.5 Bayesian Information Criterion

Finally, we used the automated clustering routine “Mclust” in the statistical software "R" to determine the optimum number of clusters and the optimum cluster shape based on the Bayesian information criterion (BIC) [174]. This method has been used previously to classify LIBS spectra [175]. The Mclust algorithm, using the principal components of the full dataset as inputs, indicated that the optimal number of clusters was 21, and that the optimum cluster shape was ellipsoids of variable size. As in the other clustering methods, a PLS2 model was generated based on the training spectra in each cluster and used to predict the composition of the test samples in the same cluster. Many of the compositions predicted using the Mclust-determined clusters were negative, which is not physically meaningful, so we also evaluated the performance after replacing all negative wt. % predictions with 0 wt. %.

4. Results

Prior to comparing the performance of the training set selection and clustering methods discussed in section 3, we investigated the influence of restricting the composition of the training and test sets using their known compositions. We defined a restricted training and test set with compositions that fall on the typical total alkali vs. silica (TAS) classification diagram: 35-85 wt. % SiO_2 and 0-15 wt. % Na_2O+K_2O. The training set samples within this composition range were used to train a PLS2 model and predict the major oxide compositions of the test set samples within the same range and the full test set. The predictions were compared with the predictions from a PLS2 model trained on the full training set, and the results are shown in Figure 4. For most elements, the TAS training set and the full training set perform comparably when predicting the TAS-composition samples, although the full training set was less accurate for CO_2 and SO_3. This is likely because carbon and sulfur have relatively weak emission lines, and so the

PLS2 model used associated elements in the full training set with bright lines such as Mg and Ca present in limestone, dolomite and gypsum. In the TAS training set, neither the training nor test samples had significant CO_2 or SO_3 content, so the low predicted values were relatively accurate. Conversely, the lack of carbonate and sulfate samples in the TAS training set led to significantly worse performance than the full training set when predicting the full range of test set compositions. The quadrature RMSE value when the full set of training spectra were used to train the PLS2 model was 20.06 wt. %. This value serves as the reference against which all of the subsequent methods will be compared.

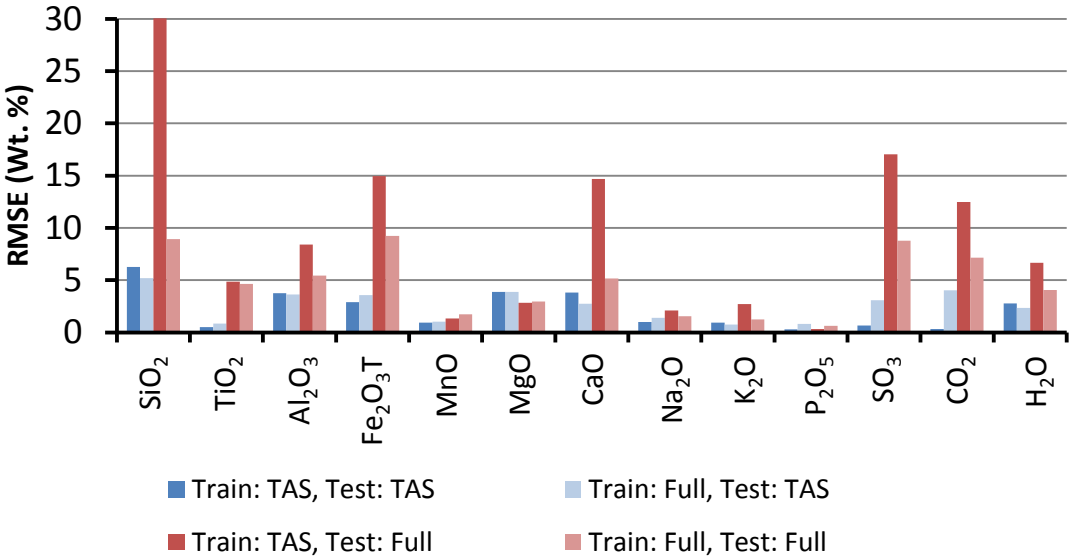

Figure 4: A comparison of the PLS2 performance using the full training set and a training set restricted to samples with compositions that plot on the total alkali vs. silica (TAS) plot (35-85 SiO_2 wt. %; 0-15 Na_2O+K_2O wt. %) to predict the composition of the full test set and a TAS-composition test set

.

Figure 5 summarizes the quadrature RMSE values for all of the methods considered, and Table 4 lists the RMSE values for each of the major element oxides for each method. Bold values in Table 4 indicate the lowest error in each column. To quantify the difference in performance when different methods were used, we followed the procedure described in [54] and calculated p-values for each pair of quadrature RMSE values. P-values are a measure of the statistical significance of the difference between two results. A common, but arbitrary, threshold

for statistical significance is a p-value of <0.05 signifying a >95% chance that the difference is meaningful and not a statistical anomaly.

Hierarchical clustering for training set selection showed relatively poor performance when only 50 training spectra were selected, and the quadrature RMSE asymptotically approached the quadrature RMSE for the full training set as the number of training spectra increased. This behavior suggests that selecting the training set with hierarchical clustering does not improve the performance of the PLS2 predictions. *K*-means clustering with 4 and 5 clusters gave the lowest quadrature RMSEs of all the methods (17.02 wt. % and 17.01 wt. %, respectively). The p-value for the comparison between the quadrature RMSE for 5 *k*-means clusters and the unclustered case was 0.14, giving an 86% level of confidence that the improvement is statistically significant. The *k*-means 5-cluster results gave the most accurate predictions of TiO_2 and H_2O of all the methods considered, while nine *k*-means clusters had the lowest RMSE for SO_3 and Al_2O_3, and ten *k*-means clusters had the lowest error for Na_2O.

We compared the three best *k*-means clustering results using the full spectral phase space (3, 4, and 5 clusters) to the results of clustering in the principal components phase space. We generated clusters using the first 4 and the first 10 PCs and found that the resulting clusters were almost identical. The RMSE values for the 4-PC clusters are listed in Table 4 and the quadrature values are shown in Figure 5. When k-means was run in the 10-dimensional or 4-dimensional PC phase space instead of the full spectral phase space, the quadrature RMSE values were very similar to the unclustered full-spectrum PLS2 results.

The quadrature RMSE values for the iterative method were lower than the unclustered quadrature RMSE value in all cases. When two iterations were used, the quadrature RMSE was

Table 4: RMSE values (wt. %) for the clustering and training set selection methods used. The lowest error in each column is bolded.

	SiO_2	TiO_2	Al_2O_3	Fe_2O_3T	MnO	MgO	CaO	Na_2O	K_2O	P_2O_5	SO_3	CO_2	H_2O	Quadrature
Full	8.93	4.65	5.44	9.22	1.72	2.96	5.15	1.54	1.23	0.61	8.76	7.14	4.05	20.06
K-Means 2	7.79	4.44	4.76	7.93	0.50	2.96	4.43	1.18	1.13	1.19	11.24	8.40	3.86	20.26
K-Means 3	8.14	3.88	5.13	7.35	1.60	3.11	4.62	1.13	1.29	1.17	5.95	8.26	4.10	17.89
K-means 4	8.11	3.86	5.14	6.73	0.55	2.60	5.31	1.15	1.24	1.23	5.86	7.16	3.48	17.02
K-means 5	8.09	**3.77**	5.16	6.66	0.69	3.72	5.45	1.32	1.26	1.24	5.58	7.04	**3.03**	**17.01**
K-means 6	8.52	3.98	5.39	7.04	0.92	2.58	5.40	1.33	1.38	1.22	7.64	7.53	3.81	18.39
K-means 7	8.21	4.77	4.81	8.39	0.42	2.72	5.35	1.10	1.33	1.19	6.83	7.47	3.67	18.44
K-means 8	8.60	4.87	4.81	8.50	0.43	2.80	5.33	1.04	1.40	1.18	6.06	7.52	3.58	18.44
K-means 9	8.79	4.99	**4.63**	8.40	1.87	2.76	5.49	0.88	1.41	1.19	**5.06**	7.30	3.66	18.22
K-means 10	9.15	4.86	4.86	8.43	0.44	2.74	4.62	**0.83**	1.45	1.15	7.70	10.46	4.12	20.52
K-Means 3 (PCA)	8.18	4.25	4.94	7.44	1.08	2.88	4.38	1.32	1.48	1.20	11.00	8.66	3.56	20.18
K-Means 4 (PCA)	7.78	4.17	4.58	7.74	1.35	2.92	4.23	1.01	1.15	1.21	10.40	8.41	3.56	19.58
K-Means 5 (PCA)	8.13	4.12	4.92	7.07	1.47	2.58	4.45	1.17	1.30	1.20	10.70	8.88	4.60	20.13
Hierarch. 50	12.35	5.19	6.55	14.45	2.95	3.59	5.63	1.74	1.39	2.51	11.73	11.11	5.11	27.98
Hierarch. 100	10.15	4.89	6.34	12.42	1.14	3.34	4.68	1.70	1.46	2.56	14.28	8.58	5.39	25.95
Hierarch. 200	9.34	4.79	5.99	10.82	0.71	3.02	4.64	1.61	1.38	1.93	12.59	8.51	4.95	23.62
Hierarch. 300	9.34	4.77	6.01	11.20	0.54	3.01	4.59	1.63	1.40	1.97	12.70	8.38	4.86	23.79
Hierarch. 400	9.11	4.75	5.93	10.36	0.51	2.92	4.69	1.64	1.38	1.35	11.84	8.30	4.69	22.73
Hierarch. 500	8.78	4.69	5.41	10.07	0.77	2.92	4.78	1.53	1.08	1.45	10.56	7.02	4.12	21.09
Hierarch. 600	8.32	4.48	5.04	7.91	0.81	2.76	4.33	1.48	1.01	1.07	12.97	6.79	3.97	20.95
Hierarch. 700	8.41	4.49	4.99	7.82	1.21	2.94	4.53	1.49	1.02	1.05	12.23	6.71	3.99	20.55
Hierarch. 800	8.16	4.42	4.91	7.55	1.13	2.88	4.45	1.53	1.03	0.93	12.08	6.59	3.96	20.15
Iteration 1	7.66	4.71	4.74	6.96	0.77	2.93	**3.83**	1.39	**0.90**	1.21	7.69	7.64	4.31	17.78
Iteration 2	**7.53**	4.71	4.65	**6.45**	0.79	2.71	5.03	1.38	1.11	1.16	6.66	7.23	3.93	17.09
Iteration 3	8.95	4.30	5.24	7.29	0.67	**2.44**	6.70	1.21	1.43	1.64	6.76	**5.96**	3.78	18.22
SIMCA	14.75	4.92	6.94	8.11	**0.39**	2.84	5.75	2.17	1.04	**0.33**	11.75	9.56	4.56	25.56
SIMCA Limit	14.71	6.00	6.80	8.99	0.40	2.94	6.13	2.20	1.06	0.33	11.59	9.61	4.55	26.06
SIMCA None	14.39	5.88	6.32	9.28	0.40	3.00	6.41	2.28	1.06	0.33	11.52	9.72	4.46	25.91
SIMCA Vote	22.26	4.88	8.02	8.29	0.43	4.69	8.35	2.24	1.18	0.33	17.12	10.66	6.74	34.68
Mclust	16.2	21.0	5.64	29.71	0.82	4.17	10.4	2.30	2.31	1.25	6.17	6.48	4.83	43.11
Mclust > 0	12.6	4.81	4.93	21.15	0.72	2.65	10.4	2.30	2.31	1.25	6.17	6.36	3.59	29.53

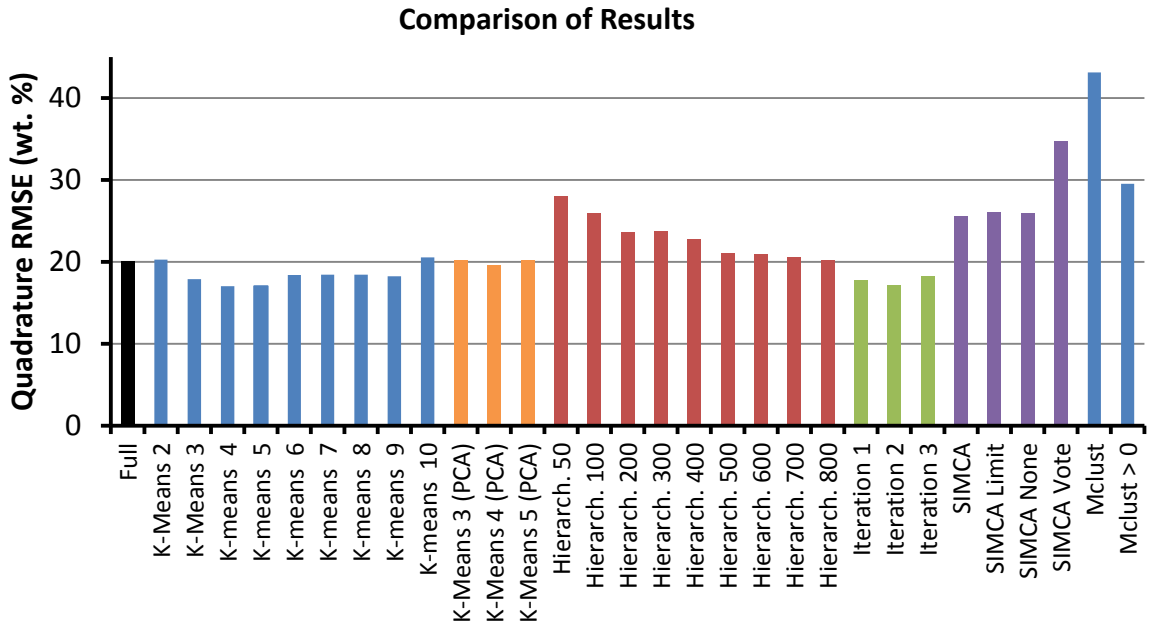

Figure 5: A summary of the quadrature RMSE values for the clustering and training set selection methods investigated. The number following "*k*-means" indicates the number of clusters used. "Heirarch." followed by a number refers to the use of hierarchical clustering to select a specified number of training samples. The results of the iterative method (Figure 2) are referred to as "Iteration" followed by the number of iterations. "SIMCA Limit" refers to the case in which the phyllosilicate and amphibole classes were only used for spectra that were not also assigned to another class. "SIMCA None" reflects the result of removing the amphibole and phyllosilicate classes entirely. "SIMCA Vote" is the result of forcing all spectra from a sample to be predicted by the PLS2 model for the class to which the majority of spectra from that sample were assigned. "Mclust" refers to the results of using the clusters identified by the Mclust algorithm, and "Mclust > 0" is the result of redefining negative predictions as zero. Refer to section 3 for more details descriptions of each method.

17.09 wt. %. The p-value for the comparison between this result and the unclustered case was 0.148, giving an 85.2% confidence level that the improvement was significant. The iterative method with one iteration had the lowest RMSE for CaO and K_2O, and two iterations gave the lowest RMSE for SiO_2 and Fe_2O_3. Three iterations gave the lowest RMSE for MgO and CO_2.

In general the SIMCA and Mclust results were significantly worse than the unclustered result. Limiting the influence of the amphibole and phyllosilicate classes or removing them entirely did not significantly improve the SIMCA predictions but the "voting" method increased the quadrature RMSE by almost 10 wt. %, suggesting that, when clustering or classification is

used, allowing the spectra from a sample to be clustered separately and predicted by separate models is beneficial. The poor performance of the Mclust algorithm likely results from the large number of clusters and therefore the very limited training set size in many of the clusters, reducing the ability to accurately predict unknown samples. As expected, replacing the physically unrealistic negative predictions with 0 wt. % improved the overall accuracy, but the performance was still worse than the other methods considered.

5. Discussion

The results of this study show that *k*-means clustering or the iterative use of *k*-means and PLS2 can modestly improve the accuracy of quantitative LIBS for a diverse suite of geologic samples. Hierarchical clustering of the training set did not result in any improvement in predictive capability, and predictions based on SIMCA classifications and the Mclust algorithm were worse than the unclustered results. The comparison between predictions using the TAS-composition training and test set and predictions using the full training and test sets illustrates the benefits of a larger, more diverse training set for most major elements.

None of the clustering or training set selection methods considered here showed a statistically significant (>95% confidence) improvement over the unclustered results, although the two best methods had confidence levels near 85%. Refinements of the iterative method using different techniques for splitting the sample sets or a larger number of iterations for larger clusters may prove beneficial. Classification of LIBS spectra based specifically on the relatively weak emission lines from geochemically important elements such as Si, C, and S while excluding bright emission lines from elements such as Mg and Ca should also be investigated as a means to improve the accuracy of LIBS classification and quantitative predictions.

In general, our results indicate that a large and diverse training set is the most reliable way to reduce the error in quantitative LIBS. Supplementing the ChemCam spectral library collected prior to instrument delivery [176] with a more diverse set of sulfate and carbonate samples and with synthetic analogs with compositions based on MER rock classes and Mars meteorites will likely improve the accuracy of ChemCam measurements on Mars.

Acknowledgments

This work was supported by the NASA Graduate Student Researchers Program, by the Mars Program Office through MSL, and by the NASA Johnson Space Center.

CHAPTER 5

INVESTIGATING METHODS FOR RELATING MULTISPECTRAL IMAGING TO COMPOSITIONAL DATA

0. Abstract

We investigated methods of relating coregistered Mars Exploration Rover Pancam observations, alpha particle X-ray spectrometer (APXS)-derived oxide values, and Mossbauer-derived Fe-bearing phases in an effort to infer compositional information about distant targets based on multispectral imaging data. Simple correlation coefficients between datasets showed primarily weak correlations in data from Gusev Crater, although restricting the targets to those that were ground by the rock abrasion tool led to improved correlations, most notably between the red-blue ratio (673 nm/434 nm) and Fe^{3+}-bearing phases. Correlations in the data from Meridiani were stronger because of the presence of several soil samples and the pyroxene-rich ejecta fragment Bounce Rock. Partial Least Squares (PLS) calculations relating Pancam spectra to APXS and Mossbauer results showed generally poor performance, although again the presence of compositionally distinct soils and Bounce Rock led to improved results for data from Meridiani. However, when the PLS model for pyroxene based on Meridiani data was used to predict the pyroxene content of Gusev targets, the results were poor indicating that even when cross-validation results are good, the PLS models are not necessarily applicable to data from other sites. Soft Independent Modeling of Class Analogy (SIMCA) classification showed mixed results for Gusev Crater data, with the diversity of Pancam spectra in some APXS-defined

classes leading to poor classifications. SIMCA classification of Meridiani targets, with classes defined by k-means clustering applied to APXS and Mossbauer data, was more successful.

This study indicates that the relationship between multispectral imaging data and APXS- and Mossbauer-derived composition is often relatively weak. To maximize the correlation, dust and surface rinds should be removed if possible. Results from MSL's ChemCam instrument may show a closer relationship to Mastcam multispectral observations because the initial laser shots analyze only the upper few microns of the surface. The clustering and classification methods used in this study can be applied to any dataset to formalize the definition of classes and identify targets that do not fit in previously defined classes.

1. Introduction

Images of the surface of Mars and measurements of its elemental composition both provide valuable insight into the planet's geologic history. Cameras have been included on every landed mission to Mars, and most missions have also been capable of in-situ compositional analysis. While multispectral imaging can be used to survey the surroundings of a rover or lander, detailed compositional information is typically restricted to localized spots close to the spacecraft. Even in the case of the laser-induced breakdown spectroscopy (LIBS) instrument ChemCam on Mars Science Laboratory (MSL), the small size of the analysis spots (~450 μm) and limited range of the laser (7 m) limit the degree to which the rocks and soils visible to the rover can be characterized remotely. It is therefore desirable to seek relationships between multispectral imaging data and elemental and mineralogical data to allow inferences to be made about the composition of objects visible in the distance but not necessarily characterized by *in situ* or stand-off compositional methods.

Although the interpretation of multispectral observations has received considerable attention, no study to date has rigorously attempted to relate Mars Exploration Rover (MER) panoramic camera (Pancam) multispectral observations to the chemical compositions and iron mineral phases derived by the alpha particle X-ray spectrometers (APXS) and Mössbauer spectrometers on the MERs. Therefore, we have used Pancam multispectral images of rocks and soils that have also been analyzed by the MER APXS and Mössbauer to investigate potential methods of combining composition data with multispectral imaging data, to extend the range and utility of both.

2. Data Sets

2.1 Previous Missions

The first Mars surface missions, the Viking landers, carried two cameras mounted on separate masts with three visible and three infrared filters[177], [178]. In addition, each Viking lander contained an X-ray Fluorescence (XRF) spectrometer capable of determining the concentration of elements heavier than Mg in soil samples [179].

The imager for Mars Pathfinder (IMP)[180] consisted of two "eyes" each with 12 filters: Four solar filters for each eye, one diopter lens for the right eye, and geology filters ranging from 440 nm to 1000 nm. The IMP cameras had an angular resolution of ~0.98 mrad per pixel, and data from both eyes were recorded on the same detector with 248 x 256 pixels per eye [180]. Although they had a comparable angular resolution to the Viking cameras, the IMP cameras were a significant improvement because of their increased multispectral capability and higher dynamic range. The Sojourner rover on the Pathfinder mission carried an alpha proton X-ray spectrometer (APXS) which provided elemental analysis of rocks and soils near the lander. The APXS instrument operated in three modes: the alpha backscatter mode which allowed analysis of

light elements; the X-ray mode for analysis of elements heavier than Na; and the alpha-proton mode, which detects protons produced by reactions between alpha particles and some light atomic nuclei [181]. A comparison of IMP multispectral parameters and APXS-derived elemental chemistry at the Pathfinder landing site did not yield any particularly strong correlations among those data sets [182].

The surface stereo imager (SSI) on the Phoenix lander was based on the IMP and the SSI on the failed Mars Polar Lander mission, but the resolution was improved to 0.24 mrad per pixel by using MER 1024 x 1024 CCDs. The SSI filter wheels have 12 positions for each eye, and in addition to filters intended for atmospheric observations, 13 of the 24 filters are intended for multispectral imaging of the surface [183]. Phoenix did not carry any instruments capable of measuring the elemental composition of samples.

2.2 MER Datasets Used in this Study

On the Mars Exploration Rovers (MERs) the panoramic cameras (Pancams) have a multispectral, stereoscopic capability similar to IMP, but higher spatial resolution using a 1024x1024 CCD pixel detector in each "eye". The filter wheel for each eye contains eight filter locations, including one solar filter for each eye and one empty position in the left eye filter wheel. The 13 geology filters sample 11 unique wavelengths across approximately the same spectral range as those on IMP: 432 nm to 1009 nm (Table 1). The angular resolution of Pancam is 0.28±0.02 mrad per pixel, approximately 3 times better than the Viking and Pathfinder cameras and comparable to 20/20 human vision [184]. Both MERs also carry an APXS instrument on their robotic arms. The MER APXS is similar to the APXS on Sojourner, but with significantly increased X-ray sensitivity. This increased sensitivity removes the need for a proton mode and the associated detector [185]. The MER APXS operational temperature is restricted to

less than -40°C [42]. The APXS oxide abundances used in this study are PDS-released data from sols 1-1368 for the Spirit rover and sols 1-696 for Opportunity [160], [161], [186].

Table 1: Pancam Filters[1]

Name	λeff (nm)	Band Pass (nm)	Filter
		Left Camera	
L1	739	338	empty slot, no filter
L2	753	20	red stereo L, geology
L3	673	16	geology
L4	601	17	geology
L5	535	20	geology
L6	482	30	geology
L7	432	32	blue stereo L, geology
L8	440	20	solar ND5
		Right Camera	
R1	436	37	blue stereo R, geology
R2	754	20	red stereo R, geology
R3	803	20	geology
R4	864	17	geology
R5	904	26	geology
R6	934	25	geology
R7	1009	38	geology
R8	880	20	solar ND5

[1]Table adapted from [Bell et al., 2003]

In addition to the MER APXS data, we also used the PDS-released Mössbauer results for sols 1-1411 for Spirit and sols 1-557 for Opportunity [187–189]. The Mössbauer spectrometers on the MERs are capable of determining the Fe-bearing mineralogy of rocks and soils. At the beginning of the mission, when the nominal source intensity was ~100 mCi, a 10 hr integration was sufficient to detect hematite and magnetite at the 1-2% level against the background signal of palagonitic tephra [190]. The Mössbauer results used in our study list the percentage of total Fe in a variety of phases, including: olivine (Ol), pyroxene (Px), ilmenite (Ilm), chromite (Chr), magnetite (Mt), nanophase iron oxides (npOx), Fe^{3+} sulfate (Fe3Sulfate), jarosite (Jar), unidentified ferric phases (Fe3D3), hematite (Hm), goethite (Gt), and Fe/Ni metal alloy (a-Fe).

3. Previous work

Several studies have searched for spectral end members and diagnostic features in panoramic camera (Pancam) spectra in an effort to interpret the composition of targets based on multispectral observations. For example, Farrand *et al.* [191] used spectral mixture analysis (SMA) of multispectral images of targets in the Gusev Crater plains and Columbia Hills. Spectral end members were interactively selected based on two-dimensional projections of the data cloud resulting from a Minimum Noise Fraction (MNF) transformation of the multispectral data. Six spectral classes were defined: Adirondack, Clovis, Lower West Spur, Wishstone, Peace and Watchtower. Although these classes share their names with several of the MER APXS classes, APXS data were not used to divide the classes discussed by [191]. SMA was also used, along with decorrelation stretch (DCS) composites to identify spectral classes at Meridiani Planum [192]. The primary Meridiani spectral classes were a buff-colored "HFS" (Higher Four hundred eighty-two to 535 nm Slope) class and a more purple-colored "LFS" (Lower Four hundred eighty-two to 535 nm Slope) class. The HFS materials are interpreted to be a weathering rind containing more oxidized material than the LFS outcrops. Johnson *et al.* [193] and Rice *et al.* [194] identified features in Pancam multispectral observations of light-toned silica-rich materials that are consistent with the presence of hydrated minerals, including many specific potential hydrated ferric sulfates. By mapping the occurrence of diagnostic Pancam spectral features in multispectral images, [194] determined that the hydration signature is widespread in the Columbia Hills. Parente *et al.* [195] developed a different spectral unmixing algorithm for multispectral analysis of the sulfur-rich soils identified in Gusev crater, and compared the identified end members with laboratory spectra to also infer the presence of hydrated sulfate minerals.

4. Methods

We restricted our study to the list of Pancam observations that contained clearly visible spots that were disturbed by the rock abrasion tool (RAT) or the Mössbauer nose-plate on the rover's instrument deployment device (IDD). This helps to ensure that the Pancam spectra correspond as closely as possible to measured APXS and Mössbauer compositions. Note that perfect correspondence is not possible because Pancam collects photons that have interacted with the upper several microns of the rocks and soils in the scene, while the average information depth for APXS ranges from several microns for lighter elements to ~40 μm for Fe [186]. Mössbauer measurements sample an even larger volume, with an average information depth of 200-300 μm in basaltic rocks [196]. In addition, the APXS and Mössbauer measurements are averages of the composition over the instrument's field of view. For APXS 95% of the signal comes from a ~2.5 cm spot [186], while the Mössbauer field of view is 1.5 cm [197].

Table 2 lists the Pancam observations from Gusev crater that were used in this study, and Table 3 lists the corresponding information for Meridiani Planum.

Neither of the Pancam filter wheels contain the full spectral range of filters, as indicated in Table 1. To create a full spectrum from the left and right eye observations, there are two methods that can be used. The first is to define regions of interest in the left and right eye images separately. Then, the average value for each filter in both eyes can be calculated, resulting in an average Pancam spectrum of the region of interest (ROI). However, some of the statistical methods used in this study rely on numerous spectra of each target, and manually defining a sufficient number of individual regions of interest is not practical. Instead, we coregistered the left and right eye images so that a full spectrum could be extracted from each individual pixel.

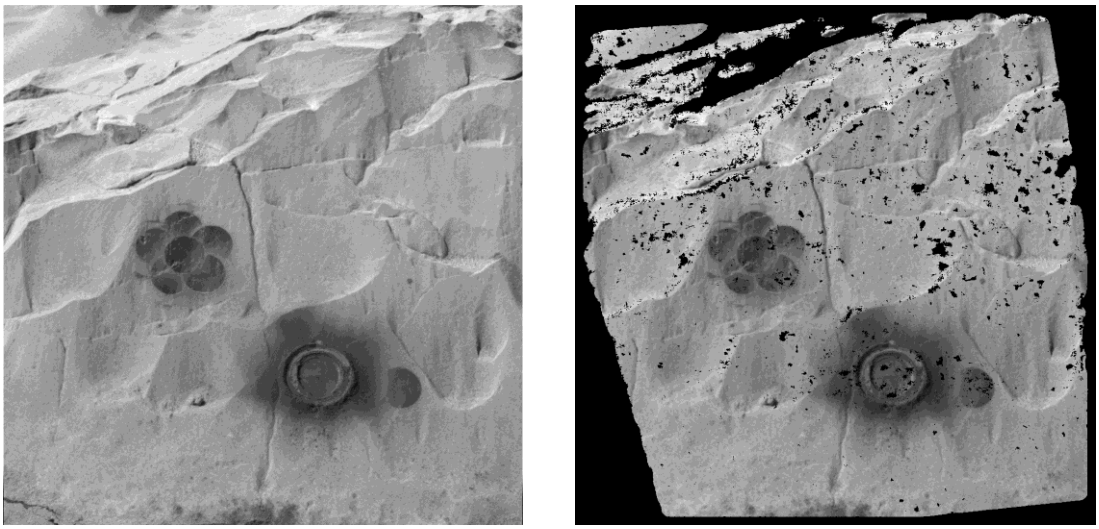

Figure 1 (a) Left eye 753 nm image of Mazatzal from Sol 87 (P2530). (b) Warped right eye 754 nm image from the same observation. Black pixels are locations with poor coregistration that have been masked. The median absolute difference in I/F values between the un-masked pixels in (a) and (b) is 0.0036 with a standard deviation of 0.0035.

This coregistration process was conducted by the Multi-mission Image Processing Laboratory (MIPL) at the Jet Propulsion Laboratory (JPL). Each image was radiometrically corrected to "I/F" values, where I is the measured radiance and πF is the incident irradiance at the top of the Martian atmosphere [184]. Next, disparity maps were generated, mapping each pixel in the right eye to the corresponding pixel in the left eye, using the left eye 753 nm image as the reference image [198]. Finally, "warped" right eye images were generated based on the disparity maps, allowing the images from both eyes to be digitally stacked using the Interactive Data Language (IDL) array processing software. This stacking allowed Pancam spectra for individual pixels to be extracted using the same pixel coordinates in both the left and right eye images.

Some pixels in the warped right eye images are masked out by the algorithm. This can occur when there is no correlation match between pixels (e.g. in areas that are visible to one eye but not the other), but other filters based on the accuracy of the correlation and the geometry of the derived ray intersections are also used [199]. The partial spectra from these bad pixels were

discarded so that they do not affect our analysis. Figure 1 shows an example of the coregistered images. In general, the coregistration is very accurate, and the masked pixels prevent any inaccurately-warped data from being used. The median absolute difference between the I/F values for the un-masked pixels in the warped right-eye image and the corresponding pixels in the left-eye image is 0.0036 and the standard deviation is 0.0035.

The values for the L2 and R2 filters, which cover essentially the same wavelength range (753±20 nm and 754±20 nm), were averaged together in the final Pancam spectra. Likewise, the L7 and R1 filters (432±32 nm and 436±37 nm) were averaged, resulting in full Pancam spectra with 11 individual wavelengths.

The name of the APXS and Mössbauer measurements corresponding to each Pancam spectrum are listed in Table 2 for Gusev Crater and Table 3 for Meridiani Planum. For Pancam spectra of brush mosaics or drilled spots that are partially covered by tailings, no APXS values were assigned because contamination of dust and tailings may have altered the surface composition. Table 2 lists the APXS class for each Pancam spectrum. These class assignments are based on the rocks listed as members of each APXS class by [161] and [186]. Figure 2 shows the average APXS and Mössbauer values for each Gusev Crater APXS class, and Figure 3 shows the average Pancam spectra for each of the APXS classes.

In the case of the Meridiani data, there are not well-defined "APXS classes" as there are for Gusev crater, so we chose to define classes based on k-means clustering of the APXS and Mössbauer results. The clustering was done in the Camo Unscrambler v9.8 software, using Euclidean distances and 500 iterations. To ensure that all APXS oxide or Mössbauer phases were considered equally, the values for each oxide or phase were mean-centered and normalized

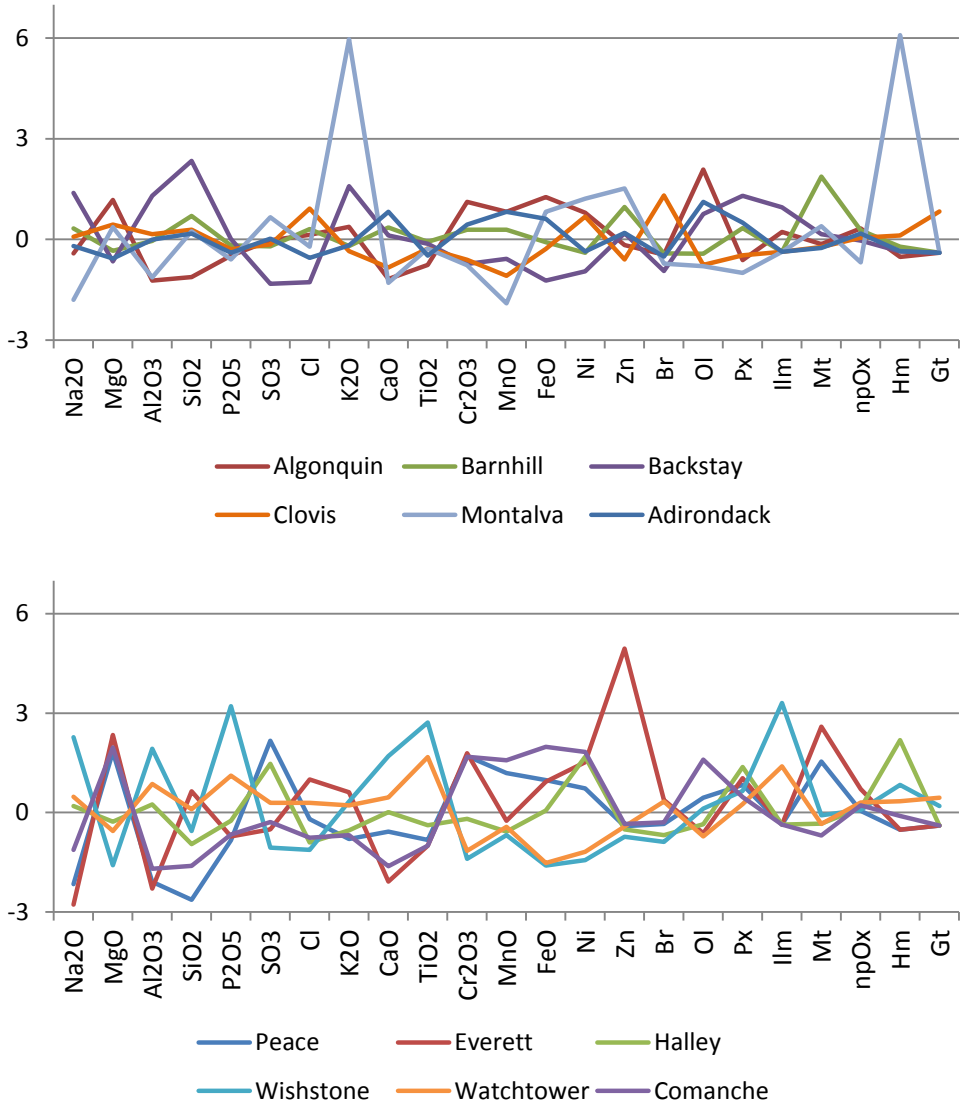

Figure 2: Average composition of the samples in the 12 APXS classes from Gusev Crater. All values have been mean-centered and scaled by the standard deviation. The classes are shown on two separate plots for clarity.

to the standard deviation of that variable. To determine the optimum number of clusters, we implemented the cluster validity parameter described by [200]. This parameter is a ratio with the average intra-cluster distance in the numerator and the minimum inter-cluster distance in the denominator. The optimum number of clusters is where this value is minimized.

Table 2: List of Spirit rover Pancam sequences from Gusev crater and corresponding APXS and Mössbauer observations.

Sol	Sequence	Target	ROI Type[1]	APXS Class[2]	APXS Observation[3]*	Mössbauer Observation[4]*	Set[5]
55	P2583	Humphrey	B	Adirondack	Humphrey_brush	Humphrey_Heyworth1	Test
60	P2597	Humphrey	G	Adirondack	Humphrey_RAT2	Humphrey_Heyworth2	Test
86	P2599	Mazatzal	BM	Adirondack	None	Mazatzal_NewYork	Test
87	P2530	Mazatzal	BM	Adirondack	None	None	Test
100	P2544	Route66	BM	None	None	Route66_SoHo	Test
226	P2569	Clovis	BM	Clovis	None	Clovis_Plano	Test
236	P2580	Ebenezer	G	Clovis	Ebenezer_RAT	Ebenezer_Ratchit2	Test
236	P2580	Ebenezer	T	Clovis	Ebenezer_Fritz_RATgrindings	None	Test
237	P2583	Ebenezer	BM/T	Clovis	None	None	Test
237	P2583	Ebenezer	G/T	Clovis	None	None	Test
237	P2583	Ebenezer	T	Clovis	Ebenezer_Fritz_RATgrindings	None	Test
238	P2585	Ebenezer	BM/T	Clovis	None	None	Test
238	P2585	Ebenezer	G/T	Clovis	None	None	Test
238	P2585	Ebenezer	T	Clovis	Ebenezer_Fritz_RATgrindings	None	Test
293	P2543	Uchben (Chiikbes)	B	Clovis	Uchben_Chiikbes_brush	None	Test
293	P2543	Uchben (Koolik)	G	Clovis	Uchben_Koolik_RAT	Uchben_Koolik	Test
362	P2530	Champagne	G	Wishstone	champagne_RAT2	Champagne_RAT2	Test
386	P2546	Alligator	B	Peace	Alligator_scale_brushed	Alligator_Jambalaya	Test
419	P2574	Watchtower (Joker)	G	Watchtower	Watchtower_Joker_RAT	WatchTower_Joker	Test
487	P2531	Davis (Jibsheet)	B	Watchtower	Jibsheet	None	Test
649	P2579	Kestrel (Kansas)	B	Watchtower	Kansas	Kansas_Kestrel	Test
690	P2575	Algonquin (Iroquet)	B	Algonquin	Algonquin_Iroquet_Brushed	Algonquin_Iroquet	Test
704	P2533	Comanche (Horseback)	B	Comanche	Comanche_Horseback	ComancheSpur_HorseBack	Test
764	P2589	JCPB(Crawford)[6]	B	Barnhill	James Cool Papa Bell_Crawford	None	Test
764	P2589	JCPB (Stars)[6]	B	Barnhill	James Cool Papa Bell_Stars	JamesCoolPappaBell_Stars	Test
867	P2548	Enderbyland (Progress)	S	None	Enderbyland_Progress 2	Enderbyland_Progress2	Test
1220	P2560	BWD[6]	B	None	None	None	Test
1220	P2561	Elizabeth Emery	B	Barnhill	Home Plate_Elizabeth Emery	HomePlate_ElizabethEmery	Test
1220	P2561	Jane Stoll	B	None	None	None	Test

1220	P2561	Mildred Deegan	B	None	None	None	Test
1431	P2564	Chanute	B	None	None	HomePlate_Chanute	Test
1967	P2533	Cyclops Eye	S	None	None	None	Test
1982	P2546	Polyphemus Eye	S	None	None	None	Test
1998	P2553	Polyphemus Eye	S	None	None	None	Test
2086	P2547	Polyphemus Eye	S	None	None	None	Test
2123	P2566	Polyphemus Eye	S	None	None	None	Test
2127	P2571	Polyphemus Eye	S	None	None	None	Test
81	P2588	Mazatzal	B	Adirondack	Mazatzal_NewYork_Brush	Mazatzal_NewYork	Train
82	P2590	Mazatzal	B	Adirondack	Mazatzal_NewYork_Brush	Mazatzal_NewYork	Train
82	P2590	Mazatzal	G	Adirondack	Mazatzal_Brooklyn_RAT2	Mazatzal_Brooklyn	Train
85	P2596	Mazatzal	B	Adirondack	Mazatzal_NewYork_Brush	Mazatzal_NewYork	Train
85	P2596	Mazatzal	G	Adirondack	Mazatzal_Brooklyn_RAT2	Mazatzal_Brooklyn	Train
86	P2599	Mazatzal	B	Adirondack	Mazatzal_NewYork_Brush	Mazatzal_NewYork	Train
86	P2599	Mazatzal	G	Adirondack	Mazatzal_Brooklyn_RAT2	Mazatzal_Brooklyn	Train
87	P2530	Mazatzal	B	Adirondack	Mazatzal_NewYork_Brush	Mazatzal_NewYork	Train
87	P2530	Mazatzal	G	Adirondack	Mazatzal_Brooklyn_RAT2	Mazatzal_Brooklyn	Train
176	P2543	Pot of Gold	G	Halley	Pot_of_Gold_RAT	PotofGold_FoolsGold	Train
200	P2556	Wooly Patch (Mastodon)	G	Clovis	Woolypatch_Mastodon_RAT	Woolypatch_Mastadon	Train
200	P2556	Wooly Patch (Sabre)	G	Clovis	WoolyPatch_Sabre_RAT	WoolyPatch_Sabre	Train
226	P2569	Clovis	G	Clovis	Clovis_Plano_RAT	Clovis_Plano	Train
304	P2553	Lutefisk (Flatfish)	B	Clovis	Lutefisk_flatfish_Brushed	Lutefisk_FlatFish	Train
304	P2553	Lutefisk (Roe)	B	Clovis	Lutefisk_RATRoe_brushed	Lutefisk_Roe	Train
337	P2569	Wishstone	G	Wishstone	Wishstone_chisel_RAT	Wishstone_Chisel	Train
342	P2571	Wishstone	G	Wishstone	Wishstone_chisel_RAT	Wishstone_Chisel	Train
381	P2543	Peace	G	Peace	Peace_RAT2	Peace_Justice2	Train
471	P2563	Methuselah (Haunch)	B	Watchtower	Methuselah_Haunch	Keystone_Haunch	Train
473	P2567	Methuselah (Keystone)	B	Watchtower	Methuselah_Keystone	Keystone_Haunch	Train
476	P2573	Methuselah (Pittsburg)	B	Watchtower	Methuselah_Pittsburg	None	Train
511	P2563	Backstay	B	Backstay	Backstay_Scuppers	Backstay_Scupper	Train
678	P2551	Seminole (Osceola)	B	Algonquin	Seminole_Osceola	Seminole_Osceola	Train

678	P2552	Seminole (Abiaka)	B	Algonquin	Seminole_Abiaka	Seminole_Abiaka	Train
704	P2533	Comanche (Palomino)	B	Comanche	Camanche_Palomino	CommancheSpur_Palimino	Train
753	P2583	Posey	B	Barnhill	Posey_Manager	Posey_Manager	Train
1073	P2534	Montalva (Troll)	B	Montalva	Troll_Montalva Offset	Troll_Montalva	Train
1180	P2596	Examine This (Slide)	B	Everett	Examine This_Slide	ExamineThis_Slide	Train
1215	P2549	June Emerson	B	Barnhill	Home Plate_June Emerson	HomePlate_JuneEmerson	Train
1371	P2547	Pecan Pie	B	Barnhill	Home Plate_Pecan Pie	Home Plate_PecanPie	Train

[1]B = Brushed, BM = Brush mosaic, G = Grind, T = Tailings, S = Soil

[2]APXS classes from [161] and [186]. Entries listed as "none" do not have a defined class in these sources.

[3]PDS-released APXS compositions from [160] and [161].

[4]PDS-released Mössbauer compositions from [187], [188].

*Entries listed as "none" in the APXS and Mössbauer observation columns do not have a PDS-released APXS and/or Mössbauer measurement associated with the Pancam observation. Brush mosaics and targets contaminated by tailings are listed as "none" because their varying dust and tailings coverage likely influences the composition.

[5]This column indicates whether the Pancam ROI and corresponding APXS and Mössbauer values were used in the training set or the test set for SIMCA classification.

[6]BWD = Betty Wagoner's Daughter, JCPB = James Cool Papa Bell

Table 3: List of Opportunity rover Pancam sequences from Meridiani Planum and corresponding APXS and Mössbauer observations.

Sol	Sequence	Target	ROI Type[1]	Cluster[2]	APXS Observation[3]*	Mössbauer Observation[4]*	Set[5]
36	P2531	McKittrick	G	6	McKittrick_RAT	McKittrick_MiddleRAT	Test
37	P2533	McKittrick	G	6	McKittrick_RAT	McKittrick_MiddleRAT	Test
55	P2543	Meringue	None	None	None	Meringue_Mbone	Test
88	P2542	Pilbara	G	6	Golf_Post_RAT_FRAM	Pilbara_Golf	Test
123	P2535	McDonnell	None	None	None	HillTop_McDonnell	Test
150	P2575	Cobble Hill	G	6	Kentucky_Cubble_Hill2_RAT	Kentucky_Coblehill	Test
150	P2575	Virginia	G	6	Virginia_RAT	LayerC_Virginia	Test
150	P2575	London	G	6	Ontario_London_RAT	Ontario_London	Test
180	P2537	Diamond Jenness	G	1	Diamon_Jenness_Holman3_RAT2	Diamondjennes_Holeman3	Test
188	P2547	Inuvik	G	1	Inuvik_Toruyuktuk_RAT	Inuvik_Tokoyuktuk	Test
217	P2576	Escher (Kirchner)	B	4	Escher_Kirchner_brushed	Escher_Kirchner_Brushed	Test
220	P2582	Escher (Otto-Dix)	None	None	None	None	Test
310	P2558	Wharenhui	B	None	Wharenhui_RAT_stalled	None	Test
310	P2558	Paikea	G	None	Paikia_RAT	None	Test
373	P2552	Trench (L. of Peanut)	S	3	Left_of_peanut_TrenchFloor	Trench_LeftOfPeanut	Test
405	P2578	Gagarin	G	6	Gagarin_RAT	Yuri_Gagarin	Test
561	P2591	FB[6] (Strawberry)	G	None	Fruitbasket_Strawberry	None	Test
561	P2591	FB[6] (Lemon Rind)	G	None	LemonRind_RAT	None	Test
639	P2562	Olympia (Ziakis)	B	None	Olympia_Ziakas	None	Test
639	P2562	Olympia (Kalavrita)	G	None	Olympia_Kalavrita	None	Test
807	P2588	Brookville	None	None	None	None	Test
821	P2595	Cheyenne	None	None	None	None	Test
896	P2558	Baltra	None	None	None	None	Test
992	P2530	Cha	None	None	None	None	Test
1036	P2538	Rio de Janeiro	None	None	None	None	Test
1170	P2544	Viva la Rata	None	None	None	None	Test
1184	P2581	Penota	None	None	None	None	Test
1351	P2598	Smith	None	None	None	None	Test

1374	P2543	Smith	None	None	None	None	Test
1374	P2543	Smith	None	None	None	None	Test
1395	P2545	Lyell	None	None	None	None	Test
1438	P2551	Buckland	None	None	None	None	Test
35	P2598	Guadalupe	G	6	Guadalupe_RAT	Guadalupe_RATLower	Train
37	P2532	Guadalupe	G	6	Guadalupe_RAT	Guadalupe_RATLower	Train
45	P2560	Flat Rock	G	6	Mojo2_RAT	FlatRock_Mojo2	Train
68	P2581	Bounce Rock	G	5	BounceRock_Case_Rat	BounceRock_Case	Train
108	P2582	Lion Stone	G	6	LionStone_Numa_RAT	LionStone_NummaNewNormal	Train
163	P2587	Millstone	G	1	millstone_Dramensfjord_RAT	Millstone_Drammensfjord	Train
184	P2544	MacKenzie	G	1	MacKenzie_Campell_RAT	Mackenzie_Campbell2	Train
195	P2551	Bylot	G	1	Bylot_RAT	Baylot_Aktineq3	Train
214	P2571	Escher (Emil Nolde)	B	4	Escher_Nolde_brushed	Escher_EmilNolde	Train
220	P2582	Escher (Kirchner)	G	6	Escher_Kirchner_RAT	Escher_Kirchner	Train
237	P2588	Auk	S	2	Auk_RAT	Auk_AukRAT	Train
373	P2551	Trench (Scruffy)	S	3	Scuff_Srcuffy	Trench_Scruffy	Train
549	P2577	Ice Cream	G	6	IceCream_RAT	IceCream_Onescoop	Train

[1]B = Brushed, G = Grind, S = Soil

[2]K-means clusters based on APXS and Mössbauer data, as described in the text. Entries listed as "none" were missing APXS and/or Mössbauer data, and were not assigned to a cluster.

[3]PDS-released APXS compositions [186].

[4]PDS-released Mössbauer compositions from [189].

*Entries listed as "none" in the APXS and Mössbauer observation columns do not have a PDS-released APXS and/or Mössbauer measurement associated with the Pancam observation.

[5]This column indicates whether the Pancam ROI and corresponding APXS and Mössbauer values were used in the training set or the test set for SIMCA classification.

[6]FB = Fruit Basket

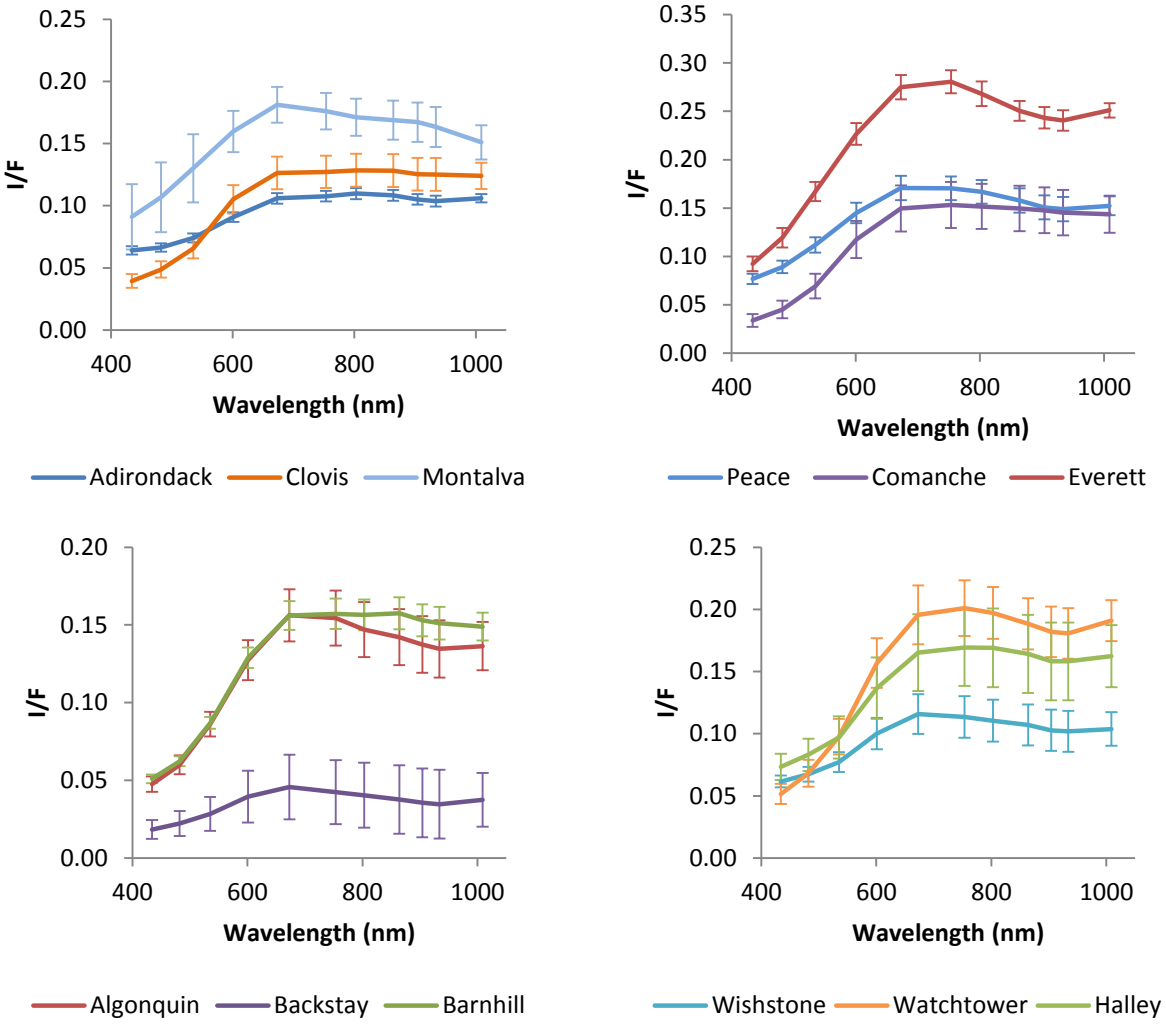

Figure 3: Average Pancam spectra of APXS classes at Gusev crater. Spectra are shown on separate plots for clarity.

Figure 4 shows the intra-cluster distance, the inter-cluster distance and the validity parameter. Although the validity is minimized at three clusters, this resulted in a single cluster with 20 of the 24 samples in it, and one of the remaining clusters included only one sample. We therefore selected the next minimum in the validity parameter, which occurs at six clusters.

The average compositions of the six clusters are compared in Figure 5, and the Pancam spectra are shown in Figure 6. Cluster 1 contains 5 members, all of which are rocks from sols 163-195, within Endurance Crater. Cluster 1 is characterized by low MgO and Br, high P_2O_5, Ni,

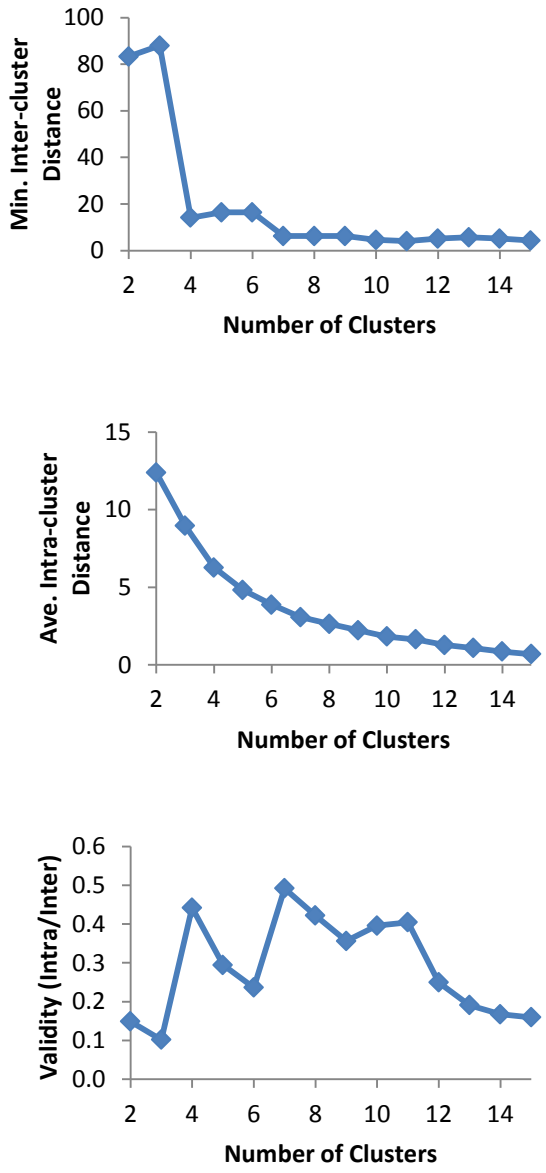

Figure 4: (a) Minimum inter-cluster distance. (b) Average intra-cluster distance. (c) Validity parameter, which is defined as the ratio of the intra- and inter-cluster distances [200].

Zn and Cl, and high jarosite, Fe3D3, hematite, and Fe^{3+}/Fe_T. Clusters 2 through 5 each have only one or two members. Cluster 2 is the dark soil Auk, which has a composition consistent with olivine basalt [201]. Cluster 3 includes two measurements from sol 373, from the wheel trench excavated on sol 366. These soil measurements have high SiO_2, Al_2O_3, TiO_2, Cr_2O_3, MnO, FeO,

olivine, pyroxene, and nanophase oxide and low P_2O_5, SO_3, Cl, K_2O, jarosite, Fe3D3, hematite, and Fe^{3+}/Fe_T. Cluster 4 comprises two brushed observations from the target Escher. These have high Na_2O, Cl, and Br and low SO_3 and MnO.

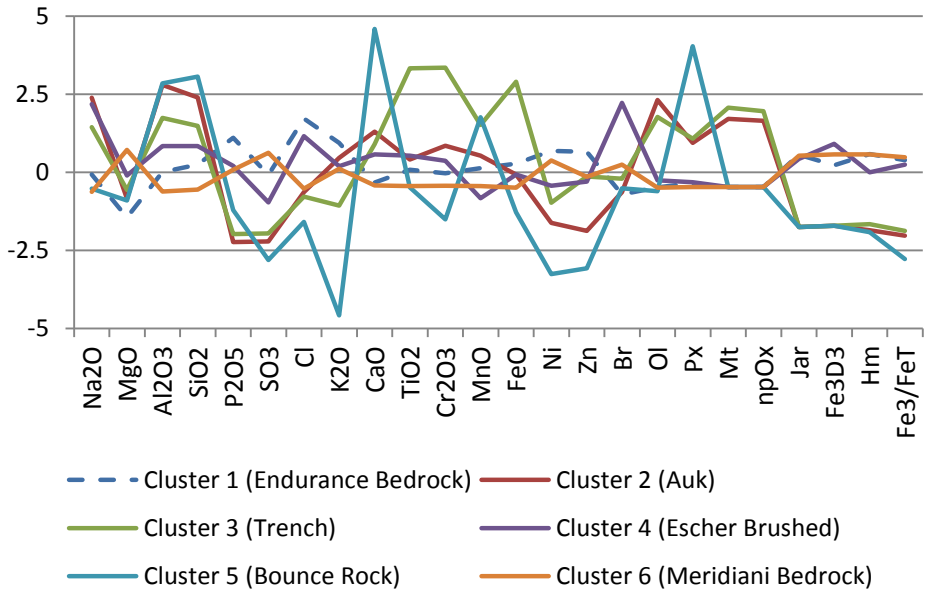

Figure 5: Average APXS and Mössbauer compositions for the six clusters of Meridiani targets. All values have been mean-centered and scaled to the standard deviation.

Cluster 5 is the pyroxene-rich ejecta fragment Bounce Rock, which has high Al_2O_3, SiO_2, CaO, MnO and pyroxene and low SO_3, Cl, K_2O, Ni, Zn and Fe^{3+} phases. The largest cluster (Cluster 6) contains 13 samples. This cluster consists of the typical Meridiani bedrock, with above-average MgO, SO_3, jarosite, Fe3D3, hematite, and Fe^{3+}/Fe_T.

5. Correlations

Prior to conducting more complex multivariate analysis of the data, we investigated the relationships between the Pancam, APXS and Mössbauer data by calculating their Pearson correlation coefficients (R). These calculations were done using the average Pancam spectra for each ROI. The resulting correlation coefficients are listed in Tables 4 and 5 for Spirit APXS and Mössbauer values, respectively. Tables 6 and 7 list the correlation coefficients for the

Opportunity APXS and Mössbauer values. The tables are color-coded to aid in interpretation, with green representing higher positive correlations, red representing stronger negative correlations and yellow for intermediate values. In addition to the correlation between each Pancam spectral channel and the APXS and Mössbauer values, we also calculated several

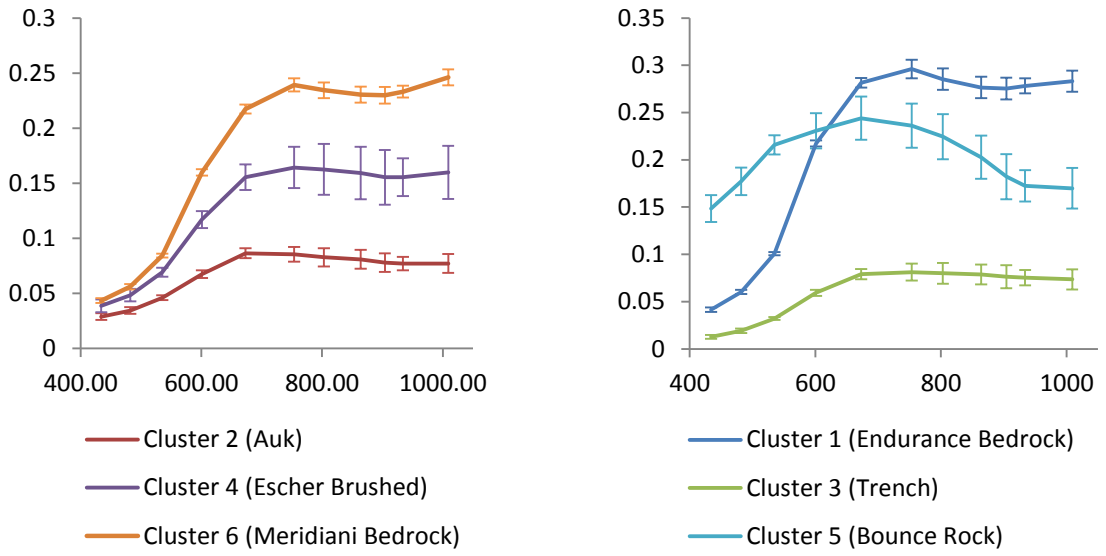

Figure 6: Average Pancam spectra for the six clusters used to group Meridiani data. The clustering was conducted using APXS and Mössbauer values but did not use Pancam data. The spectra have been separated into two plots for clarity.

Pancam spectral parameters and found their correlation with APXS and Mössbauer results. The spectral parameters included those used by [191] and [202].

To aid in the interpretation of the correlations, we also calculated the critical value for the correlation coefficient to be statistically significant at the 95% and 99% levels. The critical R value for 95% confidence ($R_{crit}^{95\%}$) is included at the top of each correlation table. For the Spirit rover data, there are 52 ROIs with corresponding APXS compositions, and 46 ROIs with corresponding Mössbauer values. This results in $R_{crit}^{95\%}$ values of 0.273 for APXS and 0.291 for Mössbauer. The $R_{crit}^{99\%}$ values for the Gusev data are 0.354 for APXS and 0.376 for Mössbauer. For Opportunity, there are 32 ROIs with APXS data and 26 ROIs with Mössbauer data,

corresponding to $R_{crit}^{95\%}$ values of 0.35 and 0.39, respectively. The $R_{crit}^{99\%}$ values for Meridiani data are 0.45 and 0.51.

The Pancam I/F values tend to anticorrelate with Na_2O, SiO_2 and Al_2O_3, which reflects the tendency for these elements to be less abundant in darker, more mafic igneous rocks. The positive correlation between P_2O_5 and Pancam bands with wavelengths longer than 601 nm at Meridiani is caused by the low P_2O_5 content and low I/F of the three soils (Auk and two observations in the wheel trench). SO_3 and Zn are positively correlated with longer wavelength Pancam bands for both sites. The relatively strong correlations between CaO and K_2O and the short wavelength Pancam bands for Meridiani data is primarily caused by Bounce Rock, which has unusually high I/F at short wavelengths, and has very low K_2O and very high CaO. Bounce rock also has a strong influence on correlations with pyroxene because of its high pyroxene concentration.

The strongest negative APXS correlations for Gusev Crater are between the 673 nm /1009 nm ratio and the SO_3 and Cl concentrations (R=-0.42 and -0.48, respectively). This is likely because targets with high 673 nm/1009 nm values are more mafic and less altered, leading to lower values of mobile elements such as SO_3 and Cl. In the Meridiani Planum data, the strongest negative correlation is likewise between the 673 nm/1009 nm ratio and SO_3. As shown in Figure 7, the majority of Meridiani bedrock has high SO_3 and relatively low 673 nm/1009 nm values, but the soil targets and Bounce Rock have lower SO_3 content and higher 673 nm/1009 nm values.

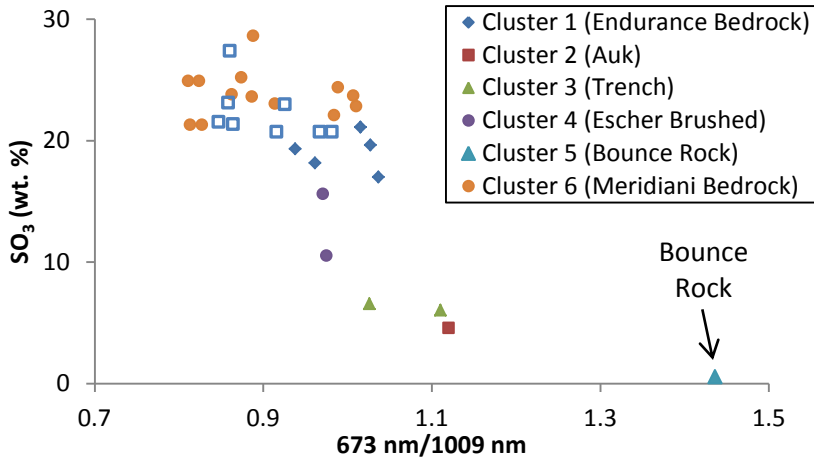

Figure 7: The strongest negative correlation from Meridiani Planum is SO_3 vs the 673 nm to 1009 nm ratio.

The correlations between Mössbauer phases and Pancam spectral bands for Meridiani shows relatively strong correlations, particularly for wavelengths greater than 601 nm. This is because the bedrock samples (Cluster 1 and Cluster 6) have high jarosite, Fe3D3, hematite and Fe^{3+}/Fe_T values, while the soils have very low values for these phases. The reverse is true for the phases olivine, pyroxene, magnetite and nanophase oxide. For Gusev Crater, magnetite generally shows a positive correlation with the brightness of the spectrum. This may be related to the presence of magnetite in the dust, as indicated by the magnetic properties experiment [203].

The strongest positive correlation with any Mössbauer phase at Gusev is R=0.44, between the 754 nm to 1009 nm slope and nanophase oxides (npOx). The strongest overall correlation at Gusev was between the 673 nm/1009 nm ratio and nanophase oxide (R= -0.59). Although the correlation coefficient is above the $R_{crit}^{95\%}$ value of 0.29, the correlation is still quite weak, as shown in Figure 8.

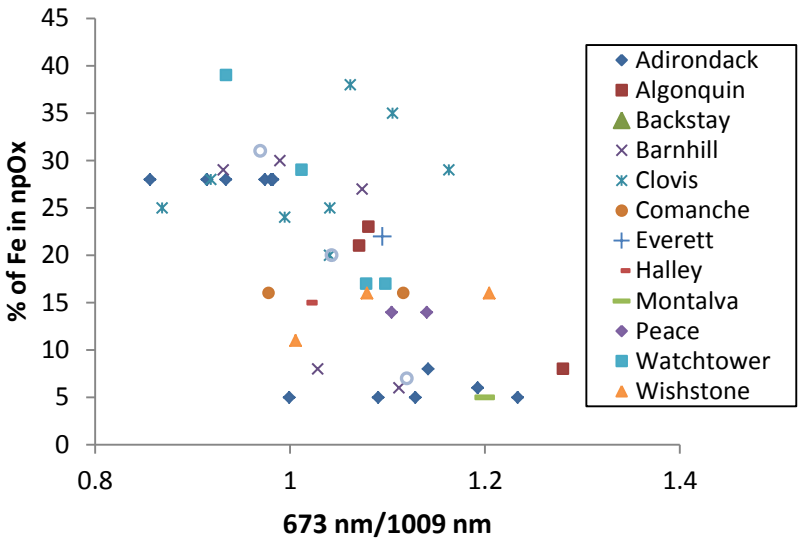

Figure 8: Scatter plot of the percent of Fe in nanophase oxides vs. the 673 nm/1009 nm ratio for Gusev Crater data. Although this is the strongest correlation from Tables 4 and 5 (R= -0.59), and is greater than the $R_{crit}^{95\%}$ value of 0.29, it lacks a clearly visible trend.

It is notable that the correlation between the fraction of Fe in nanophase oxides (npOx) does not strongly correlate with the red/blue (673 nm/434 nm) spectral ratio at either landing site. For Gusev data the correlation coefficient is 0.21, and for Meridiani the correlation coefficient is only 0.04. The lack of correlation may be caused by the different sampling depths of Mössbauer and Pancam measurements. This interpretation is supported by examining the correlation between red/blue ratio and npOx content in brushed and ground ROIs. The ground ROIs at Gusev show a significantly higher correlation (R = 0.74) than the brushed ROIs (R = -0.28), as shown in Figure 9.

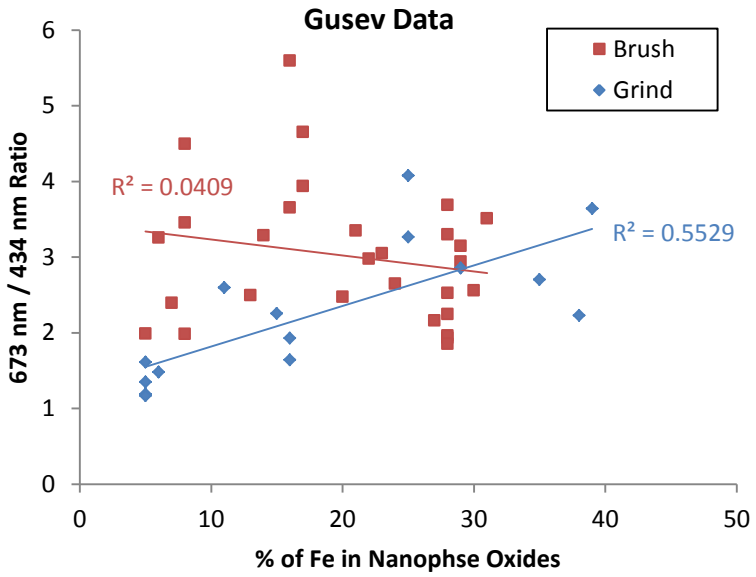

Figure 9: Scatter plot of the Gusev red/blue ratio (673 nm / 434 nm) vs. the fraction of Fe in nanophase oxides. There is essentially no correlation for brushed spots (Red), but relatively strong correlation for grind spots (Blue).

6. Multivariate methods

After examining the simple correlations between Pancam spectra and APXS and Mössbauer data, we used two multivariate methods in an effort to identify more subtle relationships between the datasets. Partial Least Squares (PLS) regression [204] is a method commonly used in multivariate calibration for chemometrics [49], [54], [205]. PLS seeks to correlate a matrix of independent variables (spectra) to a corresponding matrix of dependent variables (composition values) by re-projecting both matrices along the principal components (PCs) that yield the largest correlation. PLS can be used to predict single dependent variables (PLS1) or multiple variables at once (PLS2). Because the number of independent variables (11 wavelengths) is lower than the number of dependent variables (16 APXS oxides and 10 Mössbauer phases), PLS2 cannot predict all of the element concentrations at once. Instead, we

Table 4: Correlation coefficients between Gusev Pancam and APXS ($R_{crit}^{95\%}$ = 0.27)

	Na_2O	MgO	Al_2O_3	SiO_2	P_2O_5	SO_3	Cl	K_2O	CaO	TiO_2	Cr_2O_3	MnO	FeO	Ni	Zn	Br
R436	-0.31	0.01	-0.16	-0.20	-0.03	0.06	-0.31	0.09	0.26	-0.08	0.28	0.31	0.22	-0.14	0.15	-0.21
L432	-0.33	0.07	-0.20	-0.23	0.01	0.07	-0.28	0.15	0.18	-0.05	0.25	0.23	0.20	-0.08	0.18	-0.19
RL434	-0.32	0.04	-0.18	-0.22	-0.01	0.07	-0.30	0.12	0.22	-0.07	0.27	0.27	0.21	-0.12	0.17	-0.20
L482	-0.37	0.12	-0.23	-0.24	0.00	0.12	-0.24	0.16	0.10	-0.03	0.25	0.20	0.18	-0.06	0.24	-0.15
L535	-0.42	0.24	-0.32	-0.26	-0.01	0.20	-0.11	0.18	-0.09	0.00	0.24	0.13	0.15	0.04	0.34	-0.07
L601	-0.33	0.27	-0.30	-0.26	0.03	0.30	0.08	0.16	-0.24	0.09	0.10	0.00	0.00	0.13	0.32	0.07
L673	-0.30	0.25	-0.29	-0.26	0.04	0.34	0.12	0.14	-0.26	0.11	0.07	-0.02	-0.02	0.15	0.32	0.09
R754	-0.29	0.22	-0.28	-0.26	0.03	0.38	0.15	0.12	-0.24	0.12	0.05	-0.01	-0.03	0.15	0.33	0.12
L753	-0.29	0.21	-0.29	-0.26	0.04	0.38	0.15	0.14	-0.24	0.11	0.04	-0.02	-0.02	0.16	0.35	0.10
RL753.5	-0.29	0.22	-0.29	-0.26	0.04	0.38	0.15	0.13	-0.24	0.12	0.05	-0.01	-0.03	0.16	0.34	0.11
R803	-0.29	0.19	-0.28	-0.26	0.03	0.41	0.16	0.12	-0.22	0.11	0.03	-0.01	-0.02	0.16	0.34	0.13
R864	-0.27	0.20	-0.28	-0.27	0.03	0.42	0.18	0.13	-0.24	0.10	0.01	-0.03	-0.04	0.19	0.33	0.16
R904	-0.27	0.19	-0.28	-0.28	0.03	0.43	0.20	0.14	-0.24	0.09	0.00	-0.04	-0.03	0.20	0.33	0.17
R934	-0.26	0.19	-0.28	-0.28	0.04	0.44	0.21	0.14	-0.24	0.10	-0.02	-0.05	-0.05	0.20	0.33	0.18
R1009	-0.23	0.16	-0.25	-0.27	0.06	0.45	0.24	0.11	-0.21	0.14	-0.04	-0.05	-0.09	0.16	0.34	0.18
L673/R1009	-0.16	0.27	-0.05	0.06	-0.09	-0.42	-0.48	0.10	-0.12	-0.11	0.36	0.13	0.19	-0.11	-0.15	-0.29
L673/RL432	0.07	0.17	-0.06	-0.05	0.00	0.17	0.22	-0.04	-0.39	0.12	-0.12	-0.16	-0.13	0.24	-0.01	0.21
RL754/RL432	0.06	0.14	-0.06	-0.07	0.00	0.22	0.23	-0.04	-0.37	0.11	-0.13	-0.14	-0.12	0.25	0.01	0.21
BD535	0.27	-0.16	0.14	-0.13	0.14	0.36	0.27	-0.11	0.00	0.23	-0.31	-0.10	-0.31	0.08	-0.12	0.22
S535-601	-0.04	0.19	-0.12	-0.15	0.08	0.32	0.33	0.05	-0.36	0.20	-0.16	-0.21	-0.22	0.21	0.14	0.26
BD904	-0.06	-0.07	0.02	-0.01	0.12	0.15	0.05	-0.15	0.08	0.24	0.01	0.06	-0.16	-0.18	0.16	-0.04
803/904	-0.07	-0.06	0.05	0.08	-0.01	-0.10	-0.29	-0.09	0.12	0.04	0.18	0.17	0.06	-0.22	0.00	-0.22
S754-864	0.23	-0.19	0.17	0.07	-0.05	0.00	0.11	-0.06	0.14	-0.12	-0.23	-0.10	-0.03	0.06	-0.22	0.19
S754-1009	0.34	-0.31	0.23	0.06	0.10	0.15	0.34	-0.14	0.22	0.07	-0.37	-0.15	-0.25	-0.03	-0.12	0.28
S934-1009	0.13	-0.18	0.11	0.04	0.21	0.18	0.28	-0.20	0.15	0.32	-0.12	-0.01	-0.32	-0.24	0.17	0.06
R1009/RL434	-0.13	0.13	-0.18	0.11	0.04	0.21	0.18	0.28	-0.20	0.15	0.32	-0.12	-0.01	-0.32	-0.24	0.17

L = Left Eye, R = Right Eye, LR = Average of left and right eyes, BD = band depth, S = slope

Table 5: Correlation coefficients between Gusev Pancam and Mössbauer ($R_{crit}^{95\%}$ = 0.29)

	Ol	Px	Ilm	Mt	npOx	Hm	Gt	Fe^{3+}/Fe_T
R436	0.15	0.11	0.00	0.08	-0.37	0.03	-0.25	-0.21
L432	0.06	0.07	0.02	0.14	-0.33	0.11	-0.23	-0.12
RL434	0.10	0.09	0.01	0.11	-0.35	0.07	-0.24	-0.17
L482	0.00	0.10	0.04	0.20	-0.31	0.11	-0.22	-0.09
L535	-0.14	0.09	0.07	0.31	-0.22	0.11	-0.16	0.02
L601	-0.30	0.07	0.13	0.32	-0.06	0.14	0.02	0.19
L673	-0.32	0.07	0.13	0.30	0.00	0.13	0.05	0.21
R754	-0.32	0.06	0.12	0.27	0.06	0.11	0.07	0.22
L753	-0.30	0.04	0.12	0.24	0.07	0.12	0.06	0.21
RL753.5	-0.31	0.05	0.12	0.26	0.06	0.12	0.07	0.22
R803	-0.31	0.04	0.09	0.23	0.10	0.12	0.08	0.23
R864	-0.36	-0.01	0.06	0.27	0.12	0.15	0.13	0.30
R904	-0.35	-0.05	0.05	0.26	0.13	0.16	0.15	0.31
R934	-0.37	-0.05	0.05	0.25	0.15	0.17	0.17	0.33
R1009	-0.37	-0.01	0.09	0.24	0.18	0.13	0.17	0.31
L673/R1009	0.21	0.26	0.13	0.14	-0.59	-0.03	-0.35	-0.36
L673/RL432	-0.23	0.01	0.06	0.05	0.21	0.02	0.20	0.20
RL754/RL432	-0.22	0.00	0.04	0.01	0.25	0.03	0.20	0.21
BD535	-0.19	-0.01	0.12	-0.23	0.28	0.04	0.37	0.21
S535-601	-0.42	0.00	0.16	0.19	0.23	0.12	0.30	0.36
BD904	-0.04	0.42	0.33	-0.06	0.06	-0.22	-0.12	-0.18
803/904	0.20	0.41	0.19	-0.12	-0.23	-0.20	-0.31	-0.39
S754-864	-0.06	-0.32	-0.32	-0.06	0.23	0.11	0.28	0.26
S754-1009	-0.13	-0.27	-0.15	-0.17	0.44	0.00	0.41	0.30
S934-1009	-0.12	0.32	0.35	-0.05	0.24	-0.28	0.03	-0.07
R1009/RL434	-0.26	-0.06	0.02	0.00	0.32	0.05	0.29	0.28

L = Left Eye, R = Right Eye, LR = Average of left and right eyes, BD = band depth, S = slope

Ol = Olivine, Px = Pyroxene, Ilm = Ilmenite, Mt = Magnetite, npOx = Nanophase Oxide, Gt = Goethite, Fe^{3+}/FeT = Ratio of Fe^{3+} to total Fe

Table 6: Correlation coefficients between Meridiani Pancam and APXS ($R_{crit}^{95\%}$ = 0.35)

	Na_2O	MgO	Al_2O_3	SiO_2	P_2O_5	SO_3	Cl	K_2O	CaO	TiO_2	Cr_2O_3	MnO	FeO	Ni	Zn	Br
R436	-0.30	-0.12	0.09	0.10	-0.09	-0.06	-0.24	-0.58	0.51	-0.42	-0.47	0.07	-0.28	-0.34	-0.25	-0.09
L432	-0.31	-0.11	0.08	0.09	-0.09	-0.06	-0.23	-0.58	0.50	-0.43	-0.48	0.07	-0.28	-0.31	-0.25	-0.08
RL434	-0.31	-0.12	0.08	0.10	-0.09	-0.06	-0.24	-0.58	0.50	-0.42	-0.48	0.07	-0.28	-0.33	-0.25	-0.09
L482	-0.34	-0.15	0.05	0.07	-0.02	-0.03	-0.17	-0.54	0.46	-0.42	-0.49	0.08	-0.27	-0.28	-0.18	-0.12
L535	-0.39	-0.19	-0.04	0.00	0.10	0.05	-0.05	-0.40	0.35	-0.43	-0.50	-0.03	-0.25	-0.17	-0.08	-0.07
L601	-0.50	-0.25	-0.36	-0.29	0.38	0.35	0.22	0.02	-0.07	-0.48	-0.51	-0.10	-0.20	0.21	0.29	-0.21
L673	-0.54	-0.20	-0.48	-0.41	0.43	0.47	0.25	0.13	-0.22	-0.51	-0.52	-0.17	-0.19	0.34	0.37	-0.18
R754	-0.55	-0.14	-0.54	-0.47	0.41	0.53	0.21	0.15	-0.28	-0.53	-0.53	-0.21	-0.19	0.38	0.39	-0.15
L753	-0.56	-0.15	-0.54	-0.47	0.43	0.53	0.23	0.17	-0.29	-0.53	-0.53	-0.21	-0.18	0.40	0.39	-0.15
RL753.5	-0.56	-0.14	-0.54	-0.47	0.42	0.53	0.22	0.16	-0.29	-0.53	-0.53	-0.21	-0.19	0.39	0.39	-0.15
R803	-0.56	-0.12	-0.55	-0.49	0.43	0.54	0.22	0.17	-0.31	-0.53	-0.54	-0.21	-0.19	0.40	0.41	-0.14
R864	-0.56	-0.10	-0.58	-0.52	0.43	0.57	0.22	0.19	-0.34	-0.53	-0.53	-0.22	-0.18	0.42	0.43	-0.14
R904	-0.56	-0.09	-0.60	-0.55	0.43	0.59	0.22	0.22	-0.38	-0.53	-0.51	-0.23	-0.17	0.45	0.45	-0.14
R934	-0.56	-0.08	-0.62	-0.56	0.43	0.61	0.23	0.24	-0.40	-0.53	-0.51	-0.23	-0.16	0.47	0.46	-0.13
R1009	-0.55	-0.05	-0.63	-0.58	0.40	0.62	0.20	0.24	-0.42	-0.54	-0.51	-0.25	-0.16	0.49	0.44	-0.10
L673/R1009	0.27	-0.37	0.79	0.80	-0.24	-0.78	-0.08	-0.55	0.82	0.33	0.19	0.40	0.01	-0.67	-0.49	-0.17
L673/RL432	-0.07	-0.11	-0.21	-0.14	0.40	0.16	0.41	0.52	-0.47	0.29	0.22	0.01	0.19	0.43	0.43	-0.12
RL754/RL432	-0.12	-0.07	-0.29	-0.21	0.42	0.24	0.40	0.54	-0.52	0.24	0.16	-0.04	0.16	0.49	0.46	-0.10
BD535	-0.32	-0.01	-0.65	-0.61	0.44	0.64	0.32	0.60	-0.70	-0.29	-0.20	-0.18	-0.02	0.69	0.60	-0.22
S535-601	-0.43	-0.22	-0.59	-0.51	0.57	0.57	0.45	0.51	-0.55	-0.34	-0.30	-0.15	-0.05	0.59	0.61	-0.29
BD904	-0.42	0.04	-0.32	-0.26	0.06	0.31	-0.03	-0.14	-0.09	-0.52	-0.56	-0.26	-0.22	0.31	0.02	0.09
803/904	0.13	-0.25	0.69	0.74	-0.27	-0.68	-0.16	-0.70	0.85	0.10	-0.09	0.24	-0.18	-0.64	-0.57	-0.01
S754-864	0.29	0.46	-0.07	-0.17	-0.12	0.09	-0.13	0.21	-0.33	0.28	0.33	0.00	0.12	0.06	0.09	0.22
S754-1009	-0.15	0.42	-0.61	-0.65	0.04	0.61	-0.04	0.43	-0.71	-0.19	-0.06	-0.28	0.08	0.59	0.36	0.19
S934-1009	-0.35	0.24	-0.55	-0.54	0.03	0.54	-0.10	0.15	-0.42	-0.45	-0.37	-0.34	-0.06	0.50	0.20	0.15
R1009/RL434	-0.20	0.00	-0.41	-0.34	0.45	0.36	0.38	0.58	-0.63	0.14	0.08	-0.09	0.14	0.59	0.51	-0.07

L = Left Eye, R = Right Eye, LR = Average of left and right eyes, BD = band depth, S = slope

Table 7: Correlation coefficients between Meridiani Pancam and Mössbauer ($R_{crit}^{95\%} = 0.40$)

	Ol	Px	Mt	npOx	Jar	Fe3D3	Hm	Fe^{3+}/FeT
R436	-0.41	0.47	-0.40	-0.40	-0.01	0.03	0.00	-0.11
L432	-0.40	0.45	-0.39	-0.39	-0.01	0.02	0.00	-0.11
RL434	-0.41	0.46	-0.40	-0.39	-0.01	0.02	0.00	-0.11
L482	-0.44	0.43	-0.42	-0.42	0.03	0.05	0.04	-0.07
L535	-0.51	0.31	-0.49	-0.48	0.16	0.15	0.14	0.05
L601	-0.65	-0.14	-0.62	-0.62	0.48	0.43	0.49	0.42
L673	-0.68	-0.29	-0.65	-0.64	0.57	0.52	0.60	0.53
R754	-0.68	-0.35	-0.65	-0.65	0.60	0.55	0.64	0.58
L753	-0.68	-0.36	-0.65	-0.65	0.60	0.56	0.64	0.58
RL753.5	-0.68	-0.36	-0.65	-0.65	0.60	0.55	0.64	0.58
R803	-0.68	-0.37	-0.65	-0.64	0.60	0.56	0.65	0.59
R864	-0.67	-0.41	-0.64	-0.63	0.61	0.58	0.66	0.61
R904	-0.66	-0.44	-0.63	-0.63	0.63	0.59	0.68	0.63
R934	-0.66	-0.47	-0.63	-0.62	0.64	0.60	0.69	0.64
R1009	-0.65	-0.48	-0.62	-0.61	0.63	0.60	0.70	0.65
L673/R1009	0.19	0.84	0.19	0.17	-0.52	-0.53	-0.63	-0.66
L673/RL432	-0.05	-0.41	0.03	0.04	0.26	0.16	0.24	0.30
RL754/RL432	-0.09	-0.46	-0.01	0.00	0.31	0.22	0.30	0.36
BD535	-0.38	-0.74	-0.38	-0.37	0.59	0.57	0.70	0.69
S535-601	-0.54	-0.58	-0.52	-0.51	0.63	0.57	0.68	0.67
BD904	-0.56	-0.15	-0.56	-0.54	0.39	0.38	0.48	0.38
803/904	0.00	0.80	-0.02	-0.02	-0.40	-0.39	-0.47	-0.55
S754-864	0.53	-0.21	0.53	0.53	-0.23	-0.16	-0.24	-0.13
S754-1009	-0.04	-0.73	-0.04	-0.03	0.36	0.39	0.47	0.51
S934-1009	-0.39	-0.49	-0.39	-0.37	0.44	0.47	0.57	0.53
R1009/RL434	-0.13	-0.56	-0.04	-0.03	0.37	0.28	0.39	0.44

L = Left Eye, R = Right Eye, LR = Average of left and right eyes, BD = band depth, S = slope

Ol = Olivine, Px = Pyroxene, Mt = Magnetite, npOx = Nanophase Oxide, Jar = Jarosite, Fe3D3 = Undefined Fe^{3+}-bearing phase, Hm = Hematite, Fe^{3+}/Fe_T = Ratio of Fe^{3+} to total Fe

used PLS1 to generate separate models for each individual element detected by APXS and each Fe-bearing phase detected by Mössbauer spectroscopy.

We implemented the PLS1 calculations in Unscrambler, using leave-one-out cross validation and the average Pancam spectrum of each ROI. The number of principal components used in each PLS1 model was the default recommendation produced by the Unscrambler software, as described in [54] and [52]. In cases where no recommendation was available (typically because of poor performance for all PCs), we used the number of PCs corresponding to the lowest cross-validation mean squared error (MSE).

We also used soft independent modeling of class analogy (SIMCA) to classify the samples using Pancam spectra. Gusev data were classified according to their APXS class, and Meridiani data were classified based on the six k-means clusters discussed above. SIMCA is a commonly used classification method (e.g. [49], [171], [172], [206]). For each class of samples, a principal components analysis (PCA) model is generated based on training samples in that class. In our analysis, we designated some of the Pancam observations of each class as training samples and the remaining observations as test samples. This designation was random, although brush mosaics were restricted to the test set because of their variable dust coverage. Pancam observations of the same rock were typically assigned to the same group, with the exception of the two Comanche spots, and the ROIs on Escher. The Comanche spots are in the same Pancam observation, but one was assigned to the test set so that Comanche would be represented in both the training and test sets. This was desirable because Comanche has been shown to contain carbonates [207] and therefore the ability to correctly classify outcrops as Comanche with Pancam would be valuable. Although both Escher observations are on the same rock, the ROIs are from different Pancam observations and are not repeat observations of the same location.

The PCA models for each class were generated using the training samples in that class. The inputs for these PCA models were the spectra for the individual Pancam pixels from the ROIs in each image. Using the individual pixel spectra rather than the average spectrum for each ROI was important because having multiple spectra allows the PCA calculation to be conducted for SIMCA classification. We retained the number of principal components for each class recommended by the Unscrambler software, as we did above for PLS.

In the classification step of the SIMCA algorithm, the spectrum of each sample from the test set is introduced and the distance between the new sample and the hyper-plane defined by the principal components for each PCA model is calculated. If the test sample is closer to the hyper-plane than a specified threshold distance, it is considered a member of the class. The Unscrambler software allows confidence thresholds to be set at 25%, 10%, 5%, 1%, 0.5% and 0.01%, where higher values correspond to more "strict" classifications (i.e. more false negatives) and lower values correspond to less "strict" classifications (more false positives) [173]. SIMCA classification is capable of assigning unknown samples to multiple classes if they are within the confidence threshold. Conversely, if the unknown sample does not fit any of the classes, it will not be classified. This trait makes SIMCA a useful method for determining whether a new observation is similar to previous observations or if it represents a novel class.

7. Multivariate Method Results

7.1 PLS1 Results

The results of the PLS1 calculations for each element and Mössbauer phase are summarized in Table 8. The modified R-squared value reported by the Unscrambler for validation results is given by $\bar{R}^2 = \frac{Var(0)_{Res} - MSE}{Var(0)_{Res}}$, where MSE is the mean squared error and the $Var(0)_{Res}$ is the residual variance of the model using zero PCs. A perfect PLS model would

Table 8: PLS1 validation results for Gusev and Meridiani Data

	Gusev Crater				Meridiani Planum		
	$\bar{R}^2$	RMSE[1]	# of PCs		$\bar{R}^2$	RMSE[1]	# of PCs
SiO_2	0.01	2.00	1*	SiO_2	0.52	2.98	4
TiO_2	-	0.65	1*	TiO_2	0.16	0.11	1
Al_2O_3	0.13	2.61	9	Al_2O_3	0.57	0.87	2
FeO	0.10	2.76	5	FeO	-	1.34	3*
MnO	-	0.09	2*	MnO	-	0.04	1*
MgO	0.16	3.95	8	MgO	0.20	0.87	3
CaO	0.24	1.56	4	CaO	0.76	0.71	3
Na_2O	0.04	0.94	2	Na_2O	0.25	0.22	1
K_2O	-	0.42	1*	K_2O	0.60	0.06	9
P_2O_5	-	1.22	1*	P_2O_5	0.31	0.07	7
SO_3	0.17	2.12	3	SO_3	0.54	4.66	2
Cl	0.23	0.53	5	Cl	0.38	0.41	3
Cr_2O_3	0.03	0.22	7*	Cr_2O_3	0.14	0.07	1
Ni	-	271.99	1*	Ni	0.55	100.33	2
Zn	0.04	221.81	6	Zn	0.38	93.16	2
Br	0.04	198.43	2	Br	-	144.34	1*
Ol	0.28	19.64	9	Ol	0.40	10.34	1
Px	0.02	10.35	5*	Px	0.83	8.08	8
Ilm	-	2.72	4*	Ilm	-	-	-
Mt	0.20	11.64	6	Mt	0.36	2.25	1
npOx	0.26	8.54	4	npOx	0.35	5.45	1
Fe3D3	-	-	-	Fe3D3	0.35	7.37	2
Jar	-	-	-	Jar	0.44	9.45	2
Hm	-	13.75	1*	Hm	0.55	10.36	2
Gt	0.34	8.13	7	Gt	-	-	-
Fe^{3+}/FeT	0.32	0.19	6	Fe^{3+}/FeT	0.51	0.20	4

[1] RMSE values for oxides and Cl are expressed in wt. %. Ni, Zn and Br are in ppm. Mössbauer phase RMSEs are in % of total Fe.

*When there is no recommended number of PCs, we report the results with the lowest RMSE.

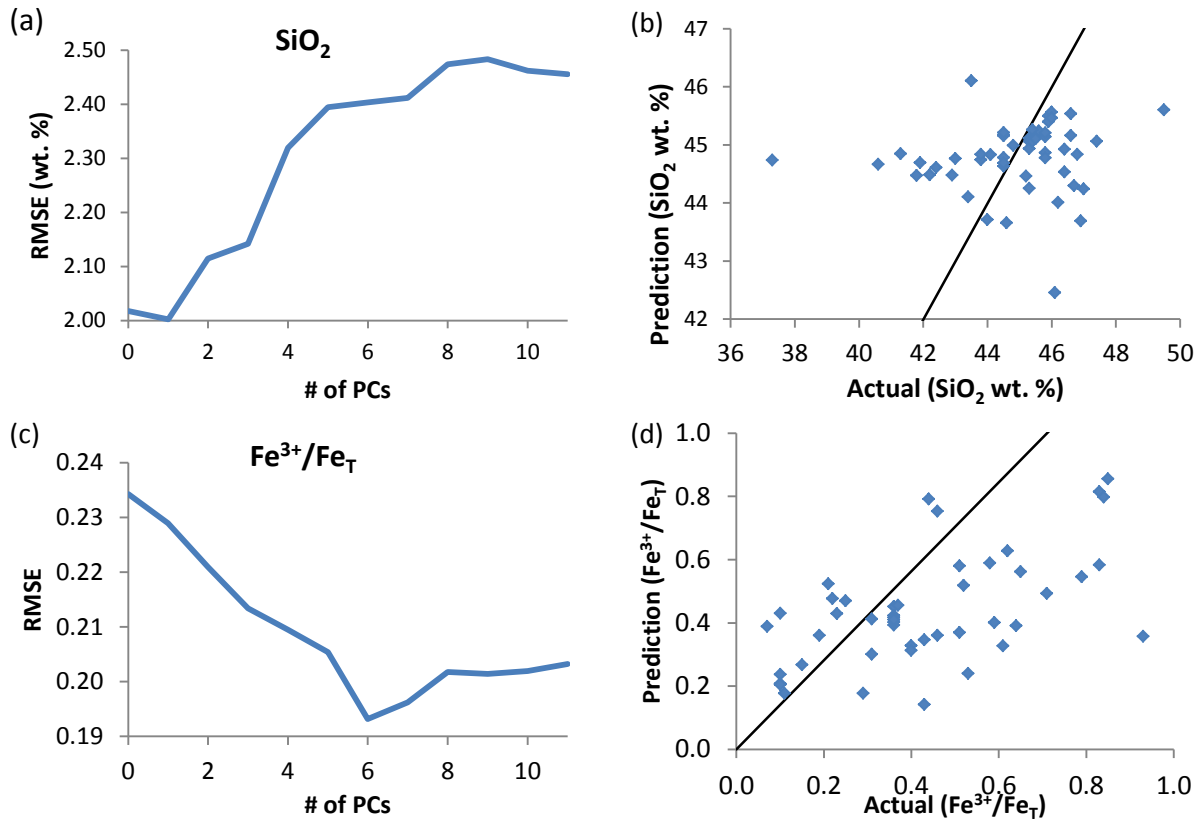

Figure 10: (a) RMSE values for PLS1 models ranging from 0 to 11 PCs for SiO2 using Gusev Crater data. (b) Scatter plot of the predicted vs actual SiO_2 validation values using the PLS1 model with the lowest RMSE. Perfect predictions would fall along the gray 1:1 line. (c) RMSE values for Fe^{3+}/Fe_T using Gusev data. (d) Scatter plot of the predicted vs actual validation values of Fe^{3+}/Fe_T. Perfect predictions would fall along the gray 1:1 line.

have an $\bar{R}^2$ value of 1 and a root mean squared error (RMSE) value of zero. Instead, the results for most of our calculations show low values of $\bar{R}^2$ and high RMSE values relative to the range of compositions. The variable with the lowest validation RMSE and the highest $\bar{R}^2$ in our calculations for Gusev Crater data is Fe^{3+}/Fe_T, while other oxides and Mössbauer phases show worse performance. Figure 10 shows plots of the RMSE for Fe^{3+}/Fe_T and SiO_2 over the full range of PCs.

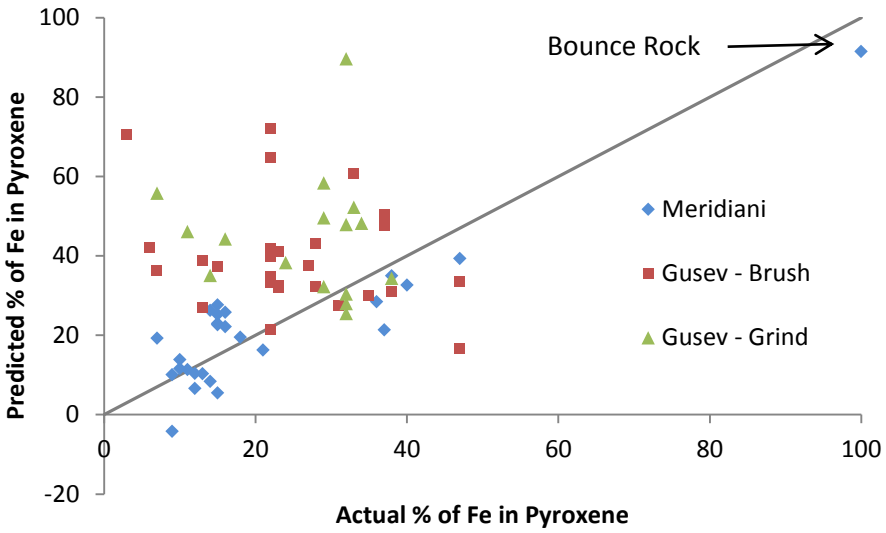

Figure 11: Scatter plot of the predicted vs. actual pyroxene values for both Meridiani Planum and Gusev Crater, based on the PLS1 model trained on Meridiani data. A perfect prediction would fall on the gray 1:1 line.

The Fe^{3+}/Fe_T error decreases as additional principal components are added, until it reaches a minimum and begins to increase again with additional PCs. This increase indicates that the additional components are not useful for predicting novel values. In contrast to the Fe^{3+}/Fe_T plot, the SiO_2 RMSE plot primarily trends upward with the addition of even the first few principal components which indicates that the model is not performing well and has little to no predictive ability.

The PLS1 results from Meridiani Planum are somewhat better than those from Gusev Crater. The highest PLS1 correlation value for Meridiani was for pyroxene, with an $\bar{R}^2$ of 0.86. This relatively high correlation is caused by the presence of Bounce Rock as an end-member in the dataset, as shown in Figure 11. The several soil samples also contribute to the improved correlation values for Meridiani by providing another composition class distinct from the typical bedrock. To test whether the pyroxene model for Meridiani is more broadly-applicable, we used the model to predict the pyroxene content of the samples from Gusev Crater based on their

Pancam spectra. The result of this prediction, shown in Figure 11, indicates that the model does not generalize well to other data. There is no clear relationship between the accuracy of the prediction and whether the Gusev ROI was brushed or ground.

7.2 SIMCA Results

SIMCA classification was implemented by classifying the spectra from each individual pixel in each ROI in the test set. For each class a value of 1 was recorded if the Pancam spectrum fell within the confidence interval for that class. Otherwise, a 0 was recorded. To summarize the results, the classification values for each individual pixel in a given Pancam ROI were averaged together, resulting in a single classification value for each class and each ROI. Thus, while the classification of a single spectrum in a given class is binary, by averaging the classification values for many pixels, our classification summary lists continuous values between zero and one. These values can be interpreted as the fraction of the single-pixel spectra in the ROI that were assigned to the class. Table 9 shows these averaged values for the 25% confidence threshold for the Gusev Crater ROIs, and Table 10 shows the averaged classification results for Meridiani data. The true class for each ROI is indicated by a black outline around the appropriate cell in the table, and the cells have been shaded to correspond to their average classification value for easier visual interpretation.

The Adirondack class ROIs in the Gusev test set were the brushed and ground spots on Humphrey and one observation of the brush mosaic on Mazatzal. All of the Adirondack training spectra were from brush and grind spots on Mazatzal. The classification results show that the spectra from the grind ROI on Humphrey (P2597) were weakly classified as Adirondack, but the brushed ROI (P2583) was primarily assigned to Clovis and Barnhill classes. The Humphrey spectrum is somewhat darker than the average Adirondack spectrum, and shows similarities to

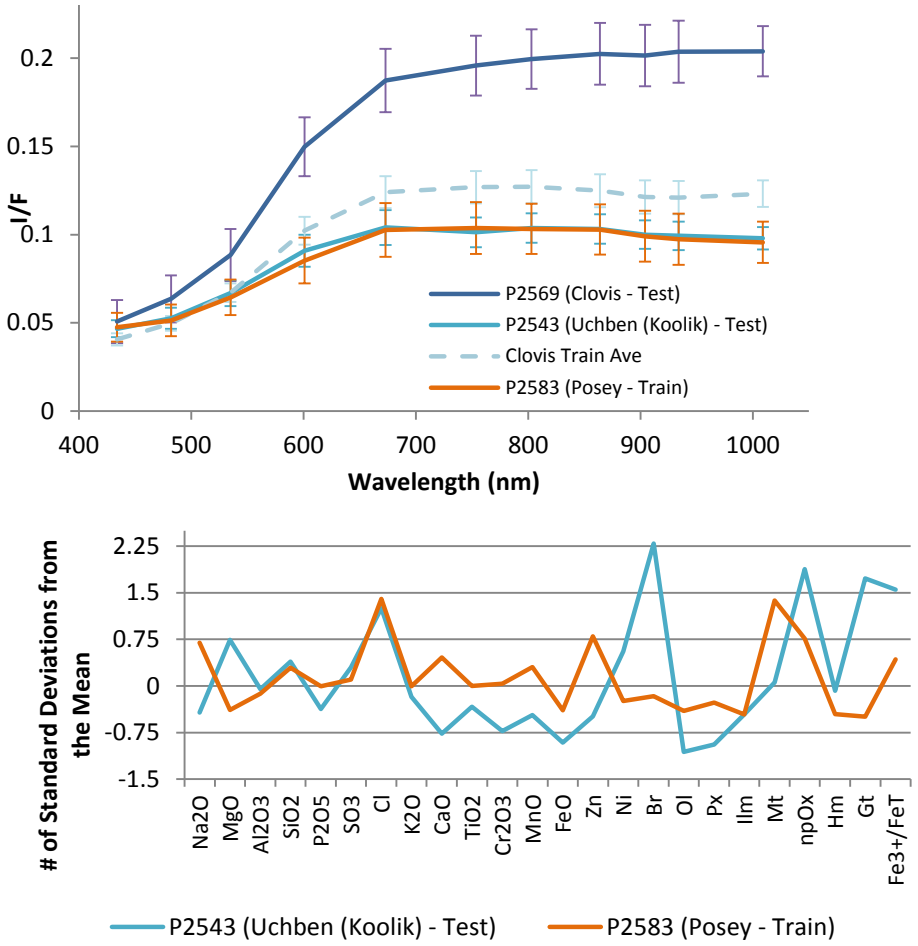

Figure 12: (a) Average spectra of the Clovis brush mosaic (P2569) and Uchben Koolik grind spot, compared with the average of the Clovis training spectra and the Barnhill Posey ROI. (b) Plots of the APXS oxides and Mössbauer phases for Uchben Koolik and Posey, which have nearly identical Pancam spectra. All APXS and Mössbauer values have been mean-centered and scaled by the standard deviation of each variable for ease of comparison.

both Barnhill training set target Posey (P2583) and the Clovis training set target Roe (P2553), which likely explains the classification response.

The spectra of Clovis had significantly higher I/F values than most of the other ROIs in the Clovis class (Figure 12), leading to relatively weak classification, even for the Clovis ROI in the training set. The Clovis-class Uchben Koolik ROI showed a very strong classification as Barnhill. This was the result of an almost identical spectrum to the Barnhill training set ROI

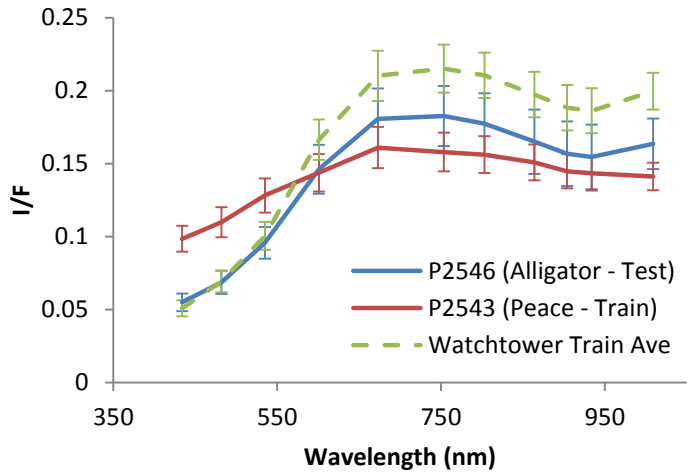

Figure 13: A comparison of the average spectra for Peace-class targets Peace and Alligator, and the average of the Watchtower-class training spectra.

Posey. However, they show significant differences in their APXS and Mössbauer values (Figure 12).

The brushed ROI on Peace-class target Alligator was classified by SIMCA as Wishstone class. This is likely because of an upturn in the spectrum at 1009 nm, which is also seen in the average of the Watchtower training spectra (Figure 13).

Two of the three Watchtower Class observations in the test set (Joker and Jibsheet) were not classified as Watchtower based on their Pancam spectra. This is likely because they are somewhat darker than the average Watchtower training spectrum, and they lack the upturn at 1009 nm that is present in the training set (Figure 14). Kansas showed the characteristic upturn, and was classified as Watchtower for 40% of the spectra in the ROI.

The test spectra from the brushed spot on Iroquet were not classified as Algonquin. Iroquet has a high peak at 673 nm, and then slopes down to a minimum at 934 nm. In contrast, the two Algonquin training spectra show relatively level spectra with only a slight downward slope from 673 nm to 1009 nm. The Comanche test ROI (Horseback) has a higher, relatively uniform I/F value at wavelengths longer than 673 nm, compared to the Comanche training ROI

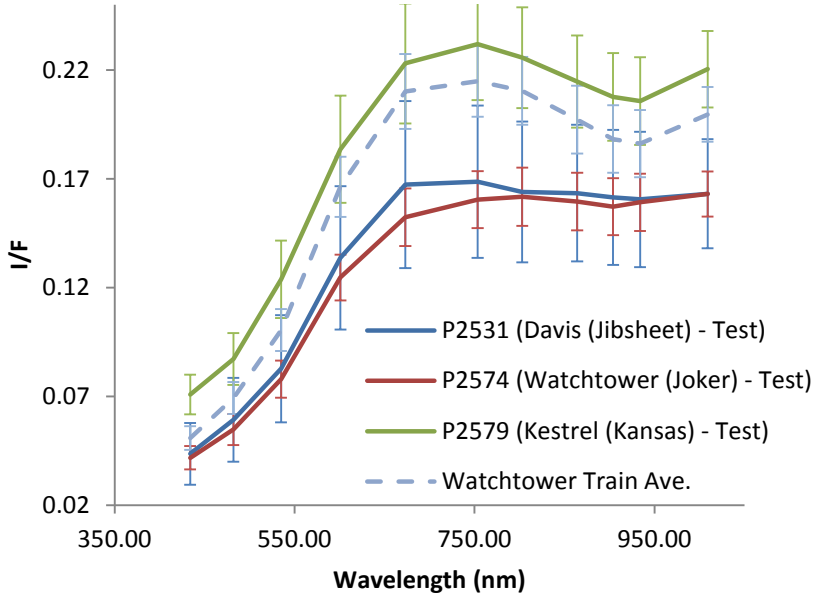

Figure 14: Average watchtower test spectra, compared with the average of the watchtower training spectra.

(Palomino) which is darker and slopes downward. This is because of a greater degree of dust coverage on Horseback, and leads to poor classification performance. The brushed spots Crawford and Stars on James Cool Papa Bell were both misclassified, likely because of their strong increase in brightness at 1009 nm. This upturn is not seen in the Barnhill training set ROI spectra, but is observed in many other ROIs.

The SIMCA classification results for the data from Meridiani Planum are generally better than those from Gusev, thanks in part to the smaller number of classes and the predominance of Meridiani Bedrock in the dataset. Most of the ROIs from sol 36 to sol 150 are primarily classified as Cluster 6 (Meridiani Bedrock), including the soil samples from sol 55 and sol 123. The sol 55 soil was also classified as Cluster 4 (Escher Brushed). The Sol 217 observation of the brushed spot Kirchner on Escher was not classified as Cluster 4 (Escher Brushed), and was instead classified as Meridiani Bedrock.

Table 9: Average SIMCA classification results from Gusev Crater

				APXS Classes[1]												
Sol	Seq.	Target	ROI Type[2]	Adirondack	Algonquin	Backstay	Barnhill	Clovis	Comanche	Everett	Halley	Montalva	Peace	Watchtower	Wishstone	
55	P2583	Humphrey	B	0.03	0.06	0.00	0.64	0.58	0.06	0.00	0.00	0.00	0.00	0.00	0.29	Test
60	P2597	Humphrey	G	0.18	0.00	0.00	0.17	0.00	0.00	0.00	0.00	0.00	0.00	0.00	0.00	Test
87	P2530	Mazatzal	M	0.62	0.60	0.00	0.18	0.44	0.13	0.00	0.24	0.01	0.00	0.00	0.49	Test
100	P2544	Route66	M	0.06	0.16	0.00	0.42	0.36	0.17	0.00	0.09	0.01	0.00	0.00	0.62	Test
226	P2569	Clovis	M	0.00	0.00	0.00	0.07	0.09	0.00	0.00	0.01	0.00	0.00	0.07	0.00	Test
236	P2580	Ebenezer	G	0.00	0.02	0.00	0.42	0.34	0.13	0.00	0.00	0.00	0.00	0.00	0.65	Test
236	P2580	Ebenezer	T	0.00	0.12	0.00	0.00	0.64	0.38	0.00	0.00	0.00	0.00	0.00	0.16	Test
237	P2583	Ebenezer	M/T	0.00	0.08	0.00	0.15	0.30	0.45	0.00	0.00	0.00	0.00	0.00	0.35	Test
237	P2583	Ebenezer	G/T	0.00	0.11	0.00	0.01	0.46	0.59	0.00	0.00	0.00	0.00	0.00	0.33	Test
237	P2583	Ebenezer	T	0.00	0.20	0.00	0.00	0.56	0.63	0.00	0.00	0.00	0.00	0.00	0.22	Test
238	P2585	Ebenezer	M/T	0.00	0.15	0.00	0.11	0.31	0.43	0.00	0.00	0.00	0.00	0.00	0.11	Test
238	P2585	Ebenezer	G/T	0.00	0.17	0.00	0.00	0.43	0.59	0.00	0.00	0.00	0.00	0.00	0.01	Test
238	P2585	Ebenezer	T	0.00	0.31	0.00	0.00	0.56	0.51	0.00	0.00	0.00	0.00	0.00	0.00	Test
293	P2543	Uchben (Chiikbes)	B	0.41	0.63	0.00	0.24	0.68	0.23	0.00	0.11	0.01	0.00	0.00	0.49	Test
293	P2543	Uchben (Koolik)	G	0.05	0.35	0.00	0.94	0.14	0.00	0.00	0.00	0.00	0.00	0.00	0.70	Test
362	P2530	Champagne	G	0.06	0.11	0.00	0.00	0.99	0.00	0.00	0.00	0.00	0.00	0.00	0.02	Test
386	P2546	Alligator	B	0.00	0.01	0.00	0.01	0.02	0.00	0.00	0.01	0.00	0.00	0.21	0.01	Test
419	P2574	Watchtower (Joker)	G	0.25	0.07	0.00	0.08	0.58	0.00	0.00	0.07	0.00	0.00	0.03	0.00	Test
487	P2531	Davis (Jibsheet)	B	0.16	0.11	0.00	0.18	0.15	0.01	0.00	0.04	0.00	0.00	0.00	0.00	Test
649	P2579	Kestrel (Kansas)	B	0.00	0.00	0.00	0.00	0.00	0.00	0.40	0.00	0.00	0.00	0.40	0.00	Test
690	P2575	Algonquin (Iroquet)	B	0.00	0.01	0.00	0.01	0.01	0.01	0.00	0.00	0.00	0.00	0.02	0.15	Test
704	P2533	Comanche (Horseback)	B	0.11	0.25	0.00	0.01	0.02	0.11	0.00	0.00	0.03	0.00	0.00	0.07	Test
764	P2589	JCPB[3] (Crawford)	B	0.81	0.93	0.00	0.01	0.81	0.27	0.00	0.00	0.00	0.00	0.00	0.46	Test

764	P2589	JCPB[3] (Stars)	B	0.56	0.57	0.00	0.01	0.26	0.46	0.00	0.01	0.00	0.00	0.00	0.66	Test
867	P2548	Enderbyland (Progress)	S	0.00	0.02	0.00	0.00	0.00	0.15	0.00	0.00	0.00	0.00	0.00	0.09	Test
1220	P2560	BWD[3]	B	0.00	0.02	0.00	0.38	0.03	0.00	0.00	0.00	0.00	0.00	0.03	0.00	Test
1220	P2561	Jane Stoll	B	0.00	0.11	0.00	0.70	0.30	0.02	0.00	0.00	0.00	0.00	0.00	0.01	Test
1220	P2561	Elizabeth Emery	B	0.01	0.04	0.00	0.10	0.04	0.01	0.00	0.00	0.00	0.00	0.00	0.00	Test
1220	P2561	Mildred Deegan	B	0.01	0.02	0.00	0.41	0.04	0.00	0.00	0.01	0.00	0.00	0.00	0.00	Test
1431	P2564	Chanute	B	0.61	0.55	0.00	0.41	0.76	0.00	0.00	0.22	0.04	0.00	0.00	0.00	Test
1967	P2533	Cyclops Eye	S	0.00	0.00	0.00	0.02	0.00	0.00	0.55	0.00	0.00	0.00	0.22	0.00	Test
1982	P2546	Polyphemus Eye	S	0.00	0.00	0.00	0.00	0.00	0.00	0.05	0.00	0.00	0.00	0.62	0.00	Test
1998	P2553	Polyphemus Eye	S	0.00	0.00	0.00	0.00	0.00	0.00	0.00	0.00	0.00	0.00	0.17	0.00	Test
2086	P2547	Polyphemus Eye	S	0.00	0.26	0.00	0.00	0.00	0.59	0.00	0.00	0.10	0.00	0.00	0.00	Test
2123	P2566	Polyphemus Eye	S	0.00	0.17	0.00	0.00	0.00	0.41	0.00	0.00	0.01	0.00	0.00	0.00	Test
2127	P2571	Polyphemus Eye	S	0.00	0.14	0.00	0.00	0.00	0.51	0.00	0.00	0.00	0.00	0.00	0.00	Test
81	P2588	Mazatzal	B	0.69	0.18	0.00	0.08	0.11	0.00	0.00	0.19	0.00	0.00	0.00	0.53	Train
82	P2590	Mazatzal	B	0.94	0.45	0.00	0.43	0.00	0.00	0.00	0.08	0.00	0.00	0.00	0.86	Train
82	P2590	Mazatzal	G	0.75	0.00	0.00	0.32	0.00	0.00	0.00	0.00	0.00	0.00	0.00	0.52	Train
85	P2596	Mazatzal	B	0.65	0.01	0.00	0.01	0.00	0.00	0.00	0.09	0.05	0.01	0.00	0.51	Train
85	P2596	Mazatzal	G	0.53	0.00	0.00	0.00	0.00	0.00	0.00	0.00	0.03	0.00	0.00	0.07	Train
87	P2530	Mazatzal	B	0.81	0.56	0.00	0.46	0.00	0.00	0.00	0.06	0.00	0.00	0.00	0.71	Train
87	P2530	Mazatzal	G	0.84	0.01	0.00	0.01	0.00	0.00	0.00	0.00	0.00	0.00	0.00	0.05	Train
176	P2543	Pot of Gold	G	0.09	0.00	0.00	0.03	0.01	0.00	0.00	0.76	0.00	0.00	0.00	0.11	Train
200	P2556	WP[3] (Mastodon)	G	0.00	0.10	0.00	0.44	0.94	0.36	0.00	0.00	0.00	0.00	0.00	0.80	Train
200	P2556	WP[3] (Sabre)	G	0.00	0.25	0.00	0.10	0.75	0.34	0.00	0.00	0.00	0.00	0.00	0.54	Train
226	P2569	Clovis	G	0.04	0.00	0.00	0.00	0.19	0.00	0.00	0.01	0.00	0.00	0.00	0.00	Train
304	P2553	Lutefisk (Roe)	B	0.23	0.43	0.00	0.71	0.48	0.07	0.00	0.04	0.00	0.00	0.00	0.87	Train
304	P2553	Lutefisk (Flatfish)	B	0.14	0.38	0.00	0.06	0.93	0.27	0.00	0.00	0.00	0.00	0.00	0.55	Train
337	P2569	Wishstone	G	0.04	0.06	0.00	0.28	0.05	0.00	0.00	0.07	0.00	0.00	0.00	0.74	Train
342	P2571	Wishstone	G	0.40	0.01	0.00	0.01	0.00	0.00	0.00	0.06	0.25	0.01	0.00	0.94	Train
381	P2543	Peace	G	0.30	0.00	0.00	0.00	0.00	0.00	0.00	0.00	0.05	0.77	0.00	0.62	Train

471	P2563	Methuselah (Haunch)	B	0.00	0.00	0.00	0.00	0.00	0.00	0.01	0.00	0.00	0.00	0.76	0.00	Train
473	P2567	Methuselah (Keystone)	B	0.00	0.00	0.00	0.00	0.00	0.00	0.00	0.00	0.00	0.00	0.73	0.00	Train
476	P2573	Methuselah (Pittsburg)	B	0.00	0.00	0.00	0.00	0.00	0.00	0.15	0.00	0.00	0.00	0.78	0.00	Train
511	P2563	Backstay	B	0.00	0.00	0.80	0.00	0.77	0.00	0.00	0.00	0.00	0.00	0.00	0.00	Train
678	P2551	Seminole (Osceola)	B	0.13	0.70	0.00	0.50	0.40	0.18	0.00	0.02	0.05	0.00	0.00	0.40	Train
678	P2552	Seminole (Abiaka)	B	0.14	0.82	0.00	0.25	0.53	0.50	0.00	0.02	0.04	0.00	0.00	0.46	Train
704	P2533	Comanche (Palomino)	B	0.02	0.48	0.00	0.15	0.18	0.75	0.00	0.00	0.01	0.00	0.00	0.36	Train
753	P2583	Posey	B	0.04	0.17	0.00	0.79	0.29	0.05	0.00	0.00	0.00	0.00	0.00	0.64	Train
1073	P2534	Montalva (Troll)	B	0.00	0.21	0.00	0.06	0.04	0.07	0.00	0.00	0.77	0.00	0.00	0.12	Train
1180	P2596	Examine This (Slide)	B	0.00	0.00	0.00	0.00	0.00	0.00	0.76	0.00	0.00	0.00	0.07	0.00	Train
1215	P2549	June Emerson	B	0.00	0.13	0.00	0.85	0.10	0.02	0.00	0.00	0.00	0.00	0.00	0.03	Train
1371	P2547	Pecan Pie	B	0.20	0.69	0.00	0.79	0.08	0.00	0.00	0.12	0.05	0.00	0.00	0.01	Train

[1] Outlines indicate the correct class for samples where it is known based on [161] and [186].

[2] B = Brush, M = Brush Mosaic, G = Grind, S = Soil, T = Tailings

[3] JCPB = James Cool Papa Bell, BWD = Betty Wagoner's Daughter, WP = Wooly Patch

Table 10: Average SIMCA classification results from Meridiani Planum

				K-Means Clusters[1]						
Sol	Seq.	Target	ROI Type	Cluster 1	Cluster 2	Cluster 3	Cluster 4	Cluster 5	Cluster 6	
36	P2531	McKittrick	G	0.04	0.00	0.00	0.00	0.00	0.80	Test
37	P2533	McKittrick	G	0.10	0.00	0.00	0.00	0.00	0.61	Test
55	P2543	Meringue	S	0.00	0.00	0.00	0.57	0.00	0.76	Test
88	P2542	Pilbara	G	0.07	0.00	0.00	0.00	0.00	0.56	Test
123	P2535	McDonnell	S	0.00	0.00	0.00	0.01	0.00	0.08	Test
150	P2575	Cobble Hill	G	0.00	0.00	0.00	0.29	0.00	0.82	Test
150	P2575	Virginia	G	0.00	0.00	0.00	0.13	0.00	0.36	Test
150	P2575	London	G	0.02	0.00	0.00	0.12	0.00	0.31	Test
180	P2537	Diamond Jenness	G	0.71	0.00	0.00	0.00	0.00	0.00	Test
188	P2547	Inuvik	G	0.38	0.00	0.00	0.00	0.00	0.00	Test
217	P2576	Escher (Kirchner)	B	0.00	0.00	0.00	0.01	0.00	0.32	Test
310	P2558	Wharenhui	B	0.13	0.00	0.00	0.00	0.00	0.77	Test
310	P2558	Paikea	G	0.29	0.00	0.00	0.00	0.00	0.14	Test
373	P2552	Trench (Left of Peanut)	S	0.00	0.00	0.04	0.17	0.00	0.03	Test
405	P2578	Gagarin	G	0.27	0.00	0.00	0.00	0.00	0.59	Test
561	P2591	Fruit Basket (Strawberry)	G	0.01	0.00	0.00	0.00	0.00	0.72	Test
561	P2591	Fruit Basket (Lemon Rind)	G	0.01	0.00	0.00	0.00	0.00	0.21	Test
639	P2562	Olympia (Ziakis)	B	0.02	0.00	0.00	0.00	0.00	0.56	Test
639	P2562	Olympia (Kalavrita)	G	0.09	0.00	0.00	0.00	0.00	0.34	Test
807	P2588	Brookville	B	0.00	0.00	0.00	0.00	0.00	0.10	Test
821	P2595	Cheyenne	B	0.01	0.00	0.00	0.00	0.00	0.25	Test
896	P2558	Baltra	G	0.00	0.00	0.00	0.00	0.00	0.00	Test
992	P2530	Cha	G	0.00	0.00	0.00	0.00	0.00	0.00	Test

1036	P2538	Rio de Janeiro	B	0.02	0.00	0.00	0.00	0.00	0.01	Test
1170	P2544	Viva la Rata	B	0.02	0.00	0.00	0.00	0.00	0.01	Test
1184	P2581	Penota	G	0.62	0.00	0.00	0.00	0.00	0.00	Test
1351	P2598	Smith	B	0.00	0.00	0.00	0.00	0.00	0.00	Test
1374	P2543	Smith	B	0.00	0.00	0.00	0.00	0.00	0.00	Test
1374	P2543	Smith	G	0.00	0.00	0.00	0.00	0.00	0.00	Test
1395	P2545	Lyell	G	0.00	0.00	0.00	0.00	0.00	0.00	Test
1438	P2551	Buckland	G	0.00	0.00	0.00	0.00	0.00	0.00	Test
35	P2598	Guadalupe	G	0.00	0.00	0.00	0.00	0.00	0.92	Train
37	P2532	Guadalupe	G	0.00	0.00	0.00	0.00	0.00	0.74	Train
45	P2560	Flat Rock	G	0.01	0.00	0.00	0.00	0.00	0.71	Train
68	P2581	Bounce Rock	G	0.00	0.00	0.00	0.00	0.76	0.00	Train
108	P2582	Lion Stone	G	0.00	0.00	0.00	0.00	0.00	0.56	Train
163	P2587	Millstone	G	0.81	0.00	0.00	0.00	0.00	0.02	Train
184	P2544	MacKenzie	G	0.62	0.00	0.00	0.00	0.00	0.00	Train
195	P2551	Bylot	G	0.80	0.00	0.00	0.00	0.00	0.00	Train
214	P2571	Escher (Emil Nolde)	B	0.00	0.00	0.00	0.78	0.00	0.59	Train
237	P2588	Auk	S	0.00	0.75	0.00	0.00	0.00	0.00	Train
373	P2551	Trench (Scruffy)	S	0.00	0.00	0.76	0.04	0.00	0.03	Train
549	P2577	Ice Cream	G	0.03	0.00	0.00	0.00	0.00	0.61	Train

[1] Cluster 1 = Endurance Bedrock, Cluster 2 = Auk Soil, Cluster 3 = Trench Soil, Cluster 4 = Escher Brushed, Cluster 5 = Meridiani Bedrock

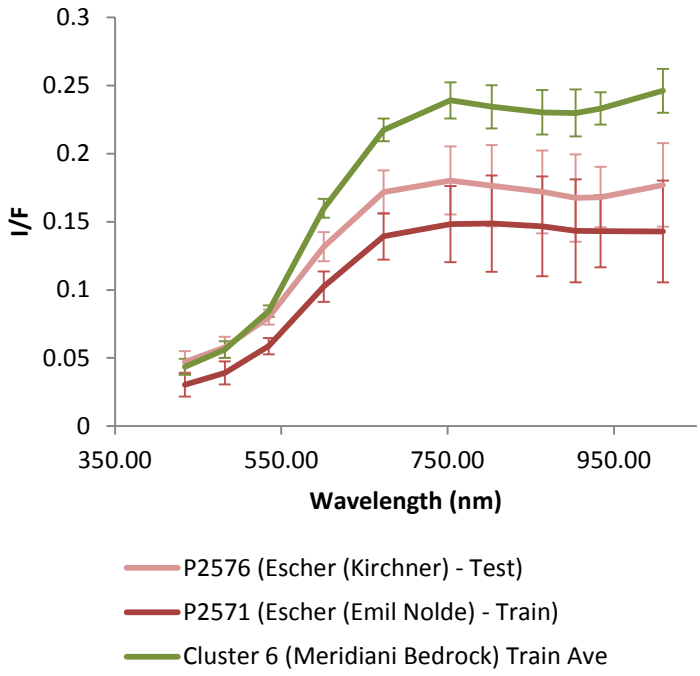

Figure 15: A comparison between the Cluster 4 (Escher) training and test spectra and the Cluster 6 (Meridiani Bedrock) training spectra.

Figure 15 shows a comparison between the average Escher spectra and the Cluster 6 (Meridiani Bedrock) training spectra. The soil target Left of Peanut was not correctly classified as Cluster 3 (Trench), likely because it has a lower I/F and lower 753.5 nm to 1009 nm slope than the training spectrum for Cluster 3.

To further investigate the relationship between APXS compositions and Pancam spectra, we ran k-means clustering on the average Pancam spectra for each ROI to divide them into spectrally similar groups. The clustering validity measure, discussed above, is minimized at ten clusters, but also shows a strong minimum at four clusters. Figure 16a shows a scatter plot of APXS FeO *vs*. CaO values, with symbols corresponding to three of the four Pancam spectral groups. Figure 16b shows a similar plot of SO_3 *vs*. MgO values. "Cluster 3" contains only a single Pancam spectrum which does not have

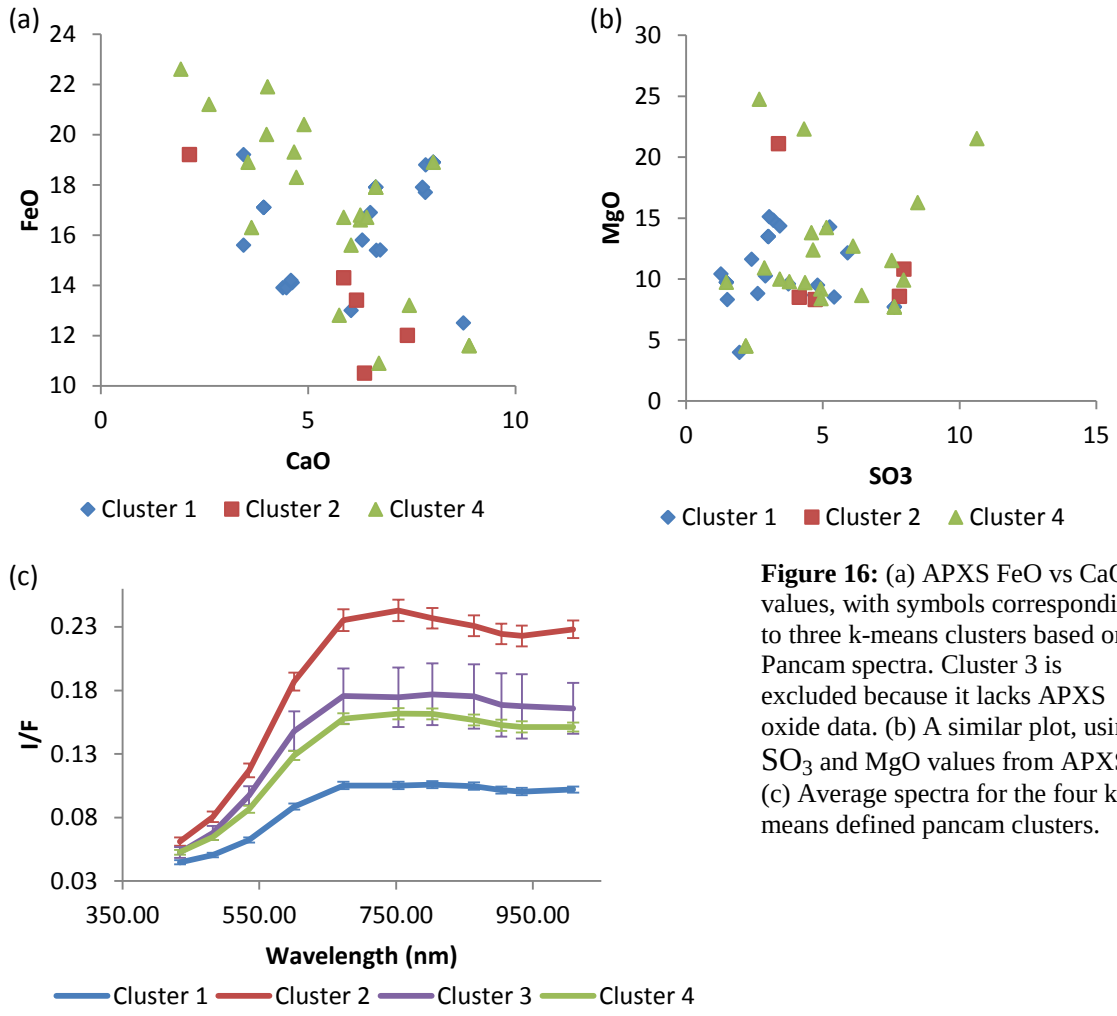

Figure 16: (a) APXS FeO vs CaO values, with symbols corresponding to three k-means clusters based on Pancam spectra. Cluster 3 is excluded because it lacks APXS oxide data. (b) A similar plot, using SO_3 and MgO values from APXS. (c) Average spectra for the four k-means defined pancam clusters.

corresponding APXS data, and is therefore not shown in Figure 16a and 16b. Figure 16c shows the average pancam spectra of the k-means defined clusters.

Although the elements Fe, Mg, Ca and S can influence the VNIR spectra of minerals, there does not appear to be any relationship between the k-means-defined Pancam clusters and the elemental concentrations from APXS.

8. Summary and Implications

8.1 Summary

Our investigation indicates that there is often little relationship between Pancam multispectral observations, APXS-derived oxide abundances, and Mössbauer Fe-bearing phase

abundances. This result is in some respects reassuring, indicating that the instruments on the MERs are complimentary, with little redundancy in capabilites.

The simple Pearson's correlation coefficients are generally weak, although many are technically above the threshold for statistical significance. The correlations were generally higher for Meridiani data than for Gusev crater data because of the presence of several soils and the Bounce Rock ejecta fragment which were spectrally and compositionally distinct from the more common bedrock targets. The correlation between ferric-bearing phases and the red-blue spectral ratio is poor when all of the Gusev ROIs are considered, but is considerably better when only spots that were ground by the RAT are considered. This indicates that the difference in sampling depth between Pancam, APXS and Mössbauer may be responsible for the lack of correlation. The higher correlations for Meridiani data may therefore also reflect the lower amount of dust cover at Meridiani Planum in comparison to Gusev Crater.

Partial least squares results were similar to the simple correlation coefficient results, with generally poor performance for most oxides and Fe-bearing phases. The presence of Bounce Rock and the soils at Meridiani leads to improved $\bar{R}^2$ and RMSE values for some phases and elements, such as Pyroxene and CaO, which were abundant in Bounce Rock. However, the application of the Meridiani Pyroxene model to Gusev data showed poor performance, indicating that the results are not generalizable to new datasets.

SIMCA classification at Gusev crater showed mixed results. Some samples were classified correctly, while others were mis-classified or were not classified at all. The errors in classification reflect the disconnect between Pancam spectra and the sample composition: in some cases nearly identical spectra have very different compositions (Figure 12), while in other cases samples in the same APXS class have very different Pancam spectra (Figure 13). The

variation in Pancam spectra of samples within the same APXS class is consistent with isochemical weathering at a relatively low water to rock ratio.

The SIMCA classification performance at Meridiani was generally better. It is possible that the improvement in Meridiani results was because the classes were automatically defined by clustering based on both APXS and Mössbauer results, while the Gusev Crater classes were manually determined based on APXS only.

8.2 Implications for Mars Science Laboratory

On the upcoming Mars Science Laboratory (MSL) rover the two stereo mast cameras (Mastcams) use a combination of RGB Bayer pattern filters bonded to the detector and filter wheels with 7 filters in each eye devoted to the collection of visible color and near-IR multispectral images. The filters range in wavelength from 447 to 1013 nm. One camera has a focal length of 34 mm, providing a wide-angle view at 0.22 mrad per pixel, while the other camera has a focal length of 100 mm and an angular resolution of 0.074 mrad per pixel. Both cameras use 1200 x 1600 pixel CCDs and have adjustable focus [32]. MSL also carries two elemental analysis instruments. The MSL APXS is similar in design to previous APXS instruments, but is capable of conducting a chemical analysis with detection limits of 20 ppm for Br and 100 ppm for Ni in only three hours, an improvement over the MER APXS by a factor of 3 [42] [http://msl-scicorner.jpl.nasa.gov/Instruments/APXS/]. Quick-look analyses with an accuracy of ~0.5% for Na, Mg, Al, Si, Ca, Fe and S can be completed in 10 minutes with the MSL APXS [http://msl-scicorner.jpl.nasa.gov/Instruments/APXS/]. This improved performance is the result of increased detector sensitivity and the placement of the alpha particle source and detectors closer to the target. This close placement was achieved by removing the detectors used in previous APXS instruments for alpha backscatter mode. The inclusion of a Peltier cooler on

the MSL APXS detector extends the operational temperature range up to 5°C, enhancing daytime data collection [42].

MSL also carries the Chemistry and Camera (ChemCam) instrument, which uses laser-induced breakdown spectroscopy (LIBS) to rapidly determine the elemental composition of targets up to 7 meters away. The ChemCam analysis spot size is 200-500 μm, but analyses of multiple spots on samples can be used to estimate bulk composition [51], [54]. The shock wave from the LIBS plasma is capable of clearing away dust on a target's surface [48] and repeated shots can be used to create a depth profile of the upper ~400 μm of the target[208]. Each individual laser shot ablates a depth of <1 μm, allowing compositional data from the upper surface of the target to be obtained. ChemCam is also capable of passive spectroscopy over the 240-850 nm spectral range, although this capability is not a mission requirement and has not been studied in detail.

The MSL mission lacks a long-range spectrometer capable of identifying rocks and minerals from a distance in the way that Mini-TES did for MER. MSL will rely on multispectral MastCam observations to identify distant targets, followed by elemental analysis from ~7 m with ChemCam. Our work with Pancam and APXS and Mössbauer data indicates that extrapolating the results of in-situ or stand-off chemical analyses to distant targets will likely be difficult, particularly given the lack of a RAT on MSL. It will be important to use the brush and/or ChemCam to clear as much dust as possible from the targets to minimize the sampling differences between Mastcam and APXS and ChemCam. The chemical compositions derived from the first several ChemCam shots on each target provide compositional information about the upper several microns, and may show a closer correlation with the MastCam spectra than APXS measurements which average over a larger volume of the target.

The methods used in this study are useful for the analysis of multispectral and compositional datasets, even if the correlations between imaging and compositional datasets are often weak. K-means clustering can be used to define classes within any dataset and appears to have been effective for the compositional data at Meridiani, with the derived clusters corresponding to real geologic differences in target types. Likewise, k-means clustering of Pancam spectra led to distinct spectral classes. Once classes have been defined, either manually or with clustering algorithms, SIMCA can be used to formalize the classification of new samples and the identification of novel classes encountered as the mission progresses.

In addition to datasets similar to those on MER (e.g. MastCam, APXS), MSL will provide additional data, including X-ray diffraction (CheMin), and both passive and active ChemCam spectroscopy. Although our studies using MER data indicate that it is challenging to draw conclusions from inter-dataset correlations, it is important to search for these correlations using the instruments available on MSL to maximize the ability to identify targets of interest from a distance.

CHAPTER 6

CONCLUSIONS AND FUTURE WORK

The work contained in the previous chapters is united by the common theme of maximizing the science return from present and future planetary datasets. The methods and results in these chapters are broadly applicable and will have real implications during the upcoming MSL mission to Gale Crater. This chapter summarizes the most significant results from the preceding sections. Section 1 discusses the Gale Crater landing site and identifies hypotheses that can be tested with the rover. Section 2 summarizes the results of Chapters 3, 4, and 5, which deal with the application of multivariate methods to spectral datasets, and discusses the implications for MSL. Section 3 identifies future work that will build on the results of the previous chapters.

1. Gale Crater

The study of Gale crater in Chapter 2 defines many of the major units that will be encountered by MSL, and provides detailed descriptions and hypotheses regarding the origin and properties of these units. The numerous science targets in the MSL landing ellipse described in this work played an important role in the final selection of the landing site. Within the ellipse, MSL will be able to determine the stratigraphic relationship between the low thermal inertia and high thermal inertia fan units and the hummocky plains. Analysis of the high thermal inertia unit with the MSL payload will reveal the origin and composition of the high thermal inertia material. If the rover lands close enough to any of the sinuous ridges or chains of mesas, it will be able to test the hypothesis that these features are related to fluvial activity and if so, interpret the flow

conditions based on the sedimentology and stratigraphy of any observed beds. If the rover lands north or west of the alluvial fan, it will have access to the light-toned polygonal features in the hummocky plains unit that we interpret as erosion-resistant cemented fractures. MSL will also be able to study the mound-skirting unit and establish its stratigraphic relationship with other crater floor units and the mound. Surface observations will determine whether the observed ridges on the surface of the mound-skirting unit are lithified aeolian bedforms. Throughout the ellipse, sedimentary materials are likely to be derived from the crater wall, providing samples of Noachian-aged material.

As the rover crosses from the crater floor units to the lowest units of the mound, it will be able to test the hypothesized stratigraphy described in this work. In particular, in-situ observations will determine whether the phyllosilicate-bearing unit is a thin, extensive layer in the mound, or confined to the trough between the light-toned ridge and the rest of the mound. Rover observations will also be able to determine whether the lower mound layers in the light-toned ridge and the dark-toned layered yardang units were deposited in a lacustrine setting, or if they are aeolian or pyroclastic in origin. The putative pyroclastic origin of the thin mantling unit and the inferred physical properties of the light-toned yardang-forming unit can also be tested with rover observations.

The notional traverse will give the rover access to the "fan-shaped" outcrop of material on the flank of the mound at the end of the filled channel. Rover observations of this unit will test the hypothesis that it is not truly an alluvial fan, but instead is an outcrop of the more extensive mound-skirting unit. The rover will also be able to access examples of the polygonal ridges on the mound, interpreted in Chapter 2 as cemented fractures.

2. Multivariate Methods and Implications for MSL

Chapters 3 and 4 deal with the application of multivariate methods for qualitatively and quantitatively assessing LIBS data. These studies were conducted in preparation for operation of the ChemCam instrument on MSL, and have direct implications for the analysis of data during the mission. Chapter 3 demonstrates that PLS is generally the most accurate method of determining the composition of geologic targets with LIBS. Automated feature selection with genetic algorithms showed mixed results. A combination of feature selection, averaging and PLS had the lowest RMSE for several elements (Chapter 3, Table 4) but in the case of SiO_2, correlations in the training set led to the selection of spectral channels corresponding to K rather than Si, resulting in decreased accuracy. Despite these issues, feature selection performed relatively well using only five spectral channels rather than 6117, which makes it an attractive method of reducing data volume to enable the downlink of tactically important ChemCam data on sols that are data-limited. The study of grain size indicates that at least 15 spots should be analyzed for an accurate bulk-rock composition, and that even more spots are highly desirable, particularly if there is evidence (e.g. from Mastcam or the ChemCam remote micro-imager) that the target is clearly heterogeneous.

In most cases, the clustering methods that were compared in Chapter 4 led to reduced accuracy when compared to a PLS model trained on the complete training set. This suggests that a diverse dataset is the most reliable method for ensuring accurate compositions based on LIBS data. However, both k-means clustering and the iterative method described in Chapter 4 showed modest improvements over the un-clustered data. It is possible that more nuanced methods of clustering LIBS spectra may lead to greater improvements in accuracy.

In Chapter 5, we demonstrated that correlations between multispectral imaging and APXS and Mossbauer data are often weak. Some APXS classes contain targets with very different Pancam spectra (Chapter 4, Figure 13), while samples in different compositional classes can have nearly identical Pancam spectra (Chapter 4, Figure 12). The improved correlation between the red/blue spectral ratio and ferric phases when only grind spots were considered in the Gusev data (Chapter 4, Figure 9) suggests that some of the disparity between Pancam and the in-situ instruments may be related to the information depth of the measurements. On MSL, which lacks a long-range spectrometer, it will be particularly desirable to relate compositional measurements to multispectral observations from Mastcam. Although MSL lacks a rock abrasion tool such as the one carried by the MERs, it is possible that the shallow sampling depth of ChemCam will lead to more reliable correlations with MastCam spectra.

3. Future Work

With the selection of Gale Crater as the MSL landing site, there is great interest in detailed mapping of potential targets and hazards within the ellipse and along the proposed traverse. The work presented in this dissertation will provide a framework for more detailed studies taking advantage of increased HiRISE stereo and color coverage and new imaging techniques such as along-track oversampling with CRISM, which can sharpen the spatial resolution of observations to 6 m/pixel in the along-track direction [209]. Measurements of bedding plane geometry based on the HiRISE digital elevation models (e.g. [210]) may provide greater insight into the nature of the layered materials in the ellipse and the mound, which can then be tested in-situ by rover observations. In addition, careful measurement of the geometry of the polygonal fractures observed in the crater floor and mound units can be used to derive information about the physical properties of the fractured beds and the environmental conditions

that led to the formation of polygonal features. Such studies can then be followed by in-situ measurements by MSL to verify the stratigraphic context of the fractured units and determine the composition and origin of the polygonal features. With ground-truth on Mars for studies of polygonal features, interpretations can be extended to other occurrences of polygonal features elsewhere on the planet.

The ChemCam team is currently developing the multivariate analysis software that will be used to classify LIBS spectra and derive quantitative measurements of target composition. This software will include many of the algorithms discussed in this dissertation, as well as other multivariate methods that have been successfully applied to LIBS data. Although clustering the data prior to creating PLS models led to only modest improvements in Chapter 4, alternative methods of narrowing the training set used for quantitative analysis are being considered. For example, logical tests could be included in the training set selection algorithm to determine the most relevant anions in the target, so that sulfates are included only when sulfur emission lines are greater than a specified threshold, carbonates are included only when carbon lines are detected, and so on.

ChemCam will be uniquely sensitive to the light lithophile elements (LLEs; Li, Be, B) and N, and it will be important to include well-characterized standards that contain these elements in a range of abundances in the database of spectra used during the mission. This may be achieved by doping known geostandard materials or by collecting and analyzing natural samples from locations that are high in LLEs and nitrates, such as Death Valley and the Atacama Desert. LLEs are useful geochemical tracers of both igneous and aqueous processes. LLE abundance in igneous rocks correlates with the degree of crustal evolution and therefore can be used to test the hypothesis that the martian crust is basaltic and undifferentiated. Li, Be and B are

also concentrated in phyllosilicate minerals during weathering and alteration, and can be used to test the hypothesis that lakes early in the history of Mars were neutral to alkaline and that their salinity and acidity increased as the planet became increasingly arid. Nitrogen is the second most abundant gas in the martian atmosphere, but its abundance in surface deposits is unknown. Detection of nitrates on the surface would test the hypothesis that there is a steady-state nitrogen cycle on Mars, and because nitrogen is an essential element for life as we know it, an estimate of the planetary nitrogen budget would have implications for the habitability of Mars.

In addition to light element standards, we are in the process of fabricating a suite of glass analogs with compositions equivalent to the volatile-free composition of the major APXS classes observed at the MER landing sites. These analogs will serve as reference samples in the LIBS spectral database, providing examples with element correlations known to exist on Mars.

As indicated above, correlations between Mastcam multispectral observations and ChemCam compositional measurements may be stronger than the observed correlations between Pancam and APXS and Mossbauer data. The significantly larger number of LIBS analyses relative to contact instrument spots will also improve the statistics leading to more robust correlations. In addition to investigating these correlations, it may also be possible to identify distant targets by using the ChemCam spectrometer in passive mode. This will likely require measurements of diverse targets in passive mode under laboratory conditions on Earth, as well as the collection of passive and active ChemCam measurements of the same targets on the surface of Mars.

Finally, many of the data analysis methods explored in this dissertation are applicable to other orbital and in-situ datasets from Mars, the Moon, and other planetary bodies. Clustering and classification have been applied in a limited capacity to some multispectral and

hyperspectral observations of Mars (e.g. [211][212][213]). Neural networks similar to those employed to analyze LIBS data in Chapter 3 are commonly applied to terrestrial remote sensing data (e.g. AVIRIS, Landsat) to identify surface materials [150][214], and a combination of genetic algorithms and neural networks has been used to automate the interpretation of laboratory Mossbauer spectra [215].

4. Conclusion

This dissertation provides a detailed description of the Gale Crater landing site that will serve as a framework for future studies, both with orbital assets and on the surface with MSL. This work also includes the most thorough comparison of multivariate methods for the quantitative analysis of geologic samples using LIBS to date, the results of which are already playing a role in the development of data analysis software in preparation for ChemCam operations on MSL. As the volume of planetary remote-sensing and in-situ data rapidly increases, similar methods of clustering, classifying and interpreting large datasets will become increasingly important as tools to maximize the science return from future planetary missions.

REFERENCES

[1] D. Goods, “First TV Image of Mars.” [Online]. Available: http://directedplay.com/first_tv_image_of_mars.html.

[2] N. Goods, “PIA14033: First TV Image of Mars (Hand Colored),” *NASA Planetary Photojournal*. [Online]. Available: http://photojournal.jpl.nasa.gov/catalog/PIA14033.

[3] R. B. Leighton, B. C. Murray, R. P. Sharp, J. D. Allen, and R. K. Sloan, “Mariner IV photography of Mars: Initial results,” *Science*, vol. 149, no. 3684, p. 627, 1965.

[4] R. B. Leighton et al., “Mariner 6 and 7 television pictures: preliminary analysis.,” *Science*, vol. 166, no. 3901, pp. 49-67, Oct. 1969.

[5] H. Masursky et al., “Mariner 9 television reconnaissance of Mars and its satellites: Preliminary results,” *Science*, vol. 175, no. 4019, pp. 294-305, 1972.

[6] H. Masursky and N. L. Crabill, “The Viking landing sites: selection and certification.,” *Science*, vol. 193, no. 4255, pp. 809-12, Aug. 1976.

[7] M. H. Carr et al., “Preliminary results from the Viking orbiter imaging experiment.,” *Science*, vol. 193, no. 4255, pp. 766-76, Aug. 1976.

[8] T. A. Mutch et al., “The surface of Mars: the view from the Viking 2 lander.,” *Science*, vol. 194, no. 4271, pp. 1277-83, Dec. 1976.

[9] D. E. Smith, “The Global Topography of Mars and Implications for Surface Evolution,” *Science*, vol. 284, no. 5419, pp. 1495-1503, May 1999.

[10] M. C. Malin et al., “An overview of the 1985-2006 Mars Orbiter Camera science investigation,” *Mars*, vol. 5, pp. 1–60, 2010.

[11] P. R. Christensen et al., “Mars Global Surveyor Thermal Emission Spectrometer experiment: investigation description and surface science results,” *J. Geophys. Res.*, vol. 106, no. 10, pp. 23823-23871, 2001.

[12] P. R. Christensen et al., “The thermal emission imaging system (THEMIS) for the Mars 2001 Odyssey Mission,” *Space Science Reviews*, vol. 110, no. 1, pp. 85–130, 2004.

[13] W. V. Boynton et al., “The Mars Odyssey gamma-ray spectrometer instrument suite,” *Space Science Reviews*, vol. 110, pp. 37-83, 2004.

[14] A. Wilson, Ed., “Mars Express: The Scientific Payload.” ESA Publications Division, Noordwijk, The Netherlands, p. 216, 2004. http://www.esa.int/esapub/sp/sp1240/sp1240web.pdf

[15] A. S. McEwen et al., “Mars Reconnaissance Orbiter’s High Resolution Imaging Science Experiment (HiRISE),” *J. Geophys. Res*, vol. 112, p. E05S02, 2007.

[16] S. Murchie et al., “Compact reconnaissance imaging spectrometer for Mars (CRISM) on Mars reconnaissance orbiter (MRO),” *J. Geophys. Res*, vol. 112, no. 5, pp. 1-57, 2007.

[17] M. C. Malin et al., “Context camera investigation on board the Mars Reconnaissance Orbiter,” *J. Geophys. Res*, vol. 112, p. E05S04, 2007.

[18] M. Malin et al., “Mars Color Imager (MARCI) on the Mars Climate Orbiter,” *J. Geophys. Res*, vol. 106, no. 8, pp. 17651-17672, 2001.

[19] D. J. McCleese et al., “Mars Climate Sounder: An investigation of thermal and water vapor structure, dust and condensate distributions in the atmosphere, and energy balance of the polar regions,” *J. Geophys. Res.*, vol. 112, no. 5, pp. 1-16, May 2007.

[20] M. Golombek, R. Cook, H. Moore, and T. Parker, “Selection of the Mars Pathfinder landing site,” *J. Geophys. Res*, vol. 102, no. 2, pp. 3967-3988, 1997.

[21] P. Christensen, R. Morris, M. Lane, J. Bandfield, and M. Malin, “Global mapping of Martian hematite mineral deposits: Remnants of water-driven processes on early Mars,” *J. Geophys. Res.*, vol. 106, no. 10, pp. 23873–23, 2001.

[22] M. Golombek et al., “Mars Exploration Rover Landing Site Selection,” *Sixth International Conference on Mars*, p. 3222, 2003.

[23] M. P. Golombek et al., “Assessment of Mars Exploration Rover landing site predictions.,” *Nature*, vol. 436, no. 7047, pp. 44-8, Jul. 2005.

[24] S. W. Squyres et al., “In situ evidence for an ancient aqueous environment at Meridiani Planum, Mars.,” *Science*, vol. 306, no. 5702, pp. 1709-14, Dec. 2004.

[25] S. W. Squyres et al., “The Spirit rover’s Athena science investigation at Gusev crater, Mars,” *Science*, vol. 305, no. 5685, p. 794, 2004.

[26] R. Arvidson et al., “Mars Exploration Program 2007 Phoenix landing site selection and characteristics,” *J. Geophys. Res.*, vol. 113, no. E00A03, pp. 1-14, Jun. 2008.

[27] P. H. Smith et al., “H2O at the Phoenix landing site.,” *Science*, vol. 325, no. 5936, pp. 58-61, Jul. 2009.

[28] J. Grotzinger, “Beyond water on Mars,” *Nature Geoscience*, vol. 2, no. April, pp. 231-233, 2009.

[29] J. A. Grant et al., “The science process for selecting the landing site for the 2011 Mars Science Laboratory,” *Planetary and Space Science*, vol. 59, no. 11-12, pp. 1114-1127, Jun. 2010.

[30] R. Milliken, J. Grotzinger, and B. Thomson, “Paleoclimate of Mars as captured by the stratigraphic record in Gale Crater,” *Geophysical Research Letters*, vol. 37, p. L04201, 2010.

[31] NASA/JPL, “NASA’s Next Mars Rover to Land at Gale Crater,” 2011. [Online]. Available: http://mars.jpl.nasa.gov/news/whatsnew/index.cfm?FuseAction=ShowNews&NewsID=1141.

[32] M. C. Malin et al., “The Mars Science Laboratory (MSL) Mast-mounted Cameras (Mastcams) Flight Instruments,” *Lunar and Planetary Institute Science Conference Abstracts*, vol. 41, no. 1123, 2010.

[33] K. S. Edgett et al., “The Mars Hand Lens Imager (MAHLI) Aboard the Mars Rover, Curiosity,” in *Workshop on the Microstructure of the Martian Surface*, 2009, p. 5.

[34] M. C. Malin et al., “The Mars Science Laboratory (MSL) Mars Descent Imager (MARDI) Flight Instrument,” *Lunar and Planetary Science Conference*, vol. 40, no. 1199, 2009.

[35] NASA/JPL, “MSL Science Corner: Sampling System.” [Online]. Available: http://msl-scicorner.jpl.nasa.gov/samplingsystem/.

[36] D. Blake et al., “The CheMin mineralogical instrument on the Mars Science Laboratory mission,” *Lunar and Planetary Science Conference*, vol. 40, p. 1484, 2009.

[37] D. Blake, “A Historical Perspective of the Development of the CheMin Mineralogical Instrument for the Mars Science Laboratory Mission,” *Geochemical Society*, vol. 144, 2010.

[38] P. Mahaffy, M. Cabane, P. Conrad, and C. Webster, “Sample Analysis at Mars (SAM) Instrument Suite for the 2011 Mars Science Laboratory,” in *Lunar and Planetary Science Conference*, 2009, vol. 40, no. 2009, p. 1088.

[39] J. Gomez-Elvira et al., “Rover Environmental Monitoring Station for MSL mission,” in *4th International Workshop on the Mars Atmosphere: Modelling and Observations*, 2011.

[40] D. M. Hassler et al., “The Radiation Assessment Detector (RAD) on the Mars Science Laboratory (MSL),” *Lunar and Planetary Science Conference*, vol. 40, no. 2297, 2009.

[41] I. G. Mitofranov, M. L. Litvak, A. S. Kozyrev, M. I. Mokrousov, A. B. Sanin, and V. Tretyakov, “Dynamic Albedo of Neutrons (DAN): Active Nuclear Experiment Onboard NASA Mars Science Laboratory,” *Lunar and Planetary Science Conference*, vol. 36, no. 1635, 2005.

[42] R. Gellert et al., “The Alpha-Particle-X-Ray-Spectrometer (APXS) for the Mars Science Laboratory(MSL) Rover Mission,” *Lunar and Planetary Science Conference*, vol. 40, no. 2364, 2009.

[43] R. Gellert et al., “The Alpha-Particle-X-Ray-Spectrometer (APXS) for the Mars Science Laboratory(MSL) Rover Mission,” *Lunar and Planetary Science Conference*, vol. 40, no. 2364, 2009.

[44] R. C. Wiens, S. Maurice, and C. Team, “The ChemCam Instrument Suite on the Mars Science Laboratory Rover Curiosity : Remote Sensing by Laser-Induced Plasmas,” *Geochemical News*, vol. 145, 2011.

[45] E. Runge, R. W. Minck, and F. R. Bryan, “Spectrochemical analysis using a pulsed laser source,” *Spectrochimica Acta*, vol. 20, no. 4, pp. 733–736, 1964.

[46] A. K. Knight, N. L. Scherbarth, D. A. Cremers, and M. J. Ferris, “Characterization of laser-induced breakdown spectroscopy (LIBS) for application to space exploration,” *Applied Spectroscopy*, vol. 54, no. 3, pp. 331–340, 2000.

[47] E. Tognoni et al., “From Sample to Signal in laser-induced breakdown spectroscopy: a complex route to quantitative analysis,” in *Laser-Induced Breakdown Spectroscopy (LIBS)*, A. W. Miziolek, V. Palleschi, and I. Schecter, Eds. New York: Cambridge University Press, 2006, pp. 122-167.

[48] T. G. Graff, R. V. Morris, S. M. Clegg, R. C. Wiens, and R. B. Anderson, “Dust Removal on Mars Using Laser-Induced Breakdown Spectroscopy,” *Lunar and Planetary Science Conference*, vol. 42, no. 1916, 2011.

[49] S. M. Clegg, E. Sklute, M. D. Dyar, J. E. Barefield, and R. C. Wiens, “Multivariate analysis of remote laser-induced breakdown spectroscopy spectra using partial least squares, principal component analysis, and related techniques,” *Spectrochimica Acta Part B: Atomic Spectroscopy*, vol. 64, no. 1, pp. 79–88, Jan. 2009.

[50] D. A. Cremers, L. J. Radziemski, and J. Wiley, *Handbook of laser-induced breakdown spectroscopy*. Wiley Online Library, 2006.

[51] J. R. Thompson, R. C. Wiens, J. E. Barefield, D. T. Vaniman, H. E. Newsom, and S. M. Clegg, “Remote laser-induced breakdown spectroscopy analyses of Dar al Gani 476 and Zagami Martian meteorites,” *J. Geophys. Res.*, vol. 111, p. E05006, 2006.

[52] J. M. Tucker, M. D. Dyar, M. W. Schaefer, S. M. Clegg, and R. C. Wiens, “Optimization of laser-induced breakdown spectroscopy for rapid geochemical analysis,” *Chemical Geology*, vol. 277, no. 1-2, pp. 137-148, Oct. 2010.

[53] R. Anderson, “Geologic Mapping and Characterization of Gale Crater and Implications for its Potential as a Mars Science Laboratory Landing Site,” *Mars*, no. 1978, 2010.

[54] R. Anderson et al., “The influence of multivariate analysis methods and target grain size on the accuracy of remote quantitative chemical analysis of rocks using laser induced breakdown spectroscopy,” *Icarus*, vol. 215, pp. 608-627, Aug. 2011.

[55] R. Greeley and J. Guest, “Geologic map of the eastern equatorial region of Mars,” *USGS Miscellaneous Investigations Series: Atlas of Mars, 1:15,000,000*, no. Map I-1802-B, 1987.

[56] N. Cabrol, E. Grin, H. Newsom, and R. Landheim, “Hydrogeologic evolution of Gale crater and its relevance to the exobiological exploration of Mars,” *Icarus*, vol. 139, pp. 235-245, 1999.

[57] N. T. Bridges, “Assessing Layered Materials in Gale Crater,” *First Landing Site Workshop for MER 2003*, no. 9033, 2001.

[58] D. H. Scott, E. C. Morris, and M. N. West, “Geologic map of the Aeolis quadrangle of Mars,” *USGS Miscellaneous Investigations Series: Atlas of Mars, 1:5,000,000*, no. 1111, 1978.

[59] D. H. Scott and M. G. Chapman, “Geologic and topographic maps of the Elysium paleolake basin,” *USGS Miscellaneous Investigations Series: Atlas of Mars, 1:5,000,000*, no. 2397, 1995.

[60] M. C. Malin and K. S. Edgett, “Sedimentary rocks of early Mars,” *Science*, vol. 290, no. 5498, p. 1927, 2000.

[61] S. M. Pelkey and B. M. Jakosky, “Surficial geologic surveys of Gale Crater and Melas Chasma, Mars: Integration of remote-sensing data,” *Icarus*, vol. 160, no. 2, pp. 228–257, 2002.

[62] S. M. Pelkey, B. M. Jakosky, and P. R. Christensen, “Surficial properties in Gale Crater, Mars, from Mars Odyssey THEMIS data,” *Icarus*, vol. 167, no. 2, pp. 244–270, 2004.

[63] B. J. Thomson, N. T. Bridges, R. Milliken, W. C. Calvin, and C. M. Weitz, “New Constraints on the Origin and Evolution of the Layered Deposits in Gale Crater, Mars,” *Lunar and Planetary Science Conference*, vol. 39, no. 1456, 2008.

[64] J. R. Zimbelman, “Preliminary Geologic Map of the MC-23 NW Quadrangle, Mars: Lower Member of the Medusae Fossae Formation,” *Lunar and Planetary Science Conference*, vol. 42, no. 1840, 2011.

[65] A. P. Rossi, G. Neukum, and M. Pondrelli, “Large-scale spring deposits on Mars?,” *J. Geophys. Res.*, vol. 113, p. E08016, 2008.

[66] A. Rogers and J. L. Bandfield, “Mineralogical characterization of Mars Science Laboratory candidate landing sites from THEMIS and TES data,” *Icarus*, vol. 203, no. 2, pp. 437-453, 2009.

[67] E. Hamilton, M. M. Osterloo, and B. S. Mcgrane, “THEMIS Decorrelation Stretched Infrared Mosaics od Candidate 2009 Mars Science Laboratory Landing Sites: Evidence for Significant Spectral Diversity,” *Lunar and Planetary Science Conference*, vol. 1725, 2007.

[68] R. Fergason, P. Christensen, and H. H. Kieffer, “High-resolution thermal inertia derived from the Thermal Emission Imaging System (THEMIS): Thermal model and applications,” *J. Geophys. Res.*, vol. 111, p. E12004, 2006.

[69] J. F. Bell III, K. Edgett, S. Rowland, and M. C. Malin, “The Gale Crater Mound: A Strong Candidate Landing Site for the 2009 Mars Science Laboratory,” *1st MSL Landing Site Workshop*, 2006.

[70] N. T. Bridges, “Studies of Martian Sedimentological History Through In-Situ Study of Gale and Oudemans Craters: Two Landing Site Proposals for the Mars Science Laboratory,” *1st MSL Landing Site Workshop*, 2006.

[71] B. J. Thomson, N. T. Bridges, J. F. Bell III, R. E. Milliken, and W. M. Calvin, “Gale Crater layered mound : A closed hydrologic system,” *2nd MSL Landing Site Workshop*, 2007.

[72] B. Thomson, N. Bridges, and J. P. L. Caltech, “Gale Crater : Context and layer diversity from HiRISE images Key Moon-Mars differences,” *3rd MSL Landing Site Workshop*, 2008.

[73] R. E. Milliken, “THEMIS, TES and CRISM Data of Gale,” *3rd MSL Landing Site Workshop*, 2008.

[74] R. Milliken et al., “Clay and Sulfate-Bearing Rocks in a Stratigrahpic Sequence in Gale Crater,” *Lunar and Planetary Science Conference*, vol. 1479, 2009.

[75] J. P. Bibring et al., “Global mineralogical and aqueous Mars history derived from OMEGA/Mars Express data,” *Science*, vol. 312, pp. 400-404, 2006.

[76] J. F. Bell III and Others, “Calibration and Performance of the Mars Reconnaissance Orbiter Context Camera (CTX),” *J. Geophys. Res*, vol. Submitted, 2011.

[77] S. Pelkey et al., “CRISM multispectral summary products: Parameterizing mineral diversity on Mars from reflectance,” *J. Geophys. Res*, vol. 112, pp. 1–18, 2007.

[78] A. Gillespie, A. Kahle, and R. Walker, “Color enhancement of highly correlated images. I. Decorrelation and HSI contrast stretches,” *Remote Sensing of Environment*, vol. 20, no. 3, pp. 209-235, Dec. 1986.

[79] M. Zuber et al., “The Mars Observer laser altimeter investigation,” *J. Geophys. Res.*, vol. 97, no. 5, pp. 7781–7797, 1992.

[80] M. J. Broxton and L. J. Edwards, “The Ames Stereo Pipeline: Automated 3D Surface Reconstruction from Orbital Imagery,” *Lunar and Planetary Science Conference*, vol. 39, no. 2419, 2008.

[81] L. J. Edwards and M. J. Broxton, “Automated 3D Surface Reconstruction from Orbital Imagery,” in *Space 2006*, 2006, vol. 2006, pp. 1-7.

[82] K. S. Edgett and P. R. Christensen, “Mars aeolian sand: Regional variations among dark-hued crater floor features,” *J. Geophys. Res.*, vol. 99, no. 1, pp. 1997-2018, 1994.

[83] J. B. Garvin, S. E. H. Sakimoto, and J. J. Frawley, “Craters on Mars: Global Geometric Properties from Gridded MOLA Topography,” *Sixth International Conference on Mars*, no. 3277, 2003.

[84] R. J. Pike, “Control of crater morphology by gravity and target type: Mars, Earth, Moon,” *Lunar and Planetary Science Conference*, vol. 11, pp. 2159-2189, 1980.

[85] C. Pain, J. Clarke, and M. Thomas, “Inversion of relief on Mars,” *Icarus*, vol. 190, no. 2, pp. 478–491, 2007.

[86] R. Williams, R. P. Irwin III, and J. R. Zimbelman, “Evaluation of paleohydrologic models for terrestrial inverted channels: Implications for application to martian sinuous ridges,” *Geomorphology*, vol. 107, no. 3-4, pp. 300-315, 2009.

[87] J. Maizels, “Raised channel systems as indicators of palaeohydrologic change: a case study from Oman,” *Palaeogeography, palaeoclimatology, palaeoecology*, vol. 76, no. 3-4, pp. 241–277, Jan. 1990.

[88] K. S. Edgett, “The International Journal of Mars Science and Exploration The sedimentary rocks of Sinus Meridiani : Five key observations from data acquired by the Mars Global Surveyor and Mars Odyssey orbiters,” *Mars*, vol. 1, pp. 5-58, 2005.

[89] J. S. Kargel and R. G. Strom, “Ancient glaciation on Mars,” *Geology*, vol. 20, pp. 3-7, 1992.

[90] K. S. Edgett and M. C. Malin, “The Sedimentary Rocks of Mars: A Global Perspective,” *Geological Society of America Annual Meeting*, vol. 37, no. 7, pp. 249-1, 2005.

[91] M. Bakalowicz, D. Ford, T. Miller, A. N. Palmer, and M. V. Palmer, “Thermal genesis of dissolution caves in the Black Hills, South Dakota,” *Bulletin of the Geological Society of America*, vol. 99, no. 6, p. 729, 1987.

[92] C. Okubo and A. S. Mcewen, “Fracture-controlled paleo-fluid flow in Candor Chasma, Mars,” *Science*, vol. 315, pp. 983-985, 2007.

[93] K. K. E. Neuendorf, J. P. Mehl, and J. A. Jackson, Eds., *Glossary of Geology*, 5th ed. Alexandria, Virginia: American Geological Institute, 2005.

[94] L. Kerber and J. W. Head, "The Age of the Medusae Fossae Formation: Evidence of Hesperian Emplacement from crater morphology, stratigraphy and ancient lava flows," *Icarus*, vol. 206, no. 2, pp. 669-684, 2010.

[95] N. Bridges, M. Banks, R. Beyer, and F. Chuang, "Aeolian bedforms, yardangs, and indurated surfaces in the Tharsis Montes as seen by the HiRISE Camera: Evidence for dust aggregates," *Icarus*, vol. 205, no. 1, pp. 165-182, 2010.

[96] J. F. McCauley, "White Rock: A Martian Enigma," *NASA Special Publications*, vol. 329, pp. 170-171, 1974.

[97] S. Ruff, P. Christensen, and R. Clark, "Mars' 'White Rock' feature lacks evidence of an aqueous origin: Results from Mars Global Surveyor," *J. Geophys. Res*, vol. 106, no. 10, pp. 23921-23927, 2001.

[98] D. M. Rubin and C. L. Carter, "Bedforms and Cross Bedding in Animation," in *SEPM Atlas Series No. 2*, Santa Cruz, CA: U.S. Geological Survey, 2006.

[99] K. Edgett, "MRO CTX and MGS MOC Observations Regarding Small Impact Craters and Substrate Resistance to Erosion on Mars," *American Astronomical Society*, vol. DPS Meetin, no. 58.06, 2009.

[100] W. B. Whalley and F. Azizi, "Rock glaciers and protalus landforms: Analogous forms and ice sources on Earth and Mars," *J. Geophys. Res*, vol. 108, no. 4, p. 8032, 2003.

[101] D. Masson, Q. Huggett, and D. Brunsden, "The surface texture of the Saharan Debris Flow deposit and some speculations on submarine debris flow processes," *Sedimentology*, vol. 40, no. 3, pp. 583–598, 1993.

[102] P. Francis, M. Gardeweg, C. Ramirez, and D. Rothery, "Catastrophic debris avalanche deposit of Socompa volcano, northern Chile," *Geology*, vol. 13, no. 9, p. 600, 1985.

[103] M. Cutigni et al., "Incoherent Simulator for Mars Surface Applied to the Analysis of Sharad Radar Data," *American Geophysical Union Fall Meeting*, vol. P11B-0546, 2007.

[104] J. J. Degenhardt and J. R. Giardino, "Subsurface investigation of a rock glacier using ground-penetrating radar: Implications for locating stored water on Mars," *J. Geophys. Res*, vol. 108, no. 4, p. 8036, 2003.

[105] J. W. Holt et al., "Radar sounding evidence for buried glaciers in the southern mid-latitudes of Mars," *Science*, vol. 322, p. 1235, 2008.

[106] R. Sullivan et al., "Wind-driven particle mobility on Mars : Insights from Mars Exploration Rover observations at 'El Dorado' and surroundings at Gusev Crater," *J. Geophys. Res*, vol. 113, p. E06S07, 2008.

[107] K. Edgett and M. Malin, "Rock stratigraphy in Gale Crater, Mars," *Lunar and Planetary Science Conference*, vol. 32, no. 1005, 2001.

[108] W. K. Hartmann and G. Neukum, "Cratering chronology and the evolution of Mars," *Space Science Reviews*, vol. 96, no. 1, pp. 165–194, 2001.

[109] B. M. Hynek, R. J. Phillips, and R. E. Arvidson, “Explosive volcanism in the Tharsis region: Global evidence in the Martian geologic record,” *J. Geophys. Res*, vol. 108, no. 9, p. 5111, 2003.

[110] L. Wilson and J. W. Head, “Explosive volcanic eruptions on Mars: Tephra and accretionary lapilli formation, dispersal and recognition in the geologic record,” *Journal of volcanology and geothermal research*, vol. 163, no. 1-4, pp. 83–97, 2007.

[111] L. Wilson, “Tephra deposition on glaciers and ice sheets on Mars: Influence on ice survival, debris content and flow behavior,” *Journal of Volcanology and Geothermal Research*, vol. 185, no. 4, pp. 290-297, 2009.

[112] J. a. Grant et al., “HiRISE imaging of impact megabreccia and sub-meter aqueous strata in Holden Crater, Mars,” *Geology*, vol. 36, no. 3, p. 195, 2008.

[113] R. E. Arvidson et al., “Localization and physical properties experiments conducted by Spirit at Gusev Crater,” *Science*, vol. 305, p. 821, 2004.

[114] C. Sagan, D. Pieri, P. Fox, R. Arvidson, and E. Guinness, “Particle motion on Mars inferred from the Viking lander cameras,” *J. Geophys. Res.*, vol. 82, no. 28, pp. 4430–4438, 1977.

[115] N. T. Bridges, J. E. Laity, R. Greeley, J. Phoreman, and E. E. Eddlemon, “Insights on rock abrasion and ventifact formation from laboratory and field analog studies with applications to Mars,” *Planetary and Space Science*, vol. 52, no. 1-3, pp. 199–213, 2004.

[116] O. Bordovskiy, “Accumulation of organic matter in bottom sediments,” *Marine Geology*, vol. 3, no. 1-2, pp. 33-82, Apr. 1965.

[117] J. Hedges, “Sedimentary organic matter preservation: an assessment and speculative synthesis,” *Marine Chemistry*, vol. 49, pp. 81-115, 1995.

[118] R. E. Summons, P. Albrecht, G. McDonald, and J. M. Moldowan, “Molecular Biosignatures,” *Space Science Reviews*, vol. 135, no. 1-4, pp. 133-159, Oct. 2007.

[119] M. J. Kennedy, D. R. Pevear, and R. J. Hill, “Mineral surface control of organic carbon in black shale.,” *Science*, vol. 295, pp. 657-660, Jan. 2002.

[120] M. Walter and D. J. Des Marais, “Preservation of biological information in thermal spring deposits: developing a strategy for the search for fossil life on Mars,” *Icarus*, vol. 101, pp. 129–143, 1993.

[121] R. Martin, *Taphonomy: A Process Approach*. Cambridge, United Kingdom: Cambridge Unviersity Press, 1999.

[122] D. Y. Sumner, “Poor preservation potential of organics in Meridiani Planum hematite-bearing sedimentary rocks,” *J. Geophys. Res.*, vol. 109, p. E12007, 2004.

[123] G. Eglinton and G. a Logan, “Molecular preservation,” *Philosophical transactions of the Royal Society of London. Series B, Biological sciences*, vol. 333, no. 1268, pp. 315-27; discussion 327-8, Sep. 1991.

[124] A. Aubrey et al., “Sulfate minerals and organic compounds on Mars,” *Geology*, vol. 34, no. 5, pp. 357-360, 2006.

[125] G. Kminek, “The Effect of Ionizing Radiation on Amino Acids and Bacterial Spores in Different Geo- and Cosmochemical Environments,” University of California, San Diego, 2003.

[126] N. L. Lanza et al., “Calibrating the ChemCam laser-induced breakdown spectroscopy instrument for carbonate minerals on Mars,” *Applied Optics*, vol. 49, no. 13, p. C211, Apr. 2010.

[127] J. B. Sirven, B. Bousquet, L. Canioni, and L. Sarger, “Laser-induced breakdown spectroscopy of composite samples: Comparison of advanced chemometrics methods,” *Anal. Chem*, vol. 78, no. 5, pp. 1462–1469, 2006.

[128] V. Motto-Ros, A. S. Koujelev, G. R. Osinski, and A. E. Dudelzak, “Quantitative multi-elemental laser-induced breakdown spectroscopy using artificial neural networks,” *Journal of the European Optical Society: Rapid Publications*, vol. 3, Mar. 2008.

[129] K. Govindaraju, “Compilation of Working Values and Sample Descriptions for 383 Geostandards,” *Geostandards Newsletter*, vol. 18, no. Special Issue, pp. 1-158, 1994.

[130] S. Mertzman, “K-Ar results from the southern Oregon-northern California Cascade Range,” *Oregon Geology*, vol. 62, no. 4, pp. 99–122, 2000.

[131] L. E. Reichen and J. J. Fahey, “An improved method for the determination of FeO in rocks and minerals including garnet,” *U.S. Geol. Surv. Bull.*, vol. 1144, pp. 1-5, 1962.

[132] S. W. Squyres et al., “Athena Mars rover science investigation,” *J. Geophys. Res.*, vol. 108, no. 12, p. 8062, 2003.

[133] M. D. Dyar, J. M. Tucker, S. Humphries, S. M. Clegg, R. C. Wiens, and M. D. Lane, “Strategies for Mars remote Laser-Induced Breakdown Spectroscopy analysis of sulfur in geological samples,” *Spectrochimica Acta Part B: Atomic Spectroscopy*, vol. 66, no. 1, pp. 39-56, Jan. 2011.

[134] J. C. Davis, *Statistics and Data Analysis in Geology*. New York: John Wiley and Sons Pubs., 1986, pp. 527-546.

[135] S. Karunatillake et al., “Recipes for spatial statistics with global datasets : A Martian case study,” *Journal of Scientific Computing*, pp. 2-49, 2010.

[136] J. F. Kenney and E. S. Keeping, *Mathematics of Statistics, Pt. 2*, 2nd ed. Princeton, Nj: Van Nostrand, 1951.

[137] R. Leardi and A. L. González, “Genetic algorithms applied to feature selection in PLS regression: how and when to use them,” *Chemometrics and Intelligent Laboratory Systems*, vol. 41, no. 2, pp. 195–207, 1998.

[138] H. C. Goicoechea and A. C. Olivieri, “Wavelength selection for multivariate calibration using a genetic algorithm: a novel initialization strategy.,” *Journal of chemical information and computer sciences*, vol. 42, no. 5, pp. 1146-53, 2002.

[139] R. M. Jarvis and R. Goodacre, “Genetic algorithm optimization for pre-processing and variable selection of spectroscopic data.,” *Bioinformatics*, vol. 21, no. 7, pp. 860-8, Apr. 2005.

[140] R. Leardi, “Application of genetic algorithm-PLS for feature selection in spectral data sets,” *Journal of Chemometrics*, vol. 14, no. 5-6, pp. 643-655, Sep. 2000.

[141] J. H. Holland, *Adaptation in Natural and Artificial Systems*. Cambridge, MA: MIT Press, 1992.

[142] R. M. Jarvis, D. Broadhurst, H. Johnson, N. M. O’Boyle, and R. Goodacre, “PYCHEM: a multivariate analysis package for python.,” *Bioinformatics (Oxford, England)*, vol. 22, no. 20, pp. 2565-6, Oct. 2006.

[143] H. Abdi, “Partial Least Squares,” in *Encyclopedia of Social Sciences Research Methods*, M. Lewis-Beck, A. Bryman, and T. Futing, Eds. Thousand Oaks (CA): Sage, 2003.

[144] M. . Gardner and S. . Dorling, “Artificial neural networks (the multilayer perceptron)—a review of applications in the atmospheric sciences,” *Atmospheric Environment*, vol. 32, no. 14-15, pp. 2627-2636, Aug. 1998.

[145] J. R. Long, V. G. Gregoriou, and P. J. Gemperline, “Spectroscopic calibration and quantitation using artificial neural networks,” *Anal. Chem.*, vol. 62, no. 17, pp. 1791-1797, Sep. 1990.

[146] Y. Ninomiya, “Quantitative estimation of SiO 2 content in igneous rocks using thermal infrared spectra with a neural network approach,” *Geoscience and Remote Sensing, IEEE Transactions on*, vol. 33, no. 3, pp. 684–691, 1995.

[147] T. Udelhoven and B. Schutt, “Capability of feed-forward neural networks for a chemical evaluation of sediments with diffuse reflectance spectroscopy,” *Chemometrics and Intelligent Laboratory Systems*, vol. 51, no. 1, pp. 9-22, May 2000.

[148] W. S. Sarle, “Neural networks and statistical models,” in *Proceedings of the Nineteenth Annual SAS Users Group International Conference*, 1994.

[149] S. Liang and A. Strahler, “Retrieval of land surface albedo from satellite observations: A simulation study,” in *Geoscience and Remote Sensing, IEEE Transactions on*, 2002, vol. 4556, no. 301, pp. 1286-1288.

[150] H. Yang, “A back-propagation neural network for mineralogical mapping from AVIRIS data,” *International Journal of Remote Sensing*, vol. 20, no. 1, pp. 97-110, 1999.

[151] D. E. Rumelhart, G. E. Hinton, and R. J. Williams, “Learning internal representations by error propagation,” La Jolla, CA, 1985.

[152] P. Inakollu, “A study of the effectiveness of neural networks for elemental concentration from LIBS spectra,” 2003.

[153] E. Ferreira, D. Milori, R. Dasilva, and L. Martinneto, “Artificial neural network for Cu quantitative determination in soil using a portable Laser Induced Breakdown Spectroscopy system,” *Spectrochimica Acta Part B: Atomic Spectroscopy*, vol. 63, no. 10, pp. 1216-1220, Oct. 2008.

[154] G. Bebis, M. Georgiopoulos, and T. Kasparis, “Coupling weight elimination with genetic algorithms to reduce network size and preserve generalization,” *Neurocomputing*, vol. 17, no. 3-4, pp. 167–194, 1997.

[155] F. F. Leung, H. K. Lam, S. H. Ling, and P. S. Tam, "Tuning of the structure and parameters of a neural network using an improved genetic algorithm.," *IEEE transactions on neural networks / a publication of the IEEE Neural Networks Council*, vol. 14, no. 1, pp. 79-88, Jan. 2003.

[156] P. Benardos and G. Vosniakos, "Optimizing feedforward artificial neural network architecture," *Engineering Applications of Artificial Intelligence*, vol. 20, no. 3, pp. 365-382, Apr. 2007.

[157] M. Mitchell, *An introduction to genetic algorithms*. The MIT press, 1998.

[158] S. E. Fahlman and C. Lebiere, "The Cascade Correlation Learning Architecture," in *Advances in Neural Information Processing Systems II*, D. S. Touretzky, G. Hinton, and T. Sejnowski, Eds. San Mateo, CA: Morgan Kaufmann, 1990.

[159] S. Nissen, "Implementation of a fast artificial neural network library (fann)," *Report, Department of Computer Science University of Copenhagen (DIKU)*, vol. 31, 2003.

[160] R. Gellert et al., "Alpha Particle X-ray Spectrometer (APXS): Results from Gusev crater and calibration report," *J. Geophys. Res.*, vol. 111, p. E02S05, 2006.

[161] D. Ming et al., "Geochemical properties of rocks and soils in Gusev Crater, Mars: Results of the Alpha Particle X-Ray Spectrometer from Cumberland Ridge to Home Plate," *J. Geophys. Res.*, vol. 113, p. E12S39, 2008.

[162] S. W. Squyres et al., "Detection of silica-rich deposits on Mars.," *Science*, vol. 320, no. 5879, pp. 1063-7, May 2008.

[163] S. Abbey, "Studies in 'Standard Samples' of silicate rocks minerals 1969-1982," *Geological Survey of Canada*, vol. Paper 83-1, pp. 1-114, 1983.

[164] A. Cousin, O. Forni, S. Maurice, J. Lasue, O. Gasnault, and R. Wiens, "Independent Component Analysis Classification for CehmCam Remote Sensing Data," *Lunar and Planetary Science Conference*, vol. 42, p. 1973, 2011.

[165] M. D. Dyar et al., "Error Analysis for Remote Laser-Induced Breakdown Spectroscopy Analysis Using Combinations of Igneous, Sedimentary and Phyllosilicate Samples," *Lunar and Planetary Science Conference*, vol. 42, p. 1258, 2011.

[166] A. Miziolek, V. Palleschi, and I. Schechter, Eds., *Laser-Induced Breakdown Spectroscopy (LIBS)*. New York: Cambridge University Press, 2006.

[167] T. Næs, "The design of calibration in near infra-red reflectance analysis by clustering," *Journal of chemometrics*, vol. 1, no. 2, pp. 121–134, 1987.

[168] P. J. Zemroch, "Cluster analysis as an experimental design generator, with application to gasoline blending experiments," *Technometrics*, vol. 28, no. 1, pp. 39–49, 1986.

[169] T. Isaksson and T. Næs, "Selection of samples for calibration in near-infrared spectroscopy. Part II: Selection based on spectral measurements," *Applied Spectroscopy*, vol. 44, no. 7, pp. 1152–1158, 1990.

[170] D. J. C. MacKay, "An Example Inference Task : Clustering," in *Information Theory, Inference and Learning Algorithms*, no. x, Cambridge, United Kingdom: Cambridge University Press, 2003, pp. 284-292.

[171] F. S. de Oliveira, L. S. Gomes Teixeira, M. C. Ugulino Araujo, and M. Korn, "Screening analysis to detect adulterations in Brazilian gasoline samples using distillation curves," *Fuel*, vol. 83, no. 7-8, pp. 917-923, May 2004.

[172] N. B. Vogt et al., "Polycyclic aromatic hydrocarbons in soil and air: statistical analysis and classification by the SIMCA method," *Environmental Science & Technology*, vol. 21, no. 1, pp. 35-44, Jan. 1987.

[173] K. Esbensen, D. Guyot, F. Westad, and L. P. Houmøller, *Multivariate Data Analysis: In Practice: An introduction to multivariate data analysis and experimental design*, 5th ed., no. 91. CAMO Process AS, 2004.

[174] C. Fraley and A. E. Raftery, "MCLUST version 3 for R: Normal mixture modeling and model-based clustering," Seattle, WA, 2006.

[175] J. Lasue, R. C. Wiens, T. F. Stepinski, O. Forni, S. M. Clegg, and S. Maurice, "Nonlinear mapping technique for data visualization and clustering assessment of LIBS data: application to ChemCam data.," *Analytical and bioanalytical chemistry*, Feb. 2011.

[176] R. C. Wiens et al., "Calibration of the MSL/ChemCam/LIBS Remote Sensing Composition Instrument," *Lunar and Planetary Science Conference*, vol. 42, p. 2370, 2011.

[177] D. Evans and J. B. Adams, "Comparison of Viking Lander multispectral images and laboratory reflectance spectra of terrestrial samples," in *Proc. Lunar Planet Sci. Conf. 10th*, 1979, vol. 10, pp. 1829-1834.

[178] T. Mutch et al., "Imaging Experiment: The Viking Lander," *Icarus*, vol. 16, no. 1, pp. 92–110, 1972.

[179] B. C. Clark et al., "The Viking X Ray Fluorescence Experiment: Analytical Methods and Early Results," *J. Geophys. Res.*, vol. 82, no. 28, pp. 4577-4594, 1977.

[180] P. Smith et al., "The imager for Mars Pathfinder experiment," *J. Geophys. Res.*, vol. 102, no. 2, pp. 4003–4025, 1997.

[181] R. Rieder, H. Wänke, T. Economou, and A. Turkevich, "Determination of the chemical composition of Martian soil and rocks: The alpha proton X ray spectrometer," *J. Geophys. Res.*, vol. 102, no. 2, pp. 4027-4044, 1997.

[182] J. Bell et al., "Mineralogic and compositional properties of Martian soil and dust- Results from Mars Pathfinder," *J. Geophys. Res.*, vol. 105, no. 1, pp. 1721-1755, 2000.

[183] M. Lemmon et al., "The Phoenix surface stereo imager (SSI) investigation," *Lunar and Planetary Institute Science Conference Abstracts*, vol. 39, no. 2156, 2008.

[184] J. Bell III et al., "Mars Exploration Rover Athena Panoramic Camera (Pancam) investigation," *J. Geophys. Res.*, vol. 108, no. 12, p. 8063, 2003.

[185] R. Rieder et al., "The new Athena alpha particle X-ray spectrometer for the Mars Exploration Rovers," *J. Geophys. Res*, vol. 108, no. 10.1029, 2003.

[186] J. Brückner et al., "Mars Exploration Rovers – Chemical Composition by the APXS," in *The Martian Surface: Composition, Mineralogy, and Physical Properties*, J. F. Bell III, Ed. Cambridge University Press, 2008, pp. 58-101.

[187] R. V. Morris et al., "Mössbauer mineralogy of rock, soil, and dust at Gusev crater, Mars: Spirit's journey through weakly altered olivine basalt on the plains and pervasively altered basalt in the Columbia Hills," *J. Geophys. Res.*, vol. 111, p. E02S13, 2006.

[188] R. V. Morris et al., "Iron mineralogy and aqueous alteration from Husband Hill through Home Plate at Gusev Crater, Mars: Results from the Mössbauer instrument on the Spirit Mars Exploration Rover," *J. Geophys. Res.*, vol. 113, p. E12S42, Dec. 2008.

[189] R. V. Morris et al., "Mössbauer mineralogy of rock, soil, and dust at Meridiani Planum, Mars: Opportunity's journey across sulfate-rich outcrop, basaltic sand and dust, and hematite lag deposits," *J. Geophys. Res.*, vol. 111, p. E12S15, Dec. 2006.

[190] G. Klingelhöfer et al., "Athena MIMOS II Mössbauer spectrometer investigation," *J. Geophys. Res*, vol. 108, no. 12, p. 8067, 2003.

[191] W. H. Farrand, J. F. Bell III, J. R. Johnson, S. W. Squyres, J. Soderblom, and D. W. Ming, "Spectral variability among rocks in visible and near-infrared multispectral Pancam data collected at Gusev crater: Examinations using spectral mixture analysis and related techniques," *J. Geophys. Res.*, vol. 111, p. E02S15, 2006.

[192] W. H. Farrand et al., "Visible and near-infrared multispectral analysis of rocks at Meridiani Planum, Mars, by the Mars Exploration Rover Opportunity," *J. Geophys. Res.*, vol. 112, p. E06S02, Apr. 2007.

[193] J. Johnson et al., "Mineralogic constraints on sulfur-rich soils from Pancam spectra at Gusev crater, Mars," *Geophys. Res. Lett.*, vol. 34, no. 13, p. L13202, 2007.

[194] M. S. Rice et al., "Silica-rich deposits and hydrated minerals at Gusev Crater, Mars: Vis-NIR spectral characterization and regional mapping," *Icarus*, vol. 205, no. 2, pp. 375-395, Feb. 2010.

[195] M. Parente, J. L. Bishop, and J. F. Bell III, "Spectral unmixing for mineral identification in pancam images of soils in Gusev crater, Mars," *Icarus*, vol. 203, no. 2, pp. 421-436, Oct. 2009.

[196] G. Klingelhöfer, R. V. Morris, P. A. de Souza, B. Bernhardt, and A. S. Team, "The miniaturized Mössbauer Spectrometer MIMOS II of the Athena Payload for the 2003 MER Missions," in *Sixth International Conference on Mars*, 2003, p. 3132.

[197] G. Klingelhöfer and R. V. Morris, "Iron mineralogy and aqueous alteration on Mars from the MERM¨ossbauer spectrometers," in *The Martian Surface: Composition, Mineralogy, and Physical Properties*, J. F. Bell III, Ed. Cambridge University Press, 2008, pp. 339-365.

[198] R. Deen, D. Alexander, and J. Maki, "Mars image products: science goes operational," in *Proceedings of the 8th International Conference on Space Operations (SpaceOps), Montreal, Canada*, 2004, no. 1.

[199] R. G. Deen and J. J. Lorre, "Seeing in Three Dimensions: Correlation and Triangulation of Mars Exploration Rover Imagery," in *IEEE International Conference on Systems, Man and Cybernetics*, 2005, vol. 1.

[200] S. Ray and R. H. Turi, “Determination of number of clusters in k-means clustering and application in colour image segmentation,” in *Proceedings of the 4th international conference on advances in pattern recognition and digital techniques*, 1999, pp. 137–143.

[201] A. D. Rogers and O. Aharonson, “Mineralogical composition of sands in Meridiani Planum determined from Mars Exploration Rover data and comparison to orbital measurements,” *J. Geophys. Res.*, vol. 113, p. E06S14, May 2008.

[202] J. F. Bell III and D. Bustani, “Correlations Between Multispectral and Compositional Properties of Soils and Rocks at the Mars Pathfinder Landing Site,” *Lunar and Planetary Science Conference*, vol. 30, p. 1388, 1999.

[203] P. Bertelsen et al., “Magnetic properties experiments on the Mars exploration Rover Spirit at Gusev Crater.,” *Science*, vol. 305, pp. 827-829, Aug. 2004.

[204] P. Geladi, “Partial least-squares regression: a tutorial,” *Analytica Chimica Acta*, vol. 185, no. 1, pp. 1-17, 1986.

[205] M. J. Adams and J. R. Allen, “Quantitative X-ray fluorescence analysis of geological materials using partial least-squares regression,” *The Analyst*, vol. 123, no. 4, pp. 537-541, 1998.

[206] C. Munson, F. Deluciajr, T. Piehler, K. Mcnesby, and a Miziolek, “Investigation of statistics strategies for improving the discriminating power of laser-induced breakdown spectroscopy for chemical and biological warfare agent simulants,” *Spectrochimica Acta Part B: Atomic Spectroscopy*, vol. 60, no. 7-8, pp. 1217-1224, Aug. 2005.

[207] R. V. Morris et al., “Identification of carbonate-rich outcrops on Mars by the Spirit rover.,” *Science*, vol. 329, no. 5990, pp. 421-4, Jul. 2010.

[208] A. Cousin et al., “Depth Profiles Studies Using ChemCam,” *Lunar and Planetary Science Conference*, vol. 42, no. 1963, 2011.

[209] R. ARVIDSON, “Coordinated CRISM and Opportunity Observations to Determine the Mineralogy and Geologic History of Meridiani Planum,” in *2011 GSA Annual Meeting in Minneapolis*, 2011, pp. 167-3.

[210] K. Lewis and O. Aharonson, “Stratigraphic analysis of the distributary fan in Eberswalde crater using stereo imagery,” *J. Geophys. Res.*, vol. 111, p. E06001, 2006.

[211] L. Galluccio, O. Michel, P. Bendjoya, and E. Slezak, “Unsupervised Clustering on Astrophysics Data: Asteroids Reflectance Spectra Surveys and Hyperspectral Images,” in *Classification and Discovery in Large Astronomical Surveys*, 2008, pp. 165-171.

[212] G. Marzo, T. Roush, A. Blanco, S. Fonti, and V. Orofino, “Cluster analysis of planetary remote sensing spectral data,” *J. Geophys. Res.*, vol. 111, p. E03002, 2006.

[213] E. Merenyi, W. H. Farrand, and P. Tracadas, “Mapping surface materials on Mars from mars pathfinder spectral images with HYPEREYE,” *International Conference on Information Technology: Coding and Computing, 2004. Proceedings. ITCC 2004.*, vol. II, pp. 607-614, 2004.

[214] H. Bischof, W. Schneider, and A. J. Pinz, “Multispectral classification of Landsat-images using neural networks,” *Geoscience and Remote Sensing, IEEE Transactions on*, vol. 30, no. 3, pp. 482–490, May 1992.

[215] P. A. de Souza Jr, “Automation in Mossbauer Spectroscopy Data Analysis,” *Laboratory Robotics and Automation*, vol. 11, no. 1, pp. 3–23, 1999.